The effects of multi-directional loading on soil liquefaction

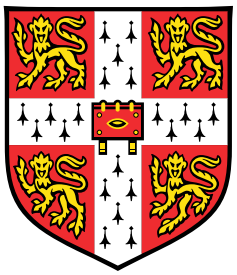

Mengchen Sun

Department of Engineering
University of Cambridge

This dissertation is submitted for the degree of
Doctor of Philosophy

St Edmund's College

May 2019

To my loving family ...

Declaration

I hereby declare that except where specific reference is made to the work of others, the contents of this dissertation are original and have not been submitted in whole or in part for consideration for any other degree or qualification in this, or any other university. This dissertation is my own work and contains nothing which is the outcome of work done in collaboration with others, except as specified in the text and Acknowledgements. This dissertation contains fewer than 65,000 words including appendices, bibliography, footnotes, tables and equations and has fewer than 150 figures.

Mengchen Sun
May 2019

Acknowledgements

I would like to express my deep gratitude to my supervisor, Dr. Giovanna Biscontin, for her insightful suggestions and enthusiastic supervision on this research work, which inspired me a lot and convinced me that the excitement of research is anything but exaggerated.

I would like to thank technicians John Chandler, Kristian Pether, Mark Smith, Chris McGinnie, Richard Adams at the Schofield centre, who helped me to install instruments, test the apparatus and machine testing accessories. I would like to thank Cooper Technology for modifying the testing apparatus, and New Era Machining for machining the redesigned top caps.

I wish to extend my thanks to the lovely colleagues in the research group: Dr. Yingyan Jin, Dr. Jeffery Lau, Dr. Stephan van Eeden, Dr. Ramesh Kannan Kandasami, Dr. Ying Chen, Gianmario Sorrentino, Christopher Wilkes, Charalampos Konstantinou, Eman Al-Swaity, Dr. Khalid Alhaj Abdalla, and lately Jikai Guo, Helen Sims for making this group so amazing. I wish to thank Prof. Gopal Madabhushi, Dr. April Bowmen, Dr. Gue Chang Ye, Dr. Njemile Faustin, Dr. Stefan Ritter, Dr. Orestis Adamidis, Dr. Srikanth Madabhushi, Dr. Talia da Silva, Dr. Raz Jabary, Dr. Peter Kirkwood, for their very kind encouragement and discussions at the early stage of my study. I would like to thank Mrs Magdalena Charytoniuk, Chuhan Deng, Fiona Hughes, Thejesh Kumar Garala, Samy Garcia Torres, Deryck Y.K. Chan, Jad Boksmati, Andrei Dobrisan and all the colleagues in Schofield centre for making our laboratory such a lovely place. I would also like to acknowledge the great colleagues who were not based at Schofield centre, Dr. Yuze Wang, Bingyu Zhao, Dr. Xiang Sun, and Tsubasa Sasaki, to name a few.

I would also like to thank all my friends for their friendship and help, which made my life in Cambridge marvelous and memorable. My gratitude goes to Dr. Hongbo Sun, Dr. Qi Wang, Dr. Luoke Hu, Zhiyou Wu, Xiao Xiao, Luming Fan, Kaiqi Hu, Wenkai Guo, Dr. Jinqi Fu, Dr. Jianzhao Geng, Dr. Shanshan Yan, Chao Li, Zixin Huang, Kexin Zhang, Benyi Cao, Tao Zhang, Yunhui Zhang, Wenting Mao, to mention but a few.

And I would like to thank my parents for their everlasting support.

Abstract

Four decades after it was investigated experimentally for the first time, the influence of multi-directional shearing on soil behaviour, especially the undrained behaviour of saturated sands, remains one of the least understood areas in geotechnics. This study developed a new test database on Hostun sand with the modified multi-directional simple shear testing apparatus. The results of uni-directional tests were examined under available analysis frameworks to validate the performance of the adopted testing techniques. Multi-directional tests were analysed and compared with their uni-directional counterparts to illustrate the remarkable change in soil response when loading paths change from uni-directional to multi-directional.

A three-dimensional $\tau - \sigma_v'$ space was established as the extrapolation of the 2D $\tau - \sigma_v'$ plane, with a 3D conical failure surface derived from 2D failure lines. The concept of the failure cone was validated by the tests with various loading paths. The failure cone hypothesis explain the unsolved questions, including why bi-directional linear stress paths do not reach the failure line in the 2D $\tau - \sigma_v'$ plane and why an inverse correlation exists between the limiting excess pore pressure ratio and shear stress amplitude.

A bimodal phenomenon was identified in terms of the phase transformation of sand under multi-directional shearing conditions. Phase transformation states form a conical surface, like failure states, in the tests with circular, oval and figure-8 loading paths but do not fall on a cone in uni-directional and bi-directional linear tests.

The effects of multi-directional loading on soil liquefaction were further investigated from the perspective of liquefaction criteria, liquefaction resistance, development of excess pore pressure and shear strain, as well as the degradation of shear modulus. The definitions of shear stress, shear strain and shear modulus were re-examined in multi-directional loading scenarios. Liquefaction resistance assessment based on $N - CSR$ curves was examined and potential alternative discussed. The shear modulus degradation predictions of Hardin and Drnevich (1972) were found to fit with the newly-proposed multi-directional secant shear modulus.

This study provides novel perspectives to understand the undrained soil behaviour under multi-directional loading and has useful implications for future potential modelling research.

Table of contents

List of figures

List of tables

Nomenclature

AR	Aperture ratio
CO_2	Carbon Dioxide
CSR	Cyclic shear stress ratio
CSR_X	Cyclic shear stress ratio in X direction
CSR_Y	Cyclic shear stress ratio in Y direction
CSR_α	Cyclic shear stress ratio in the direction of static shearing
CSR_{dir}	The maximum CSR across all directions
CSR_{field}	Standardised liquefaction resistance
CSR_{perp}	Cyclic shear stress ratio in the direction perpendicular to that of CSR_{dir}
C_M	Liquefaction resistance correction factor for earthquake magnitude
D_r	Relative density
D_{50}	Median particle diameter
G	Secant shear modulus
G_2	The secant shear modulus of the second loading cycle
G_s	Specific gravity
G_{max}	Small-strain shear modulus
I_s	State index
K_0	Lateral stress coefficient

K_α	Liquefaction resistance correction factor for initial static shearing
K_μ	Liquefaction resistance correction factor for multi-directional loading
K_σ	Liquefaction resistance correction factor for consolidation stress
$K_{0,min}$	The minimum K_0 in a simple shear test
N	Number of cycles
N_L	Number of cycles to liquefaction
PT	Phase transformation
RP	Reversal parameter
R_c	Relative contractiveness
SSR	Shear stress ratio
SSR_X	Shear stress ratio in X direction
SSR_Y	Shear stress ratio in Y direction
$SSR_{X,0}$	Initial shear stress ratio in X direction
$SSR_{Y,0}$	Initial shear stress ratio in Y direction
SSR_{cyclic}	Shear stress ratio in the direction perpendicular to that of initial static shear stress
SSR_{dip}	Shear strain ratio in the dip direction
SSR_{strike}	Shear strain ratio in the strike direction
$SSR_{total,min}$	Maximum resultant shear stress ratio
$SSR_{total,min}$	Minimum resultant shear stress ratio
SSR_{total}	Resultant shear stress ratio
Δu	Excess pore pressure
α	Initial static shear stress ratio
$\delta\gamma_{total}$	Resultant strain increment

ε_a	Axial strain
γ	Shear strain
γ_X	Shear strain in X direction
γ_Y	Shear strain in Y direction
γ_{DA}	Uni-directional double-amplitude shear strain
γ_{dip}	Shear strain in the dip direction
$\gamma_{dir,DA}$	Maximum double-amplitude shear strain across all directions
γ_{dir}	Shear strain in a certain direction
γ_{strike}	Shear strain in the strike direction
$\gamma_{total,DA}$	Double-amplitude total shear strain
γ_{total}	Resultant shear strain
μ_s	Coefficient of kinetic friction
ϕ'	Angle of internal friction
ϕ_{FL}	Angle of the failure line
ϕ_{PT}	Angle of the phase-transformation line
ψ	State parameter
σ_1	Major principal stress
σ_3	Minor principal stress
σ_v	Vertical stress
σ'_v	Effective vertical stress
$\sigma_{v,i}$	Initial vertical stress
τ	Shear stress
τ_X	Shear stress in X direction
τ_Y	Shear stress in Y direction

τ_{cyclic}	Shear stress in the direction perpendicular to that of initial static shear stress
$\tau_{dir,DA}$	Maximum double-amplitude shear stress across all directions
τ_{dir}	Shear stress in a certain direction
τ_{static}	Initial static shear stress
τ_{total}	Resultant shear stress
a, b	Curve fitting parameters
c	Cohesion
e	Void ratio
e_{λ}	Void ratio from isotropic consolidation line
e_{cs}	Void ratio at the critical state
e_{max}	Maximum void ratio
e_{min}	Minimum void ratio
p'	Mean effective stress
q	Deviatoric stress
r_u	Excess pore pressure ratio
$r_{u,1}$	The maximum excess pore pressure in the first loading cycle
$r_{u,max}$	The maximum excess pore pressure ratio in the liquefaction cycle
$r_{u,min}$	The minimum excess pore pressure ratio in the liquefaction cycle
B-value	Skempton's B-value

Chapter 1

INTRODUCTION

1.1 Motivation of the research

Soil liquefaction is a seismic phenomenon experienced by sands, which results in severe damage including foundation failure, sinking and overturning of structures as well as destruction of infrastructure. The loss of life and economic damage induced by soil liquefaction is costly, so there has been much effort towards understanding the cause of liquefaction and the behaviour of saturated sands under cyclic shearing. Early studies focusing on static undrained tests have shown that the occurrence of soil liquefaction is closely related to strain-softening undrained response of sands, which may lead to either unlimited or limited runaway deformation (Castro, 1969). However, it has been widely demonstrated that strain softening is not the exclusive cause of the excessive deformation under cyclic undrained conditions. Cyclic accumulation of plastic strain, termed cyclic mobility, also occurs with or without transient states of zero effective stress states (Castro, 1975; Seed, 1979; Vaid and Chern, 1985; Vaid and Thomas, 1995). It is evident that the type and path of shearing can actively influence the response of sands.

In terms of laboratory research with respect to soil liquefaction, direct simple shear apparatuses, which have been utilised successfully for decades in characterising static and dynamic soil properties, are often preferred, especially when it is desirable to produce a condition where the rotation of the principal stress directions occurs continuously. Most

existing simple shear apparatuses can only shear specimens in a single horizontal direction, and thus preclude the consideration of multi-directional loading paths in experimental work. However, it is widely recognised that earthquakes apply multi-directional cyclic shearing on soils. The differences between the realistic loading conditions and their simplified counterparts hampered the investigation of soil behaviour in actual earthquakes.

To improve the situation, several multi-directional direct shear devices have been developed and a limited number of multi-directional shearing tests on sands have been conducted. Casagrande and Rendon (1978) developed a gyratory shear apparatus and observed that sand behaviours differ greatly when multi-directional loading is involved. Ishihara and Yamazaki (1980) developed another pioneering multi-directional simple shear apparatuses to investigate the effects of the change of loading directions on liquefaction resistance. Subsequently, some researchers used this apparatus to perform multi-directional simple shear tests, concluding that rotation of stress directions tends to result in a lower liquefaction resistance (Fukutake and Matsuoka, 1989; Ishihara and Nagase, 1988; Nagase and Ishihara, 1987; Tokimatsu and Yoshimi, 1982; Yamazaki et al., 1985). Later, DeGroot (1992) developed a new type of multi-directional direct simple shear (MDSS) apparatus at Massachusetts Institute of Technology. Although they used this device to investigate the effect of different directions of static shear loading and ice shear loading on the response of Boston Blue Clay, their observation that the peak undrained resistance of clay was affected significantly by the angle between the two shear forces is similar to the preceding results for sand.

Simultaneously, Boulanger and his colleagues, developed another type of multi-directional simple shear apparatus, the UC Berkeley bi-directional simple shear device (UCB-2D) to study the effects of multi-directional loading on the strength of modified Sacramento River Sand (Boulanger, 1990; Boulanger et al., 1993; Boulanger and Seed, 1995). They observed that stress reversal can exert significant influence on generation of pore water pressure and liquefaction resistance. One of the most comprehensive and systematic investigations into the effect of multi-directional loading and initial static driving shear on the response of sands and clay was conducted with this device by Kammerer (2002), Wu (2002), Biscontin et al. (2004) and colleagues. They confirmed an inverse linear relationship between shear stress

amplitude and limiting pore pressure ratio reported by Boulanger (1990). They also proposed that stress rotation aids particle rearrangement and densification of soil, and that the initial static shear affects the extent of stress rotation. Moreover, the stress rotation appears to be even more important than cyclic stress amplitude in terms of pore pressure generation and shear strain.

Rutherford and Biscontin (2013) developed a new multi-directional direct simple shear apparatus (TAMU-MDSS), which Rutherford (2012) used to investigate the cyclic shear response of Gulf of Mexico Clay. Later, Bernhardt (2013) used this device to validate the numerical simulation with the discrete element method (DEM).

More multi-directional simple shear testing database was developed with the variable direction dynamic cyclic simple shear device (VDDCSS) by GDS (Li et al., 2016; Mirbaha, 2017; Rudolph et al., 2014). However, they conducted equivalent undrained tests rather than actual undrained tests. They adopted constant height conditions, regarding the reduction of vertical stress as the generation of excess pore pressure. Although such a boundary condition is accepted as an effective alternative to actual undrained condition, the actual discrepancies between the methods are difficult to estimate.

Despite all these efforts, multi-directional simple shear test data are still scarce and the effects of multi-directional loading are far from being fully understood. Firstly, there has not been a theoretical framework under which multi-directional simple shear testing results can be interpreted consistently. Furthermore, whether the concepts of failure line and phase transformation line derived for $\tau - \sigma'_v$ plane can be extrapolated into 3D $\tau - \sigma'_v$ space has not been investigated. The reason why the stress paths of bi-directional linear tests cannot reach the failure line remains unanswered. The mechanism responsible for the inverse correlation between limiting excess pore pressure and shear stress amplitude has not been elucidated.

Secondly, the widely adopted liquefaction assessment method proposed by Seed and Harder (1990) has not been assessed in multi-directional loading scenarios. Although the consensus reached by previous studies is that multi-directional loading tends to result in a lower liquefaction resistance, the claimed degree of reduction varies from study to study. Moreover, cyclic shear stress ratio cannot be conveniently defined in multi-directional

shearing conditions, which is challenging for the assessment of liquefaction resistance through $N - CSR$ curves.

Thirdly, there has been little discussion of excess pore pressure development, strain accumulation and shear modulus degradation in multi-directional simple shear loading. The definition of stress, strain and shear modulus needs to be re-explored and modified to provide a compatible interpretation of multi-directional testing results.

Consequently, this study was designed to gain insights into these unsolved questions, using the multi-directional simple shear testing apparatus developed by Rutherford and Biscontin (2013) as the experimental platform with which to develop a new multi-directional test database. The test results were then analysed and discussed to further our understanding on the mechanical response of saturated sand to multi-directional shearing.

1.2 Scope of work

The objective of this project was to investigate the effects of multi-directional loading on soil liquefaction. A series of undrained multi-directional simple shear tests were conducted on saturated Hostun sand with the modified multi-directional simple shear testing apparatus. The top cap of the sample assembly and sample preparation procedures were redesigned to overcome membrane problems caused by the outward water pressure gradient. The desired physical confinement and satisfactory saturation were achieved with the modifications.

Firstly, the uni-directional test results were analysed and compared against available theories regarding undrained behaviour of sands, not only to validate the performance of the modified testing techniques, but also to provide the baseline for further comparisons. Multi-directional tests were then analysed to illustrate how soil behaviour is altered when loading paths change from uni-directional to multi-directional.

The 2D $\tau - \sigma'_v$ plane was extrapolated into the 3D $\tau - \sigma'_v$ space, with the failure line transformed to a conical failure surface. The concept of the failure cone was verified by the tests with bi-directional linear, circular, oval and figure-8 loading paths. The reason why the stress paths of bi-directional linear tests cannot reach the failure line in the 2D $\tau - \sigma'_v$ plane

was elaborated. The inverse correlation between limiting excess pore pressure ratio and shear stress ratio was also explained with the newly-proposed failure cone.

A bimodal phenomenon was identified in the phase transformation of sands. For circular, oval and figure-8 tests, phase transformation states fall onto a conical surface. For uni-directional and bi-directional linear tests, however, phase transformation states do not form a cone.

The effects of multi-directional loading on soil liquefaction were investigated from several aspects of liquefaction assessment and the definition of liquefaction was reassessed. The influence of multi-directional loading on liquefaction resistance was investigated and a potential alternative to the conventional $N - CSR$ based liquefaction assessment method was discussed. The development of excess pore pressure with multi-directional shearing was explored and compared with that in uni-directional tests. The accumulation of shear strain was investigated and its relationship with excess pore pressure clarified. The definition of secant shear modulus was re-examined and a newly-proposed multi-directional secant shear modulus was found to follow the degradation prediction of Hardin and Drnevich (1972) at large strain.

The findings of this study provide new perspectives to understand soil behaviour under multi-directional shearing and have useful implications for potential work including numerical modelling and liquefaction assessment modifications.

1.3 Organisation of the dissertation

Chapter one introduces soil liquefaction and the importance of research into the effects of multi-directional loading. A literature review on the fundamentals of soil liquefaction, element-level testing, as well as the effects of multi-directional loading is presented in chapter two to provide an overview of the current progress of research on these topics.

Chapter three details the simple shear testing techniques used in this study, the properties of Hostun sands, the testing apparatus and discusses the sample preparation methods and membrane problems. The parameters and a summary of the performed tests are also included.

The results of the uni-directional and multi-directional tests are analysed in chapter four and five. Uni-directional test results are compared against the well-established theories to validate the performance of the testing techniques in this study. Multi-directional test results are analysed to determine the differences between the soil behaviour under multi-directional and uni-directional loading conditions.

Chapter six introduces 3D $\tau - \sigma'_v$ space and the concept of a conical failure surface. It demonstrates that the phenomenon that the stress paths of bi-directional linear tests cannot reach the failure line in 2D $\tau - \sigma'_v$ plane and the inverse correlation between limiting excess pore pressure ratio and shear stress ratio can be explained effectively by the failure cone. Conversely, phase transformation exhibits bimodal characteristics, with phase transformation states forming a conical surface in the tests with circular, oval and figure-8 loading paths, but do not produce a cone in uni-directional and bi-directional linear tests.

Chapter seven examines the liquefaction criterion, liquefaction resistance assessment, development of excess pore pressure and shear strain as well as the degradation of shear modulus in multi-directional shearing condition. The challenges are discussed, and the implications are scrutinised.

Lastly, the insights obtained in this study are summarised in chapter eight. The suggestions for future work are also outlined.

Chapter 2

LITERATURE REVIEW

2.1 Fundamentals of soil liquefaction

2.1.1 Undrained monotonic response of saturated sands

Since soil liquefaction was recognised to be a major cause of the damage in the 1964 Niigata Earthquake and Alaska Earthquake, much effort has been made towards developing in-depth understanding of the mechanisms of this phenomenon. It is well established that soil liquefaction is caused by the generation of positive excess pore pressure during shearing.

When saturated loose sand is sheared, it can exhibit a tendency to contract, which will lead to a decrease in volume if excess pore water can dissipate instantly. However, the permeability of sands is usually not large enough to allow instant excess pore water dissipation when subjected to fast earthquake loading. Since pore water is not dissipated rapidly, the volume change of sands is inhibited and positive excess pore pressure is hence generated.

Early studies focusing on monotonic tests showed that the undrained response of saturated clean sands can be generally categorised into three types: flow liquefaction (or strain softening), dilation (or strain hardening) and limited liquefaction (Castro, 1969), as shown in Figure 2.1.

Flow-liquefaction behaviour is commonly observed in very loose sands or the sands under extremely high confining pressures. Pore water pressure accumulates rapidly and can

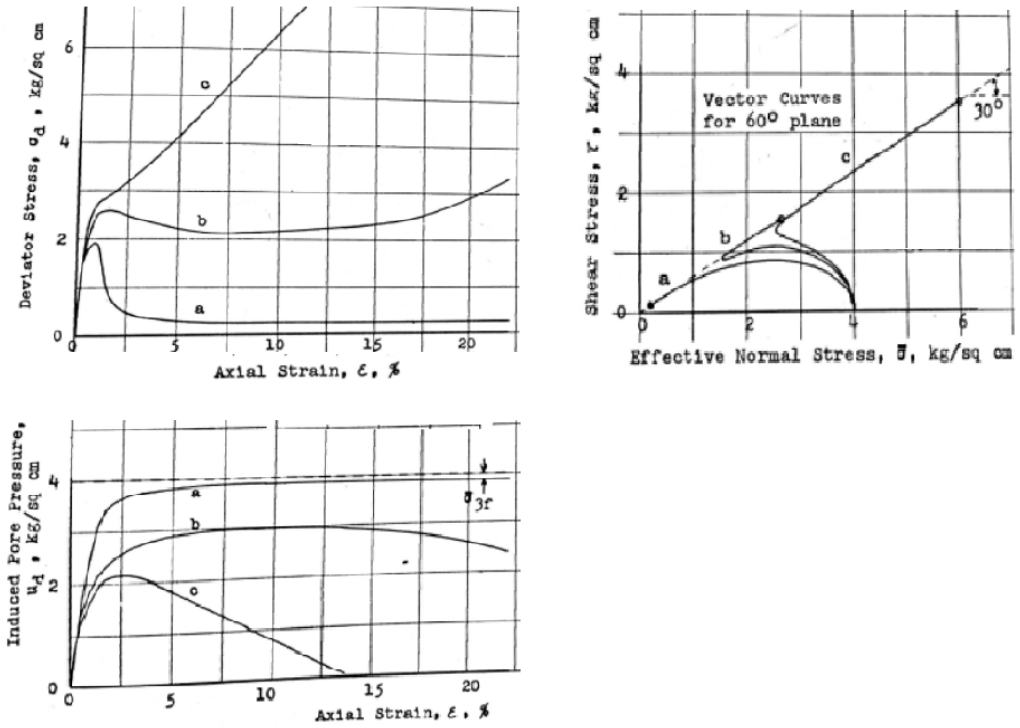

Fig. 2.1 Different types of undrained monotonic response of sands. a: liquefaction; b: limited liquefaction; c: dilation (Castro, 1969)

become equal to the initial confining pressure as a result of the contractile tendency of sand. Sand specimens can thus be softened to such an extent where large strain can occur suddenly and sand cannot bear any increase in shear stress, indicating that the critical state of sands has been reached. In $q - p'$ space, both deviator stress (q) and mean effective stress (p') decreases rapidly after a peak deviator stress is reached, and no regain in either q or p' will be seen thereafter. Similar trends can also be observed in $\tau - \sigma'_v$ space, since both the deviator stress q and shear stress τ are the indicators of the shear strength of sands.

On the contrary, the undrained response of dense sands under moderate confining pressure is dilative. Excess pore water pressure increases in the initial stage of shearing but decreases after a small strain level is accumulated. In $q - p'$ space, mean effective stress may or may not decrease at the early stage depending on the properties of sands, but the deviator stress does not always reduce during the whole process of shearing. Sand never loses its shear strength completely in this case. This dilative behaviour can also be reflected by $q - \varepsilon_a$ plots,

in which deviator stress keeps increasing with the accumulation of axial strain. Critical state cannot be reached within a small range of deviator stress and axial strain.

Limited liquefaction behaviour, by contrast, involves a significant transformation of the sand behaviour. In the early stage of shearing, sand exhibits liquefaction-like response. Positive excess pore pressure is generated, deviator stress drops and a stage of strain developing rapidly without increase in deviator stress is encountered. Nevertheless, as shearing continues, excess pore pressure will hit the peak and then decreases, which marks the transition in the response of sands from contraction to dilation, and liquefaction behaviour is terminated at this point as sand starts to dilate. In $q - p'$ space, this transformation can be reflected by an abrupt turn on stress paths, beyond which a regain in both q and p' is seen.

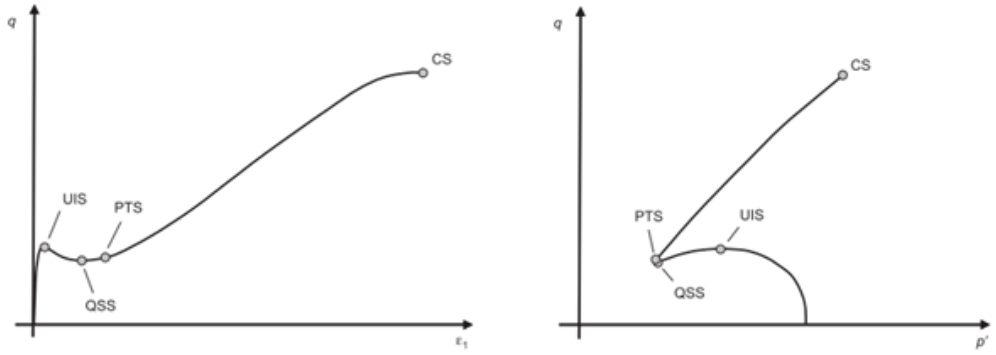

Fig. 2.2 Characteristic states of undrained shearing behaviour of sand: critical state (CS), phase transformation state (PTS), quasi-steady state (QSS), and undrained instability state (UIS).(Murthy et al., 2007)

Conventionally, limited liquefaction behaviour is of the most interest to geotechnical engineers and researchers partly because it is much more dangerous than dilation behaviour but more common than flow-liquefaction, and partly because it contains the features of both of the two other types of soil behaviour. Four distinguishable states can be determined for limited liquefaction behaviour: undrained instability state, quasi-steady state, phase transformation state and critical state, as shown in Figure 2.2 (Murthy et al., 2007). The undrained instability state is the point where the deviator stress reaches a local peak for the first time and liquefaction initiates. After this point, deviator stress keeps decreasing until the quasi-steady state is reached, where a local minimum deviator stress is obtained. It is

termed quasi-steady state because the inclination angle of the $q - \varepsilon_a$ curve becomes zero at this point, suggesting that strain develops without change in stress, just as it does at the critical state. But this is not the true critical state point because the constant deviator stress does not continue to larger strain.

Deviator stress begins to increase again after the quasi-steady state point, while mean effective stress continues to decrease until a local minimum value is reached at the phase transformation state (Ishihara et al., 1975). The minimum mean effective stress is a result of the maximum excess pore pressure, which indicates the undrained response of sands changes from contraction into dilation. In $q - p'$ space, quasi-steady state and phase transformation state are so closely located that they are usually regarded as the same point, but it should be noted that these two states are not the same and their differences become noticeable in $q - \varepsilon_a$ plots. As shearing proceeds thereafter, sands exhibit a dilative response until the critical state is reached, beyond which strain can develop without change of stress. Given the limitation of testing devices, critical state may not be reached if sands exhibit dilative behaviour, but this rarely affects the interpretation of the undrained response of saturated sands. The definitions of the four distinct states are applicable to flow-liquefaction response and dilative behaviour as well, though the former does not show quasi-steady state and phase transformation state, while the latter does not have quasi-steady state.

2.1.2 Undrained cyclic response of saturated sands without fines

As soil liquefaction is a phenomenon that is most commonly triggered by seismic loading, understanding the undrained behaviour of sands subjected to fast cyclic shearing becomes important. Much research has been conducted towards this goal and huge progress has been made. Generally, seismic soil liquefaction results from the generation of positive excess pore pressure induced by cyclic ground motion. When pore water pressure increases to be equal to the initial confining pressure, soil liquefaction is initiated and flow-type deformation ensues (Seed and Lee, 1966).

The earliest laboratory attempt to investigate cyclic soil liquefaction was made by Seed and Lee (1966). They conducted cyclic triaxial tests on sands with different densities to

observe and compare undrained response of loose and dense sands. The stress-controlled testing results for loose and dense sands from Seed and Lee (1966) are presented in Figure 2.3. For loose sands, both the peak and residual pore pressure of each cycle accumulate smoothly in the pre-liquefaction cycles until a sudden jump takes place and peak pore pressure equals the initial confining pressure. Large or unlimited shear strain will suddenly occur almost simultaneously with the abrupt increase of pore pressure. For dense sands, by contrast, excess pore pressure also increases within the pre-liquefaction cycles but with a lower accumulation rate. After pore pressure equals the initial confining pressure, however, there is not a sudden increase in shear strain; instead, shear strain develops gradually.

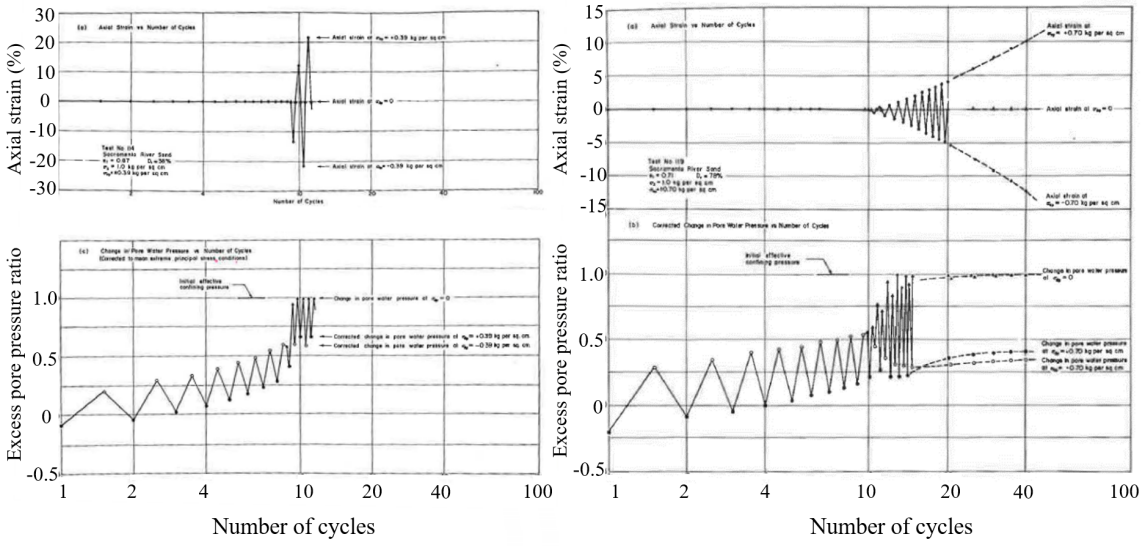

(a) Loose sands

(b) Dense sands (cyclic mobility)

Fig. 2.3 Stress-controlled cyclic triaxial test results for loose and dense sands (modified from Seed and Lee (1966))

Much research has been carried out since Seed and Lee published their pioneering paper. An important feature of the strain development of dense sands under cyclic loading was unveiled: there appears to be a cyclic strain level which cannot be exceeded no matter how many cycles of loading are applied. It suggests dense sands can withstand unlimited number of cycles of a given stress amplitude without witnessing runaway deformation (Seed, 1979).

This type of response was termed “cyclic mobility” by Castro (1975) or “initial liquefaction with limited strain potential” by Seed et al. (1975).

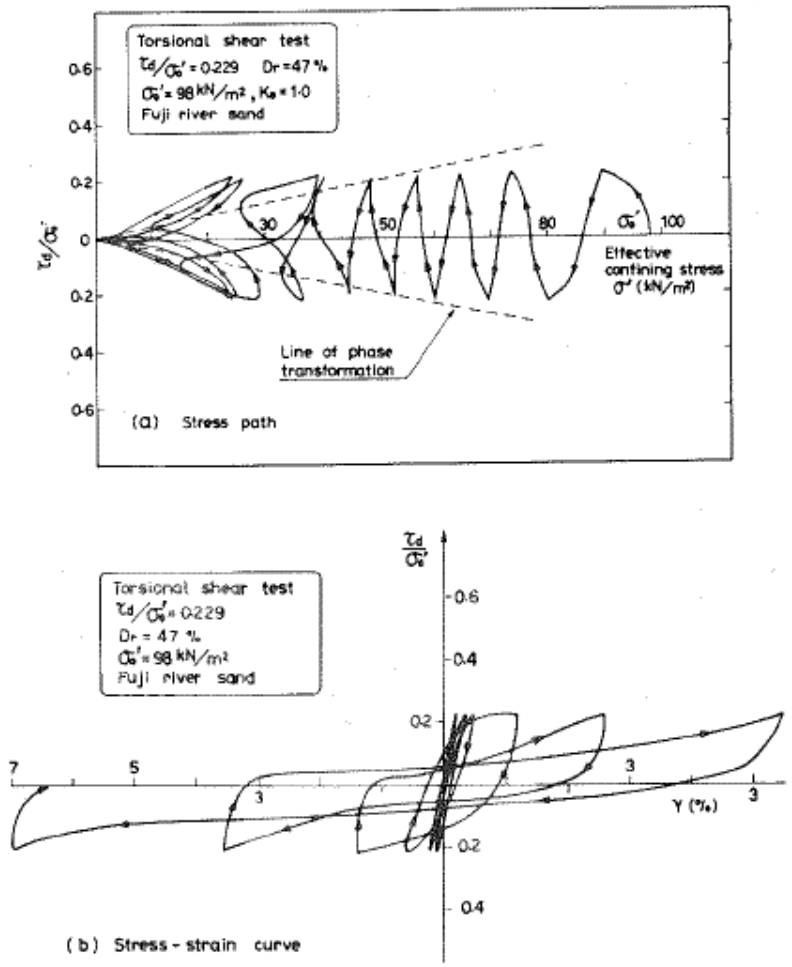

Fig. 2.4 Stress parth and stress-strain curve for loose sand (Ishihara, 1985)

The differences between the response of loose sands and dense sands can be more clearly observed in stress-strain hysteresis loops as suggested by Ishihara (1985). The results of Ishihara (1985) are shown in Figure 2.4 and Figure 2.5. When excess pore pressure equals the initial confining pressure, the deformation of loose sands develops abruptly, resulting in the stress-strain loops being enlarged and flattened rapidly. It takes only a few cycles for shear strain to become tremendous. For dense sands, the shear strain develops gradually and the stress-strain loops also grow in such a manner.

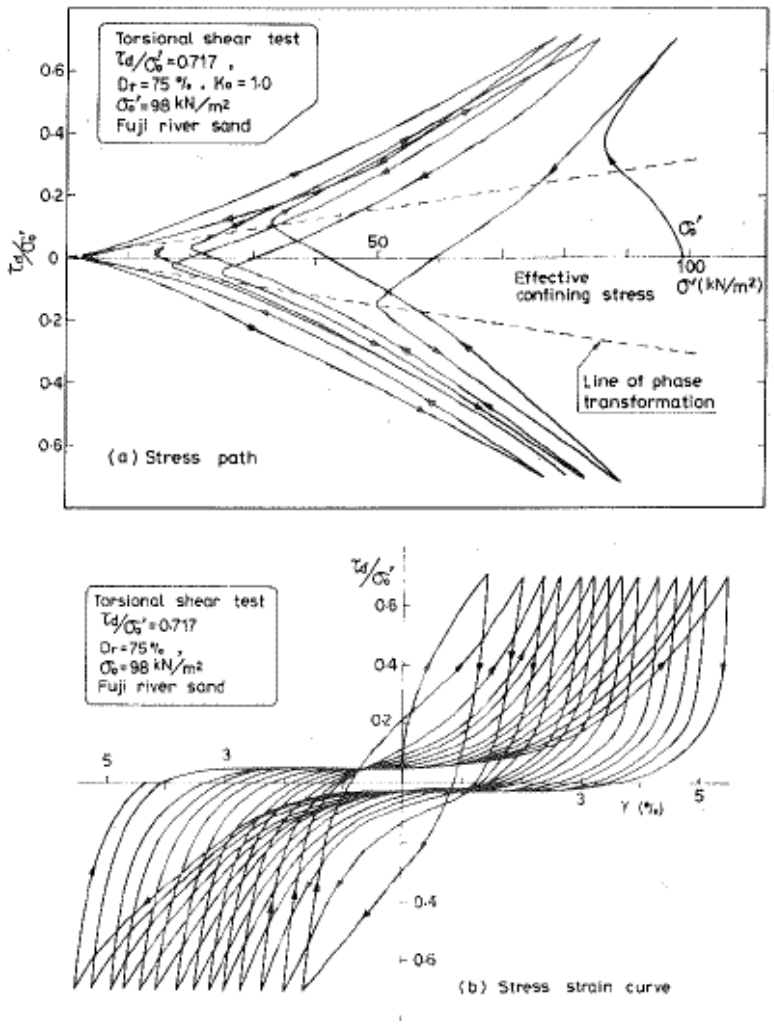

Fig. 2.5 Stress parth and stress-strain curve for dense sand (Ishihara, 1985)

While pattern of strain development differs for loose sands and dense sands, their response in the stress space is rather similar. The cyclic behaviour of sands in terms of stress is closely associated with the phase transformation states of sands. As defined in the preceding section, phase transformation lines divide the stress space of sands into a contractive region and a dilative region. Crossing the phase transformation line means the behaviour of sands changes from contraction to dilation or vice versa. Before the stress path intersects the phase transformation lines, positive excess pore water pressure accumulates steadily with cyclic stress application, accompanied by a steady decrease in effective confining pressure.

Once the stress path intersects the phase transformation lines, the behaviour of sands will change dramatically. During the loading phase of a cycle, sands exhibit generally contractive behaviour prior to reaching the phase transformation line. Excess pore pressure increases and shear strain develops rapidly without much change in shear stress (the section of the stress-strain loops corresponding to this state is relatively flat). After the phase transformation line is crossed, sands exhibit a dilative response, with excess pore pressure decreasing and stress-strain curves becoming steep. The soil behaviour during the loading phase under cyclic loading resembles the limited-liquefaction behaviour under monotonic shearing. During the unloading phase, by contrast, the dilation state of sands is reversed. Excess pore pressure increases with decreasing loading. Therefore, if a stress cycle involves crossing the phase transformation line, the change of excess pore water pressure within this cycle should contain two valleys (at the maximum shear stress points) and two peaks (at the phase transformation points), as shown in Figure 2.6.

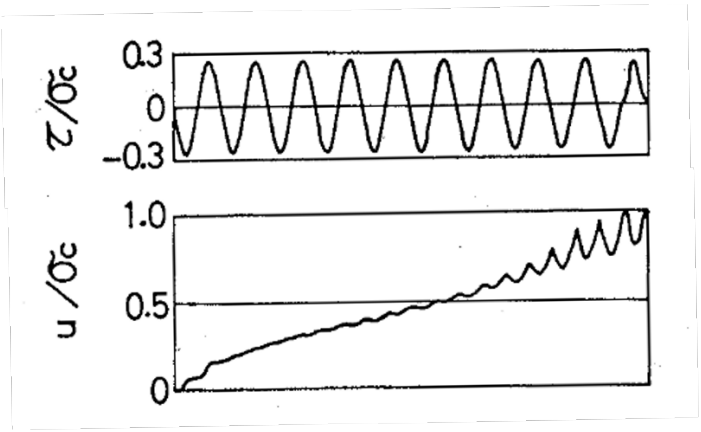

Fig. 2.6 Typical records of the measurements of shear stress and excess pore pressure (Ishihara and Yasuda, 1975)

2.1.3 Interpretation of undrained monotonic behaviour of saturated sand in Critical State Theory

It has been suggested by numerous researchers that initial void ratio and effective confining pressure can exert an influence on the behaviour of soil. Roscoe et al. (1958) summarised the

test results of Hvorslev and Taylor to develop Critical State theory. Readers are directed to the paper of Roscoe et al. (1958) and the book of Schofield and Wroth (1968) and Schofield (2005) for more details on this well-established subject. Debates on whether critical states are the same as the steady states of Casagrande (1936) were settled by Been et al. (1991). Jefferies and Been (2015) attributed the differences previously observed between the two concepts to different testing methods rather than an intrinsic behaviour. For the sake of simplicity and consistency, these two states are regarded as the same in this work.

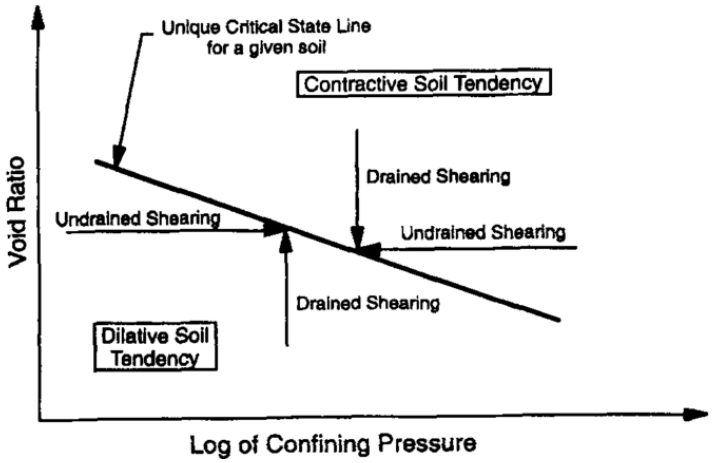

Fig. 2.7 Schematic diagram of critical state theory (Yamamuro and Lade, 1998)

According to Critical State theory, initial void ratio and initial confining pressure collectively determine the initial state of soil. If the initial state of sands is located in the 'wet' region (above the critical state line in $e-\sigma'$ or $e-\log\sigma'$ plane as shown in Figure 2.7), sands will show a contractive behaviour under monotonic shearing, which can lead to liquefaction. On the contrary, if the initial state of sand is located on the 'dry' side, sand exhibits dilative tendency, preventing liquefaction under monotonic shearing.

To illustrate the interpretation of undrained monotonic response of clean sands in the Critical State framework, Figure 2.8 is presented here to give a typical example of undrained monotonic triaxial test on sand specimens with the same initial void ratios, but different initial confining pressure. For specimens with equal initial void ratios, higher confining pressure leads to a more contractive behaviour because higher confining pressure pushes the

initial states towards the 'wet' side, whereas lower initial confining pressure leads to a more dilative behaviour.

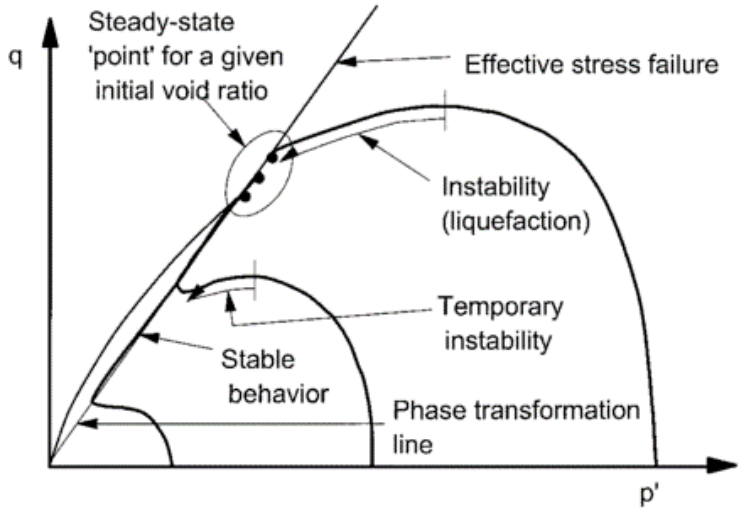

Fig. 2.8 Undrained monotonic behaviour of sands with different initial confining pressure (Yamamuro and Covert, 2001)

Since Critical State Theory has been demonstrated as capable of explaining the instability of saturated sands, whether it is effective in predicting liquefaction potential becomes an intriguing topic. Based on Critical State theory, parameters which can reflect the relative relationship between initial states and critical states can be used as the indicator of different types of sand behaviour. Efforts have thus been made towards this subject, among which the most well known is the state parameter ψ proposed by Been and Jefferies (1985). ψ is defined as:

$$\psi = e_\lambda - e_{cs} \tag{2.1}$$

where e_{cs} is the void ratio given by critical state line at a designated confining stress, and e_λ is the void ratio determined from the one-dimentional isotropic consolidation line at the same confining stress. The definition is illustrated in Figure 2.9. A positive state parameter generally indicates sands have initial states on the 'wet' side and hence a potential for liquefaction.

While this approach sounds reasonable, the state parameter was criticized by Ishihara (1993) for its inability to give reliable analysis for loose sands under low confining pressure.

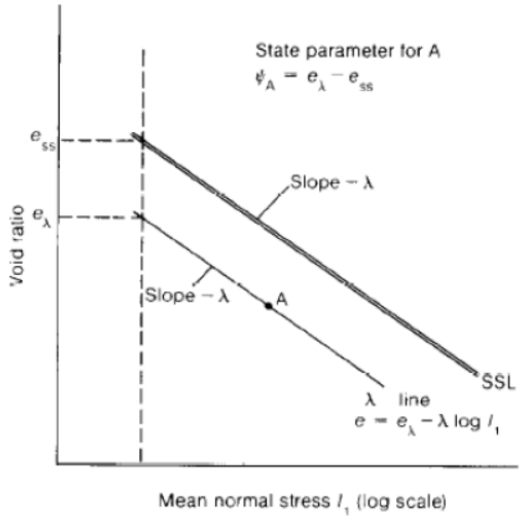

Fig. 2.9 Defination of state parameter ψ (Been and Jefferies, 1985)

Other types of parameters were then proposed by researchers to provide alternatives to state parameter. For example, Ishihara (1993) proposed a state index I_s based on the void ratio of sands at quasi-steady state. Verdugo and Ishihara (1996) proposed relative contractiveness R_c which was defined in a similar way to relative density. Nevertheless, all these parameters have their own limitations, hindering their application (Coelho, 2007). Furthermore, when fines content is involved, all these state parameters seem to lose meaning. Thus, the state parameter proposed by Been and Jefferies (1985) remains the most used parameter to characterise the state of sands, based on which many well-known models, such as Nor-sand (Jefferies, 1993), were established.

Although to interpret test results with state parameter sounds attractive, however, it is out of the scope of this study. On the one hand, sands usually cannot reach critical state before shear strain accumulates to a huge amount. The performance of available testing apparatuses, however, become inevitably inadequate at such a large level of shear strain. It is difficult to obtain consistent critical states, if at all, and the interpretation of test results with state parameter may thus mislead the investigation of the primary subject of this study. On the other hand, since the principal objective of this study is to investigate the effects of loading paths on soil liquefaction, the variation of other factors including density and confining pressure is restrained to a small range to minimise their interference. Thus, the

Table 2.1 Idealized in situ boundary conditions for earthquake-induced soil liquefaction (After Kammerer (2002))

Simplification	Idealized in situ Boundary condition
Constant vertical load	Although there are cases where the vertical load (overburden) is reduced, for a majority of cases the soil above the liquefiable layer remains in place
No lateral strain	It is assumed that the deposit is of large lateral extent such that lateral strains can be neglected
Constant height	Because the volume is constant and there are no lateral strains, the height must also be constant
Constant volume	No drainage or pore pressure redistribution during loading

effects of state parameter cannot be examined systematically in this study, though a study of it is recommended for future work.

2.2 Element-level laboratory testing for soil liquefaction

To investigate the response of soil whose behaviour is largely dependent on the in situ condition, the most important and essential consideration is certainly to reproduce realistic boundary conditions as much as possible. In terms of earthquake-induced soil liquefaction, the cyclic shear stress induced on soil elements is primarily due to the upward propagation of horizontally polarised shear waves (Seed, 1979). The idealized in situ stress condition experienced by a soil element under a level ground surface is presented in Figure 2.10, while the idealized in situ boundary condition for soil liquefaction was summarized by Kammerer (2002) in table 2.1. In situ testing would be the ideal way to study the accurate response of soil. However, inevitable inconveniences arise from the lack of low-cost methods to apply loading in field, measure soil response and achieve soil variability in a controlled manner, which makes it unfeasible to conduct in situ research extensively, especially in the area of earthquake-induced soil liquefaction.

Many laboratory experimental techniques were developed to provide alternative research method to in situ testing. They can be divided into two primary categories: physical modelling and element-level testing. Physical modelling uses devices including centrifuge, shaking

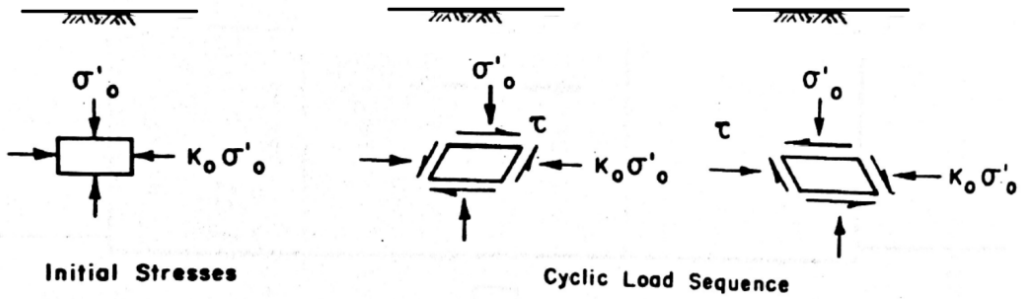

Fig. 2.10 Idealized field loading condition (Seed, 1979)

table, etc. to model the soil and the structures at single or multiple gravity levels. Physical modelling is suitable for research into failure mechanisms, settlement distribution and pore water movement. It can replicate the in situ conditions to a large extent, which makes it suitable for boundary value problems, but the accuracy of the results from such testing still suffers from the disturbance caused by testing devices and the limitations in terms of measurement techniques.

In contrast, element-level testing involves making uniform soil specimens from which the behaviour of a soil "element" can be investigated. Due to the inability to simulate pore water redistribution across soil layers, the liquefaction resistance evaluation from element-level tests can be rather different from reality. However, fundamental trends of soil behaviour and liquefaction resistance can be reflected by element-level test results, making it still one of the most useful research tools in geotechnics. Although the ability to replicate in situ condition is very limited and the effectiveness of element-level experiment results can be affected by issues such as imperfect sample preparation and inhomogeneous specimen deformation, this testing method is still the most convenient research path when the amount of variables is large and required number of tests is high.

There are three most widely used element-level testing methods: triaxial testing, simple shear testing and torsional testing. As they all have their own advantages and limitations, the trade-offs must be evaluated before the decision is made on methodology. Since element-level laboratory testing will be the main research method of this study, a review of different element-level laboratory testing methods is presented in this section to clarify the research methodology.

2.2.1 Triaxial testing

The earliest attempt to use triaxial testing to investigate the undrained behaviour of soil under an earthquake scenario was made by Seed and Lee (1966). They carefully analysed the stress conditions of the triaxial tests and suggested that earthquake loading can be simulated through triaxial testing with necessary corrections on measured pore water pressure, as shown in Figure 2.11. As triaxial testing devices had already been available and easily accessible around the world by that time, their implication ignited the passion of researchers all over the world, making triaxial testing a favourite in the field of soil liquefaction research.

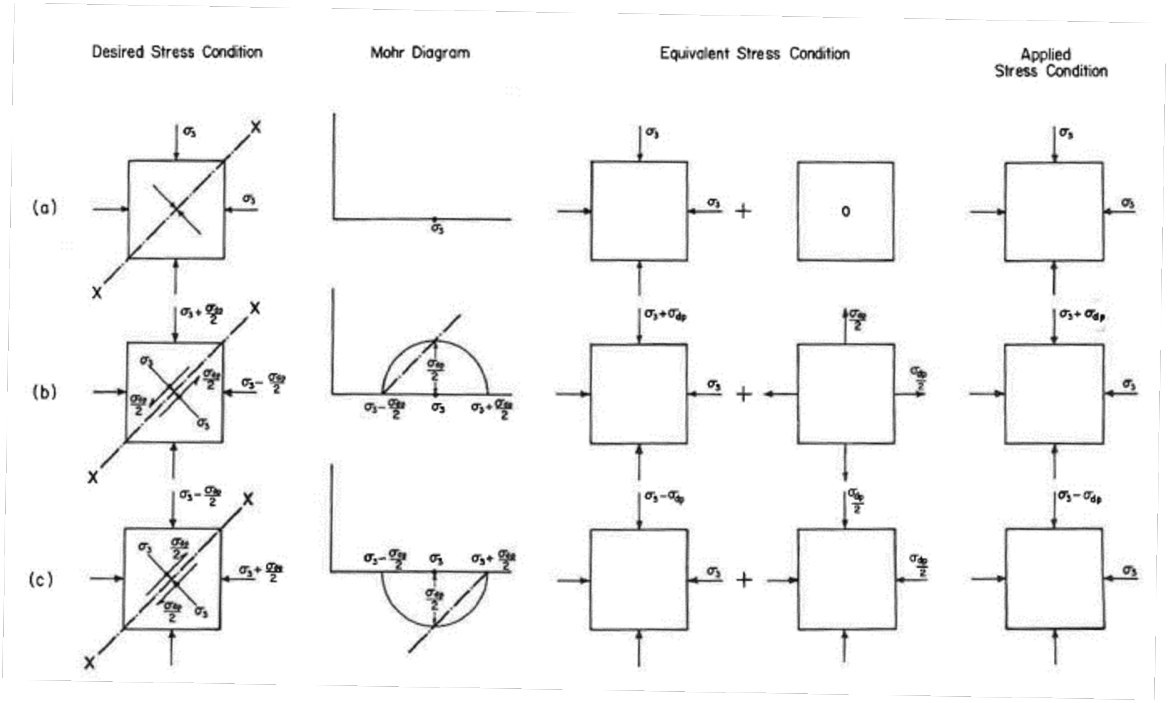

Fig. 2.11 Stress conditions for triaxial test on saturated sand under simulated earthquake loading conditions (Seed and Lee, 1966)

Triaxial tests can be divided into two categories according to the loading condition applied. If the confining stress is smaller than the axial stress (case b in Figure 2.11), the specimen will contract, and this condition is termed compression. On the contrary, if the confining stress is larger than the axial stress (case c in Figure 2.11), the specimen will extend in the axial direction, and this stress scenario is extension. The compression condition and extension condition create shearing on two principal planes perpendicular to each other,

which is equivalent to applying shearing on a single plane if the specimen is an idealized soil element. However, realistic specimens are not an ideal soil element, and the shearing applied on two perpendicular planes usually leads to different soil responses. In cyclic triaxial tests which involve both of the two loading conditions, the principal stress axes rotate 90° instantaneously when the stress condition changes from compression to extension or vice versa. They do not describe actual shear wave propagation in the soil with smooth rotation of principal stresses.

In terms of boundary conditions encountered in soil liquefaction problem, actually none of the conditions in table 2.1 can be maintained in triaxial testing. To start with, the vertical load has to change since shearing is applied through axial loading, although according to Seed and Lee (1966), the normal stress working on the shearing plane can be kept constant. As for lateral strain, since the membrane used to isolate soil from cell water is not reinforced, triaxial specimens usually experience some lateral strain (usually bulging) during shearing, unless cell pressure is carefully controlled and adjusted with loading to counter lateral deformation. Correspondingly, although the overall volume of specimen can be kept constant in undrained triaxial tests, the local volume can change and pore water redistribution may occur during shearing due to the deformation of soil samples (DeGroot et al., 1994; Escribano et al., 2018). The difference between triaxial boundary conditions and in situ boundary conditions, in addition to the abrupt stress rotation issue, makes triaxial testing a less desirable method to investigate earthquake-induced liquefaction. Thus, if a database is to be established for development of numerical modelling, triaxial tests should not be the preferred testing method.

2.2.2 Simple shear testing

Simple shear testing has been used in geotechnical research for many decades. Various versions of simple shear devices have been developed by different researchers (Bjerrum and Landva, 1966; Boulanger, 1990; Casagrande, 1976; DeGroot, 1992; Franke et al., 1979; Ishihara and Yamazaki, 1980; Roscoe, 1953; Rutherford and Biscontin, 2013). Although some discrepancies exist in the results obtained with different apparatuses, simple shear testing techniques, as a whole, are still regarded as an effective element-level test method to

replicate in situ loading conditions shown in Figure 2.10. When it comes to the effects of multi-directional loading, the advantages of simple shear test become even more compelling.

The earliest use of simple shear in the study of earthquake-induced soil liquefaction was conducted by Peacock (1968) with the type of simple shear apparatus designed by Roscoe (1953). They compared their test results with those obtained with triaxial testing from Seed and Lee (1966) and found the liquefaction resistance obtained from cyclic simple shear test is much lower than that from cyclic triaxial test, suggesting simple shear can give more reliable results due to its ability to provide closer simulation of the stress conditions in the field.

The limitations of simple shear test, however, lie in three major aspects. The foremost drawback is its inability to measure lateral stresses. In NGI-type simple shear devices which use short and wide specimens, either a stack of rings or a wire-reinforced membrane is used to confine the specimen and ensure zero lateral strain. As a result, the measurement of lateral stress with conventional stress monitoring techniques becomes impossible. The lack of information about lateral stress results in the inability to determine the stress state accurately, which makes it sometimes necessary to designate a K_0 value to conduct stress state determination, increasing the inaccuracy of the analysis. No effective solution to this problem has been proposed, and this disadvantage continues to be the weak point of this testing technique. This inability is acceptable if it does not affect the accuracy of the test results of interest, which, fortunately, is often the case in research of soil liquefaction.

The second significant drawback of simple shear test rests in the difficulty in controlling the drainage condition. Since back pressure is not usually used in simple shear test, full saturation is hard to maintain and direct measurement of pore water pressure cannot be made. However, this problem has been overcome by the recent versions of simple shear devices, such as the ones reported by Boulanger (1990) and Rutherford and Biscontin (2013). A cell chamber similar to that used in triaxial devices was introduced, which allows the application of back pressure to ensure a full saturation condition. Excess pore water pressure can be measured directly using these apparatuses. These improvements have made the simple shear test results much more accurate and make in-depth investigation of the behaviour of saturated or partly saturated soil possible.

The third major drawback of existing simple shear devices is the lack of applied complementary stresses to the vertical boundaries of the specimen. This discrepancy from the in situ stress conditions leads to such a result that the moment created by the shear stresses on horizontal planes cannot be countered or balanced. Soil specimens thus have a tendency to rotate, resulting in stress concentrations and the change of local density at the portion where stress concentrations occur (Casagrande, 1976). Nevertheless, the influence of this problem can be minimized by using specimens having large diameter-to-height ratio. As suggested by Franke et al. (1979), a diameter-to-height ratio of 3.75 and 7.5 does not give much difference on undrained cyclic test results, indicating that a diameter-to-height ratio over 3.75 is large enough to minimize the effects of this issue. This conclusion was also supported by Vucetic and Lacasse (1982) and has been widely accepted.

In conclusion, most of the major drawbacks of simple shear test can be minimized or overcome by advanced testing devices with careful considerations, except for the lack of information about lateral stress. In this study, although the unknown lateral stress restricts the ability to assess the variation of K_0, it does not influence the investigation into the effects of multi-directional loading in the $\tau - \sigma'_v$ space. Therefore, the simple shear test is a reasonable choice for this research.

2.2.3 Torsional shear testing

Two primary types of torsional shear test were developed to provide alternatives to triaxial test and simple shear test: hollow cylinder test and non-hollow torsional shear test. The non-hollow torsional shear test which uses tall cylindrical sample is so similar to the triaxial test in many aspects that it was called triaxial torsion shear test by Ishihara and Li (1972). By contrast, the torsional ring shear uses short soil sample, which resembles the simple shear test. The torsional ring shear test is one of the best element-level test methods to obtain residual strength condition because it can achieve “an unlimited amount of continuous shear displacement” (ASTM D6467-13, 2013), with which the residual shear strength of soil can be adequately mobilised.

Hollow cylinder testing further increases the number of controllable stress components by replacing the centre cylinder of the soil specimen with water, through which an interior cell pressure can be applied and controlled in addition to the exterior cell pressure. The specimen of a typical hollow cylinder test is shown in Figure 2.12. The advantage in achieving complex stress paths and stress states and improving the non-uniform strain distribution along the radius has made hollow cylinder test preferable to its non-hollow counterpart in the research on soil liquefaction.

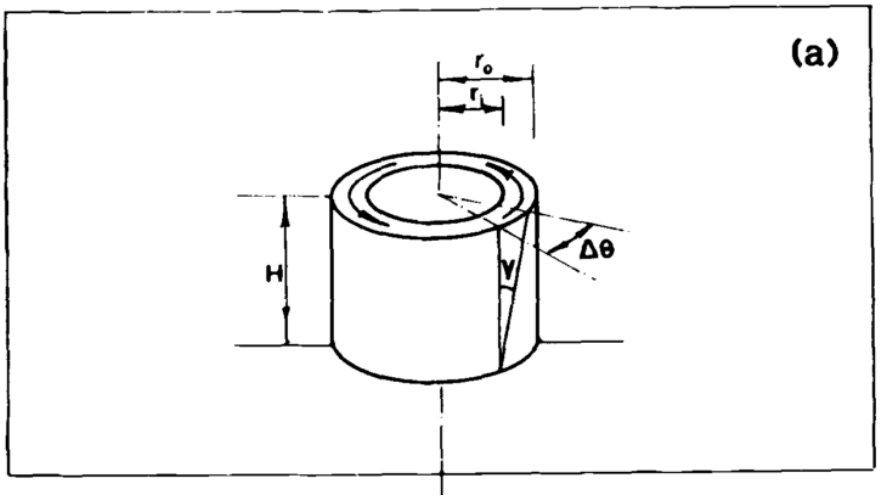

Fig. 2.12 A hollow cylinder specimen under torsional shear (Ampadu and Tatsuoka, 1993)

Compared with the triaxial test, the hollow torsional shear test can achieve continuous rotation of principal stresses and controls more stress components. Compared with simple shear, torsional shear allows measurement of the lateral stress and can shear the specimen into the large strain range.

Nevertheless, the hollow cylinder test has limitations as well. Many drawbacks of the triaxial test similarly exist in the hollow cylinder test. On the one hand, the measurement of lateral stress is achieved at the price of the development of lateral strain and local volume change, reducing the reliability in terms of the boundary conditions for earthquake-induced liquefaction. On the other hand, general multi-directional loading paths cannot be achieved conveniently in either the hollow cylinder torsional test or the torsional ring shear test. Since the objective of this study is to investigate the effects of multi-directional loading on soil

liquefaction, the torsional shear test is not the appropriate methodology choice, even though it features the advantage of a known lateral stress.

2.3 Multi-directional loading

Earthquakes apply shear loading on more than one direction. As waves propagate through layered geological materials of decreasing density, the direction of propagation becomes more vertical, resulting in the general simplification of treating seismic waves as vertical propagating and horizontally polarised. The earthquake, however, is not limited to one direction on the horizontal plane. An example of seismometer traces recorded during San Fernando Earthquake is shown in Figure 2.13. The multi-directional characteristic of earthquake loading is evident.

Fig. 2.13 Seismometer traces recorded in Dry Canyon Dam during 1971 San Fernando Earthquake (Pyke et al., 1975)

Multi-directional loading on the horizontal plane is widely recognised to have significant influence on the behaviour of soil. Pyke et al. (1975) conducted shake table tests to study the settlement of sands. A schematic of the gyratory loading path they used and the test results from their study is presented in Figure 2.14. They compared the settlement induced

by uni-directional loading with that by gyratory loading path, and found the accumulation of settlement under gyratory loading is approximately twice that in uni-directional counterpart.

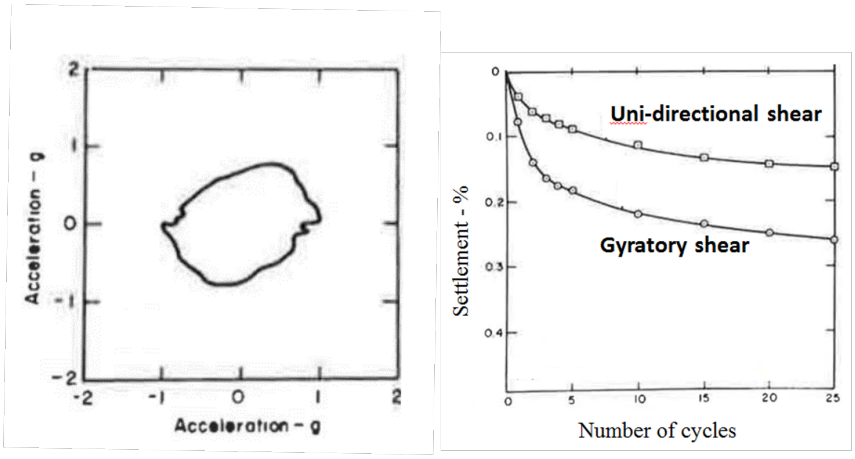

(a) Gyratory loading path (b) Settlement of sands

Fig. 2.14 The schematic diagram of gyratory loading path and settlement of sands (Pyke et al., 1975)

Seed et al. (1978) proposed a pore pressure development model and extended the research carried by Pyke to investigate the effects of multi-directional loading on pore water pressure. Their calculation results indicate pore pressure increases faster under multi-directional shaking than under uni-directional loading as shown in Figure 2.15.

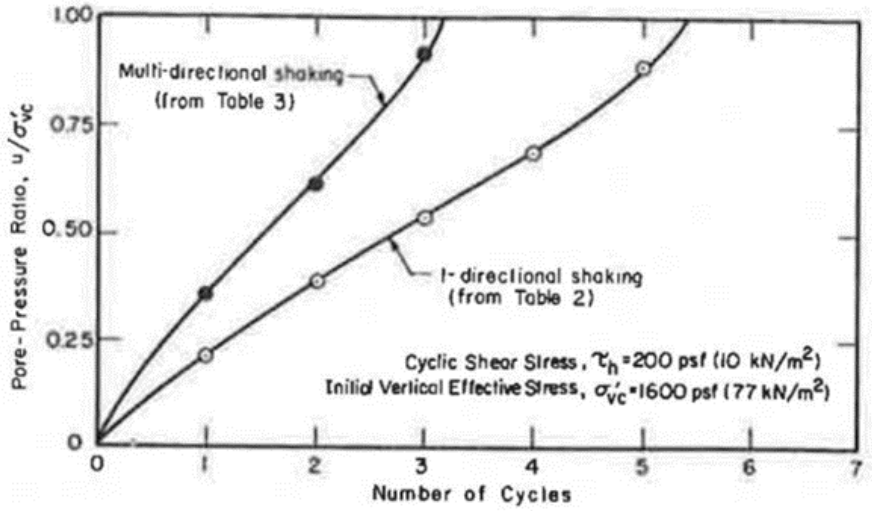

Fig. 2.15 Pore pressure development (Seed et al., 1978)

Casagrande and Rendon (1978) developed a gyratory shear apparatus and tested Ottawa "Banding sand" at various relative densities under uni-directional linear shearing and gyratory shearing. They showed that the development of excess pore pressure under gyratory loading condition is different. Firstly, it takes fewer cycles to reach the maximum pore pressure, indicating liquefaction resistance reduces in gyratory shearing. Secondly, the maximum excess pore pressure under gyratory loading cannot increase to the value of initial vertical stress, which is an important feature of circular loading and was further supported by the experimental evidences from later research. Thirdly, the cyclic pore pressure fluctuations in gyratory loading are smaller than in uni-directional cyclic tests. All these observations indicate that sand behaviours differ when multi-directional loading is involved.

Ishihara and Yamazaki (1980) developed one of the pioneering multi-directional simple shear apparatus and conducted multi-directional cyclic shearing tests on saturated sands to investigate the effects of changing loading directions on liquefaction resistance. They applied elliptical and bi-directional linear loading paths to water-pluviated Fuji River Sand specimens. Three important observations were obtained by their study. Firstly, excess pore pressure is not able to reach the value of the initial confining pressure under elliptical and circular loading paths. Therefore, the use of the liquefaction criterion which requires excess pore pressure ratio (excess pore pressure over initial confining pressure) to reach unity may be un-conservative in these cases. The authors attributed this behaviour to the initial shearing which locks some dilative deformation in the specimen. When the stress is released back to zero, the dilative deformation is unlocked and the excess pore pressure could increase to the value of the initial confining pressure. The second conclusion obtained by the authors was that multi-directional loading reduces liquefaction resistance compared with unidirectional shearing. The maximum reduction of the shear stress ratio required to induce 3% single amplitude shear strain within a certain number of cycles was approximately 30% for circular paths and 25% for bi-directional linear paths in their study, much greater than 15% proposed by Seed et al. (1978). Furthermore, it was noted that the negative effect of multi-directional loading on liquefaction resistance is maximised when two perpendicular components of loading have the same amplitude.

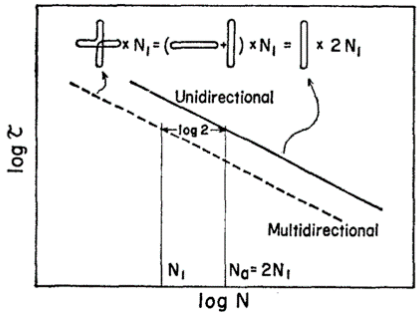

Fig. 2.16 Comparison between multidirectional and unidirectional shaking using the proposed method (Tokimatsu and Yoshimi, 1982)

Based on the experimental results in the two studies above, Tokimatsu and Yoshimi (1982) proposed a method to estimate the effects of multi-directional shaking. They assumed that the generation of excess pore pressure in one direction is independent of the other, which suggests that the influence of loading along two directions can be superposed, as shown in Figure 2.16. It was concluded that the intensity of the effect of multi-directional shaking is related to the values of two parameters, which reflect the initial generation rate of pore water pressure and the gradient of $\log \tau - \log N$ curves under unidirectional loading. The earlier the excess pore pressure starts to increase and the steeper the $\log \tau - \log N$ curves are under unidirectional shaking, the more significant the effects of multi-directional loading become. The initial generation rate of pore pressure was later demonstrated to be affected by multi-directional loading paths, cyclic stress ratio and cementation (Clough et al., 1989).

Yamazaki et al. (1985) developed a numerical model to estimate the development of the effective stress path and deformation of soil during earthquakes. They applied this model to investigate the effects of bi-directional loading on liquefaction resistance of soil and concluded that the liquefaction potential increases when the loading pattern changes from unidirectional lines to ellipses, and further to circles. The results of their numerical analysis showed that soil tends to become more prone to liquefaction under bi-directional loading than under unidirectional loading.

Nagase and Ishihara (1987) also used the bi-directional simple shear apparatus developed by Ishihara and Yamazaki (1980); however, in that study they investigated the effect of irregular unidirectional loading, rather than multi-directional loading, on cyclic strength of

water deposited Fuji River sands. Samples were prepared at three different relative densities corresponding to loose, medium dense and dense states respectively, and all consolidated at a vertical overburden pressure of 196 kPa. They selected six pairs of earthquake horizontal acceleration records based on which the cyclic stress to be applied can be determined because the time history of shear stress, as they claimed, should be analogical to that of accelerations with merely a phase difference. According to the results obtained in the study, the ratio of peak shear stress versus initial confining pressure required to induce a specified value of maximum shear strain within 20 cycles under irregular loading condition is higher compared to uniform loading. Nonetheless, this effect is dependent on the factors including relative density, maximum shear strain and wave form of loading. They concluded that the effect of irregular loading tends to decrease with increasing relative density. Denser sands produce a smaller amount of progressive shear strain, whereas they are not affected appreciably by maximum shear strain or wave form of loading.

Ishihara and Nagase (1988) conducted undrained simple shear tests with the bi-directional simple shear apparatus to investigate the effect of bi-directional horizontal loading as a part of extension work on their previous study to develop irregularity factors for Japanese bridge design code (Nagase and Ishihara, 1987). The experiment settings in terms of material, sample preparation method and relative density of specimens were generally the same in these two studies. Through extracting the coefficients of irregularity from the total differences between the stress ratios required to induce a certain amount of maximum strain by multi-directional irregular loading paths and by unidirectional uniform loading, they decoupled the effect of loading multi-directionality from that of irregularity, thereby making the conclusion that multi-directional loading decreases liquefaction resistance of sands. The resistance reduction caused by multi-directional loading is shown to be generally independent of relative density though with a slight decline for dense sands. It should be noted that although it is the combined influence of irregularity and multi-directionality that dominates the response of soil, the research on regular loading paths is still necessary to develop a better understanding of the soil behaviours under multi-directional shearing.

Fukutake and Matsuoka (1989) proposed that the volumetric strain under multi-directional shearing is composed of cumulative strain and resultant strain. Cumulative strain is related to the plastic volumetric deformation accumulated during shearing and thus is irreversible, whereas resultant strain is the reversible strain which is dependent on the magnitude of strain vector at a given time. They conducted drained multi-directional simple shear tests to verify the model they developed. Although numerical modelling is not in the scope of this study, their hypothesis on the mechanism of strain accumulation under drained multi-directional simple shear tests is still inspiring because the generation of excess pore pressure under undrained condition is considered closely related to the volumetric change of soil in drained condition.

Clough et al. (1989) used a cubical shear box to conduct multi-directional cyclic shearing tests to investigate the effects of multi-directional loading on liquefaction resistance of cemented sands. They reported that multi-directional loading always leads to a lower liquefaction resistance compared with unidirectional loading, and the reduction can be as high as 15%-40%.

Reddy and Saxena (1992) summarized the results of previous studies to develop a model to estimate the generation of excess pore pressure and liquefaction resistance of cemented soil under multi-directional stress paths. The experimental results they used were obtained through true triaxial tests and indicated that the liquefaction resistance could be decreased by up to 50% for uncemented sands, which was again in accordance with the widely-made observation of multi-directional loading reducing liquefaction resistance.

Boulanger and his colleagues (Boulanger, 1990; Boulanger et al., 1993; Boulanger and Seed, 1995) developed the U.C. Berkeley Bi-directional Simple Shear Device (UCB-2D) to study the effects of bi-directional loading on the strength of moist tamped modified Sacramento River Sand. An important improvement of this device was a chamber that allows the application of back pressure for saturation. The bi-directional loading here refers to the category of paths in which an initial static driving shear is applied in dip direction before cyclic shearing is applied in perpendicular direction (strike direction), which represents the loading situation encountered in sloping ground. It was suggested by their study that soils'

shear resistance becomes lower in the case where cyclic shearing is perpendicular to initial static driving shear because this loading scenario allows larger amount of shear stress reversal and larger extent of axis rotation. Furthermore, they noticed that there exists an inverse linear correlation between the largest maximum and minimum excess pore pressure within a cycle and shear stress amplitude.

Another type of multi-directional direct simple shear (MDSS) apparatus is the one concurrently developed by DeGroot (1992); DeGroot et al. (1993); Degroot et al. (1996) at the Massachusetts Institute of Technology. They studied the effects of different directions of static shear loading and ice shear loading on the response of Boston Blue Clay. They observed that the peak undrained resistance of tested clay is affected significantly by the angle between the two shear forces, which is similar to the previous results for sands.

Meneses et al. (1998) used a bidirectional simple shear apparatus to investigate the influence of cyclic shearing superimposed on monotonic shearing in an orthogonal manner, which represents a situation of small seismic shearing continuing after the main shaking of an earthquake. The previous observation that superimposing cyclic shearing onto the monotonic loading will reduce the strength of sand is further confirmed. Furthermore, the magnitude and frequency of post-main-shaking cyclic loading was shown to influence the behaviour of sands with same initial relative density and confining pressure.

Matsuda et al. (2011, 2004) developed their multi-directional cyclic simple shear test apparatus and conducted strain-controlled tests on Toyoura sand and granulated blast furnace slag (GBFS). Two sinusoidal signals were input into the two perpendicular loading actuators with a phase difference which is controlled and changed to produce different loading paths. Their test results showed that the number of cycles to trigger liquefaction decreases with increasing phase difference, indicating again that multi-directional shearing can reduce liquefaction resistance.

Sako and Adachi (2004) investigated the generation of excess pore pressure of air pluviated Toyoura Sand subjected to uni-directional and bi-directional loading. It was shown that excess pore pressure increases the fastest under bi-directional loading condition. The suggested bi-directional excess pore pressure development can be virtually simulated

through scaling the pore pressures induced by unidirectional loading inputs by a modification coefficient. The modification coefficient obtained in this study ranges from 1.08 to 1.26, demonstrating an increased liquefaction potential when shearing is applied in bi-directional manner.

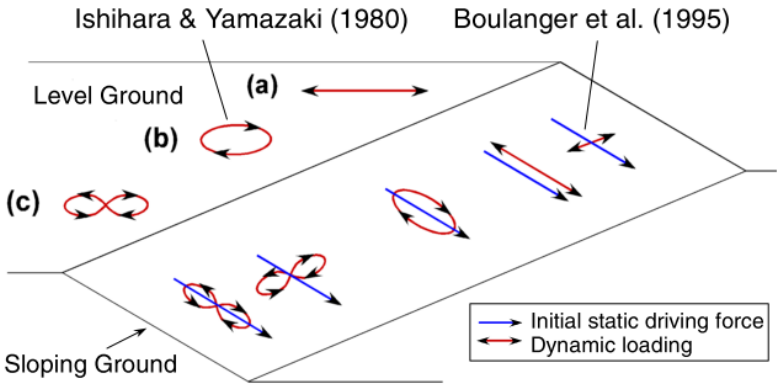

Fig. 2.17 Schematic illustration of idealized multi-directional loading (Kammerer et al., 2004b)

A comprehensive investigation into the influence of multidirectional stress paths (both magnitude and direction) and initial static shear stress on saturated sands was conducted by Kammerer, Wu and colleagues (Kammerer et al., 2004a,b; Kammerer, 2002). Water pluviated saturated Monterey #0/30 Sand was tested with the improved U.C. Berkeley Bi-directional Simple Shear Device (UCB-2D). The stress paths performed can be categorized into three groups: bi-directional linear path, circular or oval paths and figure-8 paths, as shown in Figure 2.17. Their results confirmed that the rotation of stress direction in the horizontal plane can result in faster generation of excess pore water pressure, which was explained by the aiding effect of stress rotation on particle rearrangement and densification of soil.

The inverse linear correlation between limiting excess pore pressure ratio and shear stress ratio reported by Boulanger (1990) was also observed by Kammerer (2002), as shown in Figure 2.18. While the author attributed it to the dilation characteristics of soil, the mechanisms behind it remain unclear.

Furthermore, Kammerer (2002) observed that the tests which have no stress reversal because of extremely large static driving shear, always have less strain potential. The counter-

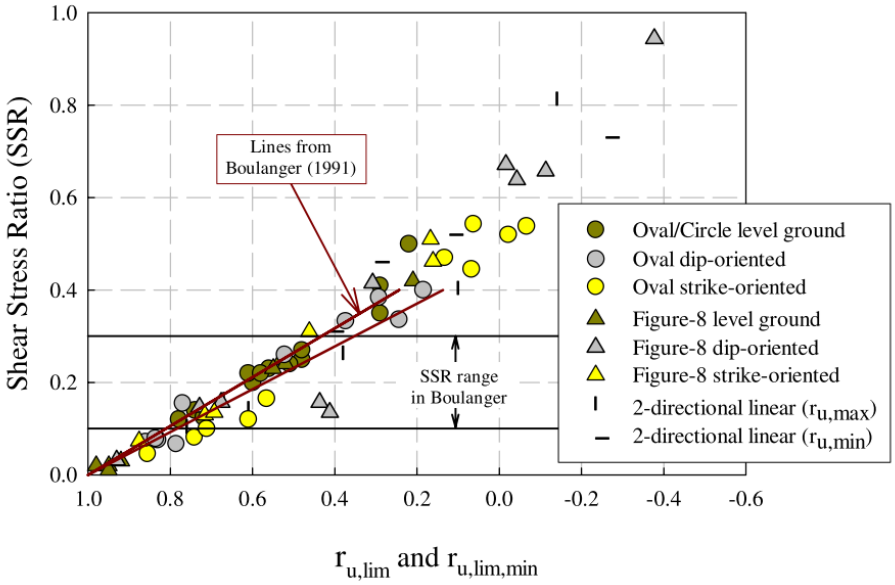

Fig. 2.18 Relationship between shear stress ratio and limiting excess pore pressure ratio (Kammerer, 2002)

intuitive findings suggested that the primary effect of the initial static driving shear is to affect the degree of stress rotation rather than to change the magnitude of the shear stress. Stress rotation exerts complex effects on the behaviour of soil and generation of pore pressure through influencing particle rearrangement and softening response. The author thus proposed that stress rotation is more important than cyclic stress amplitude in terms of pore pressure generation and shear strain.

In order to compare loading paths in a consistent manner, Kammerer (2002) proposed to use aperture ratio and reversal parameter as the parameters to characterise loading paths. It was shown that increasing aperture ratio (from oval to circular for instance) could cause a decline in liquefaction resistance. But this negative effect itself tends to reduce with higher aperture ratios.

Ueng and colleagues (Ueng et al., 2005) conducted two-dimensional shaking table tests on Vietnam Sand to examine the influence of multi-directional shear on the re-liquefaction of sands. It was suggested by the authors that peak pore pressure becomes higher under two-dimensional shaking compared with one-dimensional loading with the same amplitude. There was not a prominent effect of two-dimensional shaking on the rate of increment of

pore pressure. It should be noted that their two-dimensional tests were conducted after one-dimensional shaking tests, and the behaviour of sands prior to initial liquefaction can be rather different from their observations.

Based on the U.C. Berkeley Bi-directional Simple Shear Apparatus (UCB-2D), a new device named the Digitally Controlled Simple Shear apparatus (DC-SS) was developed by Duku et al. (2007). The major advantage of this device compared with the Berkeley one rests on its ability to apply earthquake broadband loading with a large frequency. This device was later mainly used to investigate the volumetric strain of sands (Duku et al., 2008; Yee et al., 2013). No published multidirectional loading tests, however, have been performed by this apparatus except for the tests conducted to demonstrate the capability of the device.

Jin et al. (2008) performed stress-controlled universal triaxial and torsional shear tests on air pluviated loose Fujian Standard Sand to investigate the effects of complex loading paths on pore pressure generation and strain development. The authors found that neither the amplitude of vertical stress nor that of horizontal stress affects the peak pore water pressure; instead, the peak pore pressure is inversely correlated to initial static shear. Their findings are consistent with the observations of Boulanger (1990) and Kammerer (2002) despite different testing techniques.

Rutherford and Biscontin (2013) from Texas AM University developed another multi-directional direct simple shear apparatus (TAMU-MDSS) and experimentally studied the cyclic shear response of Gulf of Mexico Clay. Rutherford (2012) observed that the largest excess pore pressure occurs under the stress paths where both the magnitude and direction of stress changes most. Furthermore, she concluded that shear strain of clay always accumulates towards the orientation of initial static shear (downhill) regardless of the direction of cyclic loading, which is in agreement with the conclusions of Biscontin et al. (2004). Although the material tested here was clay rather than sand, the observations are still inspiring since similar tendency can also be found in the tests on sands such as those conducted by Boulanger (1990) and Kammerer (2002). The tests reported in this dissertation were conducted with the modified TAMU-MDSS. The modification as well as the redesigned top cap and sample preparation procedures will be detailed in chapter 3.

Rudolph et al. (2014), Li et al. (2016) and Mirbaha (2017) developed their multi-directional simple shear testing database, respectively, with the variable direction dynamic cyclic simple shear device (VDDCSS) of GDS Instruments Ltd. The reduction of liquefaction resistance in multi-directional loading condition was also supported by these studies. Due to the limitations of VDDCSS, they conducted equivalent undrained tests rather than actual undrained tests. They adopted constant-height boundary condition and regarded the reduction of vertical stress as the generation of excess pore pressure. Although this type of tests is accepted as an effective approximation of undrained tests, the actual discrepancies between them are difficult to estimate, especially when the degree of saturation exerts an influence.

In conclusion, despite all the efforts outlined above, multi-directional simple shear test data are still scarce and there has not been any well-established theoretical framework to account for the effects of multi-directional loading. Although the consensus seems to be that multi-directional shearing can reduce the liquefaction resistance of sands, the degree of reduction varies from one study to another. The mechanisms behind the extensively-reported inverse correlation between limiting excess pore pressure and shear stress amplitude remains unclear. There have been no conclusions about the effects of loading paths on the stress paths and shear modulus degradation. Clearly, more efforts are required before the effects of multi-directional shearing can be explained consistently from a theoretical point of view, and this study aims to contribute new insights towards this goal.

Chapter 3

MULTI-DIRECTIONAL SIMPLE SHEAR TESTING

3.1 Material tested

The sand used in this study is Hostun S28 Sand. It is poorly graded and quartz dominated (Ezaoui and Benedetto, 2009). The particles of Hostun Sand are sub-round to sub-angular in shape as shown in Figure 3.1. The maximum void ratio, minimum void ratio and specific gravity measured by Mitrani (2006) are used in this study, as summarized in table 3.1.

The particle size distribution of the sand was investigated with the conventional sieve analysis method, following the procedures prescribed by ASTM D6913. The particle size distribution curve is presented in Figure 3.2. The median particle diameter D_{50} is 0.35 mm.

Table 3.1 Properties of Hostun S28 Sand (Mitrani, 2006)

Properties	Values
e_{max}	1.01
e_{min}	0.555
G_s	2.65

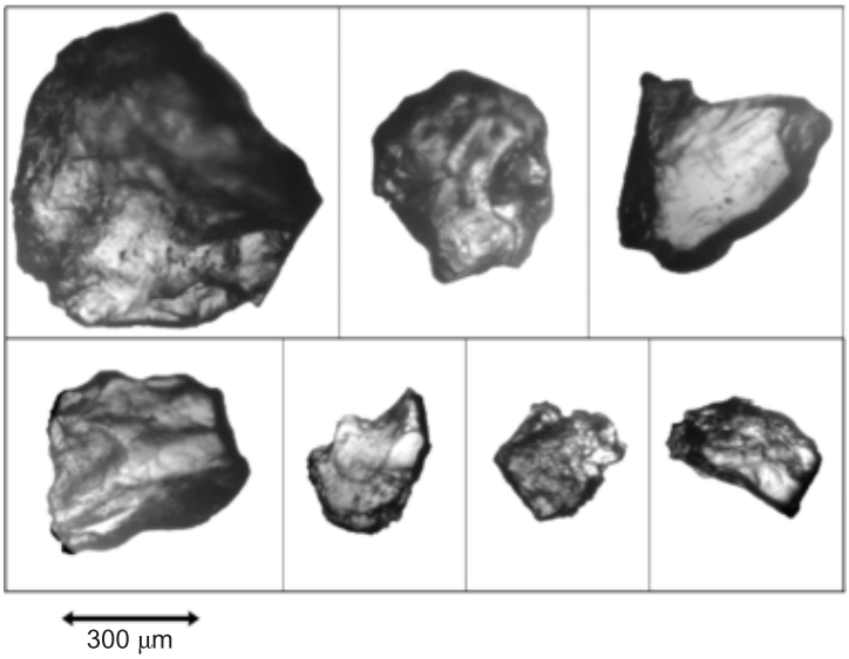

Fig. 3.1 Shape of Hostun Sand particles (Ezaoui and Benedetto, 2009)

3.2 Review on specimen preparation technique

If the element-level laboratory tests are expected to give results that can represent the in situ soil behaviour and satisfy the standards of numerical modelling, the technique used to create reconstituted soil specimen has to be carefully selected. The ideal method is supposed to convincingly simulate the fabric of in situ soil and the process of deposition, and produce uniform specimens, which is the fundamental requirement of element-level testing. It is thus worthy to review existing specimen preparation methods for sands.

3.2.1 Moist Tamping

The oldest specimen preparation method used to create reasonable reconstituted specimen is moist tamping, in which a series of layers are poured into the mold to designated height with each layer surface being levelled and tamped before placing the next layer (Lambe, 1951). This method effectively mimics the soil fabric of rolled construction fills for which the method was originally designed (Kuerbis and Vaid, 1988).

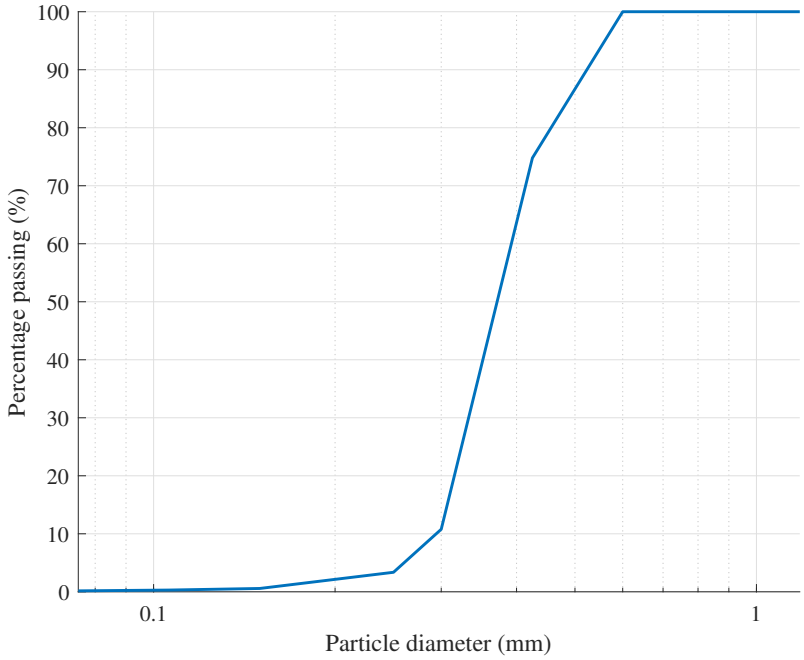

Fig. 3.2 Particle size distribution curve of tested Hostun Sands

The moist tamping method can produce specimens with relative density ranging from as low as near zero to approximately unity. As loose sands and silty sands are considered most susceptible to liquefaction, the extremely loose state which can be achieved through water tension force herein has naturally been a source of the interest in using this technique, while other specimen preparation methods can hardly create such loose specimens.

However, this apparent advantage also serves as the primary cause of criticism. Casagrande (1976) suggested that as a result of capillary forces, the moist condition induces the generation of a "honeycomb" structure by which the structure of soil is supported. During the saturation process, water tension is gradually removed and the honeycomb structure can collapse. For some silty specimens which have finer particles and thus experience large water tension forces, a large strain can be observed due to this (Casagrande, 1976; Chang and Whitman, 1988; Sladen et al., 1985). As for those specimens which do not exhibit a large strain during saturation, though there is a chance that they behave in an incompressible manner during consolidation and remain at large void ratios, the extremely loose specimens are usually metastable and thus have a lower liquefaction resistance (Kuerbis and Vaid,

1988), that is, the loose specimens obtained through moist tamping may be not reliable. Another drawback concerning this specimen preparation technique rests in its relatively low uniformity compared with other methods. Miura and Toki (1982) conducted miniature cone penetration test and concluded that non-uniformity in moist tamped specimens is remarkably higher than that of pluviated specimens.

It should be noted, however, that moist tamping has been applied in most of the triaxial tests on extremely loose Hostun sands in literature. The results of these tests should be treated and interpreted with caution.

3.2.2 Air Pluviation

Air pluviation uses a funnel to pluviate sand from a designated height with a desired rate of deposition to control the relative density of specimens (Miura and Toki, 1982; Vaid and Negussey, 1988). The higher the drop height is, the larger the input energy becomes, and thus the denser the specimen is. The loosest state is obtained through keeping the nozzle right above the surface of the pluviated soil while lifting the funnel. The relative density range that has been successfully achieved with this method is not as wide as that of moist tamping method, but is still satisfactory for most of the research on soil liquefaction.

The uniformity of air pluviated specimens is desirable (Miura and Toki, 1982; Mulilis et al., 1978) when preparing specimen made of well-sorted sand or well-sorted silt because it simulates directly the natural deposition process of aeolian deposits (Kuerbis and Vaid, 1988). However, when it comes to well-graded sand with fines content, the performance of the air pluviation technique is no longer reliable due to particle-segregation issues. If the drop height is strictly restricted to be rather small, the segregation during drop of particles may not be severe, though the saturation process will still induce segregation by washing out the fine particles (Kuerbis and Vaid, 1988).

In addition to segregation, bulking is also an issue encountered in specimens with fine contents prepared by air pluviation. Kuerbis and Vaid (1988) reported air-pluviated silty sands exhibited a metastable behaviour with large strain developing during saturation and

consolidation. Extremely loose specimens prepared by air pluviation also undergo a reduction in liquefaction resistance, just as their moist tamped counterparts.

For medium to dense clean sands with minimal silt content, nevertheless, the segregation and bulking problems are not severe. Samples prepared by air-pluviation can provide promising and consistent results. Furthermore, for the samples with low height-to-diameter ratios, the control of nozzle and particle drop height is straightforward. This sample preparation technique is hence an adequate method for simple shear testing.

3.2.3 Under-compaction Moist Tamping

To overcome the issue of segregation when fines content is involved, the under-compaction moist tamping method was proposed by Ladd (1978). Generally, this method is a modified version of moist tamping with the lower layers not fully compacted. When the upper layers are added, the compaction of the upper layer can simultaneously compact the lower ones, so that the specimen will become uniform as a whole.

Although the issue of segregation can be improved to some extent, other drawbacks of the moist tamping method, especially those related to the unrealistic soil fabric, cannot be overcome by the under-compaction technique. Therefore, the test results obtained with this sample preparation technique should also be treated carefully.

3.2.4 Water Pluviation

Water pluviation has been widely used in many previous studies regarding liquefaction resistance of sands, clean sands in particular. The essence of this reconstitution technique is rather similar to air pluviation, except that sands are pluviated through water instead of air (Lee and Fitton, 1968).

Considering that the falling velocity of particles in water is much lower than in air due to the clearly different buoyancy and friction, the energy input, provided mainly by gravity, is thus much lower for water pluviation than air pluviation. The maximum void ratio obtained by water pluviation is usually larger than its air counterpart. It is worth noting that Vaid and

Sivathayalan (2000) contended it is unlikely that water-deposited in situ sands exist in a state looser than the loosest state achievable by water pluviation, indicating that the extremely loose specimens of hydraulic sands, such as those produced by moist tamping method, are not realistic.

Similar to air pluviation, unwanted segregation is also an issue encountered by this method (Amini and Qi, 2000). The falling velocities of fine particles are generally slower than those of coarse particles in water, just as in air, causing fines sitting on the top of the coarse particles as long as they have the same drop height. The uniformity of water pluviated specimens can be impaired severely due to the layering of different-diameter particles. Although stratification is encountered in situ from time to time, it is not acceptable in element level experiments. Thus, again, the use of water pluviation technique is limited to research on sand without fines content. Actually, when the effect of fine contents is involved, neither a pluviation method nor moist tamping is preferred.

However, the advantages of this technique are significant since it is known to be able to mimic the natural fabric of hydraulic sediments (Miura and Toki, 1982; Oda et al., 1978; Vaid and Sivathayalan, 2000). This desirable feature is highly valued by geotechnical experimentalists partly because hydraulic deposit is a type of fill of particular interest in the area of liquefaction research and partly because the more realistic the fabric is, the more meaningful the test results are. Furthermore, in terms of uniformity, Vaid and Negussey (1988) suggested that the specimens prepared by water pluviation have better uniformity compared with moist tamped ones. This method has been adopted by numerous researchers in the last a few decades and is still widely employed now. Høeg et al. (2000), based on comparison of stress-strain-strength behaviour of reconstituted specimens with undisturbed in situ specimens, recommended that the most promising reconstitution technique is water pluviation combined with vibration as long as segregation issue is avoided for very well-sorted sands.

Nevertheless, the use of this sample preparation technique is not preferable in this study. When the membrane is pulled over the top cap, a volume of air is inevitably trapped between the membrane and the sidewall of the top cap. In triaxial tests, the influence of this issue is

not pronounced partly because the radial stress acts inward and partly because the overall volume of sample is much larger compared with the volume of trapped air. In simple shear tests, however, resultant radial stress acts outward when positive excess pore pressure is generated and the volumetric proportion of trapped air is significant. As a consequence, the degree of saturation is lowered if the sample is reconstituted using water-pluviation. Some pilot tests were conducted in this study with water-pluviated samples and the Skempton's B-value of these tests were never higher than 0.7. This technique was therefore not adopted in the subsequent tests.

3.2.5 Slurry Deposition

Slurry deposition, initially developed by Kuerbis and Vaid (1988), is another widely-used reconstitution method proposed to cope with segregation of the particles of different sizes while inheriting the advantages of water pluviation. The initial version of this method used a tube filled with de-aired water to fully mix fines slurry and sand slurry before transferring the mixture from the tube to the triaxial cell. Segregation can be inhibited by mixing fines and sand adequately. Various versions of slurry deposition technique were later developed by researchers including Høeg et al. (2000), Salgado et al. (2000) and Carraro (2004). However, no matter how the detailed procedures differ, the crucial consideration remains that the fines and coarse particles should be mixed thoroughly and the mixture should deposit from the suspend-in-water state.

Such procedures were demonstrated by many researchers (Kuerbis and Vaid, 1988) to produce specimens with attractive properties such as full saturation and a soil fabric similar to natural deposits, as well as excellent duplication and high uniformity regardless of gradation. It is these appealing features that make the slurry deposition method a fascinating reconstitution technique, especially for research on the effects of fines content and gradation.

In this study, however, slurry deposition suffers from the same drawback as water-pluviation method. Air can be trapped inside the sample when the membrane is clamped to the top cap, resulting in a low degree of saturation. This technique is thus not applicable to undrained simple shear tests either.

3.2.6 Air pluviation with CO_2 flushing

The in situ fabric of soil and natural deposition process should be simulated as closely as possible by the selected specimen preparation technique. Given that the sands of interest are generally fluvial and hydraulic-deposited, air pluviation or water pluviation should be the preferred methods to prepare samples. However, a low degree of saturation can result from the air trapped inside the samples when top caps are mounted and sealed. This issue cannot be solved if sands are pluviated into water, but can be reduced with air-pluviation followed by a carbon dioxide flush. After CO_2 is flushed through air-pluviated samples, the trapped air is replaced by soluble CO_2 that will dissolve into water with the help of increased back pressure in the saturation phase.

CO_2 has been extensively used in both element-level laboratory tests and physical modelling tests (Ishihara and Nagase, 1988; Stringer and Madabhushi, 2009).Takahashi et al. (2006) compared the P-wave velocity in the physical models saturated with different techniques and concluded that carbon dioxide percolation and vaccum technique can achieve high degree of saturation.

However, such a procedure cannot be applied if the sample is filled with water which blocks the movement of air and isolates it. Thus, air pluviation with CO_2 flushing was selected as the best sample preparation for the simple shear tests conducted in this study. Only 4 out of the 79 tests had B-value lower than 0.9, with the lowest one at 0.85.

3.3 Inflation problem in undrained simple shear tests

When it comes to the differences between simple shear tests and triaxial tests, there is an aspect that is not often discussed, that is, the different confining stress condition in undrained tests. In triaxial tests, lateral confining stress σ_3 can be controlled by the difference between cell pressure and back pressure. In most cases, cell pressure is always larger than back pressure to keep soil samples confined by positive σ_3 unless liquefaction happens. Therefore, the generation of positive excess pore pressure in triaxial tests will not result in the resultant radial stress turning from inward to outward.

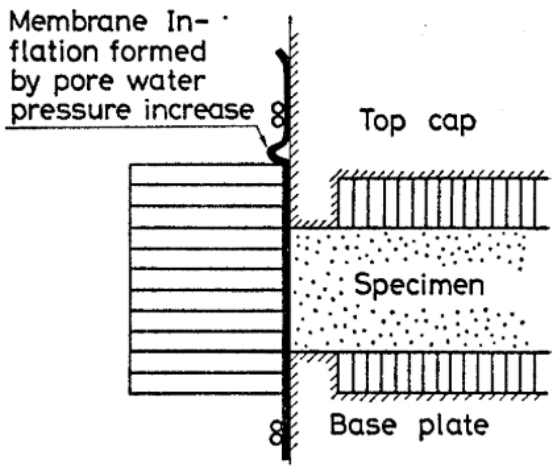

Fig. 3.3 Inflation of the rubber membrane (Ishihara and Yamazaki, 1980)

By contrast, what is simulated by simple shear tests is zero lateral deformation condition of soil. Lateral confining stress is equal to vertical overburden stress multiplied by a lateral stress coefficient K_0. If the variation of K_0 with shearing were well established, the condition of zero lateral deformation could be conveniently achieved by controlling the lateral stress, just as it is done in triaxial tests. Unfortunately, the knowledge of the variation of K_0 with shearing is still limited, which eliminates the possibility of achieving zero lateral deformation in laboratory tests by controlling exclusively lateral stress. Instead, the most widely accepted method to ensure zero lateral deformation in the simple shear tests is to provide physical confinement, such as a reinforced membrane or stacked rings, with the price that the information about K_0 is sacrificed.

Under this circumstance, if the cell pressure is set higher than back pressure, an additional lateral stress will be applied. If the additional lateral stress is smaller than $\sigma_v \cdot K_0$, the stress condition of soil will not be altered because the difference can be compensated by lateral confinement. But when the additional lateral stress is larger than $\sigma_v \cdot K_0$, the stress condition of the soil will change and the in situ K_0 condition cannot be reproduced. Therefore, a convenient and safe choice is to require that the cell pressure be equal to the back pressure, so that all lateral stress is provided exclusively by lateral confinement.

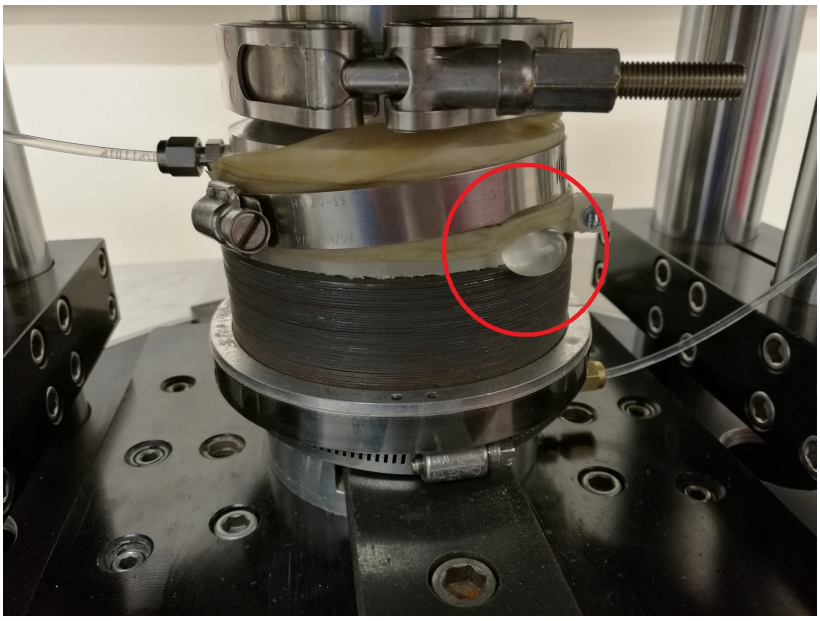

Fig. 3.4 The photo of water pouch forming in a sample which has outward water pressure gradient of 60 kPa

However, such a testing condition produces issues in undrained tests where positive excess pore pressure is generated. Ishihara and Yamazaki (1980) reported an inflation issue of the rubber membrane as shown in Figure 3.3. When excess pore pressure increases, the actual back pressure becomes higher than the cell pressure, from which an outward water pressure gradient arises. As a result, water can be expelled from the soil sample and accumulates at the place where physical confinement ends, leading to the phenomenon in Figure 3.3. The apparent consequence of water discharge is the reduction of sample height. By holding constant vertical load, the height of soil sample should remain constant if there is no volume change. Once water flows out from the sample, on the contrary, sample height reduces dramatically (more than 10% recorded in pilot tests), which not only makes the constant volume assumption of undrained testing invalid but also results in uncontrolled compression of soil samples.

To reduce the effects of the outward water pressure gradient, cell pressure can be raised but cannot exceed $\sigma_v \cdot K_{0,min}$ with $K_{0,min}$ representing the minimum value of K_0 that can be experienced during a test. Boulanger (1990) compared soil samples consolidated under a series of lateral stresses and concluded that initial K_0 is closest to 0.4. While the value of

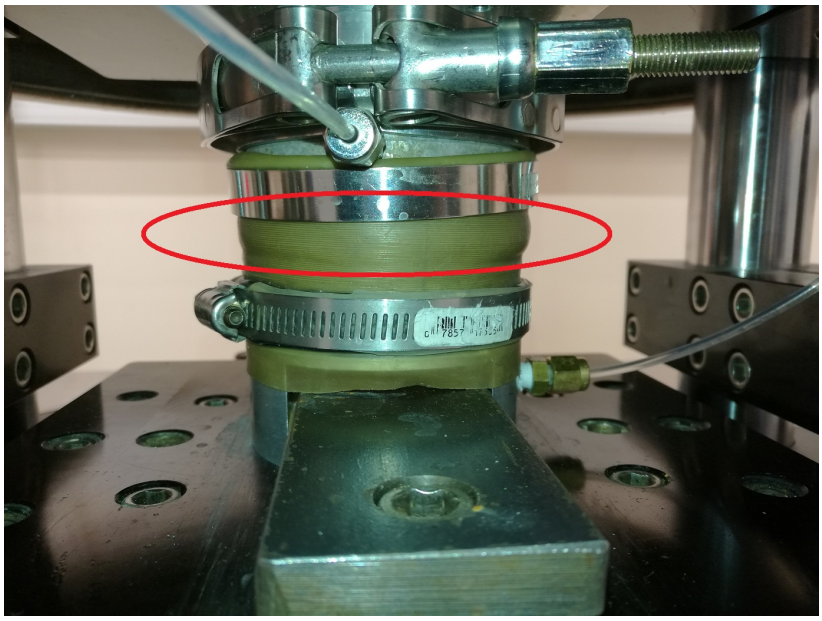

Fig. 3.5 The photo of reinforced membrane deformed by outward water pressure gradient

$K_{0,min}$ can vary with the degree of saturation and is difficult to determine, a general assumption is to regard $K_{0,min}$ as equal to initial K_0. With this assumption, the maximum allowable difference between cell pressure and back pressure is 40 kPa for a sample consolidated with vertical overburden stress of 100 kPa. When liquefaction takes place and excess pore pressure increases to be close to vertical overburden stress, the resultant outward water pressure gradient can be reduced from 100 kPa with equilibrated cell and back pressures to 60 kPa, with 40 kPa positve cell pressure. Figure 3.4 presents the photo of a soil sample whose outward water pressure gradient is 60 kPa. The startling water pouch indicates clearly that the inflation issue still exists at this amount of outward water pressure gradient.

Another potential method to solve the problem is to apply a physical constraint to the full height of the membrane, eliminating the space for the expelled water to accumulate. If stacked rings are used, it can be achieved by clamping O-rings right on the top of stacked rings. But when top cap is lowered to maintain constant vertical load, the clamps and O-rings will contact and press the stacked rings, resulting in undesirable vertical stress condition. This issue can be avoided if a reinforced membrane is used instead of stacked rings and O-rings are clamped at the bottom of the top cap. Although the vertical stress condition can

be guaranteed, however, the high outward pressure can deform the membrane severely even if it is reinforced, as shown by the photo in Figure 3.5.

As all the convenient options were not effective, the top cap and sample preparation procedures were redesigned in this study to minimise the issue of inflation. Figure 3.6 shows the schematics of a soil sample in preparation (a) and after preparation (b). The modified sample preparation method allows physical confinement to be applied to the full height of membrane. The modified specimen procedure will be detailed in the next section.

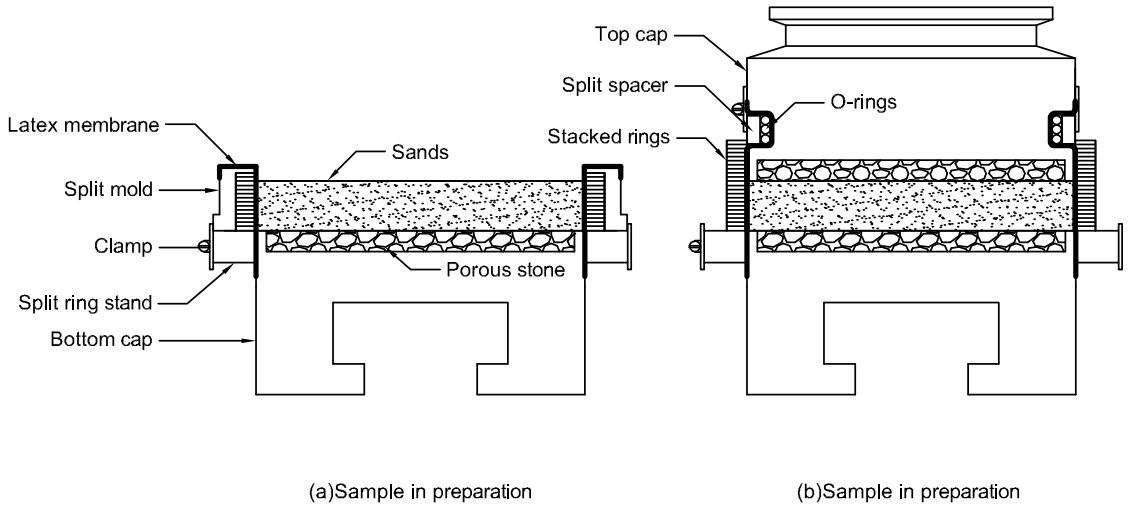

Fig. 3.6 The schematics of a soil sample in preparation and after preparation

Table 3.2 The summary of transducer replacement

Replaced transducers	Measurement/ Control	Current model
X Load cell	Force in X direction	Strainsert universal flat load cell Model FL025U(C)2NSPKT. Capacity: 250 lbf (1.11 kN). Non-Linearity: ±0.10% F.S.
Z Load cell	Force in Z direction (vertical)	Interface Force universal load cell Model 1010-AF-500. Capacity: 500 lbf (2.22 kN). Non-Linearity: ±0.04% F.S.
Pore pressure transducers 1	Pore pressure at the bottom of volume change measurement	Festo pressure transducers Model SPTW-P6R-G14-VD-M12
Air pressure controller	Control the air pressure inside chamber	SMC pressure controller Model ITV2030-31F2BL3
Volume change pressure controlled	Control the volume change regulation air pressure	SMC pressure controller Model ITV2030-31F2BL3

3.4 Testing details

3.4.1 Multi-directional direct simple shear apparatus

The multi-directional direct simple shear apparatus developed by Rutherford and Biscontin (2013) has been upgraded and used for the experimental program in this study. A photo of the testing device is shown in Figure 3.7.

The apparatus is composed of four primary parts: loading chamber, data acquisition and control system, hydraulic power system and back pressure system. The loading chamber contains a vertical loading actuator and two horizontal loading actuators, as well as two arms to uplift or lower the chamber. The power of the chamber lifting arms and load actuators

is provided by the hydraulic power system. The air pressure in the chamber and the water pressure in soil sample are controlled through the back pressure system. Data acquisition and loading programming is conducted through control software *Dimension*. The schematic and more details about the device can be found in Rutherford and Biscontin (2013).

The load cells, hydraulic system and data acquisition system were modified to provide better control of testing conditions. The load applied by vertical and horizontal actuators is measured by load cells. The displacements are measured by LVDTs. Cell pressure and back pressure is controlled by pressure controllers and measured by pressure transducers. Excess pore pressure is measured directly by a differential pressure transducer. A summary of the replacement of transducers and digital controllers and their function is tabulated in table 3.2. The information of other transducers was reported by Rutherford and Biscontin (2013).

This apparatus has two primary features. Firstly, the testing system has two horizontal tables that can move in perpendicular directions independently. The application of multi-directional shearing is thus made possible. Secondly, a chamber encloses the specimen, allowing air confining pressure to balance back pressure so that the measurement of excess pore pressure is viable. The photo of the chamber with a mounted sample is presented in Figure 3.8, with the components inside the loading chamber indicated.

As shown in Figure 3.8, soil samples are reconstituted between bottom cap and top cap, and enclosed by an unreinforced latex membrane. A stack of lubricated thin steel rings is employed to confine lateral deformations of the soil sample. The stacked rings are the same as those used by Bernhardt (2013) with average inner diameter of 101.6 mm. The stacked rings are lubricated regularly with Teflon spray to reduce friction between the rings. Following Franke et al. (1979), the height of samples was ensured to be lower than 25 mm so that the diameter-to-height ratios of all soil samples were always larger than 3.75 to reduce the effects of the lack of complementary stresses.

3.4.2 Specimen preparation procedures

The schematics of samples in preparation and after preparation are shown in Figure 3.6 with the essential components indicated. The procedures of specimen preparation are as follows:

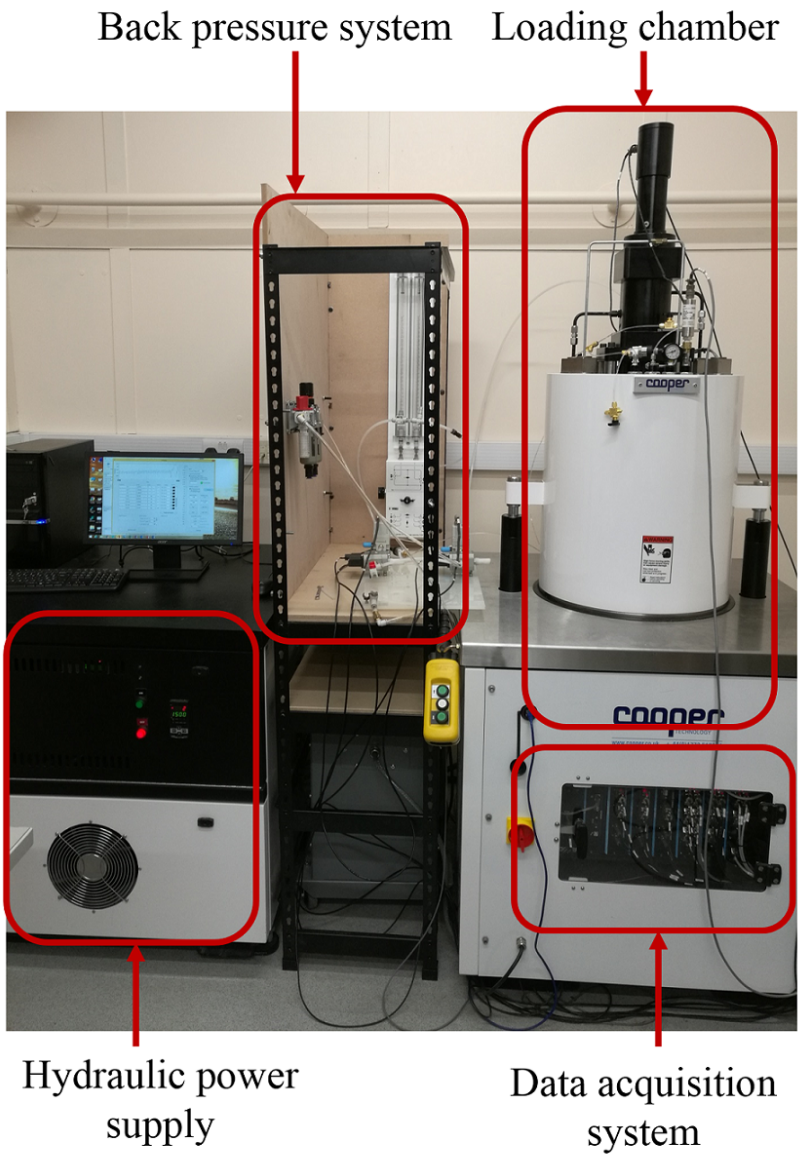

Fig. 3.7 A photo of the multi-directional direct simple shear testing apparatus

(1) **Assembling the split ring stand.** Latex membrane and split ring stand are assembled on the bottom cap. The top surface of the ring stand needs to be aligned with that of the bottom cap to ensure the stacked rings can move horizontally when the sample is deformed. The latex membrane is enclosed by the split ring stand and the ring stand is fastened with a clamp to provide a bottom seal for soil samples.

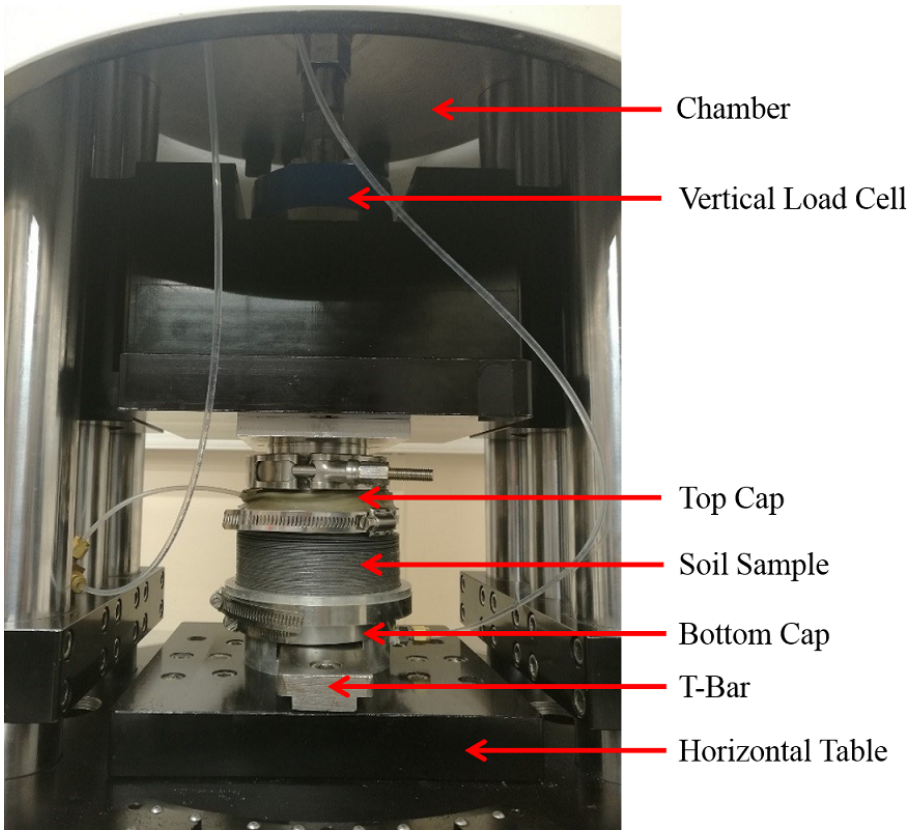

Fig. 3.8 A photo of the testing device with a sample mounted

(2) **Assembling the split mold.** Steel rings are stacked on the ring stand followed by the split mold assembled. The split mold and ring stand are aligned and clamped together to hold the rings in the correct position. The membrane is rolled over the mold and held temporarily by O-rings. A small vacuum is applied to the split mold to help the membrane cling to the stacked rings.

(3) **Air pluviation of sand and surface levelling.** A funnel is used to pluviate sand into the mold. The nozzle of the funnel is kept at the top of sand surface and moved in a spiral path to produce samples in a loose state. Vibration is applied to the mold with a rubber hammer to densify soil samples, if required. A leveller is used to flatten the top surface of sands and remove redundant sand. The surface of the sand should be slightly lower than the mold to leave the necessary space for mounting the top cap.

(4) **Mounting the top cap.** The top cap is placed onto the sand surface. The membrane is stretched and pulled over the sidewall of the top cap. Three O-rings are used to clamp the membrane into the groove on the top cap. More steel rings are placed onto the existing ones until they are stacked to the lower edge of the groove. A pair of split spacers is put into the groove and fastened by a clamp.

(5) CO_2 **flushing.** CO_2 is flushed through the reconstituted sand sample via the inlets on the bottom cap and top cap. The speed of CO_2 flow needs to be controlled carefully to avoid sample blow up. The three-way valves at the outer ends of the cap pipes are closed for sample transfer when the CO_2 flushing is finished.

(6) **Transferring the sand sample to the testing device.** The sand sample is placed into the multi-directional direct simple shear testing apparatus and aligned with the vertical loading ram. The vertical loading ram is lowered until a small amount of seating load (around 5 kPa) is applied to the sample. The top cap and the vertical loading ram are clamped together. The T-bar is then tightened to fix the sample assembly. This prevents pre-shearing of the specimen.

(7) **Water flushing.** The two ports on the three-way valves of the top cap and bottom cap are connected to the back pressure system and a water reservoir, respectively. A small amount of vacuum (around 5 kPa) is applied to the water reservoir connected to the top cap, while de-aired water is filled into the water reservoir connecting to the bottom cap. The port to the top cap water reservoir is first opened, then the bottom cap one. De-aired water in the bottom cap reservoir will be sucked into the sample and flow out into the top cap reservoir when the sample is fully filled with de-aired water. The process is reversed and repeated for several times until no visible air bubbles can be observed in the tubes. The ports on the three-way valves, which connect to the back pressure system, are finally opened.

A sample is successfully prepared by this point. With the newly-designed top cap, physical constraints can be fully applied to the specimen. The bottom of the sample is sealed by the clamped split ring stand. The top is fastened by the clamped split spacers and O-rings.

Steel rings are stacked along the full height between the top and bottom. A water pouch was not formed in the tests prepared with this method and the largest reduction of sample height was 2.2%. B-values above 0.9 were obtained in 75 of the 79 tests in this study. The B-values in this study were generally lower than the typical values (above 0.95) seen in literature because the capacity of pore pressure transducer did not allow the application of higher back pressure. But the test results were considered valid since a B-value of 0.9 still gives a nearly complete saturation, with the saturation degree over 99.5% according to Black and Lee (1973).

3.4.3 Simple shear testing procedures

Once water flushing is finished and the connections of the sample assembly are switched to back pressure system, the chamber is closed while the sand specimen is still confined by seating load. The testing procedures adopted in this study are as follows:

(1) **Saturation.** Cell pressure is raised in small increments to a target value (usually 270 kPa). Back pressure is increased simultaneously but always kept slightly lower than cell pressure to ensure a small net compressive pressure. The sample is saturated with the high cell pressure and back pressure for a period of time (usually 1 hour). Vertical overburden stress remains at the seating load in this phase.

(2) **B-value check.** B-value check is conducted at the end of the saturation phase. The valves are closed and the cell pressure is increased rapidly by a small amount. The change of pore pressure inside soil sample is measured and the B-value is calculated. Back pressure is then raised to a value slightly lower than cell pressure. Valves are opened and pore pressure stabilises. These steps are repeated until a sufficient saturation is reached.

(3) **Consolidation.** Once B-values reach satisfactory values, the vertical stress is ramped up to the required consolidation stress while cell pressure and back pressure remain constant. The consolidation phase ends when the volume change becomes insignificant and excess pore pressure is dissipated.

(4) **Initial static shearing.** If the loading path to be tested does not pass through the origin, a ramp stress phase needs to be conducted to avoid abrupt increase of shear stress. Static shearing is applied with drainage open. LVDT readings are zeroed when initial static shear stress target is reached.

(5) **Shear testing.** Valves are closed to conduct undrained shear tests. Monotonic tests are displacement-controlled with increasing displacement at a constant rate (5%/hour). Cyclic tests are stress-controlled with required loading amplitude and waveform.

3.5 Data correction

Frictions and cross-coupling are two of the major issues concerning multi-directional simple shear tests. The measurement of applied load can be biased by the frictions that exists in loading tables and stacked rings or by the cross-coupling between the two horizontal strokes. Some pilot tests were conducted to probe the effects of friction and cross-coupling and the results of an example test are shown in Figure 3.9 and 3.10. This example test was conducted with sample assembly (caps and stacked rings) but without soil. Cell pressure was increased to 280 kPa to reproduce actual pressure situation. Sinusoidal displacement with amplitude of 1 mm was applied in X direction at a frequency of 0.1 Hz to simulate cyclic loading scenario.

Figure 3.9 presents the measurements of horizontal load and displacement in this test. Synchronization is found between the variation of X-load and X-displacement. Since the sample assembly had no sand in it, the load readings should come from either friction or transducer noise. Load readings are thus filtered through a low pass Butterworth filter as shown in Figure 3.10(a). The filtered loads are replotted versus X-displacement in Figure 3.10(b). The correlation between filtered X-load and X-displacement evidences the existence of friction which can be determined from the angle of inclination at approximately 0.003 kN/mm, corresponding to a shear stress of 0.36 kPa/mm. It should be noted that the actual load cell readings can drift away from the calculated friction because of device oscillations and imbalanced motion of the load actuator. The correction for friction will not be consistent and accurate under this circumstance. Fortunately, the effects of friction are not pronounced

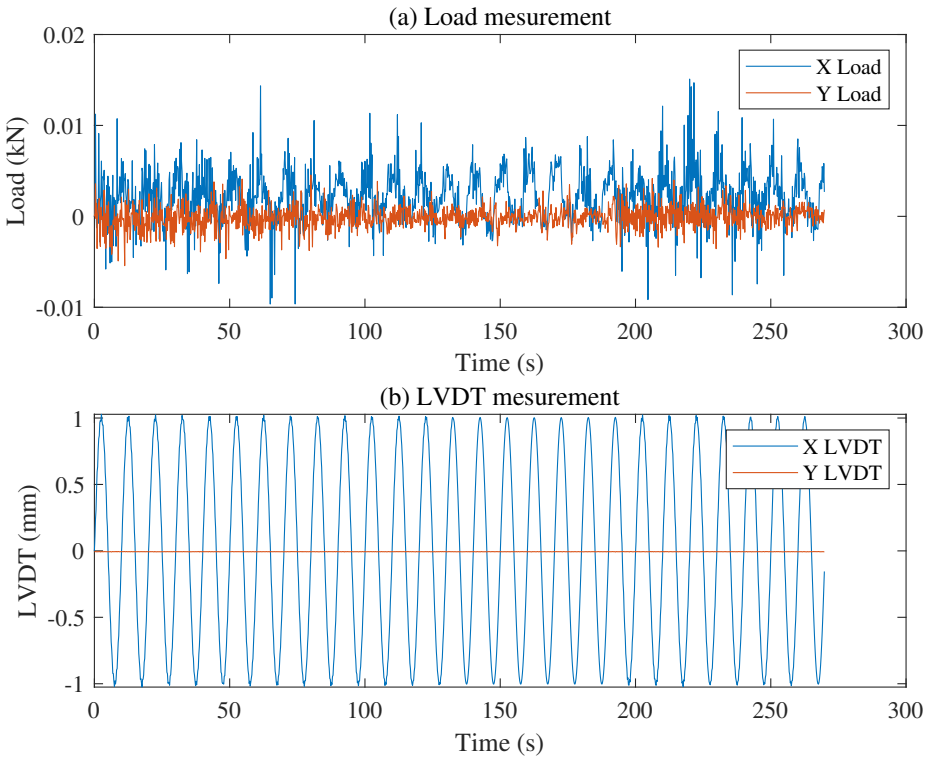

Fig. 3.9 The measurements of horizontal load and displacement load in a pilot test

in this study, considering the amplitude of shear stress applied in this study is always above 15 kPa and displacement becomes higher than 2 mm only when liquefaction takes place. The friction can be further reduced if the horizontal strokes and steel rings are lubricated regularly by oil and Teflon spray, respectively, as done in this study.

The variation of Y-load and Y-displacement with X-displacement, by contrast, is minimal. It indicates that the effects of the cross-coupling between horizontal loading tables are not significant. It should be noted, however, that the cross-coupling phenomenon can become more discernible in the tests with actual soil samples, which can be observed clearly in the results of bi-directional linear tests such as Figure 5.5b. It is impossible to determine whether this is a result of device limitations or due to the anisotropy of the soil samples. Corrections to account for the effects of cross-coupling are thus not applied in case inaccurate “correction” misleads the understanding of test data.

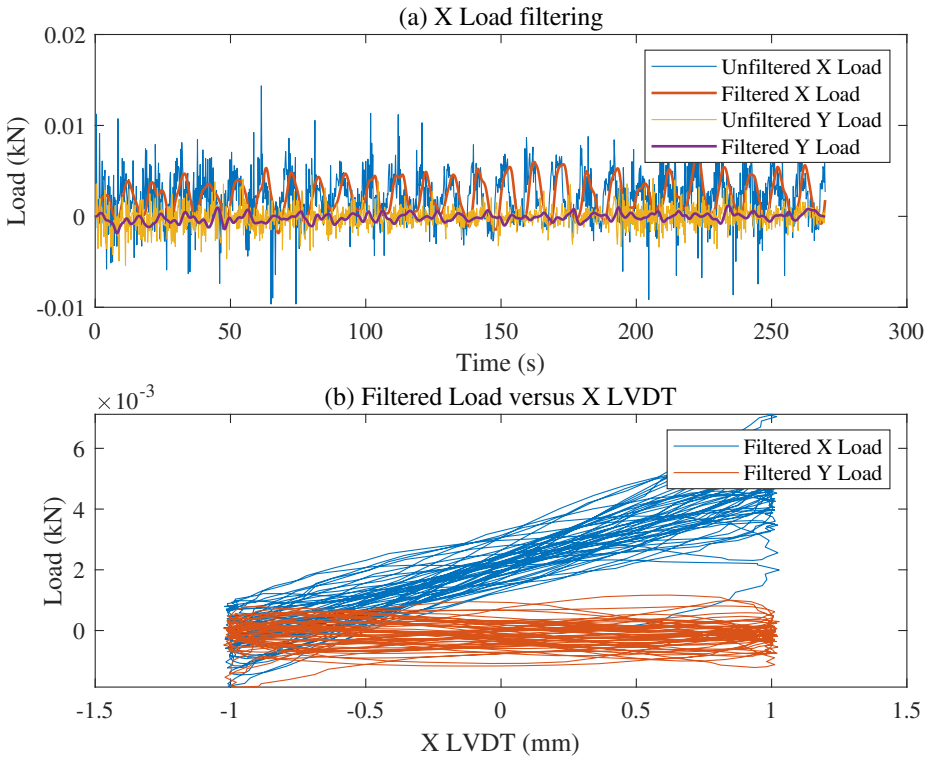

Fig. 3.10 Filtered load versus X displacement

Other potential corrections including membrane penetration and inertial loading were demonstrated by Boulanger (1990) and Wu (2002) to be insignificant for the grain size and loading frequency used in this study. Thus, no corrections are made to the test data presented in this study. All the test results shown in this dissertation are based on uncorrected data.

3.6 Liquefaction criterion

A consistent liquefaction criterion in simple shear tests is required to compare liquefaction resistance and understand liquefaction phenomenon of sands. There are two widely accepted categories of liquefaction criterion. The first category of liquefaction criterion relates liquefaction to an excess pore pressure ratio of unity (Seed and Lee, 1966). Since early studies considered the cause of liquefaction as the complete loss of effective confining pressure, this criterion was generally effective, especially in the tests with uni-directional loading.

However, the existing results of multi-directional simple shear tests indicated that excess pore pressure ratio does not always increase to unity in multi-directional loading conditions. Thus, this criterion may not be applicable to the tests in this study. The other category of liquefaction criterion relates liquefaction to a certain level of shear strain because a large strain level indicates sand's resistance to deformation has been reduced significantly. There are various strain-based liquefaction criteria in the literature. For instance, Tatsuoka et al. (1982) defined liquefaction as double amplitude shear strain of 15%, while Vaid and Sivathayalan (2000) used single amplitude shear strain of 3.75% as the requirement of liquefaction. In one of the earliest liquefaction studies, however, Seed and Lee (1966) indicated that sand loses resistance to deformation after shear strain exceeds 3%. The 3% shear strain criterion was subsequently used by Ishihara and Yamazaki (1980) in the earliest multi-directional simple shear tests on saturated sands. Realising the shear strain in uni-directional cyclic simple shear tests is not always symmetrical, Kammerer (2002) and Wu (2002) included a double amplitude shear strain of 6% in their liquefaction criterion. The criterion selected for uni-directional tests in this study follows this criterion to define liquefaction as either single-amplitude shear strain over 3% or double-amplitude shear strain over 6%, whichever happens first. A discussion on the liquefaction criterion for multi-directional loading will be made in Chapter 7.

3.7 Parameter definition

Figure 3.11 presents a graphical illustration of a figure-8 loading path, which starts from the point S. Some important parameters that will be used for the analysis in this dissertation are illustrated on the graph. *SSR* is shear stress ratio, which is the ratio of shear stress over initial effective vertical stress. *CSR* is cyclic stress ratio and equals half of the range of shear stress ratio. Although Figure 3.11 is plotted in shear stress ratio coordinates, the definition of the parameters can be transformed straightforwardly to shear stress and shear strain coordinates.

Dip direction (or downhill direction) is defined as the direction along which an initial static shearing is applied. Strike direction is perpendicular to dip direction. It is worth to

mention that the loading system has a different coordinate system, with two axes named as X and Y. In most of the tests performed, initial static shearing is applied only in X direction, that is, X direction of loading system is also the dip direction. But there are also some tests where Y direction or other directions (such as Figure 3.11) of the loading system become the dip direction. For simplicity, X and Y direction are preferred in this study to present test data in an intuitive manner, while dip and strike direction are used to facilitate the calculation of certain parameters and the analysis of certain loading paths (bi-directional loading in particular).

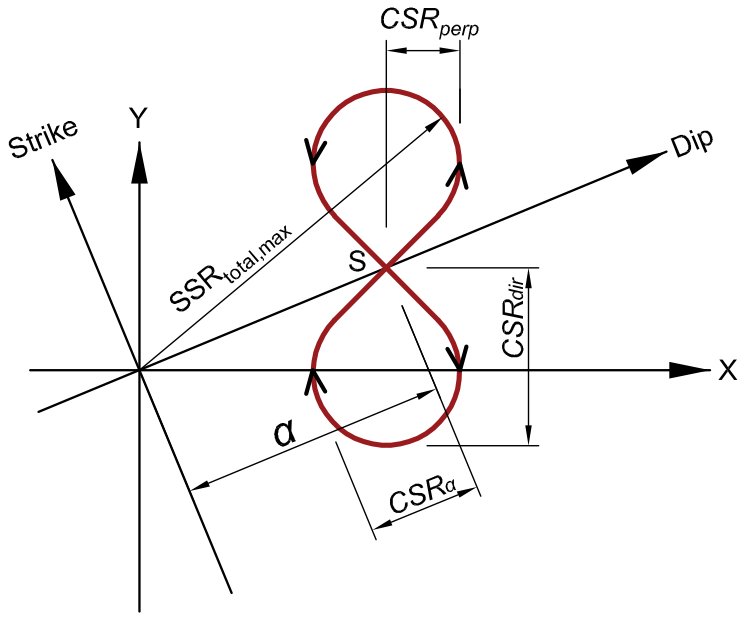

Fig. 3.11 Graphical illustration of a figure-8 loading path and the definition of directions and parameters

The subscript *total* is used to indicate the calculation is based on resultant shear stress or strain and directionality is not taken into consideration. The subscript *dir* means a parameter is defined with directionality considered. For instance, CSR_{dir} is the maximum cyclic shear stress ratio across all directions.

Kammerer (2002) proposed to use aperture ratio (AR) and reversal parameter (RP) to characterise a loading path, which are defined as follows:

$$AR = \frac{CSR_{perp}}{CSR_{dir}} \tag{3.1}$$

$$RP = \frac{CSR_{\alpha} - \alpha}{CSR_{dir}} \tag{3.2}$$

where CSR_{perp} represents to the cyclic shear stress ratio in the direction perpendicular to the orientation along which CSR_{dir} is determined, α is the initial static shear stress ratio and CSR_{α} is the cyclic shear stress ratio in the direction of static shearing. Initial static shear refers to the shearing condition at the geometric center of a loading path in this study, unless indicated otherwise.

The definition of other parameters will be given when they are introduced in the following chapters.

3.8 Summary of tests

The summary of the tests performed is tabulated in table 3.3. Four monotonic and seventy five cyclic undrained simple shear tests were conducted on clean Hostun sands in this study. The relative density of sand samples ranged from 30.3% to 77.8%, though 77 out of the 79 tests had relative density between 46.8% and 68.7%. All the tests started with initial vertical overburden stress of 100 kPa except for test LM-4 which was consolidated under $\sigma_{v,0}$ of 20 kPa. Four tests had Skempton's B-values lower than 0.9 (test LS8, C15-2, C20-2 and E2010-2) with the lowest value at 0.854. All the other tests held B-values higher than 0.9 which corresponds to a degree of saturation over 99.5% according to Black and Lee (1973).

Constant vertical load was adopted as the boundary condition of all the tests. The largest change of height was measured in test C20-4 where the height of the soil sample reduced by 2.2% (from 16.785 mm to 16.415 mm) when the test was terminated, manifesting that satisfactory undrained condition was maintained with the modified top cap and sample preparation procedures.

Cyclic loading was applied in a sinusoidal manner. Uni-directional and bi-directional linear tests had sinusoidal shear waves in only one direction with a frequency of 0.1 Hz. Circular, oval and figure-8 tests had shear waves in both X and Y direction with the same master frequency of 0.05 Hz but different frequency multiplier (figure-8 tests), amplitude and phase difference (circular and oval tests).

These loading paths were widely used in previous research and were thus selected to provide a baseline for comparisons. The loading condition of these tests is summarized in table 3.3. CSR_X and CSR_X represents the amplitude of cyclic shear stress ratio in the X and Y direction of the loading system, while $SSR_{X,0}$ and $SSR_{Y,0}$ indicates the initial shear stress ratios along X and Y direction. The direction of the resultant initial static shear force is the dip direction (or downhill direction), which will be discussed when certain loading paths (bi-directional loading in particular) are analysed. Again, the dip and strike directions are not necessarily aligned to X or Y direction.

Some of the important results that will be used in the analysis in the following chapters are also included in table 3.3. $r_{u,max}$ is the maximum excess pore pressure ratio recorded in a test by the cycle where liquefaction takes place. $r_{u,min}$ refers to the minimum excess pore pressure ratio in the liquefaction cycle. K_μ is the coefficient of multi-directional loading based on directional cyclic shear stress ratio CSR_{dir}, which will be clarified in chapter 7.

Table 3.3 Summary of the conducted tests

Test name	**Test type**	D_r (%)	B-value	N_L	$\sigma_{v,0}$	$SSR_{X,0}$	CSR_X	$SSR_{Y,0}$	CSR_Y	$r_{u,max}$	$r_{u,min}$	K_μ
LM-1	Uni-directional monotonic	61.1	0.944	0	100							
LM-2	Uni-directional monotonic	59.7	0.92	0	100							
LM-3	Uni-directional monotonic	57.4	0.922	0	100							
LM-4	Uni-directional monotonic	57.4	0.922	0	20							
LC1	Uni-directional linear	55.8	0.97	86	100	0	0.149	0	0	0.95	0.54	
LC2	Uni-directional linear	56.1	0.96	138	100	0	0.148	0	0	1.01	0.78	
LC3	Uni-directional linear	50.5	0.915	39	100	0	0.152	0	0	0.99	0.78	
LC4	Uni-directional linear	51.7	0.932	83	100	0	0.152	0	0	0.97	0.69	
LC5	Uni-directional linear	53.9	0.97	44	100	0	0.195	0	0	0.92	0.69	
LC6	Uni-directional linear	57.4	0.95	27	100	0	0.195	0	0	0.95	0.64	
LC7	Uni-directional linear	60.7	0.97	62	100	0	0.197	0	0	0.93	0.65	
LC8	Uni-directional linear	65	0.943	132	100	0	0.199	0	0	0.99	0.68	
LC9	Uni-directional linear	58.5	0.944	41	100	0	0.195	0	0	0.96	0.69	
LC10	Uni-directional linear	61.9	0.93	19	100	0	0.244	0	0	1.02	0.69	
LC11	Uni-directional linear	60	0.959	10	100	0	0.246	0	0	0.90	0.54	
LC12	Uni-directional linear	67	0.953	51	100	0	0.301	0	0	0.96	0.56	
LC13	Uni-directional linear	58.2	0.969	67	100	0	0.164	0	0	0.87	0.49	

Table 3.3 continued from previous page

Test name	Test type	D_R (%)	B-value	N_L	$\sigma_{v,0}$	$SSR_{X,0}$	CSR_X	$SSR_{Y,0}$	CSR_Y	$r_{u,max}$	$r_{u,min}$	K_μ
LC14	Uni-directional linear	58.4	0.9228	121	100	0	0.195	0	0	0.93	0.69	
LC15	Uni-directional linear	57.5	0.931	2	100	0	0.259	0	0	0.97	0.66	
LC16	Uni-directional linear	77.8	0.921	90	100	0	0.298	0	0	0.94	0.44	
LC17	Uni-directional linear	59.9	0.945	4	100	0	0.246	0	0	0.92	0.54	
LC18	Uni-directional linear	57.7	0.931	6	100	0	0.295	0	0	1.00	0.49	
LC19	Uni-directional linear	67.8	0.937	12	100	0	0.344	0	0	0.89	0.41	
LC20	Uni-directional linear	50.9	0.95	5	100	0	0.194	0	0	0.89	0.53	
LC21	Uni-directional linear	61.1	0.913	32	100	0	0.194	0	0	0.96	0.66	
LS1	Uni-linear/static shear	57.6	0.936	46	100	0.033	0.209	0	0	1.01	0.59	1.11
LS2	Uni-linear/static shear	66.7	0.961	222	100	0.048	0.210	0	0	1.02	0.62	1.04
LS3	Uni-linear/static shear	53.4	0.958	5	100	0.058	0.255	0	0	1.00	0.51	1.16
LS4	Uni-linear/static shear	58.4	0.941	74	100	0.061	0.257	0	0	0.95	0.51	1.42
LS5	Uni-linear/static shear	58.6	0.948	31	100	0.076	0.256	0	0	1.00	0.58	1.26
LS6	Uni-linear/static shear	56.6	0.933	50	100	0.059	0.260	0	0	1.01	0.44	1.43
LS7	Uni-linear/static shear	58.2	0.948	28	100	0.122	0.255	0	0	1.01	0.43	1.25
LS8	Uni-linear/static shear	60.5	0.89	2	100	0.074	0.260	0	0	0.97	0.44	0.81
LS9	Uni-linear/static shear	63.5	0.911	2	100	0.158	0.309	0	0	0.99	0.20	0.70

Table 3.3 continued from previous page

Test name	Test type	D_R (%)	B-value	N_L	$\sigma_{v,0}$	$SSR_{X,0}$	CSR_X	$SSR_{Y,0}$	CSR_Y	$r_{u,max}$	$r_{u,min}$	K_μ
LS10	Uni-linear/static shear	55.5	0.94	5	100	0.207	0.254	0	0	0.98	0.25	1.07
LS11	Uni-linear/static shear	59.9	0.919	1	100	0.292	0.265	0	0	0.58	0.00	0.80
Bilinear-1	Bi-directional linear	55.8	0.954	40	100	0.104	0	0	0.251	0.90	0.61	1.37
Bilinear-2	Bi-directional linear	56.7	0.941	20	100	0	0.248	0.067	0	0.97	0.62	1.21
Bilinear-3	Bi-directional linear	61.5	0.924	2	100	0	0.248	0.076	0	0.93	0.50	0.69
Bilinear-4	Bi-directional linear	55.7	0.967	3	100	0.072	0	0	0.302	0.95	0.50	1.19
Bilinear-5	Bi-directional linear	61.2	0.931	2	100	0.119	0	0	0.313	0.86	0.47	0.89
Bilinear-6	Bi-directional linear	30.3	0.926	1	100	0.152	0	0	0.201	0.78	0.58	
Bilinear-7	Bi-directional linear	49.9	0.949	3	100	0.152	0	0	0.147	0.85	0.75	0.73
Bilinear-8	Bi-directional linear	61.1	0.922	4	100	0.153	0	0	0.305	0.81	0.46	0.98
Bilinear-9	Bi-linear/ static shear	55.9	0.939	1	100	0.153	0	0.111	0.092	0.82	0.67	0.31
Bilinear-11	Bi-linear/ static shear	56.9	0.901	3	100	0.154	0	0.145	0.169	0.76	0.47	0.64
Bilinear-12	Bi-directional linear	48.7	0.955	2	100	0.304	0	0	0.176	0.55	0.48	0.84
Bilinear-13	Bi-directional linear	59.9	0.902	3	100	0.296	0	0	0.295	0.53	0.34	1.03
C15-1	Circular	56	0.952	6	100	0	0.150	0	0.149	0.84	0.76	0.64
C15-2	Circular	57	0.882	58	100	0	0.154	0	0.151	0.78	0.73	0.85
C15-3	Circular	57.6	0.951	40	100	0	0.151	0	0.150	0.79	0.73	0.78

Table 3.3 continued from previous page

Test name	Test type	D_R (%)	B-value	N_L	$\sigma_{v,0}$	$SSR_{X,0}$	CSR_X	$SSR_{Y,0}$	CSR_Y	$r_{u,max}$	$r_{u,min}$	K_μ
C15-4	Circular	58.9	0.961	17	100	0	0.151	0	0.151	0.88	0.80	0.68
C15-5	Circular	59.7	0.954	63	100	0	0.154	0	0.151	0.80	0.73	0.81
C20-1	Circular	59.6	0.97	26	100	0	0.203	0	0.200	0.73	0.66	0.95
C20-2	Circular	60.5	0.892	2	100	0	0.201	0	0.200	0.71	0.64	0.62
C20-3	Circular	63.1	0.956	19	100	0	0.201	0	0.201	0.77	0.72	0.70
C20-4	Circular	63.3	0.961	6	100	0	0.202	0	0.199	0.81	-0.01	0.57
C20-5	Circular	49.2	0.975	20	100	0	0.201	0	0.199	0.71	0.68	1.19
C25-1	Circular	60.9	0.966	2	100	0	0.245	0	0.245	0.72	0.65	0.73
C15-X7.5-1	Circular/static shear	55.4	0.901	33	100	0.072	0.152	0	0.153	0.94	0.69	0.82
C15-X15-1	Circular/static shear	56.4	0.965	89	100	0.147	0.152	0	0.150	0.84	0.55	0.90
C20-X05-1	Circular/static shear	53.2	0.971	8	100	0.050	0.202	0	0.200	0.81	0.62	0.98
C20-X05-2	Circular/static shear	60.6	0.973	92	100	0.049	0.201	0	0.200	0.80	0.64	1.06
C20-X10-1	Circular/static shear	54.8	0.975	6	100	0.098	0.201	0	0.201	0.81	0.52	0.89
C20-X10-2	Circular/static shear	58.6	0.96	1	100	-0.1	0.200	0	0.199	0.86	0.58	0.63
C20-X15-1	Circular/static shear	62.2	0.973	12	100	0.148	0.201	0	0.199	0.94	0.55	0.69
C20-X20-1	Circular/static shear	62.6	0.965	20	100	0.201	0.201	0	0.200	0.98	0.42	0.74
E1713-1	Oval	58.3	0.969	26	100	0	0.170	0	0.130	0.79	0.74	0.73

Table 3.3 continued from previous page

Test name	Test type	D_R (%)	B-value	N_L	$\sigma_{v,0}$	$SSR_{X,0}$	CSR_X	$SSR_{Y,0}$	CSR_Y	$r_{u,max}$	$r_{u,min}$	K_μ
E2010-1	Oval	54	0.954	19	100	0	0.200	0	0.100	0.95	0.72	1.04
E2010-2	Oval	57	0.854	30	100	0	0.203	0	0.101	0.85	0.69	1.04
E2010-3	Oval	62.6	0.938	60	100	0	0.202	0	0.100	0.90	0.70	0.89
E2010-4	Oval	68.7	0.963	62	100	0	0.200	0	0.102	0.86	0.68	0.77
F8-1	Figure-8	47.1	0.96	27	100	0	0.151	0	0.149	0.88	0.71	0.93
F8-2	Figure-8	55	0.976	78	100	0	0.150	0	0.148	0.92	0.72	0.91
F8-3	Figure-8	46.8	0.982	11	100	0	0.151	0	0.148	0.90	0.73	0.84
F8-4	Figure-8	48	0.982	5	100	0	0.151	0	0.149	0.94	0.74	0.78
F8-5	Figure-8	53.4	0.977	20	100	0	0.153	0	0.149	0.86	0.74	0.82
F8-6	Figure-8	52.5	0.96	32	100	0	0.153	0	0.072	0.90	0.75	0.89
F8-7	Figure-8	50.8	0.965	86	100	0	0.151	0	0.073	0.89	0.76	1.01

* $SSR_{X,0}$ and $SSR_{Y,0}$ represent the initial static shear stress ratio in X and Y direction. CSR_X and CSR_Y indicate the amplitude of cyclic shear stress ratio in X and Y direction. $r_{u,max}$ is the maximum excess pore pressure ratio in a test. $r_{u,min}$ refers to the minimum excess pore pressure ratio in the liquefaction cycle. K_μ is the coefficient for liquefaction resistance under multi-directional loading based on the discussions in chapter 7.

Chapter 4

UNI-DIRECTIONAL SIMPLE SHEAR TEST RESULTS

4.1 Uni-directional linear tests

Uni-directional loading is the most commonly tested category of loading paths that have been used in existing research regarding the cyclic behavior of soil, with liquefaction-related research being no exception. A group of uni-directional tests were thus conducted in this study, including both monotonic tests and cyclic tests, with or without initial static shearing Together, these tests illustrate the sand behaviour under uni-directional loading scenarios and provide the baseline for the comparisons with the multi-directional tests.

4.1.1 Uni-directional tests without static shearing

Monotonic Tests

Four uni-directional linear monotonic tests were conducted to investigate the fundamental soil behaviour and characteristics of clean Hostun sand. The angle of the failure line and phase transformation line for the sand used in this study can be determined through these tests. The relative density of the sample after consolidation varies from 57.4% to 61.1%. Test

LM-1, LM-2 and LM-3 were consolidated with an initial vertical stress at 100 kPa while test LM-4 was consolidated to 20 kPa.

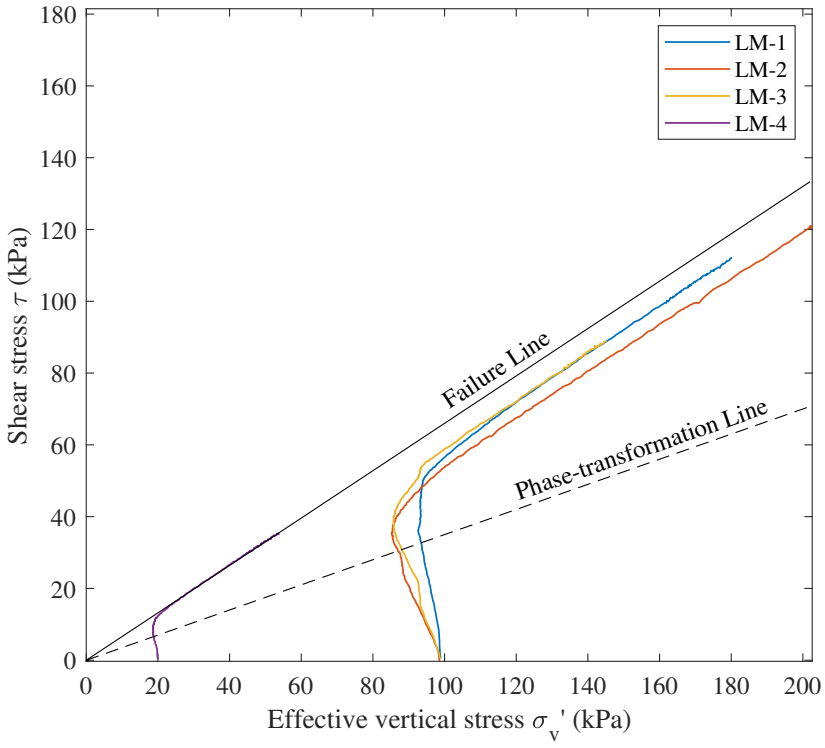

Fig. 4.1 The stress paths of the four monotonic uni-directional tests

Figure 4.1 shows the stress paths of all the four monotonic tests. The solid black line in the graph represents the failure line and the dashed black line is the phase transformation line. The angle of the failure line is 33.4°, and the angle of phase transformation line is 19.3°. It is found that the angle of failure of the four tests did not converge to a single value. This is attributed partly to the inability of the tests to reach steady state since they were all stopped at a shear strain smaller than 20%, and partly to the friction in testing system. Judgement was thus made in determining the value. The determined angle of 33.4° is comparable to the value of 33° by Mitrani (2006) and 33.7° by Doanh et al. (1997).

All the samples exhibit typical dilative behaviour as described by Castro (1969). While shear stress increases, the effective vertical stress decreases slightly first because of the generation of positive excess pore pressure. As the stress paths approach and hit the phase

transformation line, however, the effective vertical stress is gradually reversed due to the mobilised dilative behaviour and the decrease of excess pore pressure thus induced. The stress paths then develop towards the failure line until they eventually reach it and develop along the critical state line. The development of excess pore pressure in the four tests is presented in Figure 4.2. The initial increase of pore pressure, followed by a turn, is clearly shown in this figure.

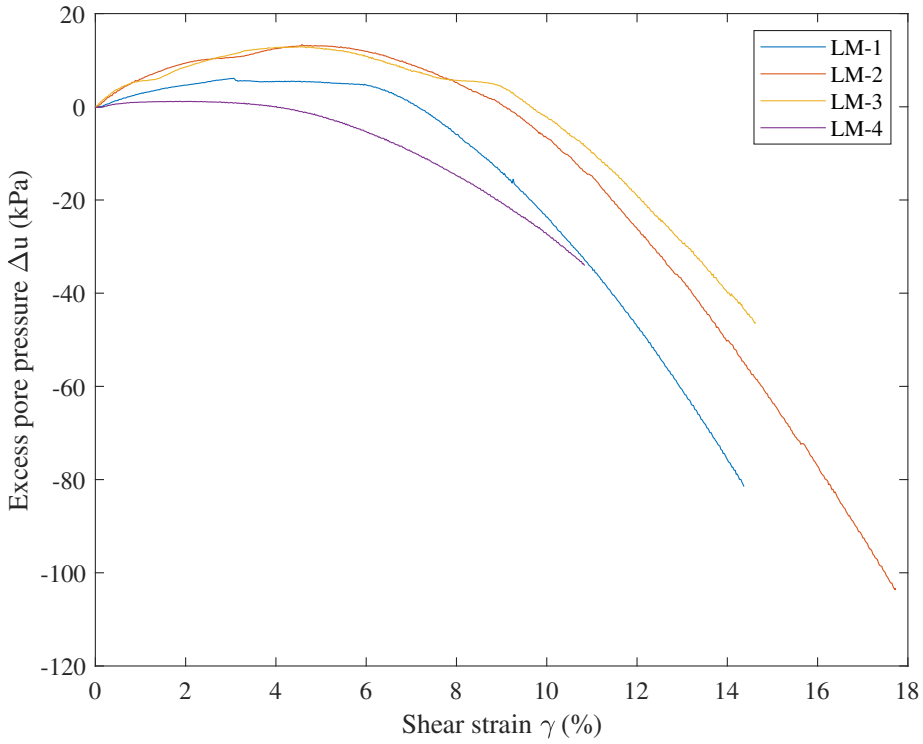

Fig. 4.2 The development of excess pore pressure in the four monotonic uni-directional tests

The dilative behaviour of the samples can also be seen from its stress-strain response, as presented in Figure 4.3. The shear stress climbs all the way up with increasing shear strain. No local peaks of shear stress are encountered and no flow-type development of shear strain is observed, confirming the dilative response of the Hostun Sand of the density range tested. The critical state point where the increment rate of shear stress becomes and remains zero is not reached before these tests were terminated.

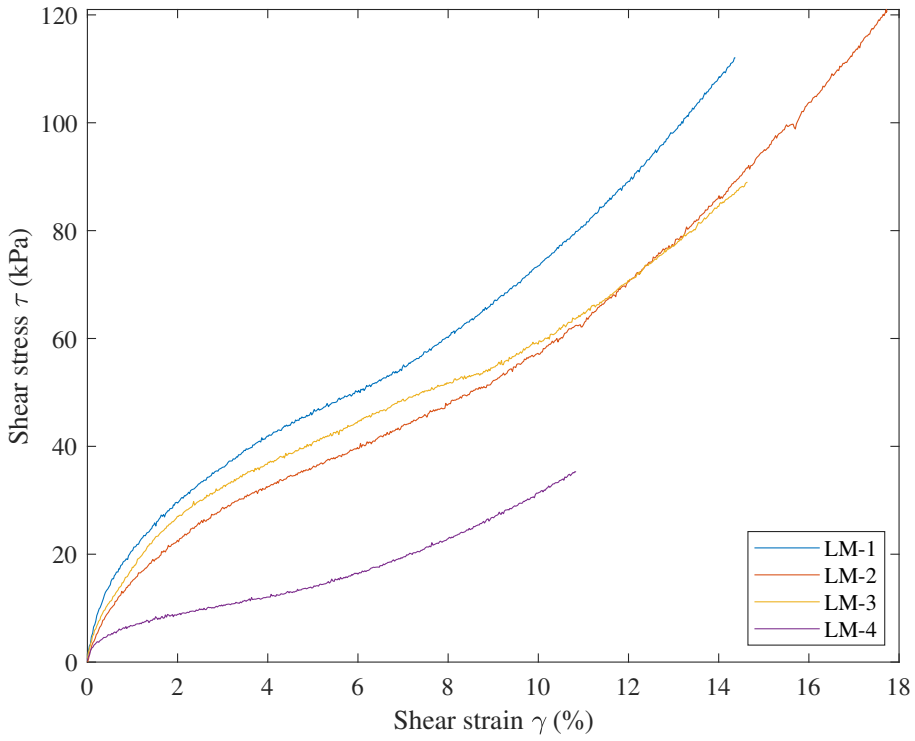

Fig. 4.3 The stress-strain relationships of the four monotonic uni-directional tests

Cyclic Tests

For a soil element underneath level ground, the earthquake loading scenarios are conventionally stimulated by uni-directional cyclic tests without static shearing (ground-level tests). As discussed earlier, the occurrence of soil liquefaction is determined when double-amplitude shear strain exceeds 6% or single-amplitude shear strain reaches 3%.

The results of an example test (LC10) are shown here to illustrate the characteristics of this category of tests. For cyclic tests, shear stress is more commonly reflected by cyclic shear stress ratio (SSR) rather than the true value of deviator stress. In simple shear tests, shear stress ratio is defined as the ratio of shear stress over initial vertical stress. This convention will be followed in this study. The example test has a relative density of 61.9% and a B value of 0.93, with an actual initial vertical stress at 98.7 kPa. The sample liquefies at the 19th cycle, sheared by a cyclic shear stress of 25 kPa (CSR=0.25) along the X direction.

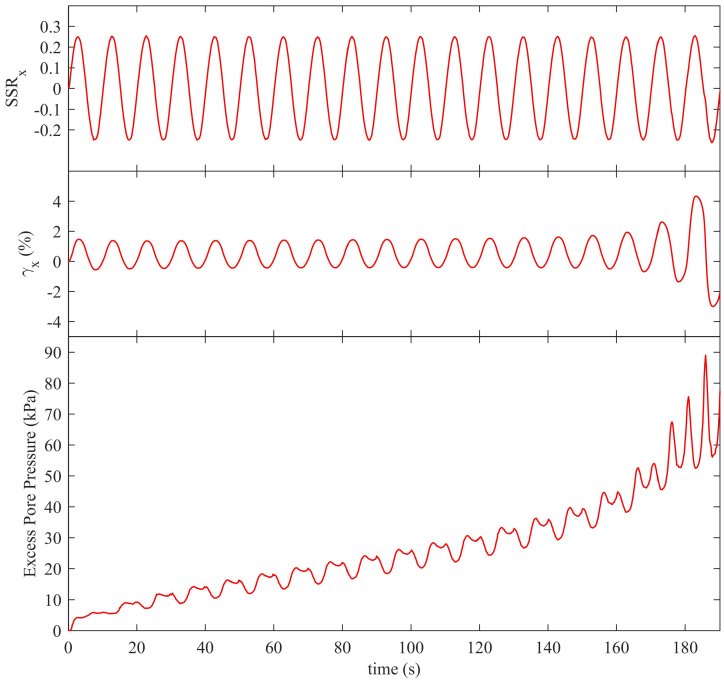

Fig. 4.4 The development of shear strain and excess pore pressure of test LC10

The development of shear strain and excess pore pressure as the shear stress is applied is presented in Figure 4.4. Excess pore pressure accumulates with shearing cycles from the very beginning of the test. Both the maximum excess pore pressure and the residual excess pore pressure of each cycle increases in general. By contrast, the shear strain does not change a lot initially, maintaining a double amplitude of around 2%, until the last few cycles where the excess pore pressure is high enough and the residual strength of the sample is much reduced due to the lowered effective vertical stress.

The stress path of the test is shown in Figure 4.5. With the generation of the excess pore pressure, the effective vertical stress declines gradually, making the stress path move towards the origin. A relatively large increase of excess pore pressure is witnessed in the first cycle, as commonly observed. In the next tens of cycles when the excess pore pressure remains low and the stress path is far away from the phase transformation line, the sample exhibits a dilative response. During the two loading phases of each cycle, the shearing, together with the dilation tendency of sand, results in a small drop in the effective vertical stress,

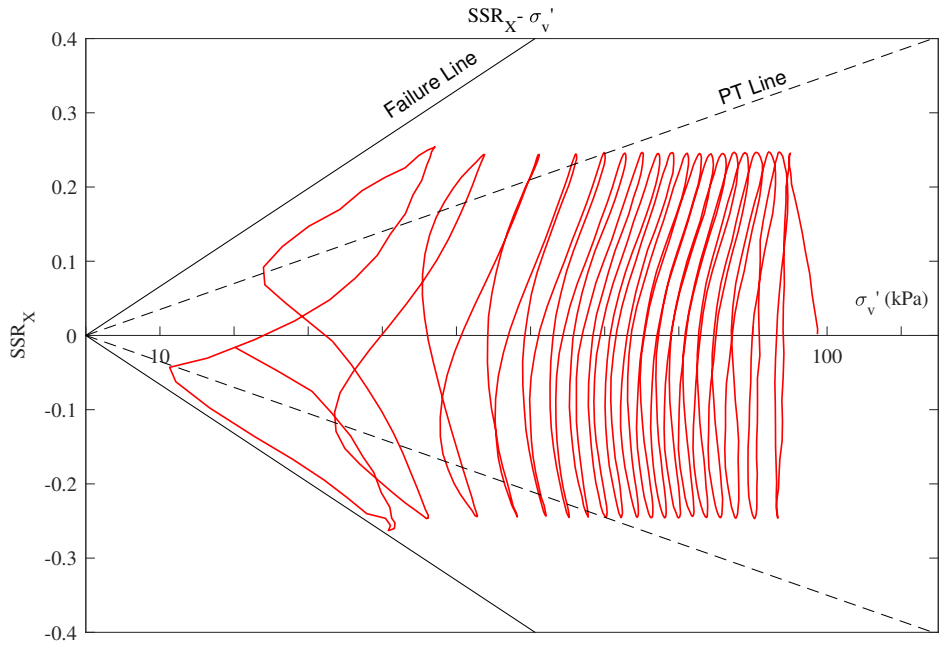

Fig. 4.5 The stress path of test LC10

if at all, or even increases with increasing SSR. In the unloading stages, by contrast, the dilation mobilised in sand is released and the effective vertical stress reduces. The excess pore pressure increases twice and decreases twice respectively within a single cycle, giving a widely-recognised "double peak" feature in the pore pressure plot, which can be seen more clearly in Figure 4.6, where the results of the 17th cycle of test LC10 are represented by solid curves and those of the 18th cycle in dashed lines. There are pairs of peaks that seem to have similar levels and are often misunderstood intuitively to be in the same cycle, but this may not necessarily be the case. The final effective vertical stress of each cycle is always lower than the initial one, since the residual excess pore pressure keeps increasing cycle by cycle, as observed in Figure 4.4 and in Figure 4.6.

When the effective vertical stress approaches zero and liquefaction is about to be initiated, the sand has softened dramatically and exhibits a contractive tendency. In the last cycle of the test, the effective vertical stress decreases dramatically during the loading phases, as a result of a contractive tendency. After the stress path intersects the phase transformation line, the sample turns from being contractive to a dilative tendency, with the effective vertical stress regained. During the unloading phase, the dilation is released again and excess pore

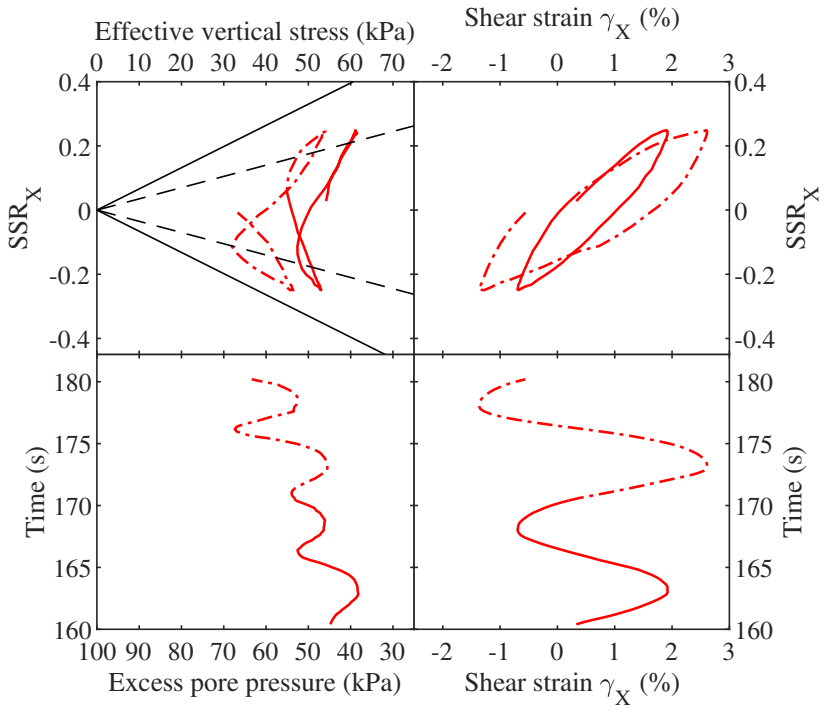

Fig. 4.6 The 4-way plot of the 17th and 18th cycle of test LC10 (the solid curves are the 17th cycle and the dashed curves are the 18th cycle)

pressure keeps growing. In the second loading stage of the last testing cycle, the stress path eventually reaches the failure line, thus the sample fails and liquefaction is triggered.

The stress strain response of test corresponds to the stress path, as plotted in Figure 4.7. For the cycles with low excess pore pressure, the hysteresis loops remain small while there is only limited shear strain developing with increasing shear stress. As the excess pore pressure increases, the peak-to-peak strain within a single cycle increases gradually, as does the shear strain that develops during the loading phases of each cycle, making flatter hysteresis loops. There is not a section, even in the last cycle of the test, where the shear strain can accumulate without the increase of shear stress (i.e. a flat period), again confirming that the sample exhibits dilation-featured response (cyclic mobility).

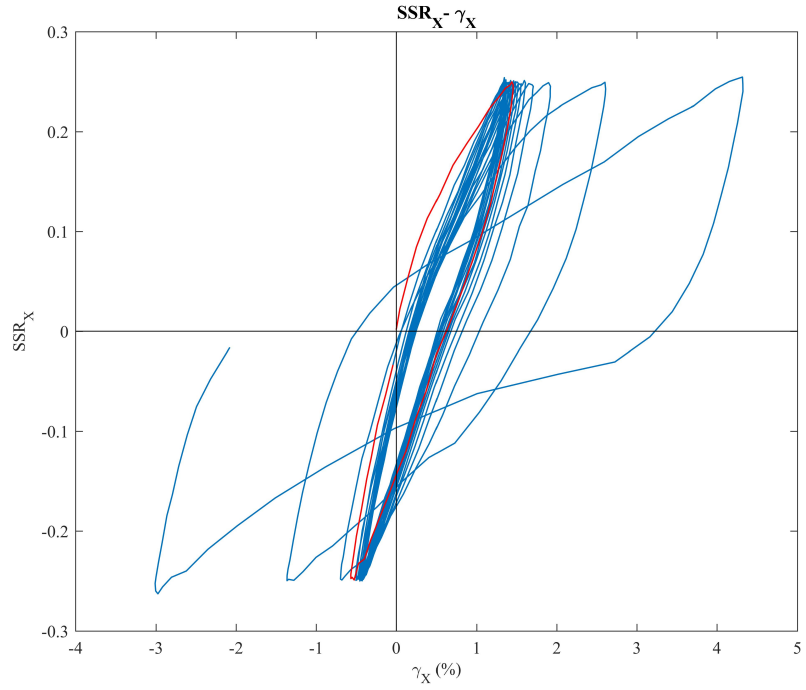

Fig. 4.7 The stress-strain response of test LC10 (the first cycle is coloured red)

4.1.2 Uni-directional tests with static shearing

For a soil element underneath a slope, however, a static shearing force determined by the inclination angle is applied constantly to the soil element in the geological dip direction. If the cyclic loading caused by earthquakes is in the direction parallel to the dip of the slope, the soil response in this loading scenario can be investigated by cyclic uni-directional simple shear tests with static shearing (also termed "dip-shaking slope tests" in this study). After saturation, the soil samples are sheared monotonically to the target shear stress with drainage open and are consolidated in a K_α consolidation condition, before an undrained cyclic shearing is applied in line with the static shearing direction.

The discussions regarding this category of tests usually involve whether shear stress reversal exists. The importance of the stress reversal rests in the widely-made observations that it determines if excess pore pressure can be fully developed or not, that is, if the stress path can reach the origin in stress space or not. When the cyclic shearing is at a phase where its shear force is in the opposite direction to the static shear force and counterbalances the

latter, the resultant shear force may be either positive or negative, depending on the relative amount of the two kinds of shear stresses. If the amplitude of cyclic shear stress is larger than the static shear stress, stress reversal will happen; otherwise, there will be no stress reversal.

The results of a test (LS7) which has stress reversal and liquefies at the 28th cycle are presented here. The sand sample of this example test has a relative density of 58.2% and a B value of 0.95, consolidated to an initial vertical stress of 99.3 kPa. The amplitude of cyclic shear stress is 25 kPa (*CSR*=0.25) and the static shear stress is 12.5 kPa (SSR=0.125). The positive direction of shear stress and strain is equivalent to the downhill direction of a real slope.

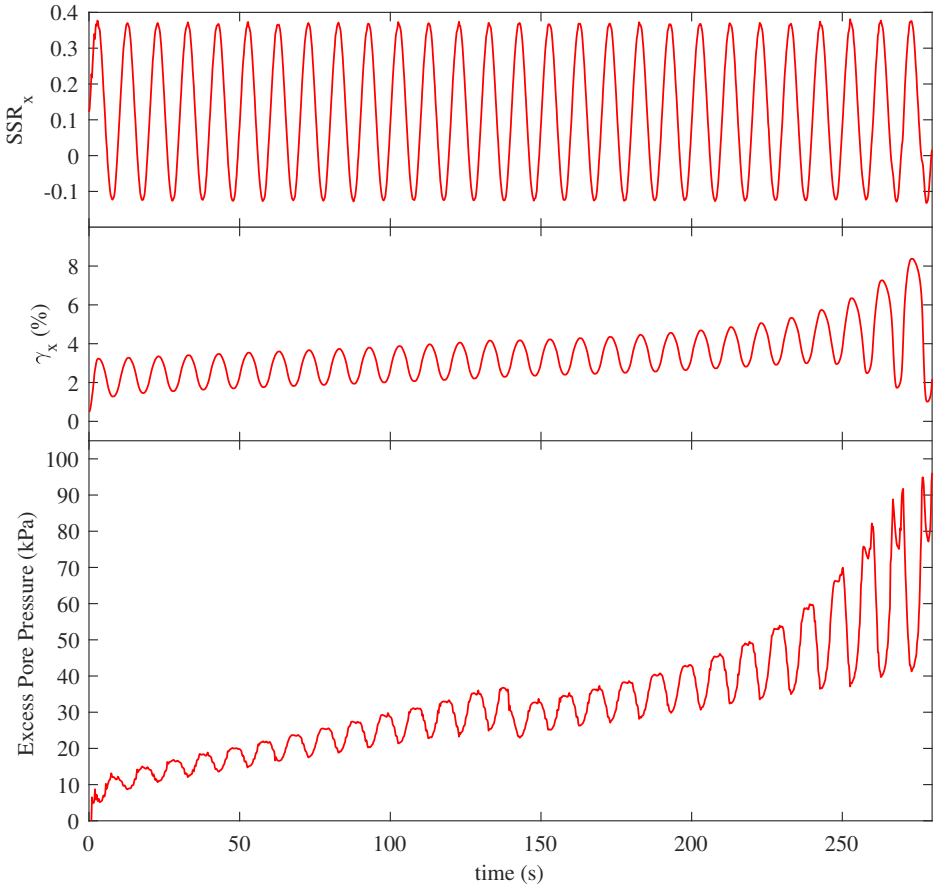

Fig. 4.8 The development of shear strain and excess pore pressure of test LS7

As shown in Figure 4.8, there is an obvious flaw in this test. The excess pore pressure temporarily decreases after the 14th cycle and climbs back afterwards. The shear strain, as well as the vertical stress and vertical displacement (Figure 4.9), nonetheless, do not have

such an abrupt change. Together with the fact that the sample is able to liquefy eventually, this eliminates the possibility of significant leakage. The most reasonable explanation left seems to be that a sudden dislocation happens in the stack of steel rings, resulting in a part of the rubber membrane deforming abruptly or even being penetrated by sand grains, which brings about an increase in the volume of the sample.

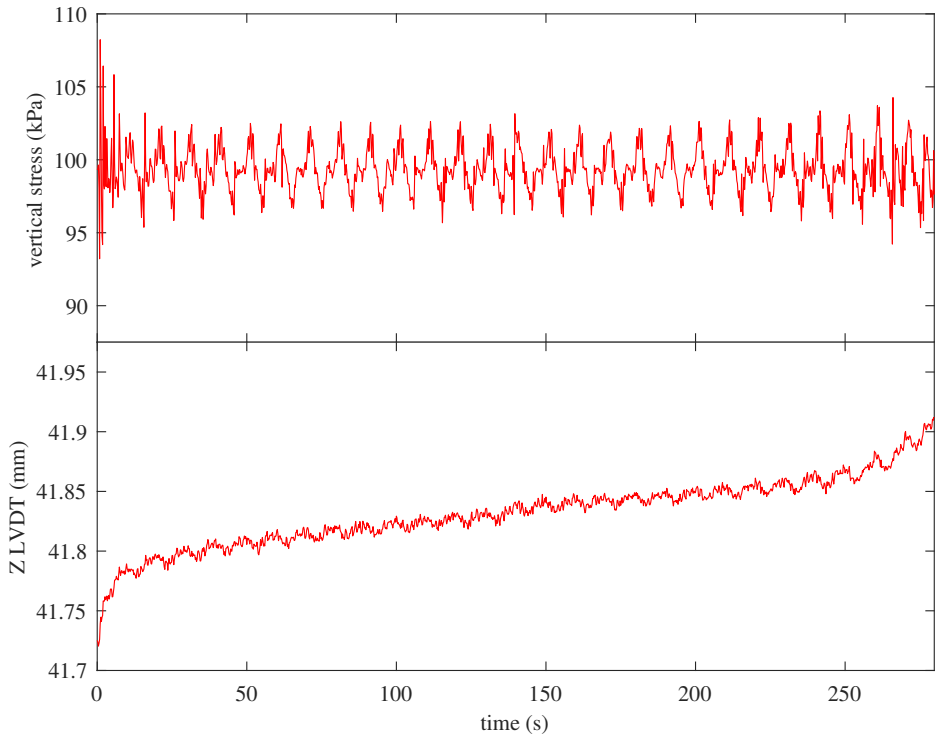

Fig. 4.9 The variation of vertical stress and vertical LVDT with time in test LS7

Considering the undesired variation is not observed in any of the other parameters, this test is reckoned to be valid and the analysis based on it is still tenable, except for the number of cycles to liquefaction. As the excess pore pressure had an unexpected decrease in the middle of the test, the number of cycles to liquefaction should have become higher correspondingly, compared with the case where no such decrease occurs. The “true” number of cycles to liquefaction should fall in a range whose upper limit is the recorded number and the lower limit is the cycle number where the abrupt change happens. To be more specific, if a cycle is considered “recovered” when both the minimum and maximum excess pore pressure in this cycle are higher than those in the cycle right before the prompt decrease

takes place, the test can be assumed to have proceeded directly to the first "recovered" cycle from the affected cycle if the problem did not happen, without going through the cycles in between. Along with this assumption, the excess pore pressure recovers at the 19th cycle in this test and the 15-18th cycles would not be there if the unanticipated drop had not occurred. The number of cycles to liquefaction is hence adjusted from 28 to 24, which means the true pre-liquefaction cycle number is very likely to fall somewhere around 24. While this adjustment is rather arbitrary, it does provide useful information for the analysis in terms of liquefaction resistance. It will be marked and clarified in the later sections whenever this adjustment is applied.

Similar to the tests without static shearing reported in the preceding session, the first cycle gives a larger increase of excess pore pressure. The so-called "double peak" phenomenon in the development of excess pore pressure can also be observed in this test. But different from the level-ground tests, the valleys between the pairs of peaks are not pronounced until the last a few cycles. This can be explained conveniently by the uneven resultant amplitudes of shear stresses, as shown in Figure 4.10. In the early cycles, except for the first cycle, the sand sample at a density similar to that of LC10 exhibits a dilative response as expected, with the excess pore pressure decreasing during loading and increasing during unloading. However, the amplitude of negative shear stress ratio is only one third of its positive counterpart, as a result of which the dilative response cannot be mobilised by negative shear stress to the same extent as by positive shearing. That is, the relatively small negative shear loading cannot counteract the increasing tendency to develop positive excess pore pressure, hence making the valleys less prominent. The valleys do not appear until the sand sample is softened so much that the inconsiderable loading phase in the negative side can also lead to a significant change of excess pore pressure from increasing to decreasing.

This can be examined more carefully in Figure 4.11, where the 4-way plots for the 25th cycle (solid) and the 26th cycle (dashed) are presented. The increase in negative shear stress in the 25th cycle fails to reach the phase transformation line or accomplish the contraction-to-dilation transition of the sand sample. The corresponding development of excess pore pressure versus time shows a temporary plateau, rather than a valley, at the maximum negative

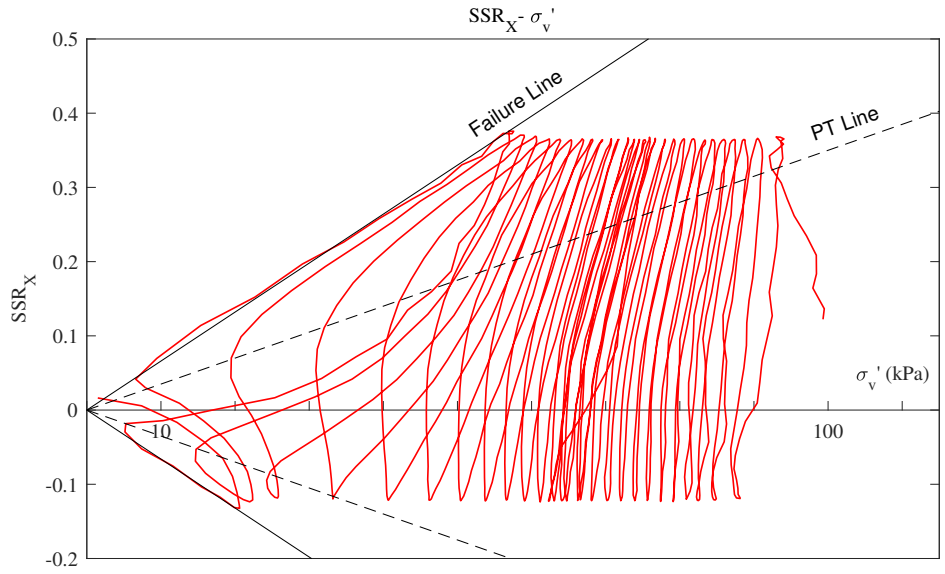

Fig. 4.10 The stress path of test LS7

shear stress, as shown in the bottom left plot. In the 26th cycle, however, the effective vertical stress has been reduced to a point where even the relatively small negative shear loading can still push the stress path to cross the phase transformation line, resulting in a significant decrease of excess pore pressure.

In addition to the discrepancy in the valleys in the excess pore pressure plots, the with-static-shearing tests also differ partly from the no-static-shearing ones in terms of strain development, as illustrated in Figure 4.12. While the stress-strain loops become flatter and flatter, indicating the same kind of strain softening behaviour as in level-ground tests, the shear strain accumulates towards the positive direction progressively, exhibiting a clear downhill preference that is not seen in level-ground tests. This is not surprising since the downhill shear stress is more dominant in this test. Wu (2002) and Biscontin et al. (2004) observed the same phenomenon on sand and clay, respectively. Furthermore, it is worth noting that prior to the cycle where the double amplitude shear strain exceeds 6%, the maximum cumulative shear strain has reached as much as 6.7%.

In stark contrast, the soil response becomes more unusual if there is no stress reversal. The test results of a test (LS11) in this category are shown in Figure 4.13 and 4.14. The sample has a relative density of 59.9% and a B value of 0.92, consolidated to an initial

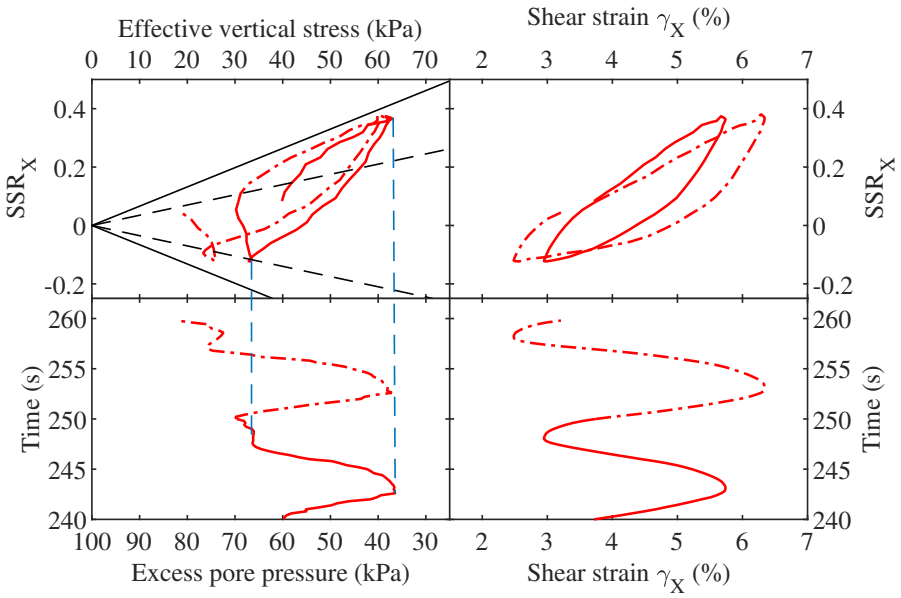

Fig. 4.11 The 4-way plot of the 25th and 26th cycle of test LS7 (the solid curves are the 25th cycle and the dashed curves are the 26th cycle)

vertical stress of 98.7 kPa. As test LC10 and test LS7, the amplitude of cyclic shear stress is 25 kPa (*CSR*=0.25). But this test has a high static shear stress at 30 kPa (SSR=0.3), higher than the cyclic shear stress amplitude. The positive direction of shear stress and strain is still equivalent to the downhill direction.

The sand sample fails in the first cycle due to the devastating single amplitude shear strain within this cycle, but the test results of the four subsequent cycles are still presented here to demonstrate the peculiar soil response in this test. The most remarkable feature rests in the inability of stress path to reach the origin, that is, the inability of excess pore pressure to develop to 100% of the vertical stress. Figure 4.13 gives the stress path of this test. During the first loading period, the stress path initially develops towards the origin with the generation of positive excess pore pressure, but soon curves back away from the origin, indicating a phase transformation resulting in the decrease of excess pore pressure. However, the exact position of phase transformation state is difficult to locate because the adaptive loading system tends to overreact at the initial stage of loading and induce significant

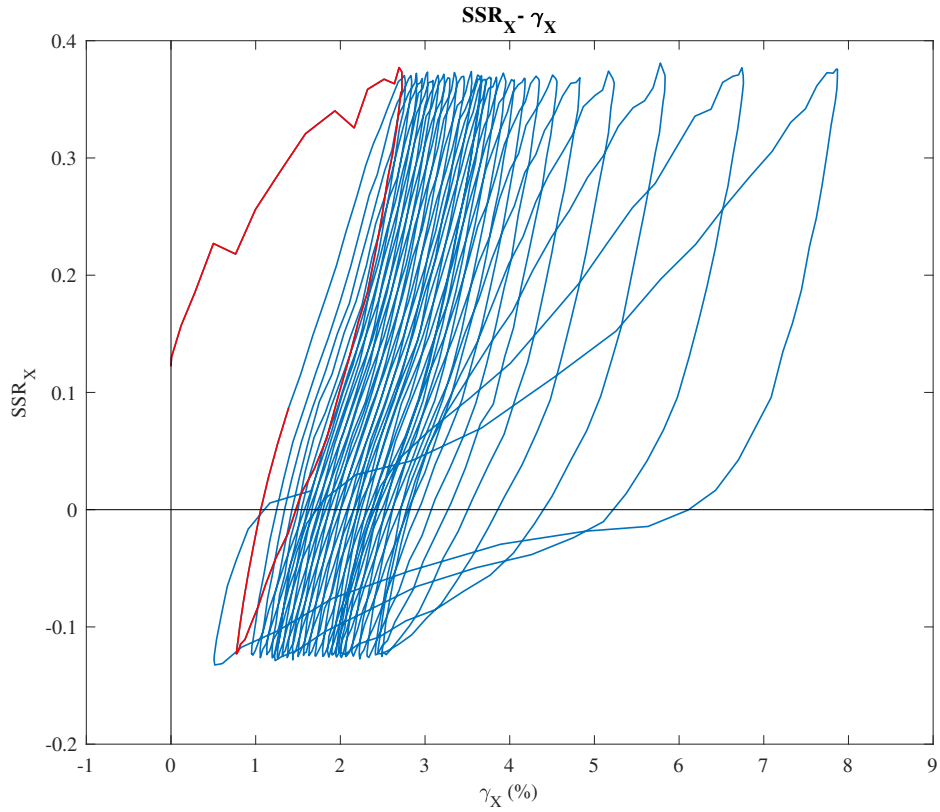

Fig. 4.12 The stress-strain response of test LS7 (the first cycle is coloured red)

oscillations of stresses. The oscillations of loading system, together with system friction, may cause the phase transformation state to deviate from the PT line. Considering this effect becomes particularly obvious when a test starts from a large initial static shear force, no conclusions on the phase transformation states were made for these tests.

As the test continues, the stress path becomes oblique, taking the weaving-shuttle loop shape. The stress path can reach the failure line, but can never reach the origin, with the minimum effective vertical stress still larger than 40 kPa. To be more specific, differently from the tests with stress reversal, only a small portion of the stress path of the failure cycles in this test is really located on the failure line, while the majority is not. For a typical liquefaction failure cycle that shows rather contractive response in test LC10 and test LS7, the increase of shear stress should generate huge excess pore pressure very rapidly and soon force the stress path to reach the failure line and stay there until unloading. By contrast, it seems the sand sample in this test cannot be softened enough by the non-reversal cyclic

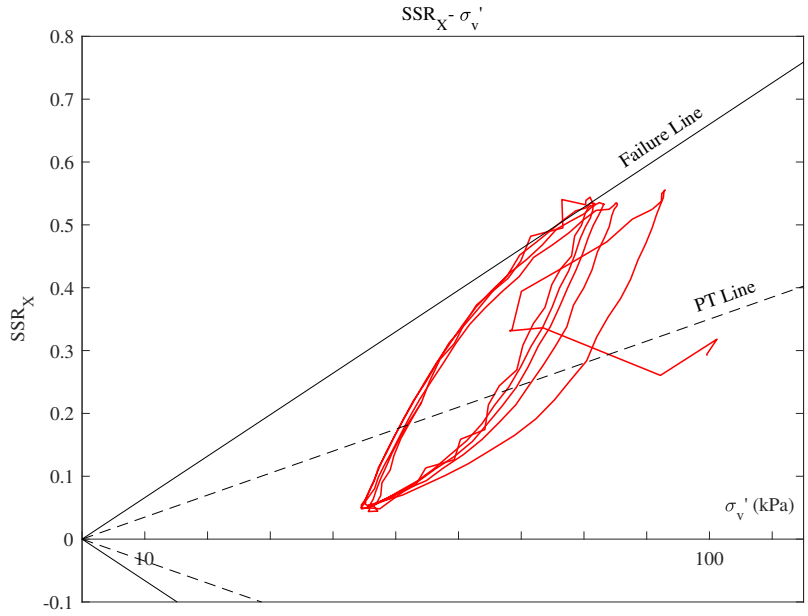

Fig. 4.13 The stress path of test LS11

shear stress before the test is terminated, so that it exhibits prominently a dilative type stress response, with the excess pore pressure decreasing with the increase of shear stress.

This peculiar dilative behaviour can be observed in the stress-strain plot as well. In Figure 4.14, the loading period in the first cycle of the test results in a shear strain over 9%, causing the sample to fail according to the single amplitude shear strain liquefaction criterion. In contrast, the subsequent cycles have only moderate double amplitude shear strains (less than 2%). The hysteresis loops of these cycles are not flat at all, also demonstrating dilative soil behaviour. While it is reasonable to attribute the phenomenon to the constantly positive resultant shear stress, the actual mechanism driving is unknow.

A fundamental question arises from these observations: is the sample in this test really liquefied? From the point of view of the shear strain liquefaction criterion, the answer is positive: the sample does liquefy in the first cycle with a large shear strain. From the perspective of hysteresis characteristics or mechanical failure, the answer is doubtful because the sample still exhibits dilative response. The results of a test with marginal stress reversal may help to further investigate this problem.

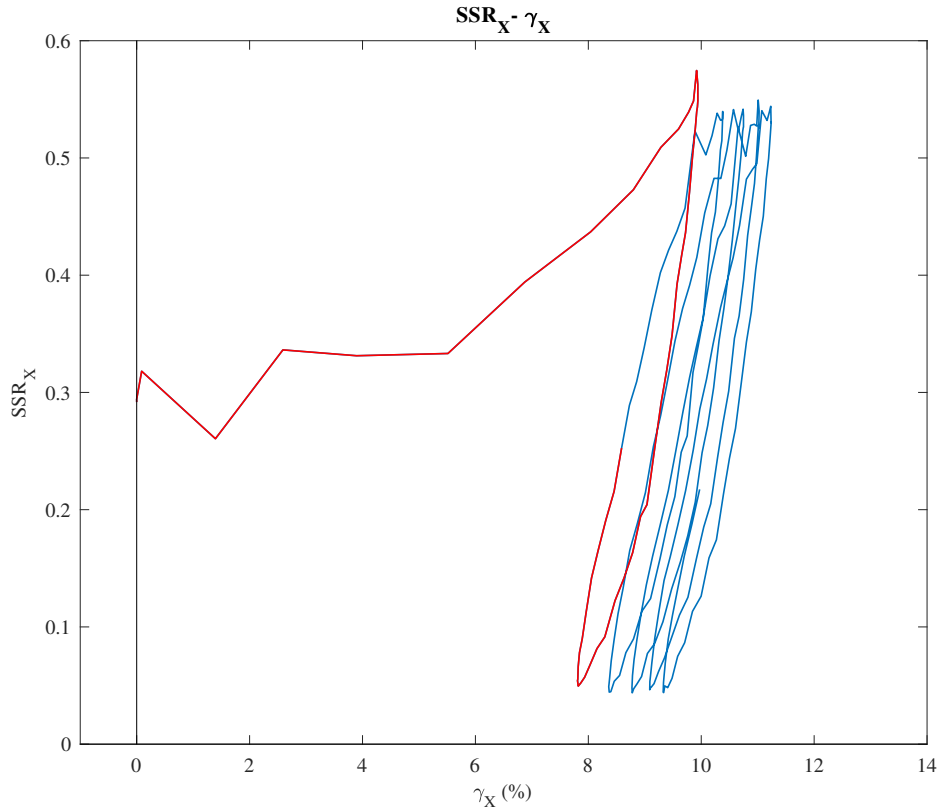

Fig. 4.14 The stress-strain response of test LS11 (the first cycle is coloured red)

Test LS10 is a test with relative density at 55.5%, a bit looser than test LS11. The Skempton's B value is 0.94. The sample is consolidated with a vertical stress at 100 kPa and an initial shear stress towards positive X direction (dip direction) at 20 kPa, before a cyclic shear stress of 25 kPa is applied. From Figure 4.16, the shear strain accumulated during the loading phase of the first cycle is up to almost 8%, therefore the sample liquefies within this cycle based on the shear strain liquefaction criterion. Similar to test LS11, however, the subsequent cycles have only moderate double amplitude shear strains and stiff-featured hysteresis loops. Correspondingly, the stress path of these cycles, as shown in Figure 4.15, is in the shape of a weaving shuttle.

In contrast, the typical behaviour of softened sands appears again in the last two cycles. The stress path of these cycles reaches the failure line at low stress level and develops along it. The minimum vertical stress is very close to zero, indicating a significant generation of excess pore pressure. The double amplitude shear strain exceeds 4% and becomes larger and

larger while the hysteresis loops become notably flatter. It seems the sample liquefies again. But differently from the first cycle, this time, the failure is caused by the stress path reaching the failure line, accompanied by large excess pore pressure, large double amplitude shear strain, and flatter hysteresis loop. From the mechanical point of view, this is more closely resembling what we expect failure to look like.

A conclusion can hence be made here: test LS11 is not liquefied from the point of view of the criterion requiring $r_u = 1$. Accordingly, a potential explanation for the peculiar soil behaviour in test LS11 is that the non-reversal shear stress hinders or prohibits a sample from developing $r_u = 1$. The soil behaviour observed is thus what it should be when the sample is not fully softened.

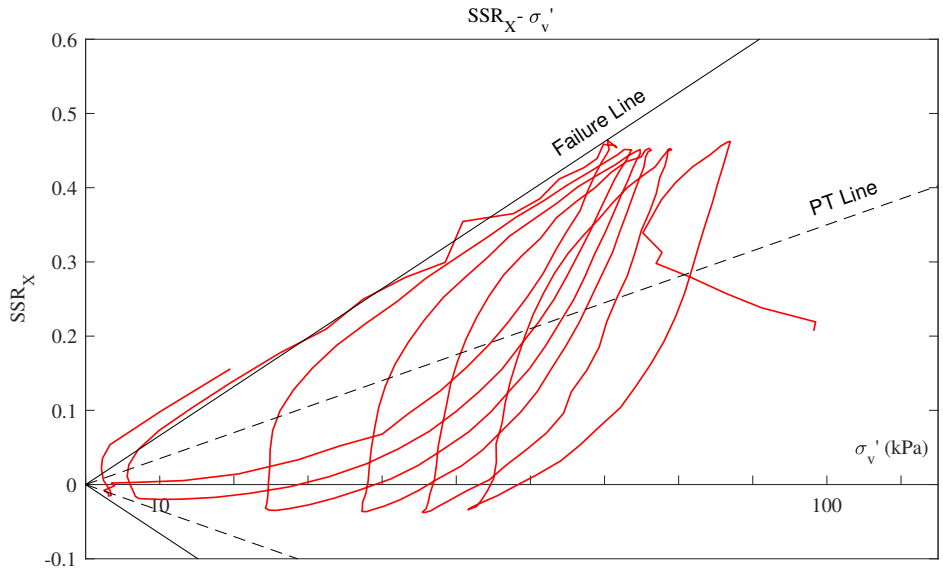

Fig. 4.15 The stress path of test LS10

It is evident that large excess pore pressure ratio (close to unity) is not achieved at the time when the shear strain exceeds criterion limit (6% double-amplitude strain) in test LS11 and test LS10. Therefore, the liquefaction resistance analysis based on shear strain criterion may be viable for practical use, but not fully useful when it comes to the mechanical assessment of soil. More detailed discussion about the definition of liquefaction and its implications will be made in chapter 7, together with the thoughts derived from multi-directional tests.

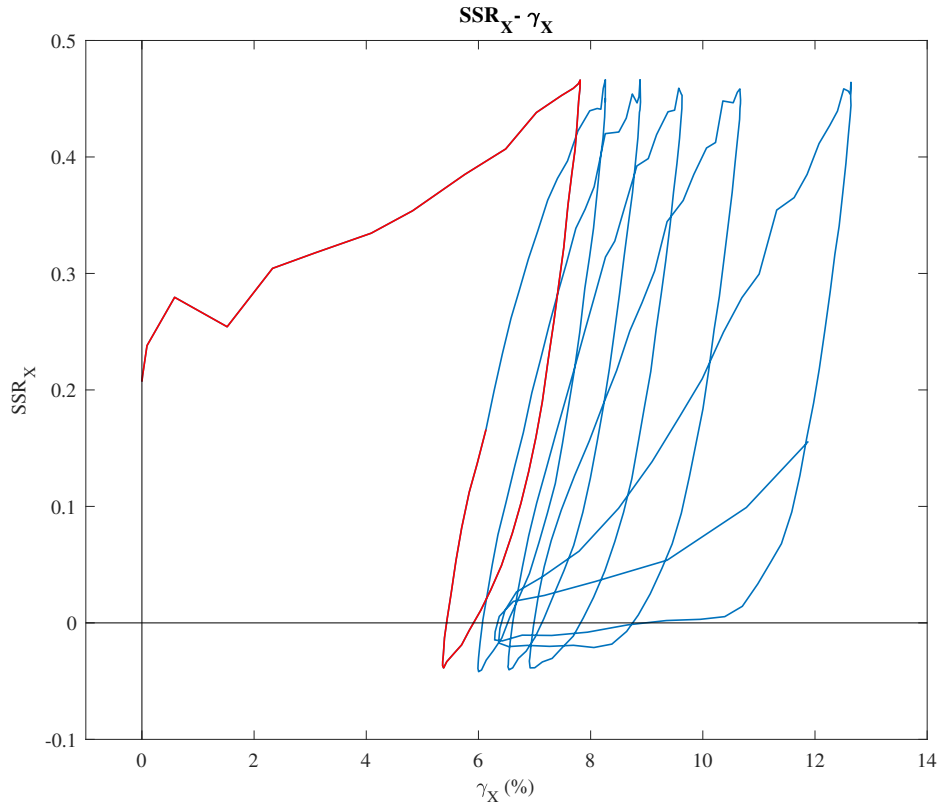

Fig. 4.16 The stress-strain response of test LS10 (the first cycle is coloured red)

4.2 Liquefaction resistance of uni-directional tests

One method to estimate the liquefaction resistance of sands is to determine the relationship between the number of cycles needed for liquefaction triggering and the cyclic shear stress ratio applied. The relationship developed from laboratory tests can only be used as a baseline for this estimate; instead, the data from field tests or actual earthquake records weigh much more in determining liquefaction resistance. The discrepancy between the liquefaction resistance derived from laboratory and that from field is large enough that it cannot be ignored. Considering the significant difference in terms of loading uniformity, loading multi-directionality, soil uniformity, density measurement, saturation conditions, etc., it is not difficult to understand why the liquefaction resistance attained in the laboratory is so different from case histories.

Therefore, there is no intention in this study to modify or develop practical charts for liquefaction hazard assessment. The reason why liquefaction resistance is still analysed here

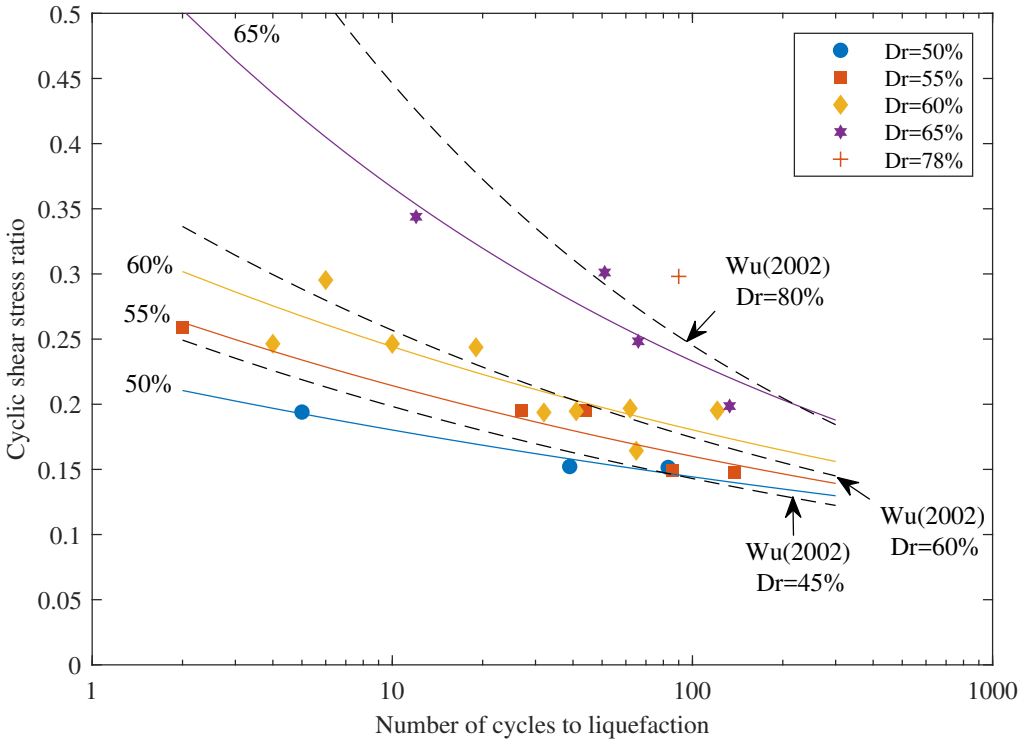

Fig. 4.17 Number of cycles to liquefaction versus cyclic stress ratio in uni-directional cyclic tests with no static shearing

is, on the one hand, to provide a benchmark against which the effects of multi-directional loading can be compared and clarified more conveniently, and on the other hand, to prepare data and implications for potential liquefaction resistance research in the future.

Figure 4.17 presents the number of cycles to liquefaction versus cyclic shear stress ratio of all the uni-directional cyclic tests without static shearing (level ground tests) in this study. The tests are divided into four groups according to relative density. A trend line that fits a power function is obtained for each group with least square minimisation, in the form of:

$$CSR = aN_L^b \tag{4.1}$$

with the values of the two parameters, a and b, tabulated in table 4.1.

The scatter of the data points is obvious, but it is not unreasonable given the fact that liquefaction resistance results are rather sensitive to sample density and loading application

Table 4.1 Fitting parameters of $N_L - CSR$ curves

Relative density	**Curve-fitting parameters**	
	a	***b***
50%	0.225	-0.097
55%	0.287	-0.127
60%	0.331	-0.132
65%	0.572	-0.193

as a rule, and the fact that it is not very likely to have perfect control of these factors in simple shear tests. Especially for the parts where the curves become flatter, liquefaction resistance results can drift away from the trend line due to a small error of mass measurement or loading measurement, not to mention the inevitable sample non-uniformity or imperfect control of loading conditions, even though much effort has been made to minimise their influence. In addition, the samples categorized into the same density group do not always have the designated density, which also aggravates the scatter.

Although scattered, however, the data in this study show the trend that is congruous with general expectations. The decrease of cyclic shear stress ratio results in the rapid increase of the number of cycles required to trigger liquefaction. The curves are steeper in the high *CSR* parts and flatter in the low *CSR* parts. A higher density leads to a higher liquefaction resistance and a steeper curve, indicating that, compared with dense samples, the liquefaction resistance of loose samples is more sensitive to the change of *CSR*.

As Monterey 0/30 sand has been used in some of the seminal work on multi-directional simple shear testing (Boulanger, 1990; Kammerer, 2002) and will provide a baseline for comparison in the following sections, the uni-directional test results of Monterey 0/30 sand are also included here. Wu (2002) performed uni-directional cyclic simple shear tests on Monterey 0/30 sand, which is a sub-rounded beach sand with a D_{50} of 0.36 mm. The samples were prepared by the wet-pluviation method. The correlation curves from one of his test series with initial vertical consolidation stress of 80 kPa are also plotted in Figure 4.17, as dashed curves. Wu's correlations were not obtained with a best fit method; instead, Wu determined these curves by assigning weights to the data. Samples whose density is closer to

the nominal density of the group are assigned more weight. This adjustment is not followed in the current study because the weight allocation process is believed not to be tenable when strict and consistent statistic assessment is not conducted. Nevertheless, from a qualitative point of view and for comparison purpose, Wu's curves can still be used as a reference to validate the data of the current study.

The trend lines of this study are generally consistent with the trends found in Wu's tests, but the liquefaction resistance of the latter has a narrower variation range. His correlation curve for loose samples (Dr=45%) is situated at the position of the curves for denser samples (Dr=50-55%) in this study, whereas the liquefaction resistance of a dense sample (Dr=78%) in this study is higher than his results for samples with relative density of around 80%. Furthermore, the liquefaction resistance obtained from this study at large *CSR* is lower than Wu's, while that at small or moderate *CSR* range is higher than Wu's. Considering that Wu used a different sand, sample preparation technique, consolidation stress and curve fitting method, this discrepancy is reasonable.

As for tests with static shear stress, the effects of initial static shearing on liquefaction resistance has been a widely discussed issue, however, the effects observed by different research groups differ significantly. Factors including density, confining pressure, sand type, particle shape and anisotropic fabric, as well as the response type (cyclic mobility or strain softening) that is determined potentially by them, exert together an influence on the effects of static driving shear force. The research conducted by Seed and Harder (1990) and Harder et al. (1997) showed that static shearing always lowers the liquefaction resistance of loose sands, and can either increase liquefaction resistance or have no effects for medium-dense to dense sands, depending on the relative density. In contrast, Vaid et al. (2001) found in their tests that the increase of static shearing always results in an increase of liquefaction resistance, even for loose sands, but this effect can reverse with static shear force increasing further in loose sands. Ishihara (1985) and Iai et al. (1992) integrated the effects of anisotropic consolidation into the effects of mean principal stress. Vaid and Chern (1985), however, concluded that the increase of static shearing reduces liquefaction resistance if the sand can develop flow liquefaction, while the effect is reversed if the sand develops cyclic mobility, which indicates

the response of sands also affects the influence of static shearing, in addition to density and confining pressure. Sivathayalan and Ha (2011) observed that the effects of static shearing are opposite on subrounded silica sands and on semi-angular Fraser River sand, as the former strain-softens while the latter strain-hardens over a large density range. The investigation into the effects of static shearing as well as the effects of anisotropic consolidation is also attempted with discrete element modelling method, from a micro mechanical point of view (Georgiannou and Konstadinou, 2014; Lashkari et al., 2017), but there is still no consistent conclusion that can be made on this issue.

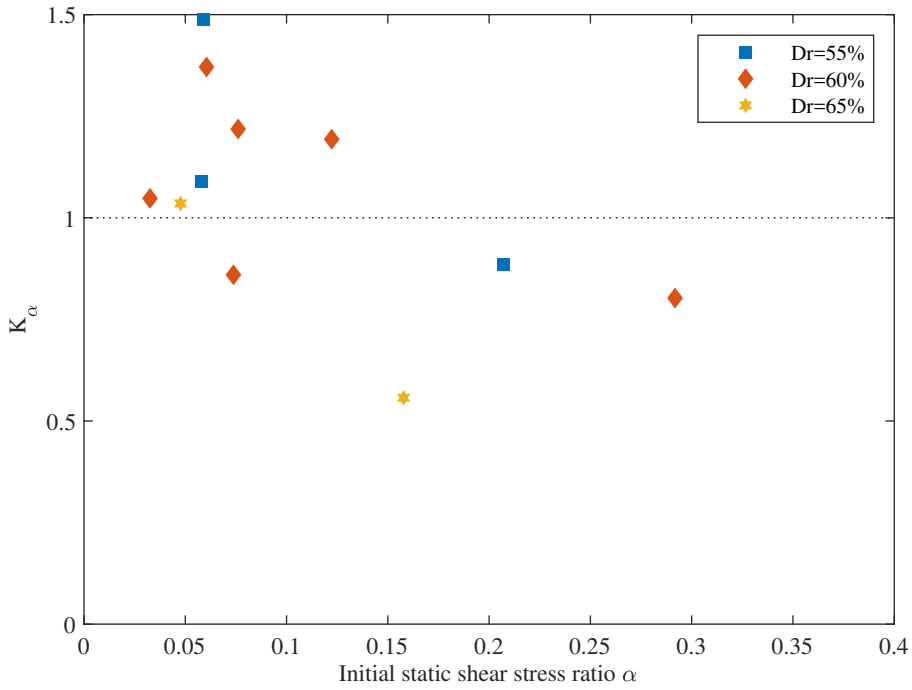

Fig. 4.18 The correction factor K_α versus initial static shear stress ratio α

The test results of the 11 uni-drectional tests conducted in this study with initial static shearing are shown in Figure 4.18. The initial static shear stress ratio α is defined as the ratio of initial static shear stress over the vertical overburden stress. The correction factor K_α equals to the ratio of the cyclic stress ratio with static shearing over that without static shearing, as proposed by Seed et al. (1983) to assess quantitatively the influence of static shear on liquefaction resistance.

$$\alpha = \frac{\tau_{static}}{\sigma_{v,i}} \tag{4.2}$$

$$K_\alpha = \frac{CSR_{\alpha=\alpha}}{CSR_{\alpha=0}} \tag{4.3}$$

Although no definitive conclusion can be made regarding how density and confining pressure affects the influence of static shearing due to the scatter and limited number of tests that have been done, a general trend can still be found. On the one hand, the increase of static shearing up to a moderate level can increase liquefaction resistance, but this positive effect no longer exists if static shearing is too large. On the other hand, the four tests with $K_\alpha < 1$ all fail within one or two cycles due to the rising single-amplitude shear strain, without the stress path reaching failure line, as discussed in the preceding session. That is, the K_α in these four tests are obtained with strain-based failure criterion while the K_α in other tests are attained with r_u based failure. Evidently, the failure criterion has also an influence on the assessment of the effects of static shearing, which can worsen the discrepancy in terms of the effects of static shearing. In general, the existence of initial static shearing is beneficial for liquefaction resistance for the sand at the density range and the vertical consolidation pressure tested in this study. But when the maximum shear stress exceeds a certain level, sands may experience an extremely large shear strain during the first a few cycles by this overwhelming shear stress, triggering strain-based failure. Practical engineering design and hazard assessment should take account of both of these two types of failure, especially when the effects of them are contradictory.

4.3 Excess pore pressure generation in uni-directional tests

The development of excess pore pressure ratio in all the ground-level tests (solid) is presented in Figure 4.19, along with the dip-shaking slope tests (dashed) which reach mechanical failure rather than failing due to overlarge single amplitude shear strain. The cycle numbers are normalized by the number of cycles required to trigger liquefaction in that test. The data

presented here are not adjusted and the influence of the drop of pore pressure artefact in some of the tests is retained.

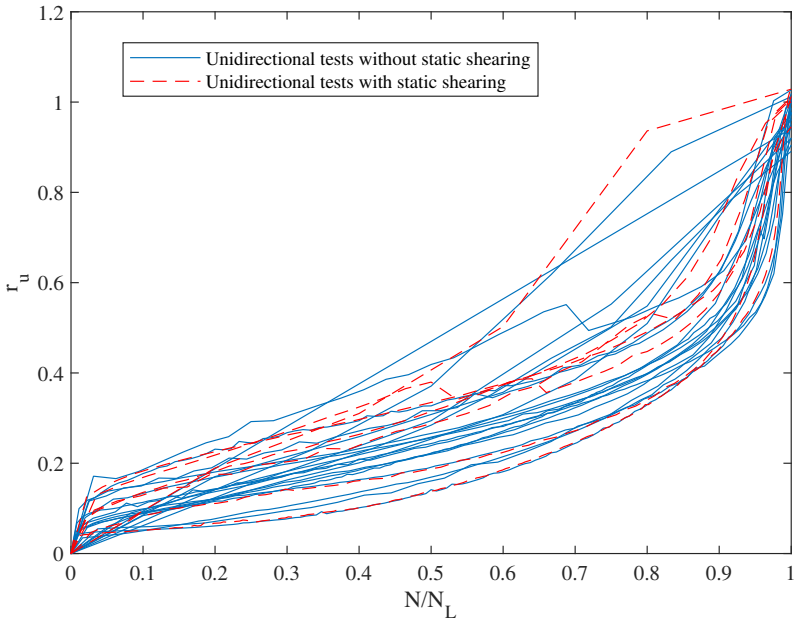

Fig. 4.19 The development of excess pore pressure ratio with normalized cycle number

The tests can be divided into two categories according to the rate of pore pressure ratio increase, as shown in Figure 4.20. Group I involves the tests that are very prone to liquefaction, in which liquefaction can be triggered usually with only a small number of shearing cycles. The excess pore pressure ratio in these tests keeps rising from the very beginning and there is no slowing-down until liquefaction is about to be initiated.

In contrast, group II, which consists of the tests that need more cycles to reach liquefaction, features a three-stage development pattern of pore pressure ratio. Excess pore pressure ratio has a jump in the first stage, followed by a period of steady increase with a smaller increment rate. As excess pore pressure is accumulated, its increment rate becomes higher and higher due to the softening of sand. When the excess pore pressure reaches a certain level and the sand is softened, a large pore pressure increase takes place and liquefaction ensues. This three-stage pore pressure development pattern is consistent with the strain-softening behaviour of sands as discussed earlier.

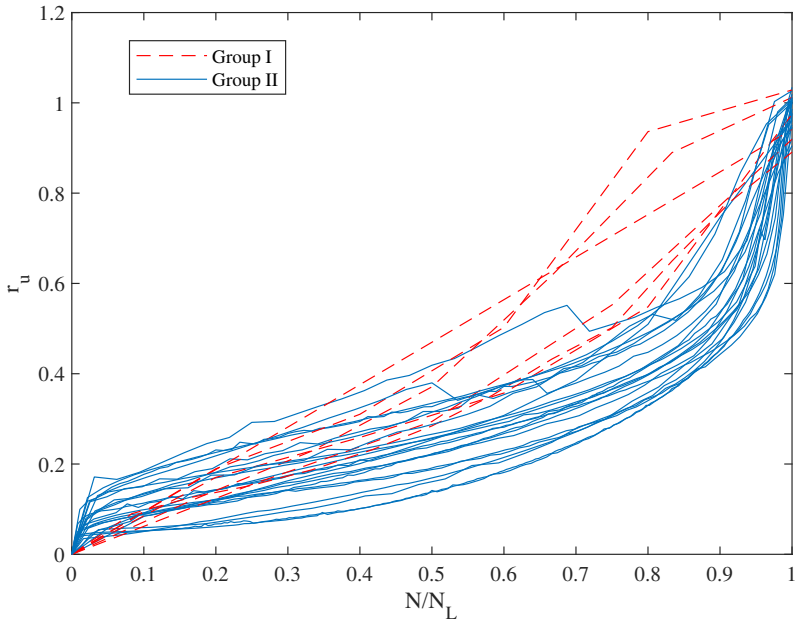

Fig. 4.20 The development of excess pore pressure ratio with normalized cycle number, with two groups recognised

Comparing Figure 4.19 and Figure 4.20, it can be observed that the pattern of excess pore pressure accumulation is not altered much by the existence of initial static shearing. The curves of the tests with static shearing fit well into the band of their ground-level counterparts and show the same characteristics of three-stage development.

Following Oda et al. (2001), the number of cycles to liquefaction is correlated to the excess pore pressure ratio of the first cycle. Qualitatively, if the excess pore pressure ratio generated in the first cycle is high, the sample should be softened more rapidly and thus initiate liquefaction with fewer cycles. Wu (2002) demonstrated that the excess pore pressure ratio in the first cycle is not sensitive to varying density and confining pressure, further validating the potential use of this relationship in liquefaction assessment. The data of all the uni-directional tests in the current study are also compatible with the correlation, as shown in Figure 4.21, with the fitted relationship:

$$r_{u,1} = N_L^{-(0.67+\frac{1.53}{N_L})} \tag{4.4}$$

where $r_{u,1}$ is the excess pore pressure ratio generated in the first loading cycle and N_L is the number of cycles to liquefaction.

The data of level-ground tests are coloured blue, with red markers for slope tests. It can be noticed that the existence of static shearing does not alter this correlation, if only the failure line can be reached.

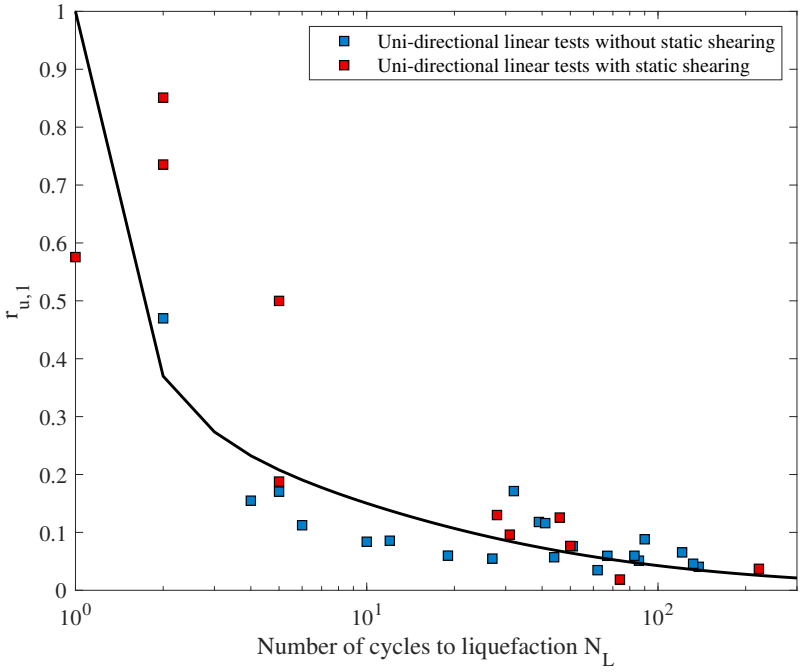

Fig. 4.21 The relationship between the excess pore pressure ratio in the first cycle and the number of cycles to liquefaction in uni-directional tests

4.4 Shear modulus degradation in uni-directional tests

The shear modulus degradation of all the uni-directional tests with and without static shearing is shown in Figure 4.22. G refers to the secant shear modulus calculated for each cycle, and it is normalized by the small-strain shear modulus G_{max} following Hardin and Drnevich (1972):

$$G_{max} = 1230 \cdot \frac{(2.973 - e)^2}{1 + e} \cdot (\sigma'_{i,0})^{0.5} \tag{4.5}$$

where e is void ratio and $\sigma'_{i,0}$ is the initial effective vertical stress in pounds per square inch.

The cyan dotted curves in Figure 4.22 represent the predicted shear modulus degradation curves following the method of Hardin and Drnevich (1972):

$$\gamma_r = \frac{\tau_{max}}{G_{max}} \tag{4.6a}$$

$$\frac{G}{G_{max}} = \frac{1}{1+\frac{\gamma}{\gamma_r}} \tag{4.6b}$$

As clarified in chapter 3, the cyclic shear stresses used in this study are moderate to high in order to liquefy the medium-dense Hostun sand samples. As a result, the double amplitude shear strain induced is larger than 1% even in the first cycle, corresponding to a G/G_{max} ratio below 0.04. There is thus not much information about small strain shear modulus degradation that can be extracted, though the comparison of test results with Hardin and Drnevich's prediction can still be made.

The shear modulus degradation curves are enlarged and plotted on the same graph for a clearer view. It can be observed that the shear modulus of the test data in this study is in agreement with the prediction at the strain range obtained. Hardin and Drnevich's correlation which was derived based on hyperbolic stress-strain curve works effectively at the large shear strain range tested in this study.

The existence of static shearing is not seen to bring about a notable difference. The shear modulus of the tests with static shearing degrades along the predicted curve, as does that of ground-level tests.

In addition to shear strain, the relationship between shear modulus and excess pore pressure ratio can also have implications since the development of excess pore pressure is recognised to soften sands and hence reduce shear modulus. The shear modulus degradation versus excess pore pressure ratios is shown in Figure 4.23. The shear modulus is not normalized by G_{max}. G_{max} is related to the elastic shear strain, which can serve as a reference for comparison in terms of shear strain, but there is no evidence that it is still relevant when it comes to excess pore pressure.

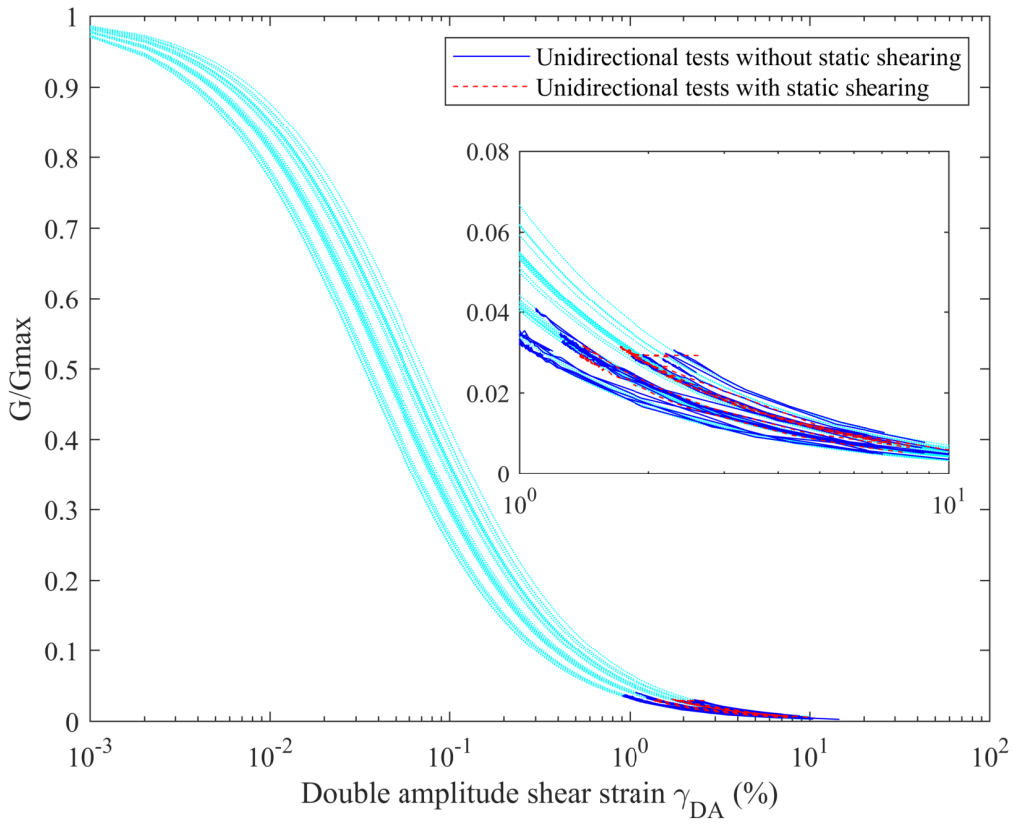

Fig. 4.22 The shear modulus degradation with double-amplitude shear strain (cyan dotted curves are the predictions following Hardin and Drnevich (1972); blue and red curves present measured data)

Instead, the shear modulus is normalized by the secant shear modulus of the second cycle in this study. The reason why the shear modulus of the second cycle is used rather than that of the first cycle rests in the overshooting issues of the testing device, that is, the adaptive loading system tends to overreact at the initial stage of loading. The loading control system takes time to adapt itself to the stiffness of sand samples, which results in overshooting in the beginning cycle and a first-cycle shear strain that is larger than the following cycles. This is reflected by the increase of shear modulus ratio in the initial stage and the fact that $G1/G2$ is usually lower than unity. Since the overshooting problem cannot be controlled or eliminated, the shear modulus in the first cycle is not reliable. By contrast, the normalization against the shear modulus of the second cycle is more consistent and less scattered. The tests which

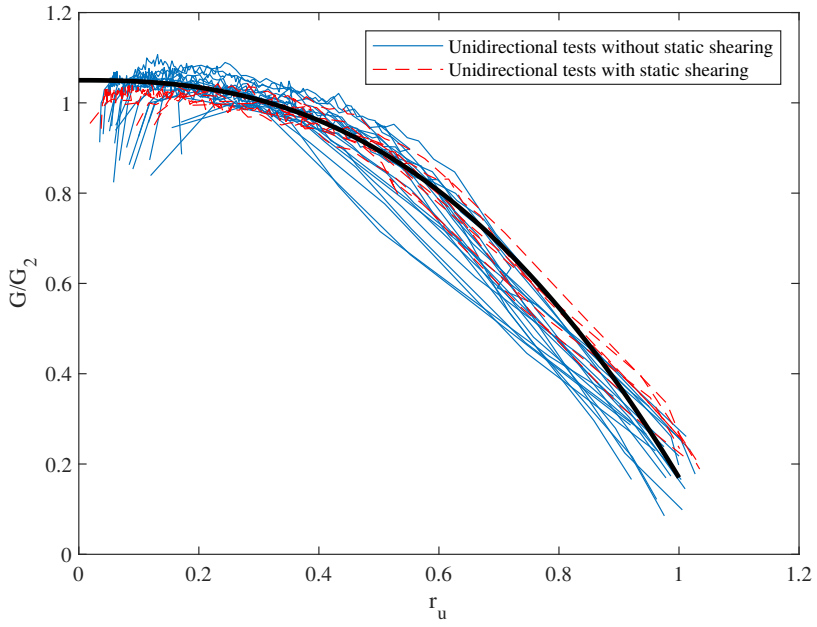

Fig. 4.23 The degradation of shear modulus with excess pore pressure ratio

fail within two cycles are removed because the G/G_2 normalization does not have much meaning for them.

The shear modulus degradation curves of all the other tests, no matter whether there is static shearing, fall into a reasonably narrow band and exhibit the same trend. The degradation process can be divided qualitatively into two phases according to the rate of the decrease of shear modulus. When excess pore pressure ratio remains low and the sand samples are not softened significantly, shear modulus degrades at a low and nearly constant rate. However, when excess pore pressure ratio exceeds a certain level around 0.3-0.4, the decrease of shear modulus accelerates. Shear modulus generally decreases to less than 40% of G_2 when liquefaction is initiated. The correlation between G/G_2 and excess pore pressure ratio can be described with a power function as follows:

$$\frac{G}{G_2} = 1.05 - 0.88{r_u}^{2.5} \tag{4.7}$$

It should be noted that the curves for the tests with static shearing also fall into the same band as ground-level tests, demonstrating the effects of initial static shearing are not

significant. The degradation of G/G_2 is therefore also a type of characteristics shared by all the uni-directional tests, which is not affected by static shearing and thus holds a potential for modelling work.

4.5 Discussion on uni-directional tests

Uni-directional cyclic loading is the most examined loading condition in seismic geotechnical study, and soil liquefaction research is no exception. A soil element under level ground is sheared by seismic loading without static shearing; by contrast, a soil element under sloping ground has a downhill static driving shear force. If the cyclic shear induced by the earthquake is along the dip direction, in an ideal situation, the soil element still experiences a uni-directional loading scenario, but with static shearing.

21 uni-directional level-ground tests and 11 uni-directional slope tests were conducted in this study to validate the ability of the testing device and form a benchmark against which multi-directional tests can be compared and studied.

An important difference between the tests with and without static shearing rests in what type of failure actually happens when the strain-based liquefaction criterion is met. For level ground tests and slope tests that have small or moderate static shearing, the strain-based failure is compatible with mechanical failure, that is, when liquefaction happens from a strain perspective, the stress path also reaches the failure line and excess pore pressure increases to a high value close to the vertical overburden stress. However, this is not necessarily true for tests holding large static shearing. In this case, the failure line may not be reached in stress space, though liquefaction is considered to have occurred because of an overlarge single-amplitude shear strain. Since the importance of serviceability is widely recognised and large strain can result in undesirable loading situation for the structures built on soil, the overlarge shear strain caused by large static shearing is still dangerous even if the sands do not technically liquefy and the excess pore pressure develops only to a moderate level.

The analysis of liquefaction resistance in this study shows that small or moderate static shearing is beneficial, while large static shearing has the opposite effect. An observation from

this is static shearing up to a certain level can help resist mechanical failure in medium-dense Hostun sands vertically consolidated at 100 kPa. But this observation should be treated cautiously because the effects of static shearing can be influenced by factors including sand type, relative density, confining stress and so forth (Harder et al., 1997; Ishihara, 1985; Seed and Harder, 1990; Vaid et al., 2001). Considering liquefaction hazard assessment in engineering practice is more often based on actual case histories and in situ testing rather than laboratory testing, there is no intention to provide new charts or correction factors in this study; instead, the analysis regarding liquefaction resistance in this study will be used to investigate the effects of static shearing and multi-directional loading qualitatively.

In terms of excess pore pressure development and shear modulus degradation, however, the existence of static shearing does not result in any notable difference under the test conditions in this study, if only the sand samples are failed mechanically. Excess pore pressure shows three-stage development pattern as widely reported in strain-softening soil behaviour. Shear modulus decreases as sands are softened. The theoretical small-strain shear modulus G_{max} and G/G_{max} degradation curve proposed by Hardin and Drnevich (1972) works effectively for the tests in this study. Shear modulus degrades at a nearly steady rate when excess pore pressure remains low. However, after excess pore pressure ratio exceeds the level at approximately 0.3-0.4, the degradation of shear modulus accelerates until the secant shear modulus drops eventually to less than 40% of G_2.

In summary, the uni-directional tests conducted in this study show that the clean Hostun sands with a relative density between 50% and 65% exhibit typical cyclic-mobility behaviour under undrained uni-directional cyclic shear. The existence of static shearing along the cyclic loading direction does not alter its characteristics in terms of mechanical failure state, excess pore pressure development, and shear modulus degradation. Compared with uni-directional tests, multi-directional tests show significant differences, which will be illustrated in the next chapter.

Chapter 5

MULTI-DIRECTIONAL SIMPLE SHEAR TEST RESULTS

5.1 Bilinear tests

The effects of initial static shearing become more complex and far less understood when the direction of static shearing is perpendicular to that of cyclic shearing. A fundamental case of such a type of loading condition refers to a soil element again under sloping ground, but with earthquake-induced shaking occurring along the strike direction rather than dip direction. Under this circumstance, the static shear stress which points downhill and the cyclic shear stress along the strike direction become orthogonal.

13 bi-directional linear tests were conducted in this study to investigate the behaviour of Hostun sands under this loading condition. After sand samples are consolidated vertically with the target vertical overburden stress, the samples are sheared with a ramp loading, with drainage open, to achieve the designated static shear stress. The ramping rate is set to 0.01 kN/min, a rate that is slow enough to allow any induced excess pore pressure to dissipate immediately but not too slow in case large strain develops prior to cyclic shearing. Right after the static shear loading is increased to the desired value, the drainage valves are closed and cyclic shearing along the perpendicular direction follows. The information of all the

bi-directional linear tests, including relative density, B-value, loading conditions and the number of cycles to initiate liquefaction, are summarized in table 3.3.

The liquefaction criterion becomes problematic in a multi-directional loading scenario. Excess pore pressure does not always increase to unity when liquefaction happens; instead, excess pore pressure is bound not to be able to reach unity in bi-directional linear tests, which will be elaborated in the subsequent section. Moreover, the strain-based criterion encounters challenges partly from the fact that there is no evidence that a certain level of shear strain in one direction can be correlated to liquefaction, and partly from the difficulties in defining a shear strain that can take directionality into account effectively.

From a point of view of serviceability, resultant shear strain which is defined as $\gamma_{total} = \sqrt{{\gamma_{dip}}^2 + {\gamma_{strike}}^2}$ may serve as a better indicator because an over-large resultant strain, no matter what direction it is in, can always threaten the serviceability of the structures built on the soil. But from a stress perspective, whether a certain resultant shear strain level can be associated reliably with stress failure states is yet to be confirmed. A more detailed discussion regarding liquefaction criterion will be made in Chapter 7.

Considering this, liquefaction is defined directly based on stress states for multi-directional tests in this study in order to develop a better and more comprehensive understanding of soil behaviour under multi-directional loading scenario. Liquefaction is not considered to occur in bi-directional linear tests until the stress path in either strike direction or dip direction reaches the failure line, whichever takes place first. The stress-related graphs presented in this section are all plotted with the data up to the cycle where the the failure line is reached, regardless of shear strain level.

The results of three examples tests (Bilinear-3, Bilinear-5, Bilinear-8) will be discussed and compared. The three tests have almost the same relative density at 61% and Skempton's B-value at 0.92, as well as the same vertical consolidation stress of 100 kPa. The target cyclic shear stress ratios applied were 0.25, 0.3 and 0.3. The primary difference among the three tests is the amount of static shear stress in the dip direction, whose effects can thus be studied. Test Bilinear-3 is consolidated with a target static shear stress ratio of 0.0625, and

failed mechanically at the 2nd cycle. Liquefaction is initiated also at the 2nd cycle in test Bilinear-5 with a target α of 0.12, and the 4th cycle in test Bilinear-8 with α of 0.15.

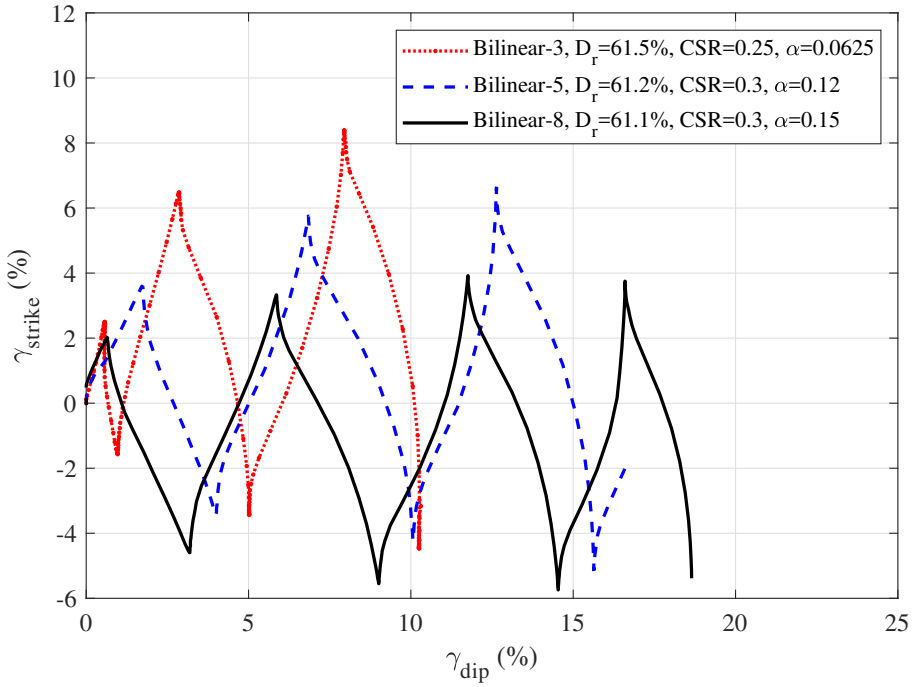

Fig. 5.1 The plan view of shear strain development of bi-directional test Bilinear-3, Bilinear-5 and Bilinear-8

The bi-directional shear strain development of the three tests is presented in Figure 5.1. One more cycle is shown for test Bilinear-3 and Bilinear-5 to illustrate post-liquefaction strain development. This is not done to test Bilinear-5 because that test was stopped when mechanical failure happens.

The shear strain of the three tests all develops in a zigzag shape, with the strain amplitude in the two directions both increasing gradually as the sand strain-softens. However, while the shear strain in the strike direction exhibits a cyclic pattern, the dip shear strain keeps increasing without ever reversing. Clearly the pattern of strain development in each direction is controlled by the type of loading that is applied in that direction: cyclic shear leads to cyclic shear strain accumulation and static shear brings monotonic increase of shear strain.

It is worth noting that the dip shear strain can develop to extremely high values (18% in test Bilinear-8 when the failure line is reached), greatly exceeding the limiting amount of shear strain accumulated in strike direction, though the latter can also reach as high as more than 6%. The dominating role of the downhill strain becomes clearer in the post-liquefaction cycles of Bilinear-3 and Bilinear-5. While the increase of dip shear strain is not necessarily high within a single cycle, the constant accumulation towards the same direction results in eventually a vast residual downhill shear strain. It is evident that static shearing in dip direction can become as dangerous as, or even more dangerous than, the cyclic shearing in strike direction. This is in agreement with the conclusions drawn for sands by Boulanger (1990) and Kammerer (2002).

Another observation from the shear strain plan view is regarding the amplitude of cyclic strain in strike direction. The double-amplitude strike shear strain in the three tests is all 10% in the cycle where liquefaction happens. But the post-liquefaction development of strike shear strain differs. Test Bilinear-3 holds the smallest α (0.06) among the three tests but its $\gamma_{strike,DA}$ increases to 13% at one cycle after liquefaction. Sheared with $\alpha = 0.12$, $\gamma_{strike,DA}$ in test Bilinear-5 increases to 11.5% within one post-liquefaction cycle. In contrast, $\gamma_{strike,DA}$ in test Bilinear-8 has stopped increasing when liquefaction happens, levelling out at 10%. The existence of static shearing in one direction appears to inhibit the potential of cyclic shear strain development in the orthogonal direction. This inhibition effect is made more clear with that fact that the test having the largest cyclic strain (Bilinear-3) was actually sheared with a lower cyclic stress ratio (0.25) compared with the other two tests (0.3).

This indicates that the existence of dip static driving shear force can reduce the degree of softening when strike cyclic shearing results in liquefaction. The stress-strain curves in strike direction of test Bilinear-3, Bilinear-5 and Bilinear-8 demonstrate the same tendency, as presented in Figure 5.2. As expected, the stress-strain hysteresis loops in the three tests all become larger and flatter with the cyclic shearing. But the final loop in test Bilinear-3 has less significant strain-hardening features with a period of the curve lying almost flat, while the final loops in the other two tests look still relatively stiff, evidencing the effects of dip static shear on orthogonal seismic softening of sands.

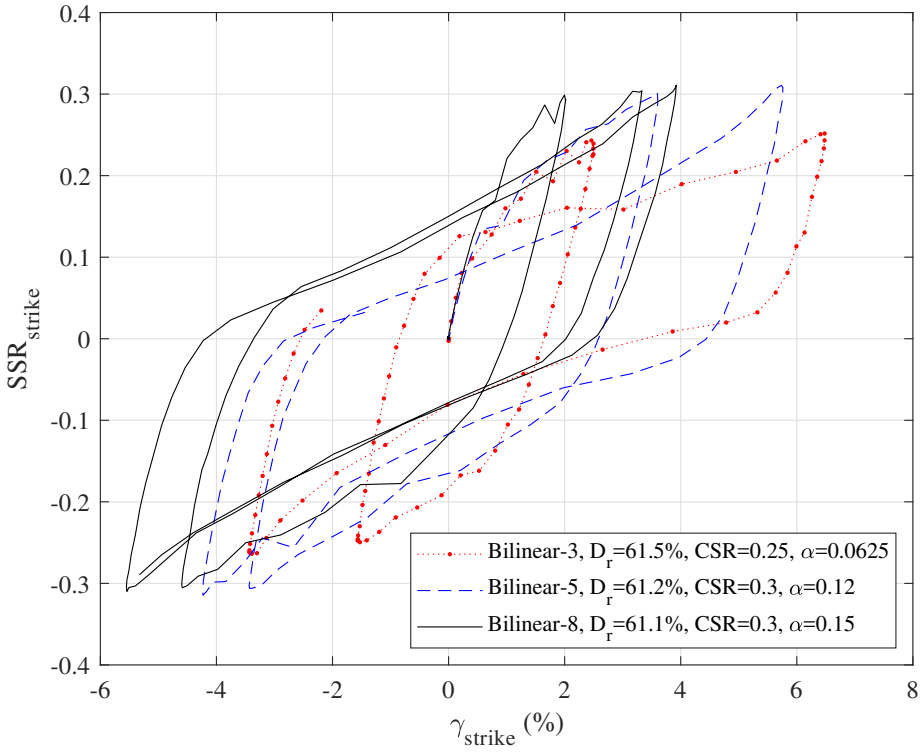

Fig. 5.2 Strike-direction stress-strain curves of test Bilinear-3, Bilinear-5 and Bilinear-8

A reasonable explanation for this counter-intuitive phenomenon can be found in the excess pore pressure developed at liquefaction in each test, as shown in Figure 5.3. The initial rate of excess pore pressure generation in test Bilinear-3 is lower than that in the other two tests because of the smaller cyclic stress, which is also suggested by the relatively small strain level at this stage. However, the maximum excess pore pressure ratio shows a different trend. With the increase of α, the maximum excess pore pressure ratio at liquefaction decreases, hence reducing the degree of softening.

Correspondingly, the stress paths show the same tendency. The stress paths of the three tests are presented in Figure 5.4, with the top graph showing the stress paths in strike direction and the bottom showing dip. The stress paths in strike direction exhibit the similar behaviour as uni-directional tests, featuring butterfly-shaped paths when it approaches failure, which is also reflected in the "double-peak" phenomenon in excess pore pressure generation. None of the stress paths in strike direction manages to reach the failure line when the dip stress paths

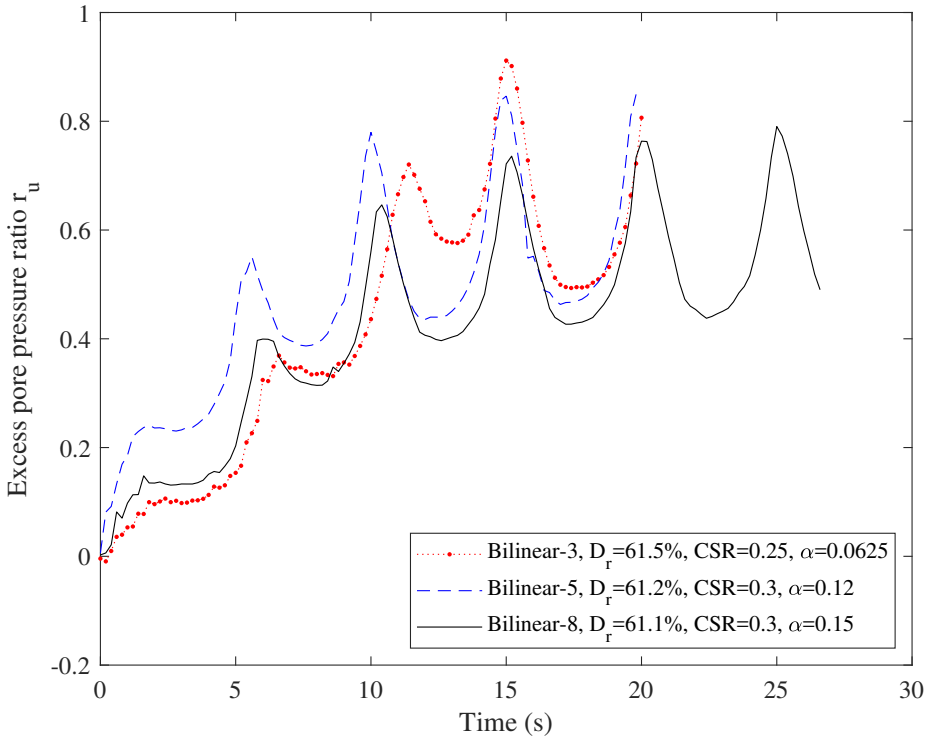

Fig. 5.3 The generation of excess pore pressure in test Bilinear-3, Bilinear-5 and Bilinear-8

arrive there. And the lower the α, the closer to the origin the stress paths in strike direction can reach.

Aiming to clarify further the effects of dip static shear on strike cyclic shear, the stress paths of test Bilinear-6, Bilinear-7 and Bilinear-8 are shown in Figure 5.5. The relative densities and cyclic stress ratio in strike direction differ hugely among the three tests, but they all share the same amount of α. An impressive but anticipated finding is that the ultimate effective vertical stress when liquefaction occurs in the three tests, or the maximum excess pore pressure at that point, are almost the same.

A more careful comparison of Figures 5.4 and 5.5 leads to the conclusion that the maximum excess pore pressure is controlled by the static shear rather than the cyclic shear in the perpendicular direction. It is not difficult to understand this because it is always the dip static shear stress paths, instead of the strike cyclic stress paths, that reach the failure line first and trigger liquefaction. When a stress path in the dip direction arrives at the failure line,

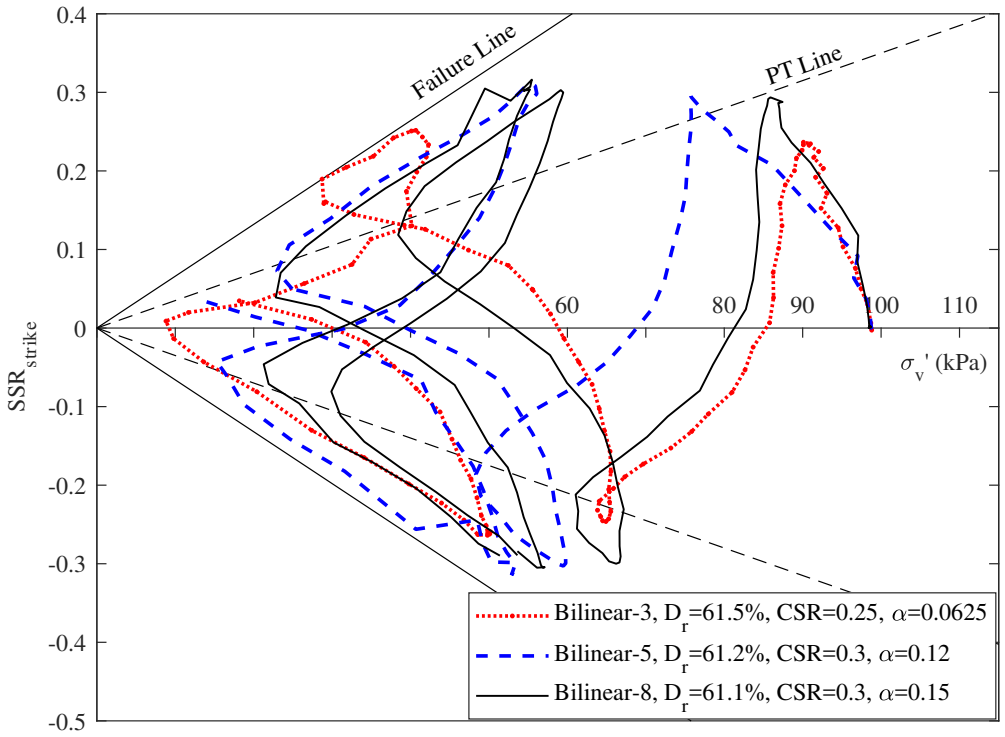

(a) Stress in strike direction

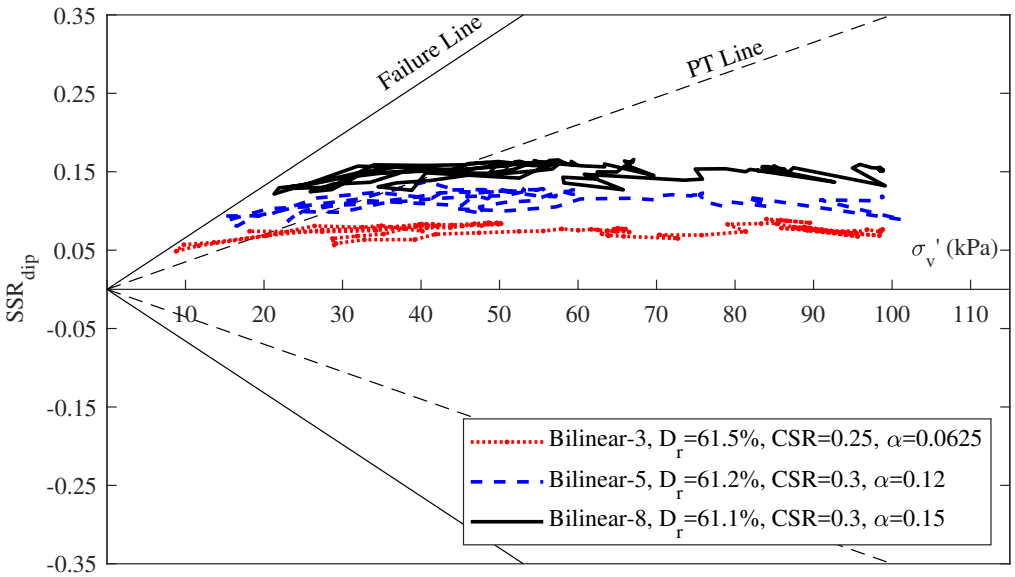

(b) Stress in dip direction

Fig. 5.4 Stress paths of test Bilinear-3, Bilinear-5 and Bilinear-8

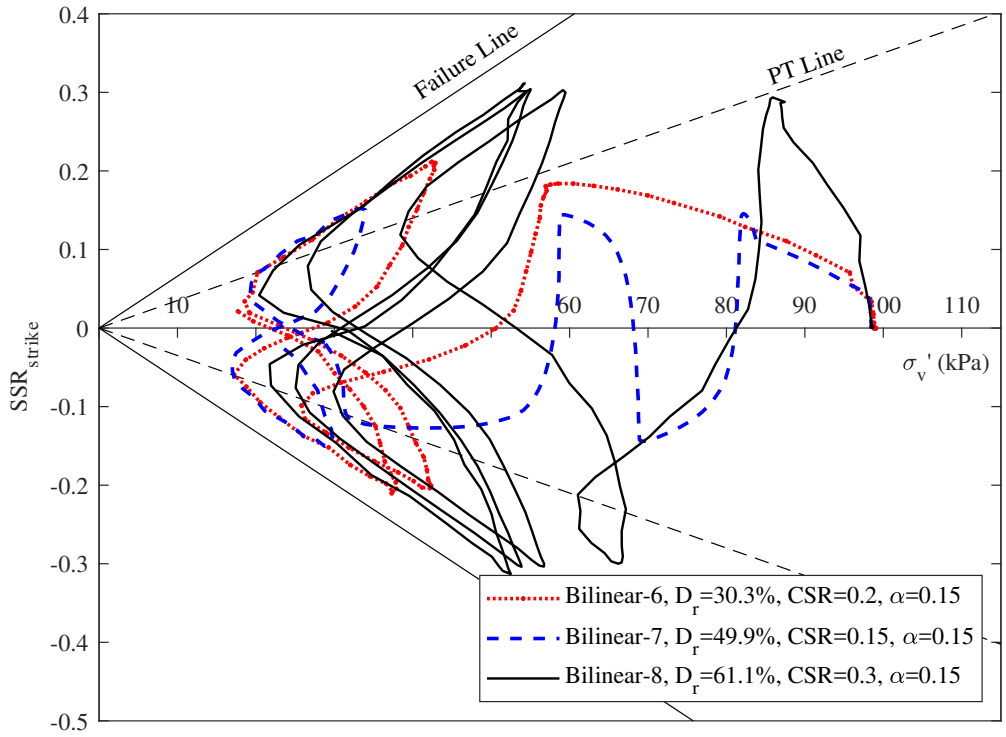

(a) Stress in strike direction

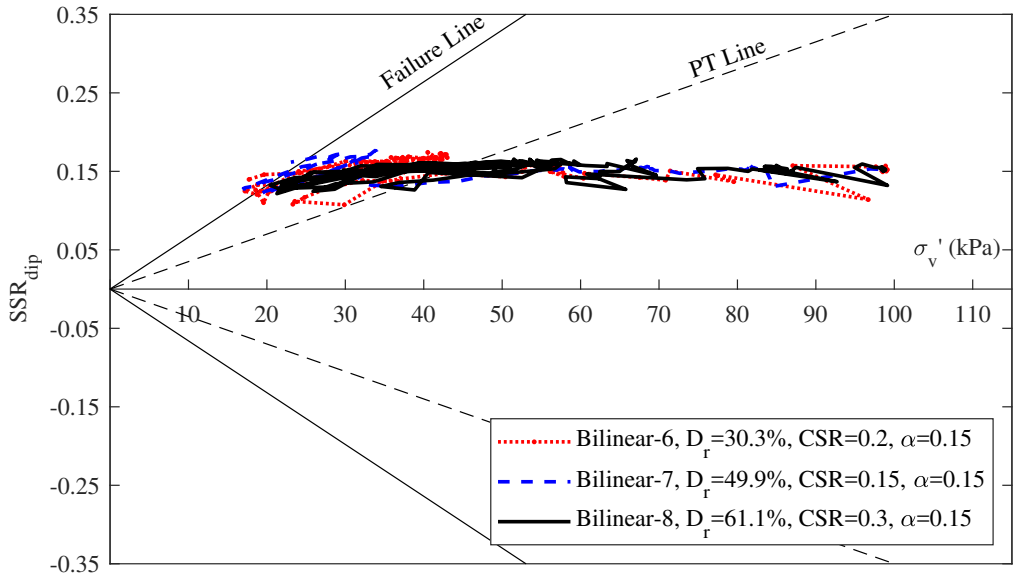

(b) Stress in dip direction

Fig. 5.5 Stress paths of test Bilinear-6, Bilinear-7 and Bilinear-8

the excess pore pressure at that crossing point becomes the maximum excess pore pressure that can be generated in the corresponding bi-directional linear loading scenario. Based on this consideration, a correlation between the static shear stress ratio and the maximum pore pressure ratio can be derived with the straightforward geometry shown in the subplot in Figure 5.6, as follows:

$$r_{u,max} = 1 - \frac{\alpha}{tan\phi_{FL}} \tag{5.1}$$

where ϕ_{FL} is the angle of failure line (33.4° in this study). This is congruous with the relationship proposed by Boulanger (1990).

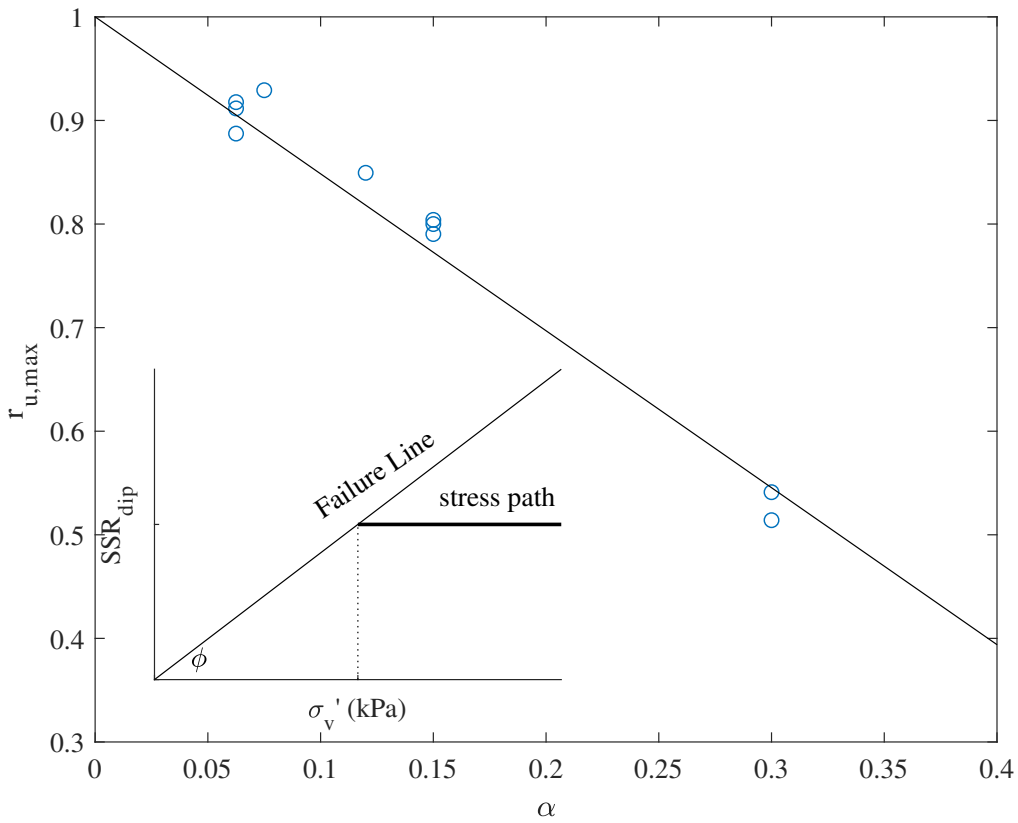

Fig. 5.6 The relationship between the maximum excess pore pressure ratio and static shear stress ratio for bi-directional linear tests, with the schematic for deriving equation 5.1

Also shown in Figure 5.6 is the maximum excess pore pressure ratio of the bi-directional linear tests conducted in this study plotted versus the dip static shear stress ratio α. The solid

line in the main graph shows equation 5.1, with the circle-marked points representing the data from tests. It can be said with a high degree of confidence that the derived correlation fits well with the measured data, validating the hypothesis.

The effects of dip static shear stress ratio on soil liquefaction resistance are presented in Figure 5.7. The solid data points are those from uni-directional tests and the unfilled ones represent those from bi-directional linear tests. No unique relationship can be developed with the large scatter, but a qualitative trend can be found. The increase of static shear stress generally results in the decrease of liquefaction resistance for the relative density range and confining pressure tested in this study. A low α is potentially beneficial for liquefaction resistance ($K_\alpha > 1$) while the effect is reversed when α enters a moderate range.

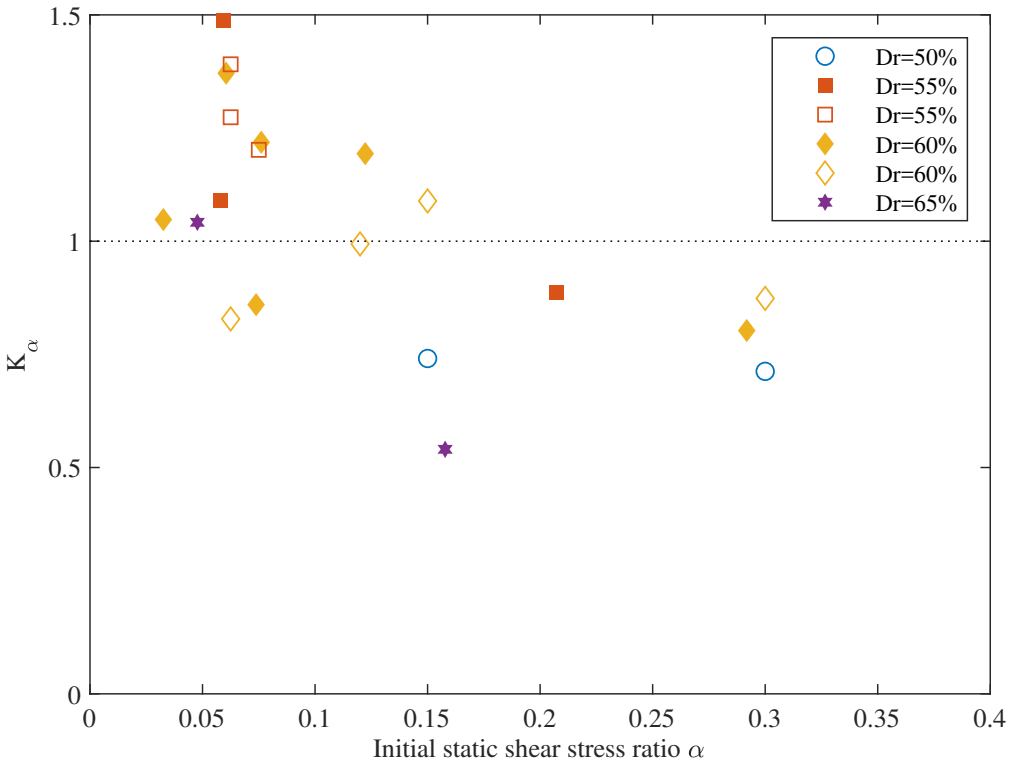

Fig. 5.7 The effects of static shear stress ratio α on K_α in uni-directional tests and bi-directional linear tests

Given the influence of dip static shearing on liquefaction resistance and excess pore pressure generation, the correlation between the number of cycles to liquefaction and the

excess pore pressure generated in the first cycle needs to be re-examined to see if it is applicable to bi-directional linear tests. Presented in Figure 5.8, the solid curve is the same one as that in Figure 4.21, following equation 4.4. The general trend is similar but the scatter at small liquefaction resistance becomes prominent, suggesting that such a correlation needs to be treated cautiously in multi-directional loading conditions. More information from other categories of multi-directional tests is needed to check how effective this correlation is.

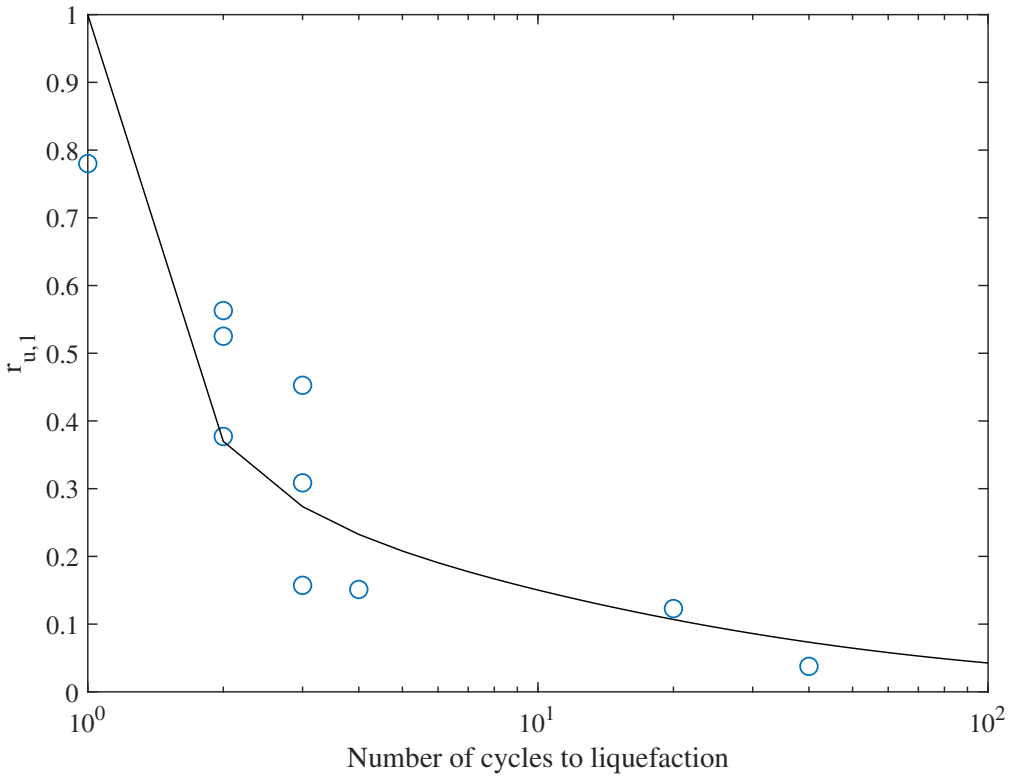

Fig. 5.8 The relationship between the number of cycles to liquefaction and the generated excess pore pressure ratio in the first shearing cycle

The G/G_{max} degradation versus shear strain is analysed and presented in Figure 5.9, with the dotted curves indicating the predictions proposed by Hardin and Drnevich (1972) and the data points representing test data from this study. A reasonable match can be found between the predicted values and test data, suggesting the shear modulus degradation curves can still be used in the direction along which cyclic shearing is applied. However, it needs to be pointed out that when loading paths become more complex, the definition of shear modulus

may become challenging. The conclusion from bi-directional linear tests may not hold true for other multi-directional loading scenarios. A discussion on this issue will be given in Chapter 7 by summarizing the results of all the tests with various loading paths.

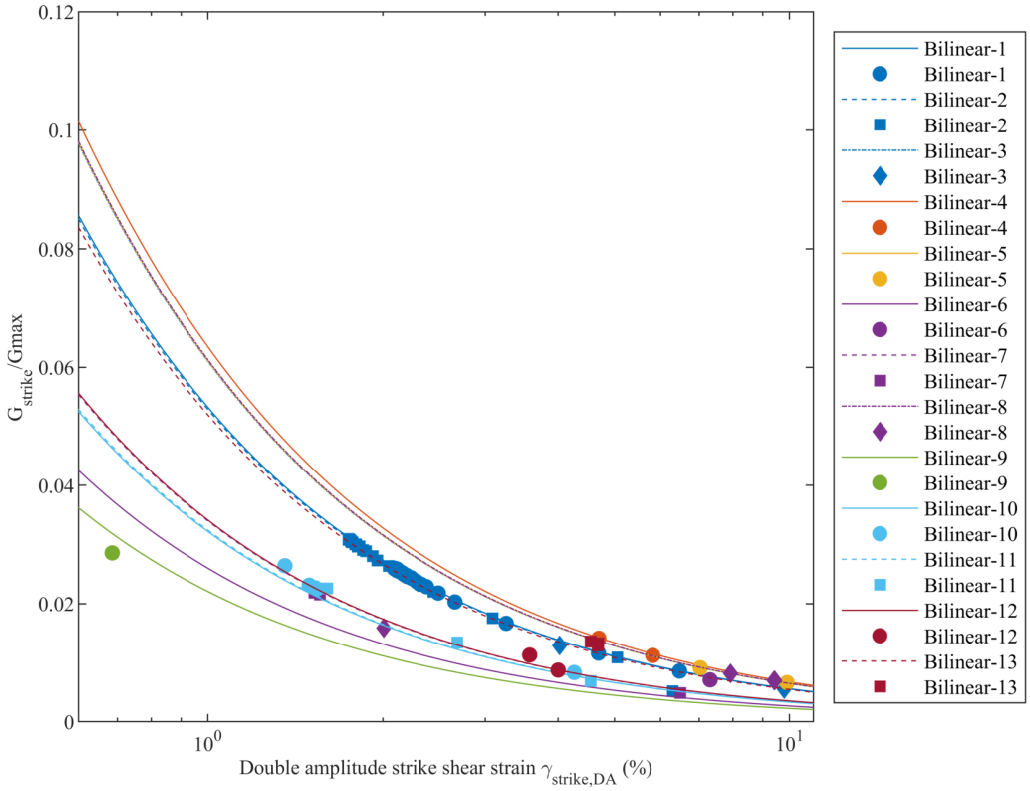

Fig. 5.9 Strike-direction Shear modulus degradation curves in bi-directional linear tests

5.2 Multi-directional tests

5.2.1 Tests with circular loading path

Realistic multi-directional loading paths can be far more complex than uni-directional or bi-directional linear ones, partly because the interaction between the variation of the amount of shear stress and the change of its direction can be more complicated and influence soil behaviour significantly, and partly because the added dimension in loading paths raises concerns about whether the conventional analysis framework is still effective. Circular loading paths without initial static shearing is a simplified, fundamental and representative type of loading condition of such kind. Compared with uni-directional or bi-directional linear tests in which the amount of shear stress varies cyclically and its direction is constrained to a single dimension, the shear stress under circular loading conditions rotates its direction smoothly, with its magnitude, however, remaining unchanged.

19 undrained cyclic circular-path tests were conducted to develop insights into the soil behaviour under this loading situation and investigate the effectiveness of the conventional liquefaction analysis framework under this circumstance. 11 of the tests had path centre located at the origin, while the other 8 tests had offset circular paths. Detailed testing information is summarized in table 3.3. Along with bi-directional linear tests, liquefaction is defined to take place when the stress states in either X or Y direction reach the failure line.

The results of test C20-3 are presented here as an example to illustrate the characteristics of soil behaviour in this category of tests. This test had relative density of 63.1%, Skempton's B value of 0.956, and initial vertical consolidation stress at 100 kPa. The assigned amplitude of circular shear stress ratio was 0.2. After vertical consolidation, ramp loading was applied towards positive X direction, increasing the shear stress ratio in X direction to 0.2, to avoid abruptly increasing the of shear stress if a circular loading path was applied directly. The shear strain measurement was zeroed at this point, before the target circular loading started.

The plan view of measured shear stress is shown in the left graph in Figure 5.10, with the round mark representing the starting point and the arrow indicating the anticlockwise direction of loading path. As discussed in the preceding chapter, the initial part of the

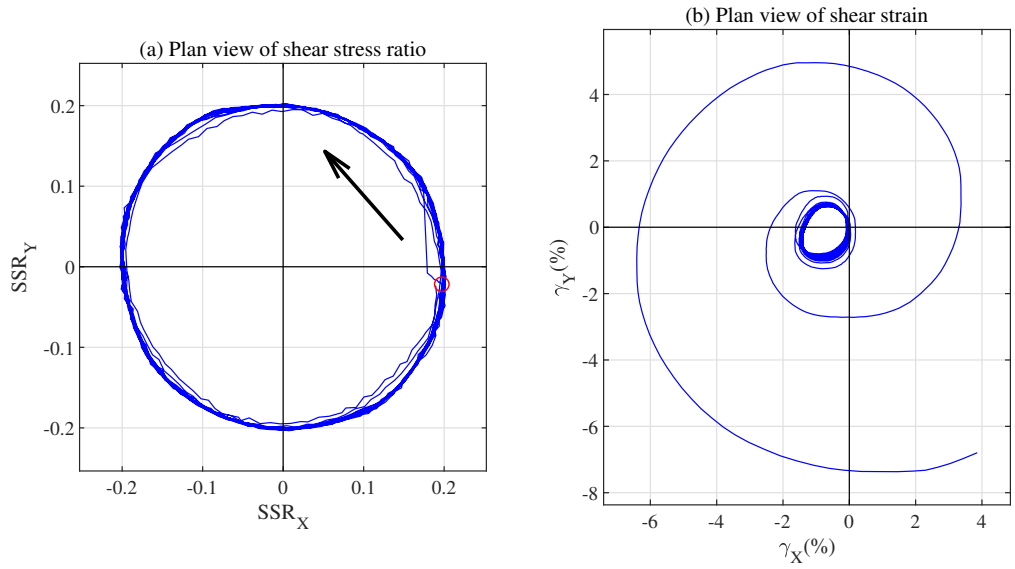

Fig. 5.10 The plan view of shear stress and shear strain of test C20-3

first cycle veers away from the theoretical path because the device control system needs to adjust its two loading strokes. The last few cycles also deviate from the theoretical circular stress path because the stiffness of the sample is reduced significantly when liquefaction is approached, making it difficult for the testing device to hold constant vertical stress and good control of shear stress. Figure 5.10(b) presents the plan view of shear strain. The strain path exhibits generally a circular shape, as expected, until the sample liquefies.

A four-way plot following Kammerer (2002) is shown in Figure 5.11. Total shear stress ratio SSR_{total} and total shear strain γ_{total} is used to provide overall characteristics in terms of shear stress and strain, with their definitions as follows:

$$SSR_{total} = \sqrt[2]{SSR_X^2 + SSR_Y^2} \tag{5.2}$$

$$\gamma_{total} = \sqrt[2]{\gamma_X^2 + \gamma_Y^2} \tag{5.3}$$

The SSR_{total} versus σ_v' and the SSR_{total} versus γ_{total} curves are almost horizontal in the top graphs, confirming the total shear stress ratio remained approximately constant and the testing device performed satisfactorily during this circular-path test.

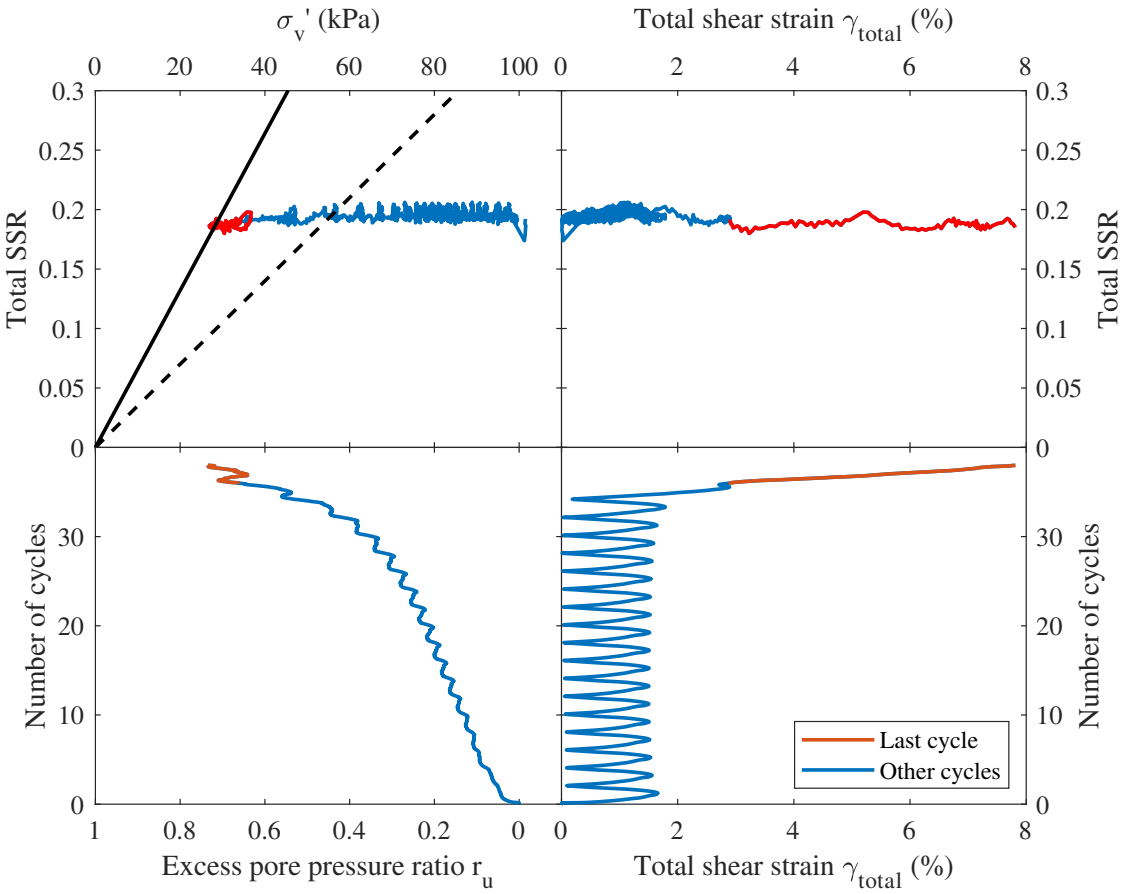

Fig. 5.11 The 4-way plot of test C20-3

Excess pore pressure in circular tests

The bottom left graph in Figure 5.11 shows the development of excess pore pressure ratio with the number of cycles. The excess pore pressure accumulates gradually and the maximum pore pressure ratio of 0.77 is reached at the 19th cycle where liquefaction is initiated. The "double-peak" phenomenon seen in linear tests is not observed; instead, there is only one pore pressure peak within a single cycle, demonstrating that the pattern of excess pore pressure accumulation differs from that in linear tests.

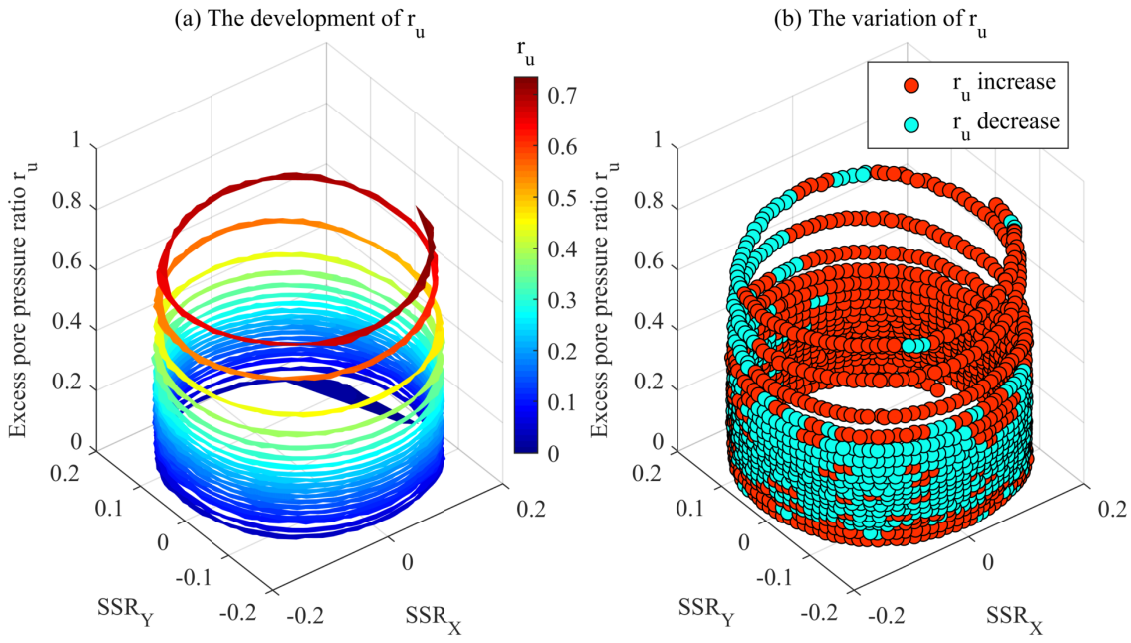

Fig. 5.12 3D development of excess pore pressure ratio of test C20-3

Actually, the cyclicity itself is unexpected. As the total shear stress remains constant like monotonic shearing, there is no distinguishable boundary between loading and unloading, and the excess pore pressure is thus anticipated to develop monotonically rather than cyclically. Figure 5.12 presents the excess pore pressure development with stress path in 3D in the left graph. The right graph shows the same plot with the red dots representing the sections where excess pore pressure increases the light blue dots presenting the portions where it decreases. When the excess pore pressure is relatively low, it increases along half of the path and decreases in the other half. In this test, excess pore pressure decreases in the semicircle corresponding from 135° to 315°, and increases in the other semicircle. In the last three cycles where excess pore pressure ratio is high, however, the pattern changes again with excess pore pressure decreasing only in the $90° - 150°$ section and increasing in the rest.

This can be seen more clearly in Figure 5.13 which illustrates the development of excess pore pressure in a polar coordinate system. The polar angles in Figure 5.13 are the angle of a point on the stress path relative to positive SSR_X direction in Figure 5.10, measured counterclockwise. The red parts indicate the increase of excess pore pressure while the blue

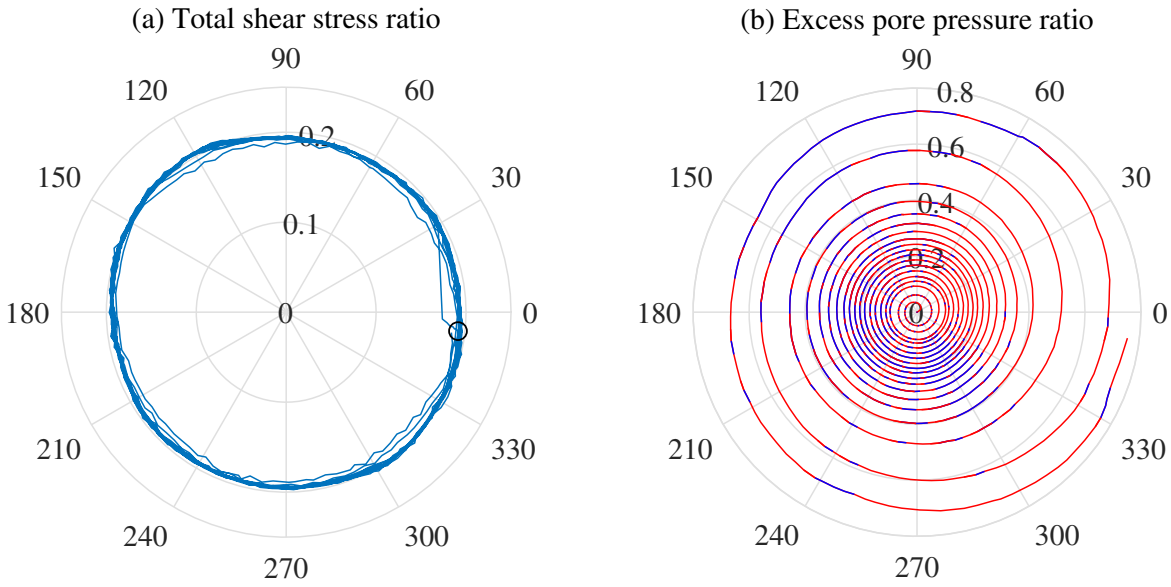

Fig. 5.13 The shear stress and excess pore pressure ratio of test C20-3 in polar coordinate system (the red parts in (b) represent increasing pore pressure and the blue parts indicate decreasing pore pressure)

sections indicate a decrease. The variation of excess pore pressure ratio follows a pattern in which the excess pore pressure grows in a semicircle and declines in the other, with the final excess pore pressure ratio of a cycle always higher than the initial one in the same cycle. The sections corresponding to pore pressure decrease shrink to $90° - 150°$ in the last three cycles, only one sixth of the whole loading path, while the majority of the loading path witnesses increase of pore pressure.

Although the other tests have the same testing procedure with this one, the portions of a cycle in which excess pore pressure cycles from increasing to decreasing or the way round is not always the same. Figure 5.14 presents the development of excess pore pressure of circular-path test C20-1 and test C20-5, which have the same total shear stress ratio of 0.2 but are different in density. It is evident that the specific partition of the increase and decrease of excess pore pressure can vary conspicuously. But it is also notable that there is a similarity among all the pre-liquefaction and on-liquefaction cycles in these tests, that is, the sections of pore pressure decrease always shrink to a small portion while pore pressure increase is seen in greater parts.

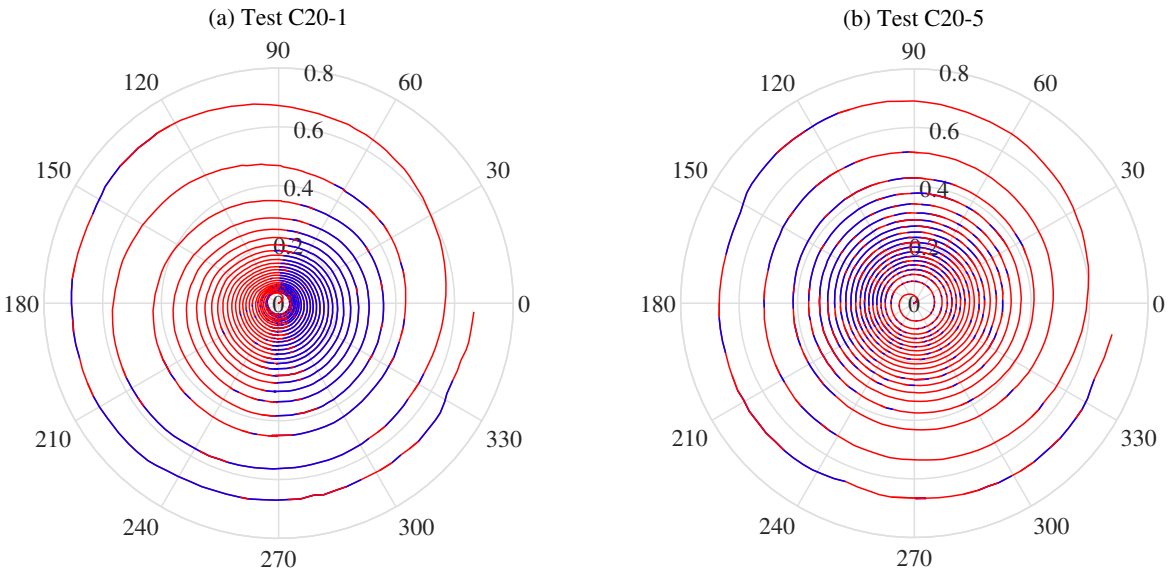

Fig. 5.14 The development of excess pore pressure ratio of test C20-1 and C20-5 in polar coordinate system (the red parts represent increasing pore pressure and the blue parts indicate decreasing pore pressure)

The mechanism behind this inconsistency is as yet unclear. On the one hand, the inevitable experimental error such as loading asymmetry can contribute to this phenomenon since it can cause latent subdivision of loading path into loading and unloading periods. But this cannot explain why the subdivision is inhibited when excess pore pressure becomes high and liquefaction is approached, since there is no evidence that the loading asymmetry is reduced at this stage. On the other hand, the rotation of shear stress can also exert influences. The anisotropic fabric in sand samples, caused by realistic but imperfect sample preparation and consolidation, is very likely to contain an indiscernible directionality that can interact with the stress rotation and thus distinguish the stress path into softer periods and stiffer periods, from which the cycling of excess pore pressure can arise. If this hypothesis holds true, the significant implications will be that, for one, the interaction between soil structure and the directionality of loading path can have prominent effects on soil behaviours, and for another, the directional non-uniformity of fabric anisotropy of sand can be either inhibited or determined by stress path when sands approach failure state or critical state, so that the cycling of excess pore pressure becomes inconspicuous at this stage. Although existing modelling and experimental work on triaxial, biaxial and uni-directional simple shear tests

have demonstrated, implicitly or explicitly, soil fabric anisotropies develop gradually towards a critical state that is controlled by stress states (Li and Dafalias, 2011; Oda, 1972; Rothenburg and Bathurst, 1989), its development under more complex loading scenario remains less well understood. More specifically designed experiments are needed in the future to verify this hypothesis.

While the pattern of the variation of excess pore pressure in early cycles varies, there exists a more noteworthy and consistent phenomenon: the maximum excess pore pressure ratios that can be generated in these tests are below unity. The excess pore pressure ratio reaches only 0.77 when liquefaction is initiated. The clue to explain this phenomenon can be found in the total shear stress path in the top-left graph in Figure 5.11. With the generation of excess pore pressure, effective vertical stress decreases, pushing the stress path leftward until it meets the failure line that is represented by the solid line. This crossing point announces the constrained final stress state that can be achieved under this loading condition. Correspondingly, the excess pore pressure at this point represents the maximum excess pore pressure in this test.

A question that follows naturally is whether the situation will change if initial static shearing is involved and total shear stress does not keep constant. Test C20-X20-1 is an extreme example of such a category of tests, which has a static shear in X direction that is so large that X shear stress is never below zero, as shown in Figure 5.15. The three-dimensional development of excess pore pressure with shear stress ratios is presented in Figure 5.16. Figure 5.17 shows the stress path and excess pore pressure ratio in polar coordinate system. The polar angles in Figure 5.17 are the anticlockwise angle of a point on the stress path relative to positive SSR_X direction in Figure 5.15, measured counterclockwise.

Evidently, the excess pore pressure develops in a different pattern compared with test C20-3. A distinct maximum can be seen in the last a few cycles, but the location of the maximum varies with each cycle. The higher the excess pore pressure, the closer to the $SSR_Y = 0$ axis the summit is situated. The reason why excess pore pressure develops in such a way can be found again in the total shear stress path illustrated in the top left graph in Figure 5.18 with the last cycle coloured red. Differently from circular tests without static

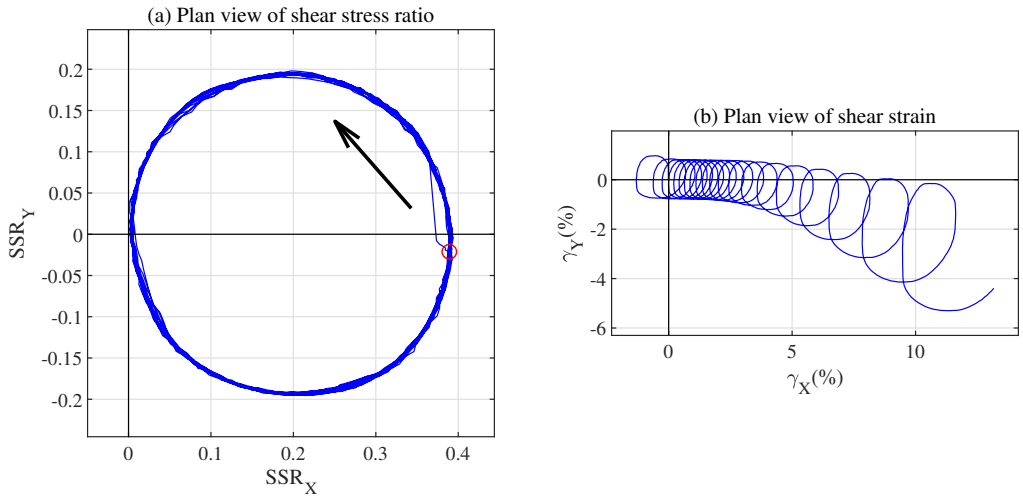

Fig. 5.15 The plan view of shear stress and shear strain of test C20-X20-1

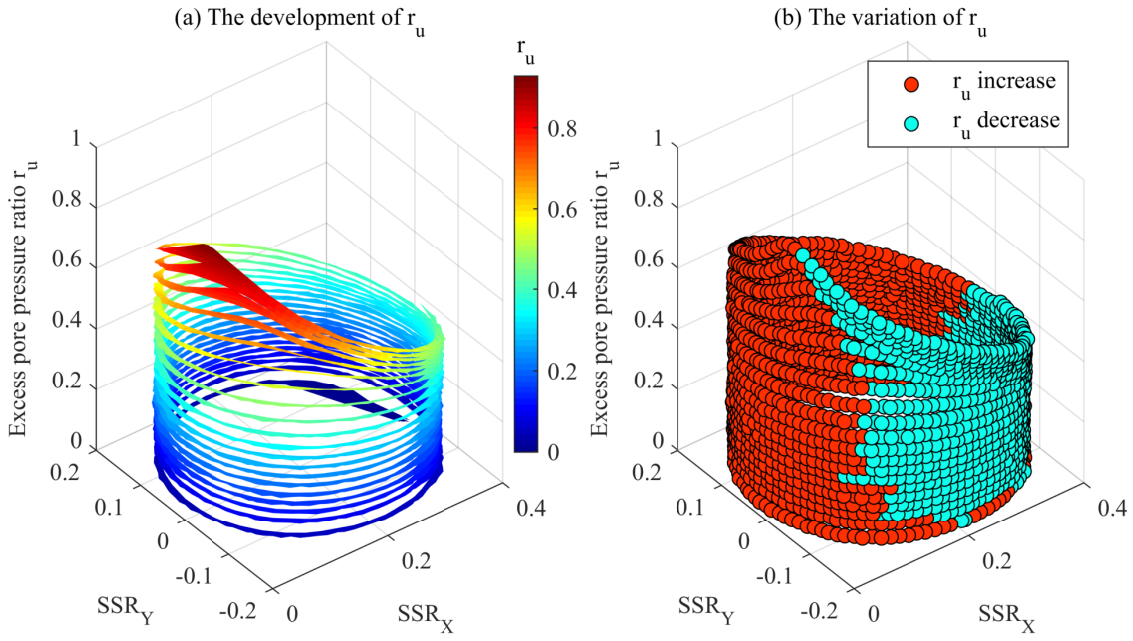

Fig. 5.16 3D development of excess pore pressure ratio of test C20-X20-1

shearing, the total shear stress in this test is not constant, instead, it cycles, decreasing in the first half of a loading cycle and increasing in the other half. In the last a few cycles when the

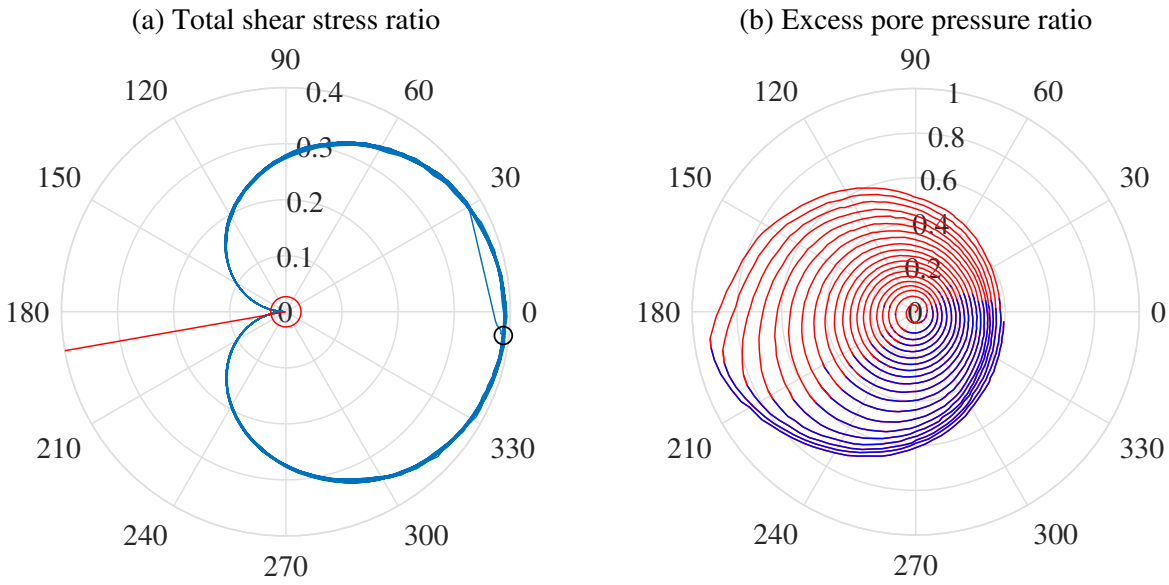

Fig. 5.17 The shear stress and excess pore pressure ratio of test C20-X20-1 in polar coordinate system (the changing angular coordinates of the points in (a) corresponding to transformation states account for the varying position of pore pressure thresholds in (b))

test approaches failure, the increase of total shear stress results in the increase of excess pore pressure initially, but after the stress path passes the phase transformation line (the dashed line in Figure 5.18), the relationship is reversed, with the further increase of total shear stress reducing excess pore pressure. The values of total shear stress at phase transformation state varies from cycle to cycle, which results in the changing position of the excess pore pressure peak in a loading cycle.

This can also be seen in polar coordinates in Figure 5.17. For instance, the value of total shear stress at the phase transformation state in the final cycle is 0.027, corresponding to the red circle in Figure 5.17(a). A ray can be drawn, coloured red in Figure 5.17(a), originating from the pole and passing through the intersection point between the red circle and the loading-phase section on the loading path. With the angular measurement of this ray, a point can an be determined on the outermost ring in Figure 5.17(b). This determined point is clearly where the variation of excess pore pressure turns from increase (red) to decrease (blue) in this cycle.

Another difference caused by the cycling of total shear stress, compared with the constant SSR_{total} test C20-3, rests in the maximum excess pore pressure ratio that can develop in a

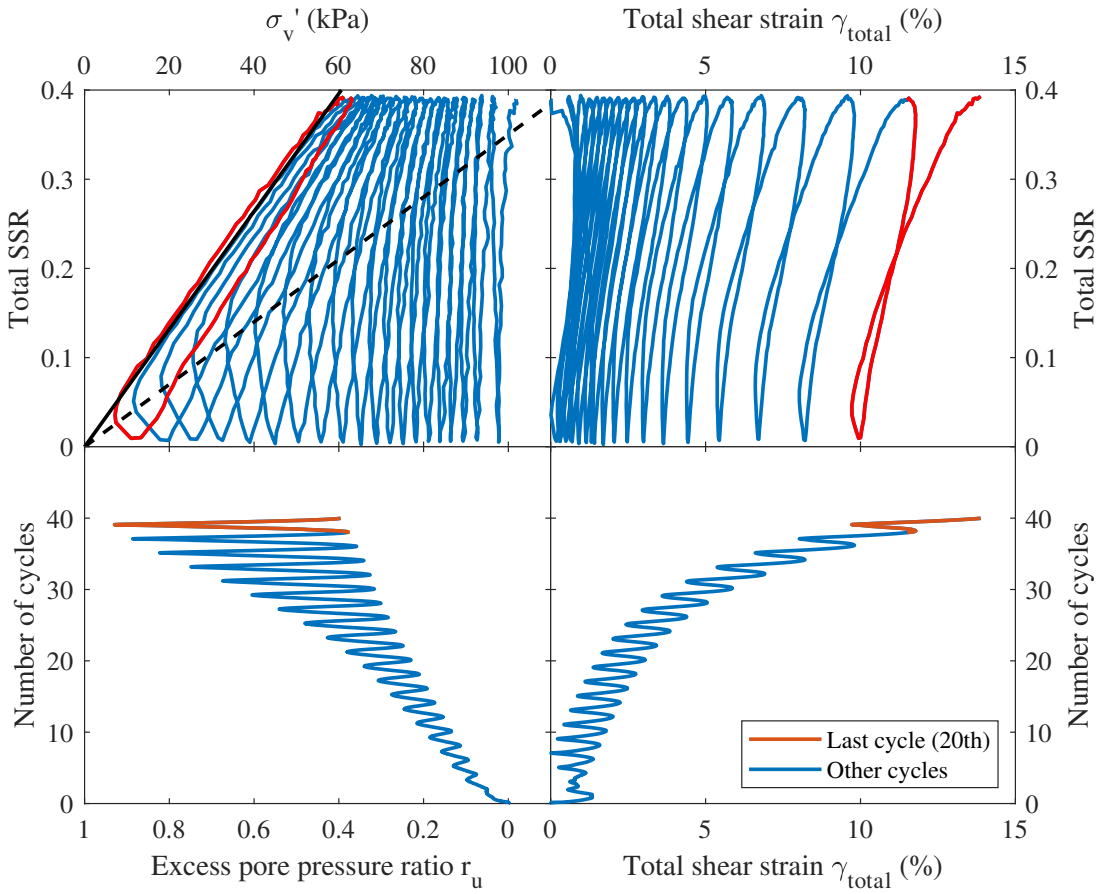

Fig. 5.18 The 4-way plot of test C20-X20-1

test. As discussed previously, the failure line constrains the ultimate stress states. In the circular tests without static shearing, maximum excess pore pressure ratio can be determined conveniently from the intersection point of total shear stress path and failure line. For the tests with static shearing, however, the ultimate stress states form a section on the failure line, which is controlled by the amplitude of total shear stress, and the lower bound of total shear stress decides the minimum effective vertical stress, or the maximum excess pore pressure. Therefore, it is rational to expect that maximum excess pore pressure ratio can be correlated to the lower limit of the amplitude of total shear stress ratio.

Figure 5.19 presents the maximum excess pore pressure ratio with the minimum total shear stress ratio in all the circular tests conducted in this study. The negative correlation between maximum pore pressure ratio and minimum SSR_{total} is in congruous with the reports of Boulanger (1990); Kammerer (2002). The solid line follows:

$$r_{u,max} = 1 - \frac{SSR_{total,min}}{tan\phi_{FL}} \tag{5.4}$$

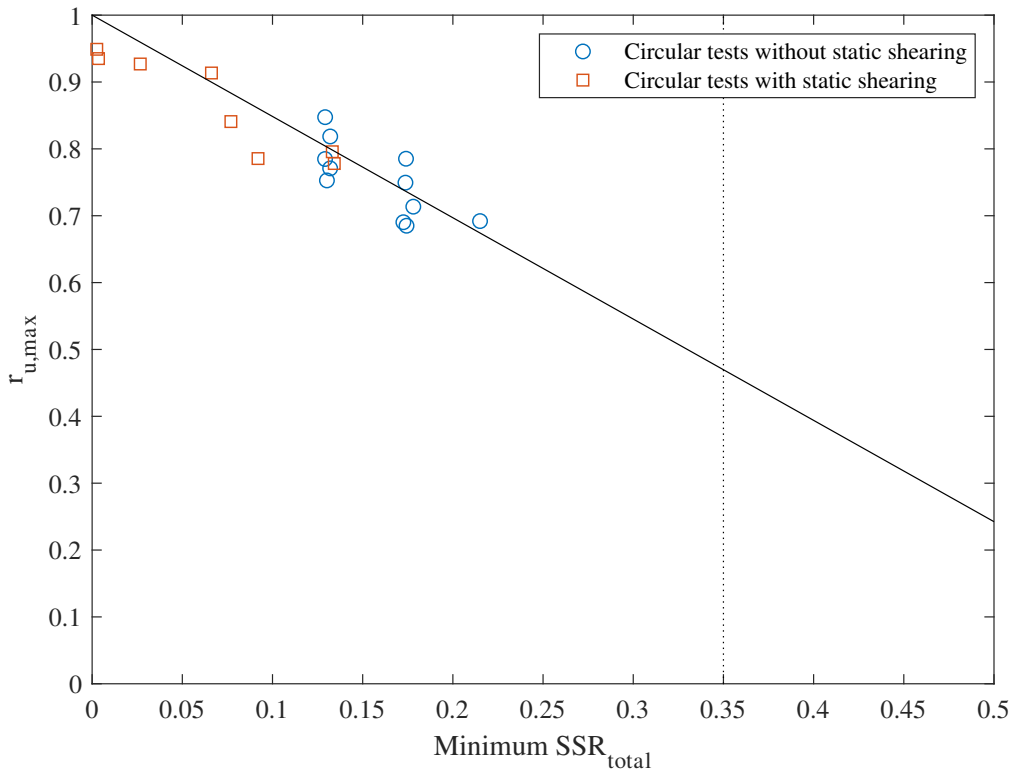

Fig. 5.19 Maximum excess pore pressure ratio versus minimum total shear shear stress in all circular tests

The development of excess pore pressure ratio with normalised number of loading cycles is shown in Figure 5.20. The three-stage increase of excess pore pressure ratio is also observed in the circular tests, no matter whether there is static shear or not.

The relationship between the excess pore pressure ratio generated in the first cycle of a test versus the number of cycles required to initiate liquefaction is shown in Figure 5.21, with the correlation equation 4.4 plotted as the solid curve. Although derived from uni-directional tests, equation 4.4 is also viable under circular loading conditions, at least qualitatively, suggesting that this relationship is also not altered by loading type.

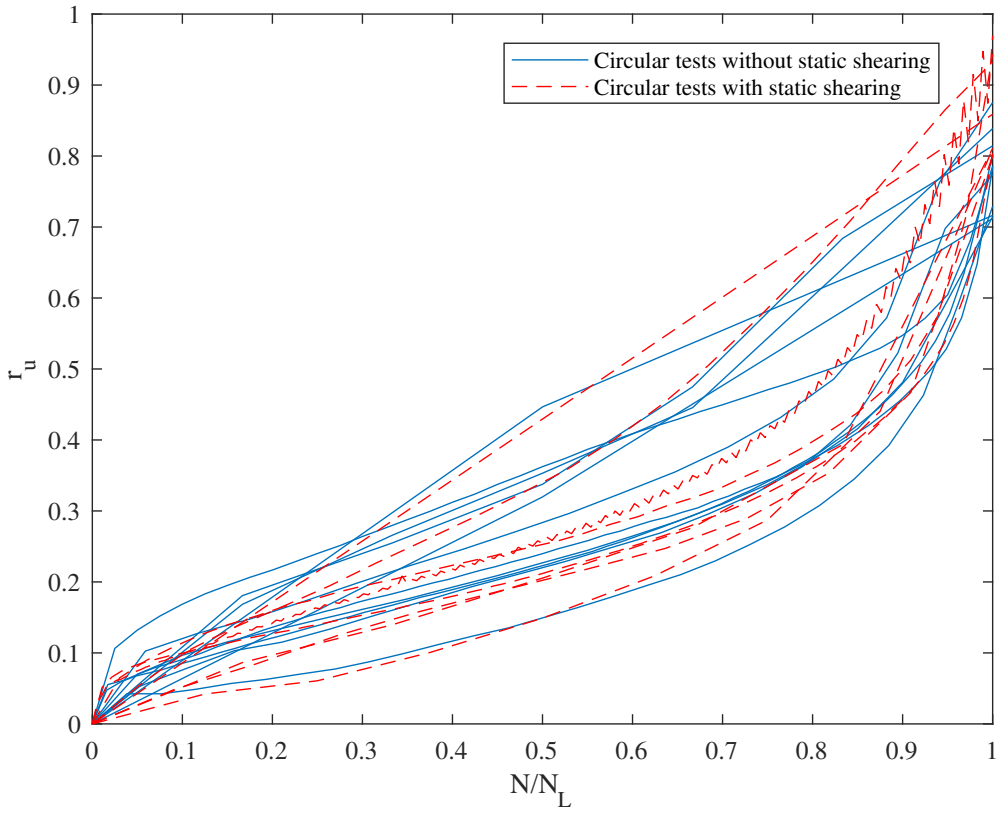

Fig. 5.20 The development of excess pore pressure with normalised number of cycles in all circular tests

Shear strain and shear modulus in circular tests

The plan view of shear strain of test C20-3 and test C20-X20-1 is shown in Figures 5.10 and 5.15. Two primary observations can be made regarding the development of shear strain. Firstly, the shear strain develops in a circular manner that is related to the circular loading paths, as anticipated. Secondly, when initial static shearing exists, the shear strain accumulated towards the static-shear direction is always larger than in the other directions. This is congruous with the results of uni-directional and bi-directional linear tests: static shearing always dominates the development of shear strain.

The situation is, nevertheless, not straightforward regarding stress-strain relationship. On the one hand, there is no consistent way to describe the relationship between total shear stress and total shear strain. For instance, the $SSR_{total} - \gamma_{total}$ curve is almost a straight

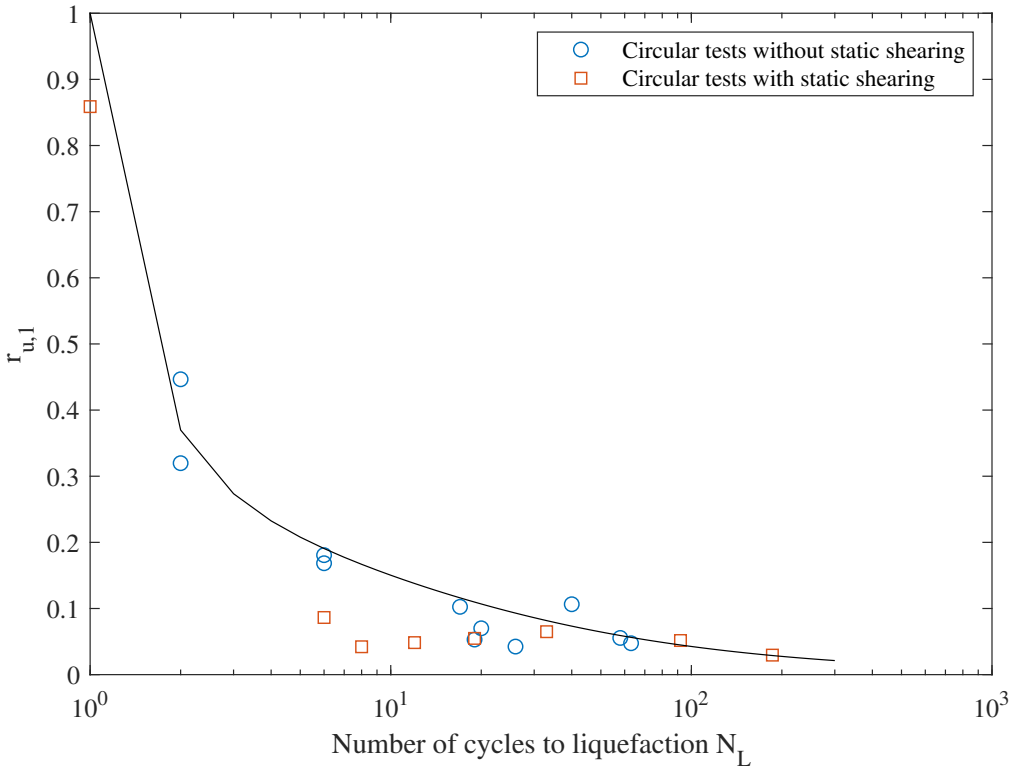

Fig. 5.21 The excess pore pressure ratio generated in the first cycle versus the number of cycles required to trigger liquefaction in all circular tests

line in test C20-3 (Figure 5.11), but becomes more similar to a uni-directional test in test C20-X20-1 (Figure 5.18). On the other hand, the actual stress-strain relationships should be four-dimensional in circular tests. The stress-strain curve in a certain direction is just the projection of the four-dimensional stress-strain relationship in that direction. Under such a circumstance, projecting the stress-strain relationships into dip and strike direction, which is the conventional method used in analysing uni-directional and bi-directional linear tests, is not applicable.

The projections of shear stress path and stress-strain curves of test C20-3 and C20-X20-1 onto X and Y direction are presented in Figure 5.22 and 5.23. The S-shaped hysteresis loops in uni-directional tests are not seen in the projections of circular tests. Instead, the projections of stress-strain hysteresis loops in test C20-3 have a cocoon-like geometry, while test C20-

X20-1 resembles pulled springs. The softening of soil can be told with these projected loops gradually becoming flatter, but shear modulus becomes an issue that needs reassessment

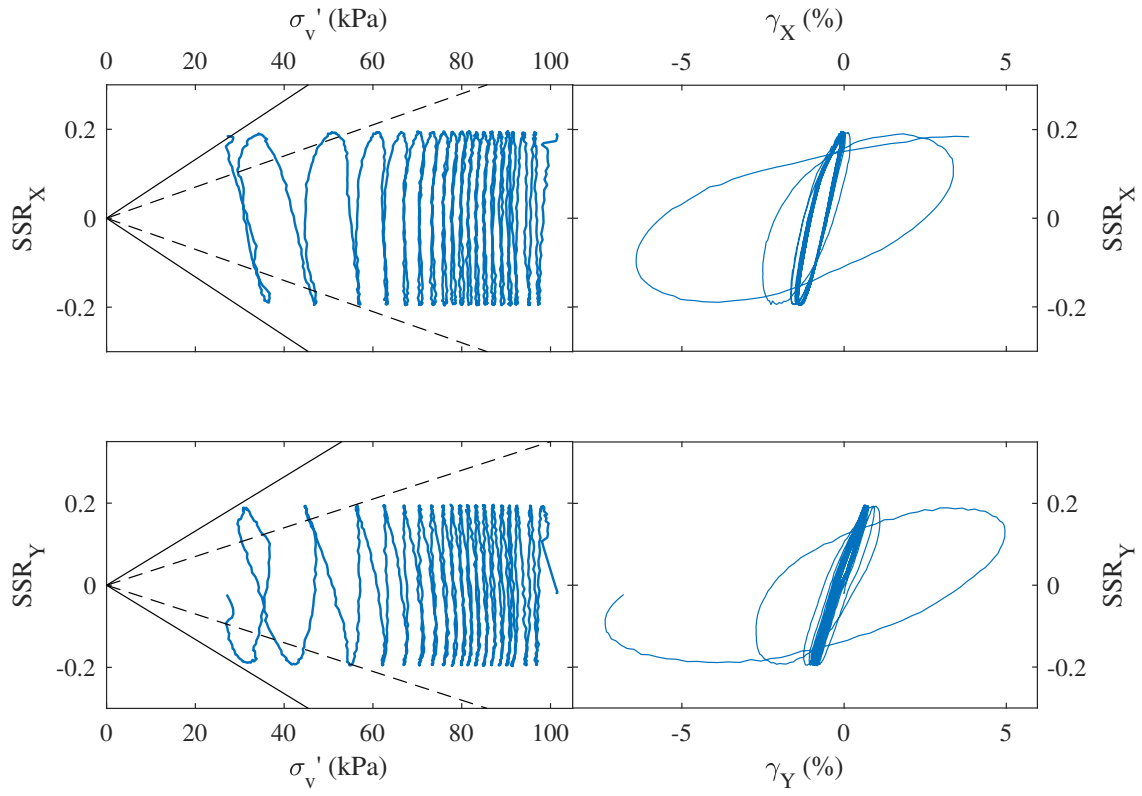

Fig. 5.22 The projections of stress paths and stress-strain relationships of test C20-3 on X and Y planes

If the directionality is not accounted for, the shear modulus calculated along uni-directional definitions is meaningless. For example, the secant shear modulus calculated using total shear stress and total shear strain, following uni-directional definition, is zero in test C20-3, as illustrated in the top right graph in Figure 5.11.

Otherwise, if shear modulus is defined by the stress-strain relationships in a certain direction, it cannot give information regarding other directions or spatial situation. Furthermore, defining a secant shear modulus in a single direction is also challenging. In direction Y in test C20-X20-1 as presented in Figure 5.23, for example, secant shear modulus cannot be determined easily because there are no distinct tips in the hysteresis loops.

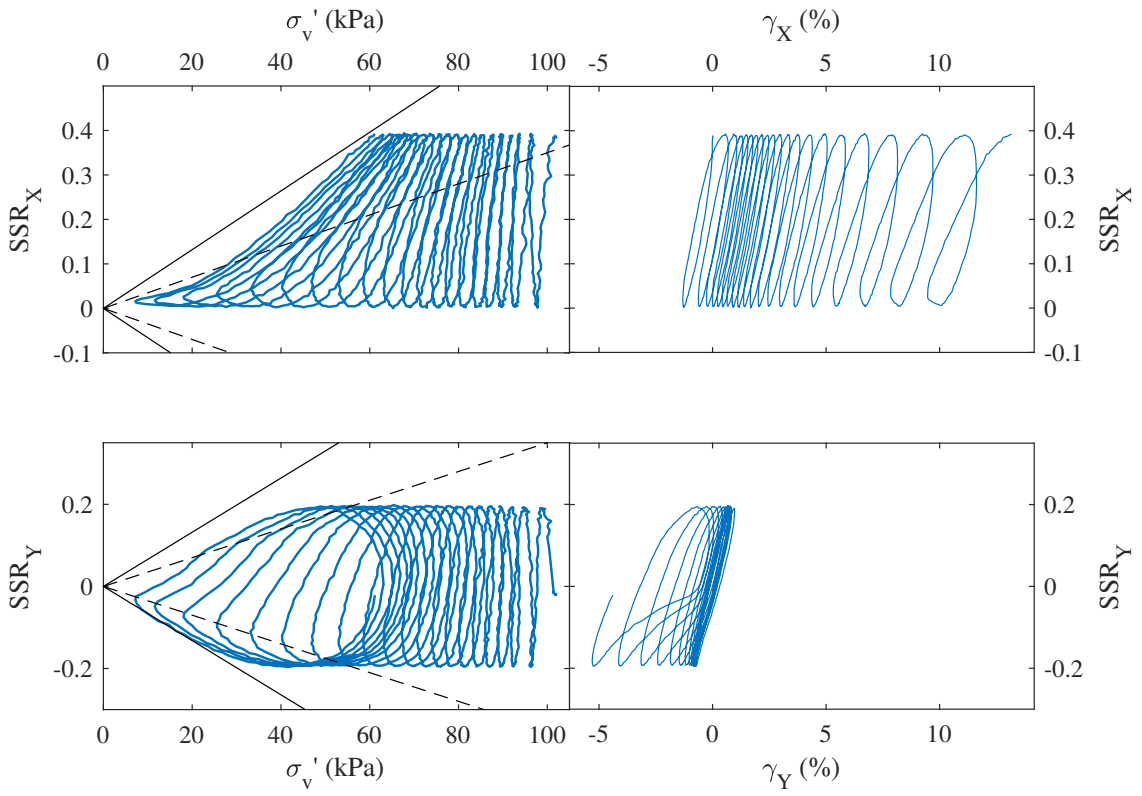

Fig. 5.23 The projections of stress paths and stress-strain relationships of test C20-X20-1 on X and Y planes

It is thus reasonable if shear modulus can be evaluated in a spatial way in the four-dimensional stress-strain space, but there are no practical or convenient mathematical tools available and the difficulties brought to engineering practice may prevent the use of such a complicated concept. Clearly, barriers in terms of the definition and application of shear modulus arise from multi-directional loading conditions, and the modelling work based on shear modulus should be careful with this issue.

5.2.2 Tests with oval loading path

An oval loading path is a type of loading condition that is rather similar to a circular path. The difference is that the shear stress not only rotates, but also changes in amount, even if

there is no initial static shearing. The comparisons between circular tests and oval tests can shed some light on the interaction of directionality and amplitude of shear stress.

Six tests with oval loading paths were conducted in this study. Four of them had a elliptical path without static shear, a shear stress ratio of 0.2 on the semi-major axis and 0.1 on the semi-minor axis, with the aim of providing comparisons against the circular tests with shear stress ratio of 0.2. Liquefaction is defined consistently with circular tests as taking place in the cycle where shear stress path on either direction reaches the failure line.

The results of an example test E2010-1 are shown here to illustrate the characteristics of soil behaviour in this category of tests. This test has relative density of 54%, B value of 0.954, and was consolidated with a vertical stress at 100 kPa. Maximum excess pore pressure ratio of 0.908 was achieved in the 19th cycle. The long axis and minor axis of this test does not coincide with the X and Y axis of the loading system, with a 15° angular difference between them. The cyclic loading was started after a ramp loading pushed the shear stress to the vertex, and shear strain measurement was zeroed before the cyclic loading began.

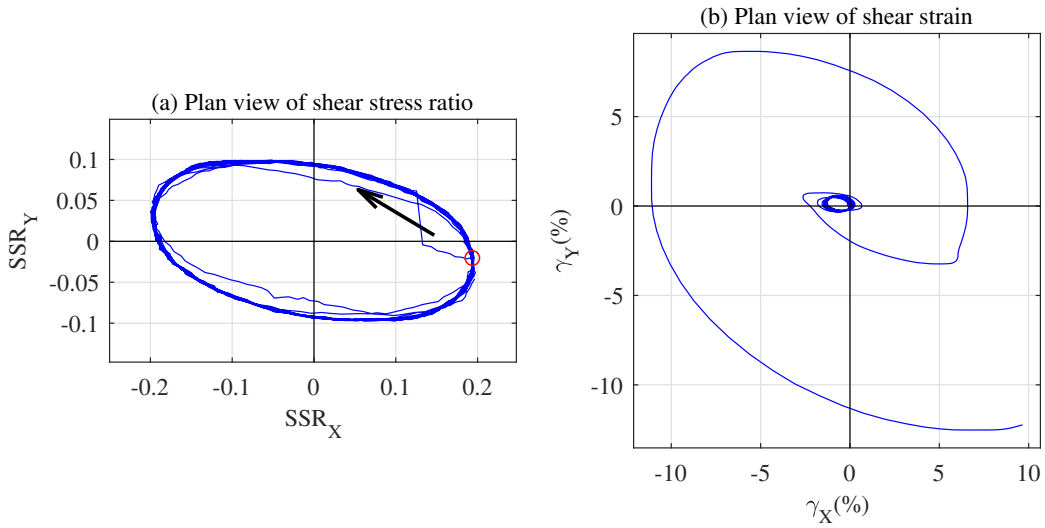

Fig. 5.24 The plan view of shear stress and shear strain of test E2010-1

The plan view of measured shear stress and shear strain is shown in Figure 5.24, and a 4-way plot is presented in Figure 5.25, with the round mark representing the starting point and the arrow indicating the anticlockwise direction of the loading path in the left graph. As in the circular tests, the initial part of the first cycle overshoots and veers away from the path because the adaptive loading system requires some time to adjust. The last cycle also deviates from the path as the stiffness of the sample is reduced significantly, making it difficult for the testing system to maintain good control. The strain path on the plan view shows a general oval shape, and the oval strain path enlarges as the test approaches liquefaction.

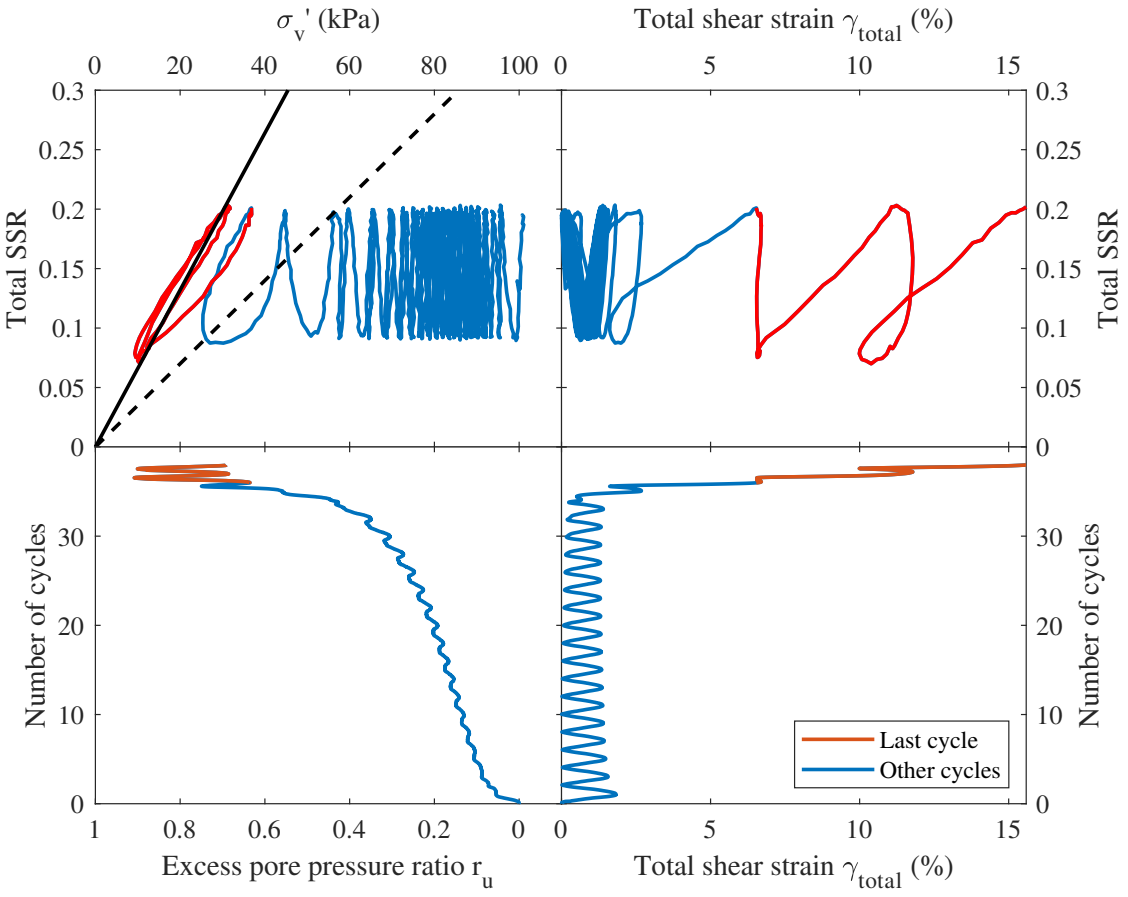

Fig. 5.25 The 4-way plot of test E2010-1

The shear stress path and stress-strain relationships on X and Y plane are presented in Figure 5.26. The stress path in Y direction and the stress-strain hysteresis loops in X direction exhibit a rather peculiar appearance. The SSR_Y versus σ_v' stress path has a crab-claw shape that is unlikely to be interpreted with the uni-directional-based concept of failure line

or phase transformation line in their direction. The hysteresis loops in X direction when liquefaction is imminent are in anomalous shape, from which secant shear modulus becomes meaningless since the tips on the loops are multiple.

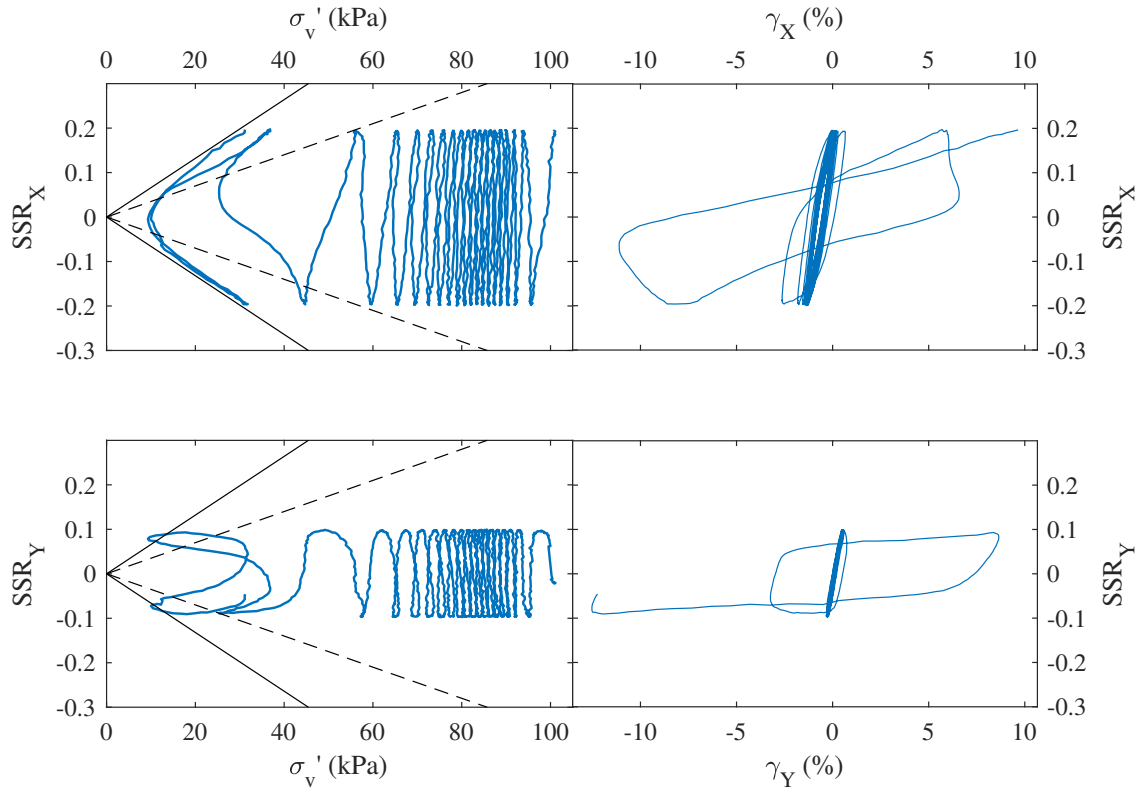

Fig. 5.26 The projections of stress paths and stress-strain relationships of test E2010-1 on X and Y planes

Viewing in a three-dimensional space, however, the peculiar stress path starts to make sense. The development of excess pore pressure ratio with loading path is shown in three-dimensional view in Figure 5.27. Since the excess pore pressure ratio can be regarded as the inverse effective vertical stress ratio, this graph is actually equivalent to a three-dimensional stress path. It is not difficult to notice that the 3D spatial structure of the excess pore pressure development in this oval test looks rather similar to uni-directional test if viewing along the minor axis. Viewing along the major axis, however, shows the "crab claw" seen in the

shear stress path in Y direction, with the “claws” being in fact the side views of the peaks of three-dimensional excess pore pressure development.

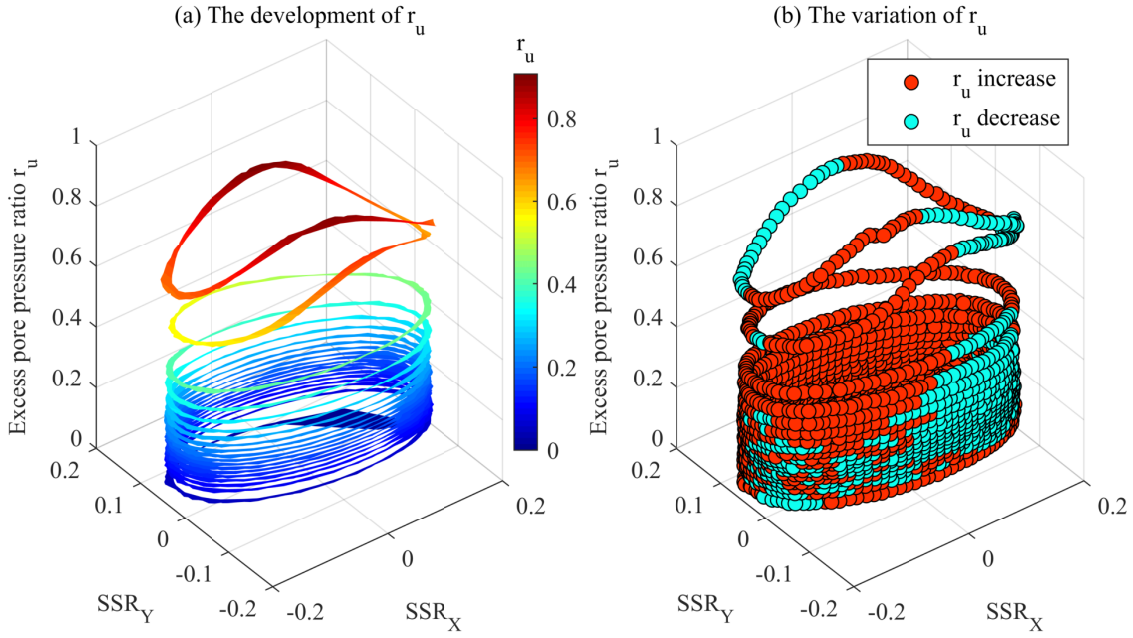

Fig. 5.27 3D development of excess pore pressure ratio of test E2010-1

The maximum excess pore pressure ratio of 0.908, with the minimum total shear stress ratio of 0.07, further demonstrating the conclusion drawn in circular tests that the minimum total shear stress dictates the maximum excess pore pressure that can develop in a test, following equation 5.4.

The variation of excess pore pressure within a single cycle on the right graph in Figure 5.27 does not have a consistent pattern in the early cycles with relatively low or moderate excess pore pressure, but in the cycle of liquefaction, a distinct pattern appears with the vertices and co-vertices becoming the partition points between the increase and decrease of excess pore pressure. The two peaks of excess pore pressure are at the co-vertices while the two valleys appear at vertices. The reasons of this phenomenon rest in the loading and unloading of shear stress. Different from circular tests, the amount of shear in oval tests is not constant. The major axis has the largest amount of shear and the minor axis has the least. Therefore, loading paths in oval tests contain distinguishable periods of loading

and unloading, with the former taking place when shearing proceeding from co-vertices to vertices and the latter in reverse. It is evident that the three-dimensional spatial structure of excess pore pressure development is influenced by the type of loading path, and the conventional 2D analysis method may mislead the understanding of soil behaviour.

5.2.3 Test with figure-8 loading path

Figure-8 or butterfly loading path is another type of fundamental loading paths that have both stress rotation and stress reversal. The most significant feature of it, compared with circular and oval loading paths, is that shear stress can pass through origin accompanied by continuous change of shear stress direction.

Seven tests with figure-8 or butterfly loading paths were conducted in this study, with varying amplitude of shear stress and shape of loading path. The results of test F8-3 are presented as an example to illustrate the soil behaviour under this type of loading condition. This test has relative density of 46.8%, Skempton's B value of 0.98, and vertical consolidation stress of 100 kPa. Liquefaction took place in the 11th cycle. The plan view of shear stress and shear strain is shown in Figure 5.28. The cyclic loading started from zero and proceeded along the direction oriented by the arrow. The amplitudes of shear stress on X and Y axis were both 0.15.

As circular and oval tests, the initial part of the first cycle has an issue of overshooting due to imperfect synchronizing of the two loading strokes in the testing device, and the last cycle deviates from the path as the reduced stiffness of the sample makes the testing system lose good control. The loading path of the last cycle is coloured red or dark to indicate whether the total shear stress is increasing (red) or decreasing (dark). The plan view of shear strain has a butterfly shape that is narrower on the positive γ_Y side and wider on the other.

The X-direction and Y-direction shear stress paths and stress-strain relationships are presented in Figure 5.29. The stress path on X direction has a peculiar behaviour (top-left graph in Figure 5.29). In the last loading cycle, after exceeding the phase transformation line (the dashed lines), the decrease of SSR_X can result in the increase of effective vertical stress. This is in conflict with the well-established theory from uni-directional tests which states the

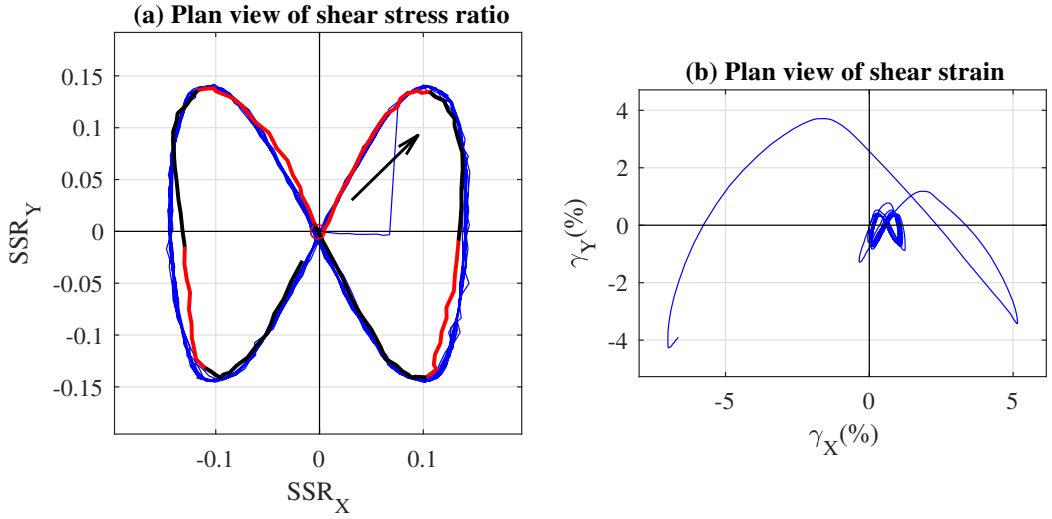

Fig. 5.28 The plan view of shear stress and shear strain of test F8-3 (the loading path of the last cycle in (a) is coloured, with red for increasing total shear stress and dark for decreasing total shear stress)

decrease of post-phase-transformation shear stress always leads to the decrease of effective mean stress. Furthermore, the stress-strain hysteresis loops in X direction are in a shape from which secant shear modulus cannot be easily defined. It is highlighted by these findings that caution should be exercised when applying uni-directional analysis to a specific projection plane under a multi-directional loading scenario. Under extreme circumstances like in this test, the conclusions drawn from a projection plane can be rather deceptive.

Viewing in three-dimensional space, the spatial structure of the shear stress path can be restored and reassessed, as shown in Figure 5.30. The counter-intuitive soil behaviour observed in X-direction stress path in Figure 5.29 is actually the projection of such a spatial structure.

The four-way plot of test F8-3 is presented in Figure 5.31. The two minimum SSR_{total} points are the starting points of the two half of the last loading cycle (coloured red). Taking the last half cycle as an example, the starting stress state is located below the phase transformation line (dashed line), as a result of which the increase of SSR_{total} leads to the increase of excess pore pressure first. After the total shear stress path reaches the phase transformation line,

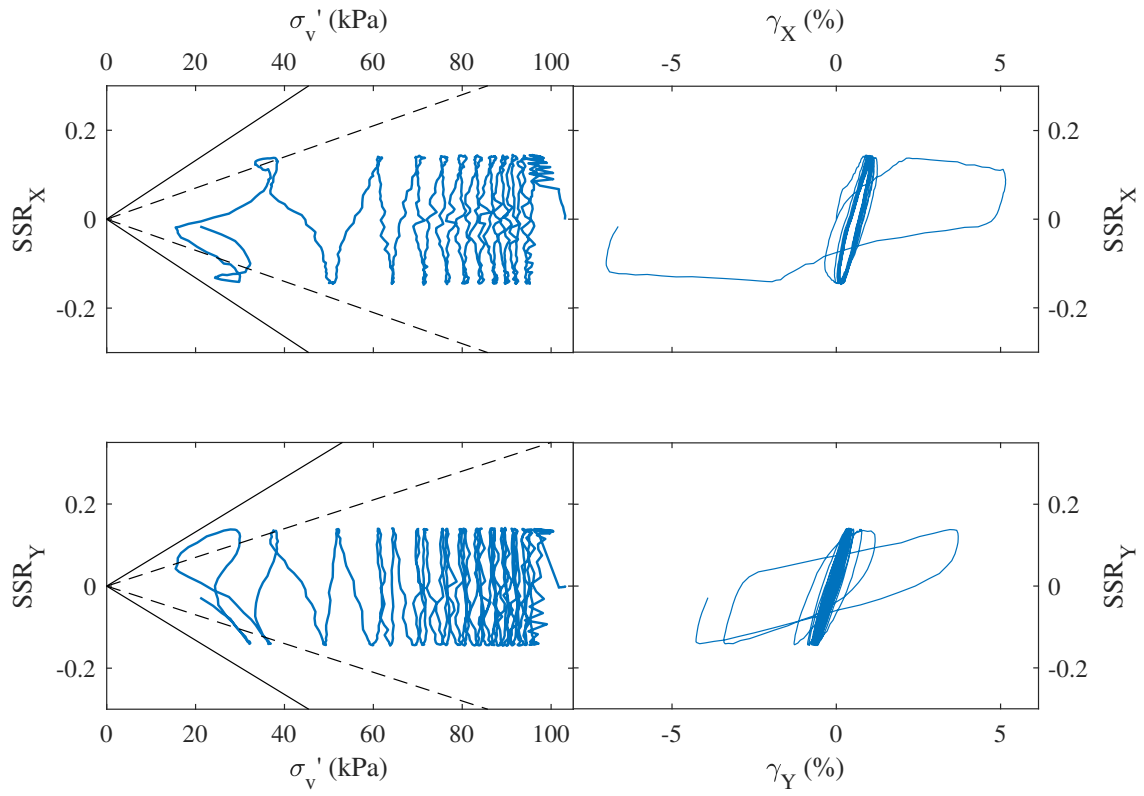

Fig. 5.29 The projections of stress paths and stress-strain relationships of test F8-3 on X and Y planes

however, the tendency is reversed, with further increase of SSR_{total} reducing excess pore pressure. This is why the initial part of the left half of the last cycle in Figure 5.30 has excess pore pressure increasing first before decreasing, although the total shear stress in this part keeps increasing. The total shear stress states in the subsequent periods remain in post-phase-transformation, where all the increase of SSR_{total} results in the decline of pore pressure and all the decrease of SSR_{total} increases pore pressure, which is compatible with the results in Figure 5.30.

It should also be noted that the maximum excess pore pressure ratio generated in this test is only 0.848, rather than the expected value of 0.95 calculated from equation 5.4 with $SSR_{total,min} = 0.015$. But this does not mean equation 5.4 is not applicalbe because this test was stopped before the failure stress states can fully develop. If more shearing cycles had

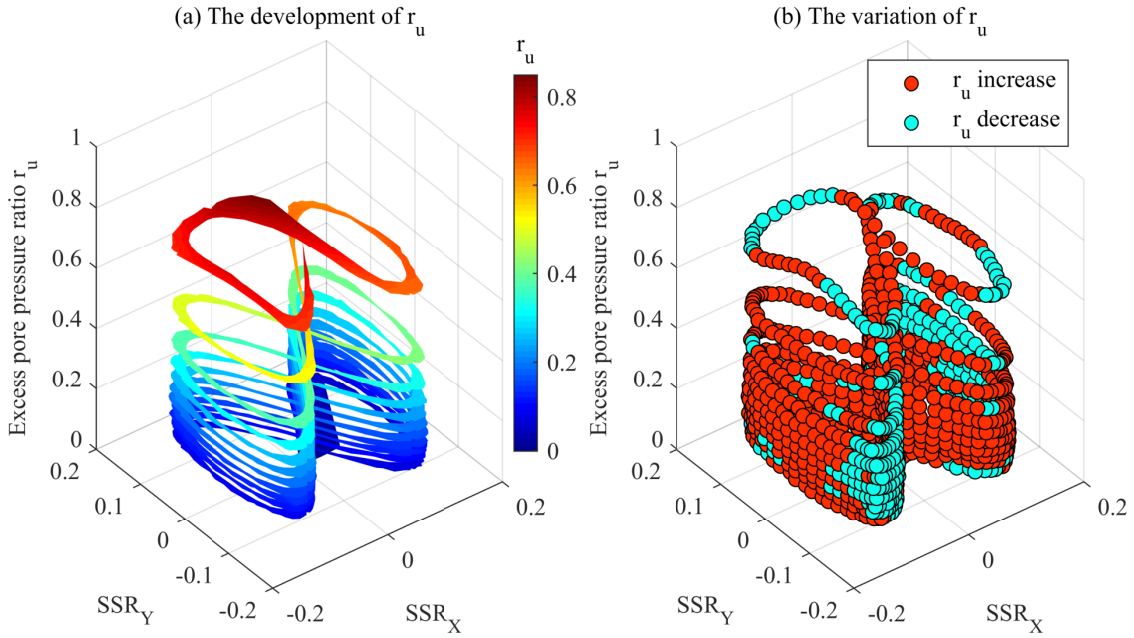

Fig. 5.30 3D development of excess pore pressure ratio of test F8-3

been applied, it was very likely that the final $r_{u,max}$ could advance towards 0.95 as the total shear stress path approaches and stayed on the failure line.

5.2.4 Discussions on the interpretation of multi-directional tests

The results of circular, oval and figure-8 tests analyzed in this chapter contain significant implications regarding the gaps in understanding the test results, which are worth of a summary and further discussion.

Firstly, the maximum excess pore pressure that can be generated in a test is closely associated with the type of loading path. On the one hand, the maximum excess pore pressure ratio in many instances is below unity. The liquefaction criterion that requires excess pore pressure ratio to reach unity as liquefaction takes place is not applicable in this situation. On the other hand, there exists a linear correlation between the maximum excess pore pressure ratio and the minimum total shear stress ratio, regardless of loading type, described mathematically by equation 5.4.

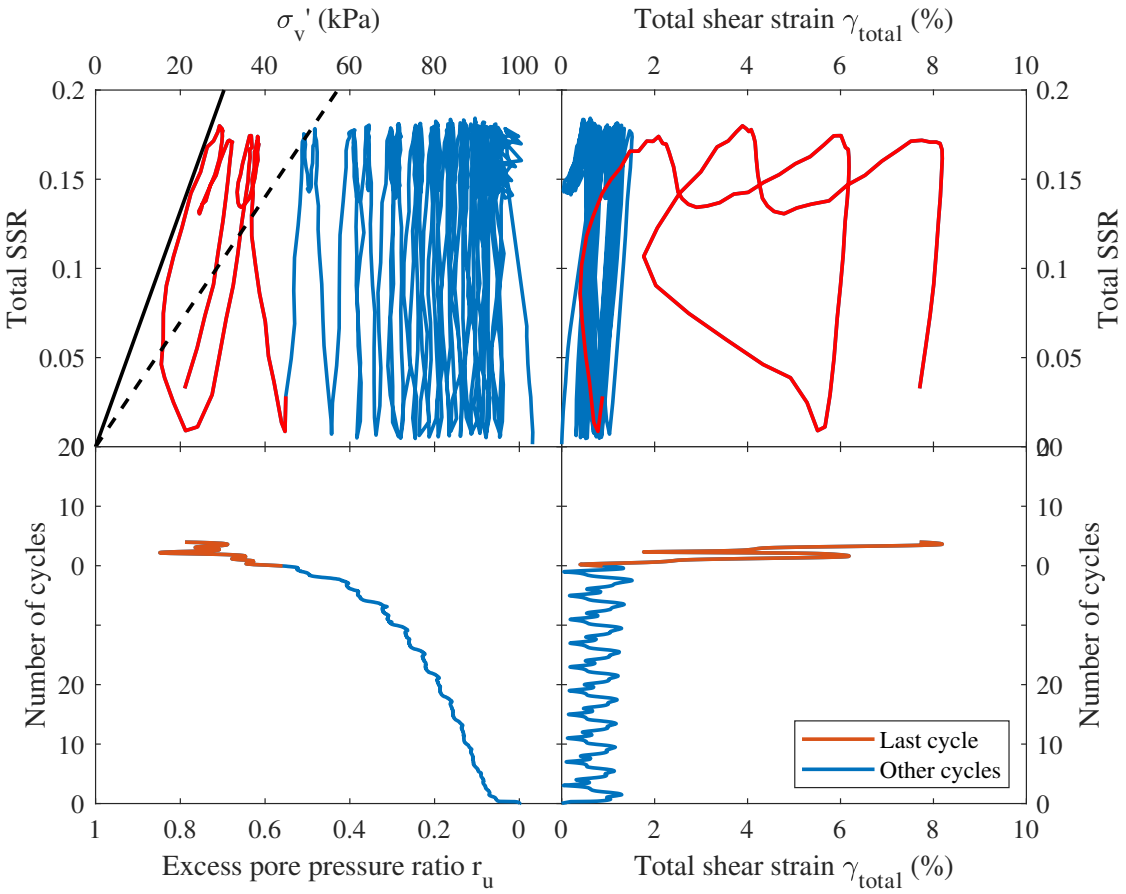

Fig. 5.31 The four-way plot of test F8-3

The reason why such a correlation should exist rests in the failure states in terms of total shear stress. SSR_{total} versus σ_v' path reaches and stays on the failure line eventually, from which the maximum pore pressure can be determined on the failure line with the minimum SSR_{total}. However, the concept of a failure line may not be fully applicable or descriptive. More detailed discussions on this will be made in the next chapter, together with the concept of conical failure surface.

Secondly, similar to the failure line, the concept of phase transformation line should also be considered in a total shear stress manner. After SSR_{total} versus σ_v' path passes through phase transformation line, any increase of total shear stress will reduce excess pore pressure while any decrease of total shear stress will result in the growth of excess pore pressure. In the figure-8 test analysed, for instance, the lack of information about phase transformation can mislead the understanding of pore pressure variation in the last loading cycle. However,

it should be noted that the application of phase transformation line to total shear stress is also an assumption. More comprehensive discussion regarding this will be given in the next chapter.

Thirdly, the shear stress path or the equivalent development of excess pore pressure should be three-dimensional under multi-directional loading conditions. The spatial structure of such a path should not be interpreted in a projection plane without caution. The results of example oval and figure-8 test demonstrates that some crucial information can be lost in the process of projecting such a spatial structure onto a plane, and the observations made from a projection can be deceptive or even erroneous. Evidently, the stress analysis of multi-directional tests should be conducted in three-dimensional space and the spatial structure of a shear stress path needs to be incorporated into the three-dimensional analysis framework.

Last but not least, stress-strain relationships become a four-dimensional issue under multi-directional loading condition because both shear stress and shear strain become planar problems. Correspondingly, the definition of shear modulus becomes challenging. The meaning of the ratio of total shear stress over total shear strain is doubtful. On the other hand, the projections of shear stress-strain relationships on a plane can be misleading. Furthermore, although constructing the definition of the shear modulus in a multiple-dimensional space is an attractive plan, there is not a straightforward or practical mathematical method to achieve this objective. Therefore, deformation-oriented constitutive models based on the shear modulus determined from hysteresis loops should be reassessed.

In conclusion, there are significant gaps in understanding the influence of multi-directional loading paths on liquefaction in simple shear tests that need to be bridged. The conventional analysis framework which is used in uni-directional tests is not necessarily effective under multi-directional loading conditions. The 2D $\tau - \sigma_v'$ analysis should be reassessed and extrapolated into 3D $\tau - \sigma_v'$ space, so that the influence of actual earthquake-induced multi-directional loading paths can be better interpreted and perceived.

Chapter 6

FAILURE AND PHASE TRANSFORMATION IN THREE-DIMENSIONAL $\tau - \sigma'_v$ SPACE

6.1 Failure cone

6.1.1 The concept of failure cone

While the results of multi-directional simple shear tests were analysed and illustrated in Chapter 5, the strain-based liquefaction criterion (6% double amplitude strain) was not applied because the variation of shear strain happens both in its amount and direction, which cannot be assessed as conveniently as in uni-directional loading scenarios. Instead, liquefaction was enabled when the shear stress in any direction reaches the failure line.

However, this liquefaction criterion relies on the assumption that the position of the failure line in any direction remains the same. If the failure of sand in simple shear tests were a pure frictional issue and obeyed Coulomb's friction law perfectly, the assumption could become equivalent to a Friction Cone problem.

For an ideal case where a block slides on a non-smooth plane and the coefficient of kinetic friction μ_s is constant in any position and direction on the plane, if the motion of a

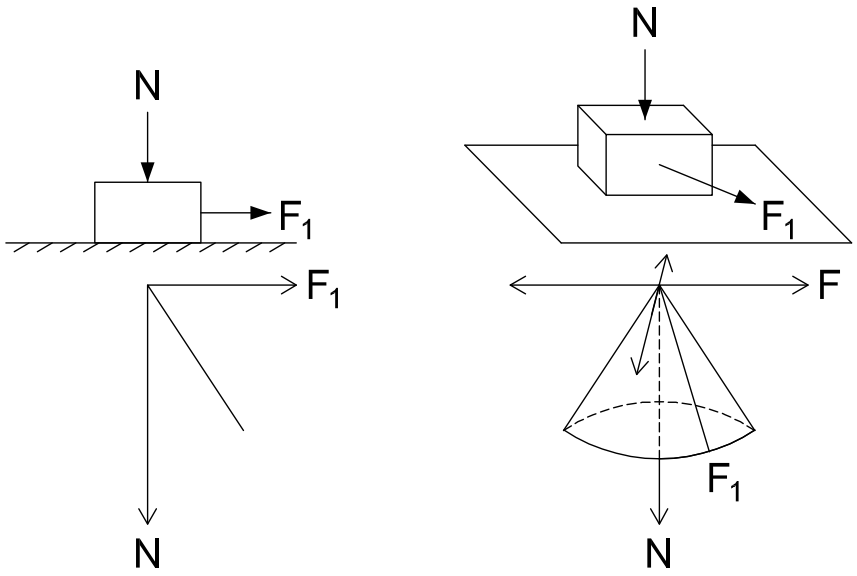

Fig. 6.1 The schematic of friction cone

block is uni-directional, the frictional force between the body and the frictional surface can be determined with Coulomb's law in that specific direction, as represented in the left graph in Figure 6.1. In contrast, if the block is allowed to move towards any direction in a plane, the same Coulomb's law should be established in all allowable directions, with its envelope forming a cone whose semi vertex angle is $tan^{-1}\mu_s$, as sketched in the right part of Figure 6.1. The line representing uni-directional friction law becomes the generatrix and the N axis serves as the axis of failure cone. It should be noted that the "cone" in friction cone theory refers to a conical surface rather than a solid body, and the terms are used interchangeably in this study.

The concept of friction cone has been widely adopted in research regarding rock mechanics since the 1950s (Goodman, 1989; John, 1968; Priest, 1985; Talobre, 1957) because the discontinuities in rocks make it necessary to analyse the stability of rock slopes in a three-dimensional manner. In the past a few decades, it was also given much attention to by researchers in the areas of computer visualization and robotics, along with other theoretical fundamentals for solving multi-face contact or multi-body motion problems (Renouf et al., 2005; Sauer and Schömer, 1998; Wriggers and Krstulović-Opara, 2004).

In contrast, the application of this concept on soil mechanics has been rather limited. The particles of soil are small enough to inhibit prominent discontinuities from happening in the profile of a single soil layer. The macro mechanical behaviour of soil is usually analysed with the framework of continuum mechanics. Furthermore, conventional laboratory testing techniques, such as triaxial and uni-directional simple shear testing, cannot simulate the multi-directional loading paths seen in real earthquakes, making it difficult to investigate the effects of multi-directional loading. Dynamic loading induced by earthquakes, wind or waves are hence simplified as uni-directional cyclic loading as a rule, and the effects of mult-directional loading are represented by an adjustment factor in engineering practice.

The test results analysed in Chapter 5, nevertheless, show that the uni-directional simplification fails to capture all the important characteristics of the generation of excess pore pressure, accumulation of shear strain and stress response under multi-directional loading. To develop a more in-depth understanding of how soil behaves under realistic complex loading scenarios, the dimensions of analysis framework should be increased so that the directionality of loading can be taken into account. The concept of a friction cone provides valuable insights in achieving this objective.

The Mohr–Coulomb failure criterion is usually adopted for simple shear conditions:

$$\tau = \sigma_v' \tan \phi_{FL} + c \tag{6.1}$$

where σ_v' is the effective vertical stress and ϕ_{FL} is the angle of the failure line.

The use of the angle of internal friction ϕ' is avoided in this study. Due to the lack of measurements of lateral stresses, the three principal stresses cannot be determined. The angle of internal friction ϕ', which equals $sin^{-1}\left(\frac{\sigma_1-\sigma_3}{\sigma_1+\sigma_3}\right)$, can not be calculated accurately. Furthermore, internal friction angle is affected by intermediate principal stress (Broms and Casbarian, 1965; Lade, 1973; Matsuoka and Nakai, 1974) but the latter cannot be determined with available simple shear tests. Thus, the angle of the failure line ϕ_{FL} is used in this study, which is not necessarily the same as internal friction angle ϕ'.

The term c was regarded as true cohesion by Terzaghi but Schofield has claimed in many of his work that c is the result of interlocking rather than cohesion. Readers are referred to *Disturbed Soil Properties and Geotechnical Design* (Schofield, 2005) for comprehensive discussions on this topic. In undrained tests on sands, however, c is usually considered as zero in either of the definitions. The failure states thus fall into its simplest form in 2D $\tau - \sigma'_v$ plane:

$$\tau = \sigma'_v \tan \phi_{FL} \tag{6.2}$$

which is congruous with Coulomb's friction law with $\tan \phi_{FL}$ serving as the equivalent coefficient of friction.

If the directionality of shear stress τ is considered, the 2D $\tau - \sigma'_v$ space needs to be expanded into a 3D space formed by τ_X, τ_Y and σ'_v, where τ_X and τ_Y are the shear stress decomposed onto two arbitrarily-assigned orthogonal directions. Correspondingly, the Mohr-coulomb failure line Equation 6.2 should be extrapolated into a failure cone having semi-vertex angle of ϕ_{FL}, as defined by:

$$\tau_X{}^2 + \tau_Y{}^2 = \sigma_v'^2 \, tan^2(\phi_{FL}) \tag{6.3a}$$

$$\sqrt{\tau_X{}^2 + \tau_Y{}^2} = \sigma'_v \tan \phi_{FL} \tag{6.3b}$$

$$\tau_{total} = \sigma'_v \tan \phi_{FL} \tag{6.3c}$$

In liquefaction analysis, shear stress is more often normalised by initial vertical stress as shear stress ratio $SSR = \frac{\tau}{\sigma_{v,i}}$. A failure cone in 3D $SSR - \sigma'_v$ space is illustrated in Figure 6.2, with the representative angle of failure ϕ_{FL} determined to be 33.4° for medium-dense Hostun sands tested in this study.

If such a failure cone exists, it should envelop all possibilities of stress states of sands in undrained simple shear tests. A shear stress path cannot run outside the cone, and flow-type deformation or rapid accumulation of shear strain should take place when the failure cone is reached.

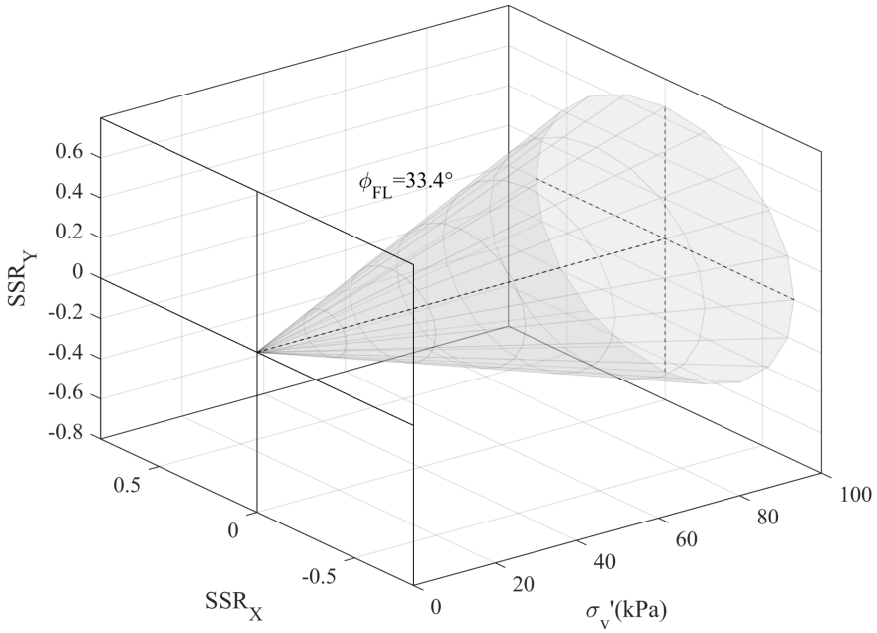

Fig. 6.2 The schematic of failure cone in 3D $SSR - \sigma'_v$ space

The existence of failure cone can be verified by examining if equation 6.3c describes the undrained soil response. The angle of failure line ϕ_{FL} does not always hold the value of 33.4°, partly because the density variation of sands leads to varying angles of failure line and partly because the loading system in this study cannot guarantee good control after flow-type deformation takes place. The angle of 33.4° is a representative average value for the range of specimens tested. Therefore, to validate equation 6.3c is actually to prove that the failure envelope for the total shear stress path is a straight line, whose inclination angle does not have to be exactly 33.4° however.

The 4-way plot of test C20-X20-1 which was analysed as an example test in Chapter 5 (Figure 5.18) is reploted in Figure 6.3, with more cycles presented. It is evident that the stress path tends to become stationary once it reaches the failure envelope, as seen more clearly in the distance between the bottom tips of every two total shear stress cycles. The cycle which has a bottom tip at σ'_v of 10 kPa (20th cycle) seems to be the turning point, before which the distance between every two cycles keeps increasing, indicating the generation of excess pore pressure is accelerating and the sample is approaching failure. After that cycle, however,

the distance between cycles gradually decreases. It appears that the total shear stress path resists to move further leftwards. A reasonable guess is that the sample has failed since the 20th cycle with the development of total shear stress path constrained thereafter, but the imperfect control of loading system results in it actually moving leftwards subsequently with a limited degree. If the loading system had ideal response to the low stiffness of soil sample at this point, it should be expected that the total shear stress path would stay on roughly the same location since the 20th cycle and proceed on the same trace after that. The total shear stress path of the 20th cycle is red in Figure 5.18, clearly overlapping equation 6.3c. Furthermore, even with the nominal last cycle (23rd cycle) of the test, coloured red in Figure 6.3, the failure envelope in $\tau_{total} - \sigma_v'$ space seem to still have the shape of a straight line, which validates equation 6.3c and the concept of the failure cone in this case.

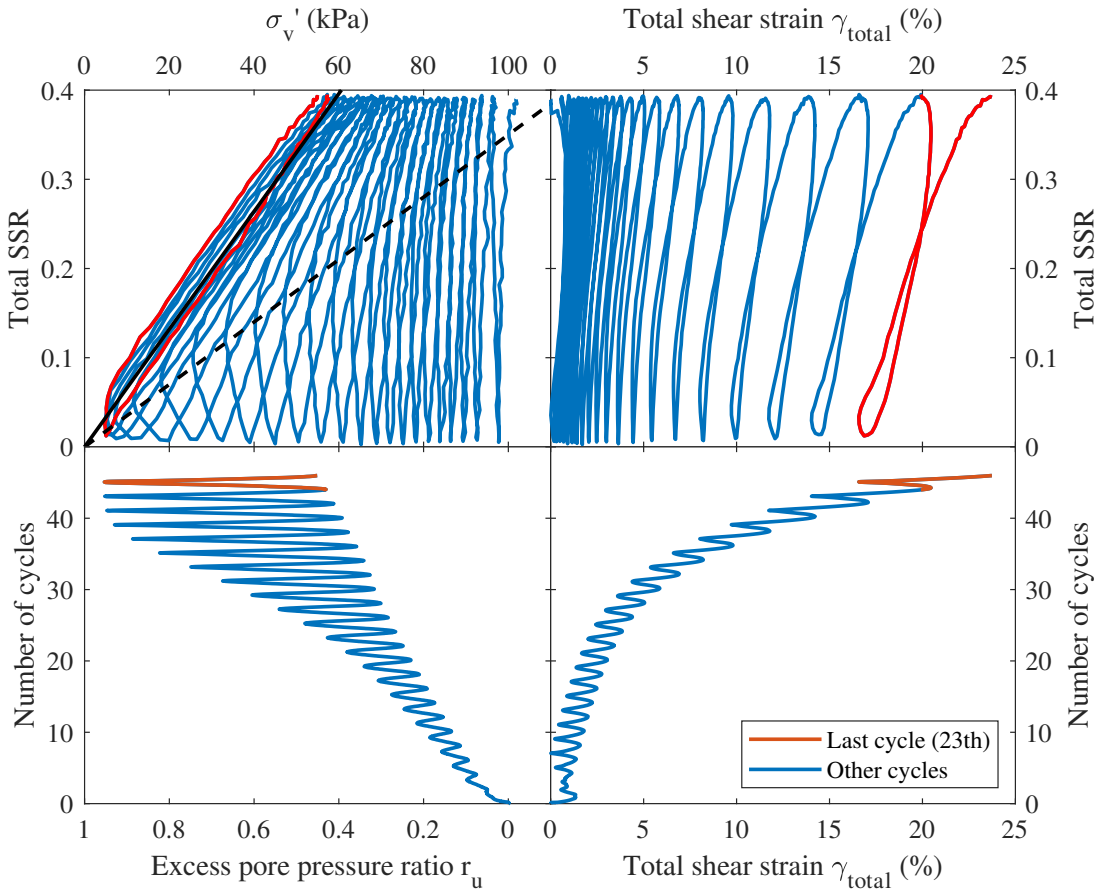

Fig. 6.3 The 4-way plot of test C20-X20-1 (C.F. Figure 5.18)

The analysis of other multi-directional loading paths leads to similar results. Oval test E2010-1 analysed in Chapter 5, for example, reaches failure at the 19th cycle, which is reflected by the sudden jump of shear strain as shown in Figure 5.26. At the time when the flow-type deformation occurs, the total shear stress path in Figure 5.25 coincides with the failure line following equation 6.3c. Similarly, the distinct flow-type development of shear strain happens in the 11th cycle in the example figure-8 test F8-3 as seen in Figure 5.31. The corresponding total shear stress path of this cycle is also observed to reach the proposed failure line.

The concept of failure cone can be validated against all the testing results in this study and it is defensible to conclude that equation 6.3c is applicable to undrained simple shear tests on medium-dense clean Hostun sands vertically consolidated to 100 kPa, no matter what the shearing path is. In addition, it is possible to expect that the failure cone exists in sand tested with other testing conditions, but the details of failure cone may vary. For drained test, the failure cone needs to be modified to a piecewise-truncated cone to account for the contribution of dilation. For soils with outstandingly anisotropic fabrics, the failure cone is likely to become elliptical to take the anisotropy into account. While these assumptions need verification by more test data in the future, it cannot be denied that a conical failure surface can be established under the testing conditions in this study.

6.1.2 Failure states of bi-directional linear tests and multi-directional tests

With the failure cone hypothesis, uni-directional linear tests represent the stress paths on the unique axial section plane that cuts the cone through its vertex and along its axis. The outline of the intersection of the cone and the plane is in the shape of two straight lines, which form the uni-directional failure lines. Similarly, through analysing the relative locations of the failure cone and loading paths, some peculiar phenomena in bi-directional and multi-directional tests can be explained. In the first instance, the failure envelope of bi-directional linear tests can be re-examined. As illustrated in Figure 5.4a and 5.5a, the failure states on the

cyclic loading direction can be altered by the static shearing on the perpendicular direction in bi-directional linear tests. An interpretation of this phenomenon can be found in the conic sections of failure cone.

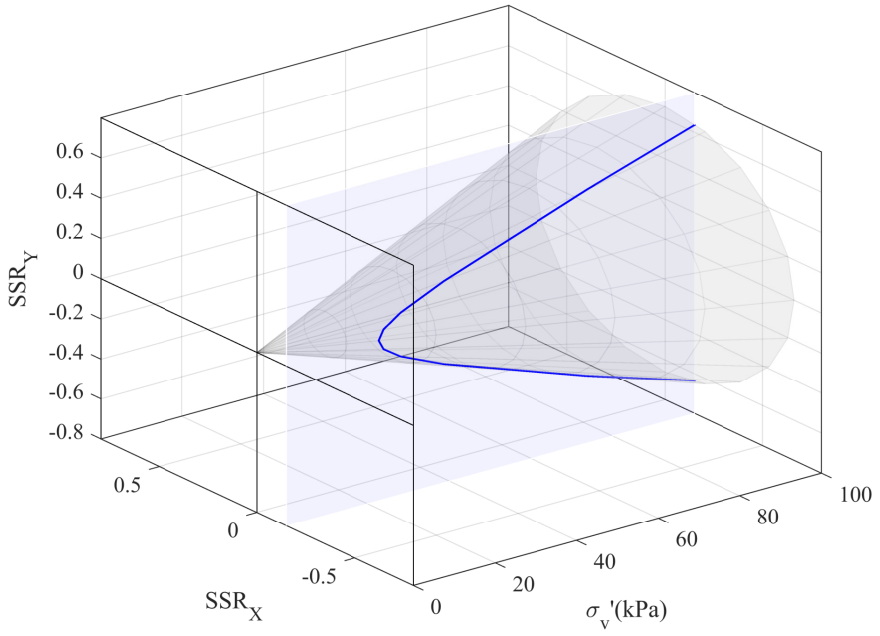

Fig. 6.4 The schematic of the failure cone intersected by a plane

In contrast with uni-directional tests, the static shearing in bi-directional linear tests is perpendicular to the direction of cyclic loading. The cyclic shearing effectively occurs on a plane cutting across the failure cone parallel to its axis, forming a conic section (a branch of and hyperbola) as illustrated in Figure 6.4. The hyperbolic outline can be described as:

$$tan^2(\phi_{FL})\frac{\sigma_v'^2}{\tau_{static}^2} - \frac{\tau_{cyclic}^2}{\tau_{static}^2} = 1 \tag{6.4}$$

The shear stress paths of test Bilinear-8 in dip and strike direction are presented as an example in Figure 6.5. The square marker indicates the end of the test and the circle marker locates the point with minimum measured static shear stress ratio. The solid hyperbola in Figure 6.5b represents the conic section calculated with τ_{static} of the end point (square-marked point) at 0.149, while the dashed one is calculated with the measured minimum

τ_{static} (circle-marked point) at 0.122. It is clear that the hyperbola derived from failure cone theory is effective in enveloping the failure states of bi-directional linear tests. A more understandable graph of the same stress path is shown in 3D $\tau - \sigma'_v$ space in Figure 6.6, which visualizes and validates the effects of failure cone on constraining potential failure states under bi-directional linear loading paths.

Three primary conclusions can be made from equation 6.4. Firstly, the asymptote of the hyperbola crosses zero, indicating that effective vertical stress σ'_v can never reach zero in bi-directional linear tests. To put it in other word, the excess pore pressure ratio can reach unity in linear tests only if orthogonal static shear is strictly zero ($\tau_{static} \neq 0$); otherwise, imperfect uni-directional linear tests which have even marginal static shear force on the orthogonal direction can still result in a maximum excess pore pressure less than unity. Secondly, the higher the static shearing, the farther the ultimate cyclic shear stress path in the perpendicular direction is away from origin. Thirdly, equation 6.4 can be transformed to give the relationship between excess pore pressure ratio and shear stress ratios as follows:

$$r_u = 1 - \frac{\sqrt{SSR_{cyclic}^2 + \alpha^2}}{\tan\phi_{FL}} \tag{6.5}$$

For cases where stress reversal is seen in the direction of cyclic loading, that is, SSR_{cyclic} can reach zero at times, the maximum excess pore pressure ratio can only be achieved when SSR_{cyclic} becomes zero. Correspondingly, the maximum excess pore pressure ratio can be correlated exclusively with α as:

$$r_{u,max} = 1 - \frac{\alpha}{\tan\phi_{FL}} \tag{6.6}$$

which is exactly the same as the correlation obtained from bi-directional linear testing data, as introduced in equation 5.1.

In addition to bi-directional linear tests, the failure states of multi-directional tests are also associated with the failure cone. The stress paths of circular test C20-3 and C20-X20-1, oval test E2010-1 and figure-8 test F8-3 are shown in Figure 6.7- 6.10. The reason why the stress path of test C20-3 cannot approach the origin is that it is constrained by the failure

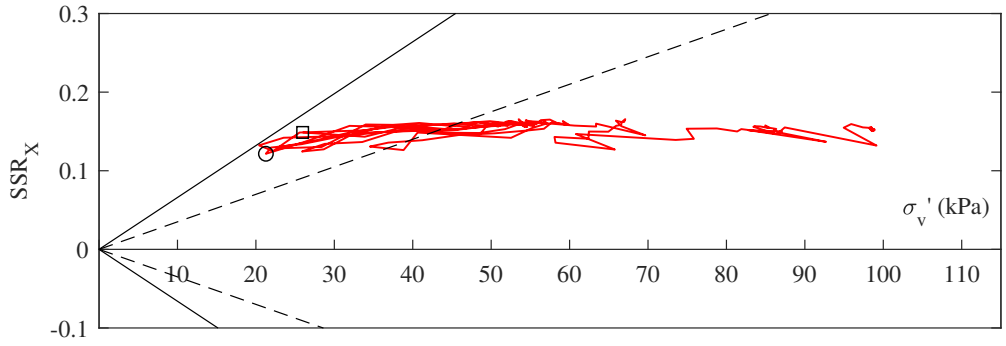

(a) Stress in dip direction (static shearing)

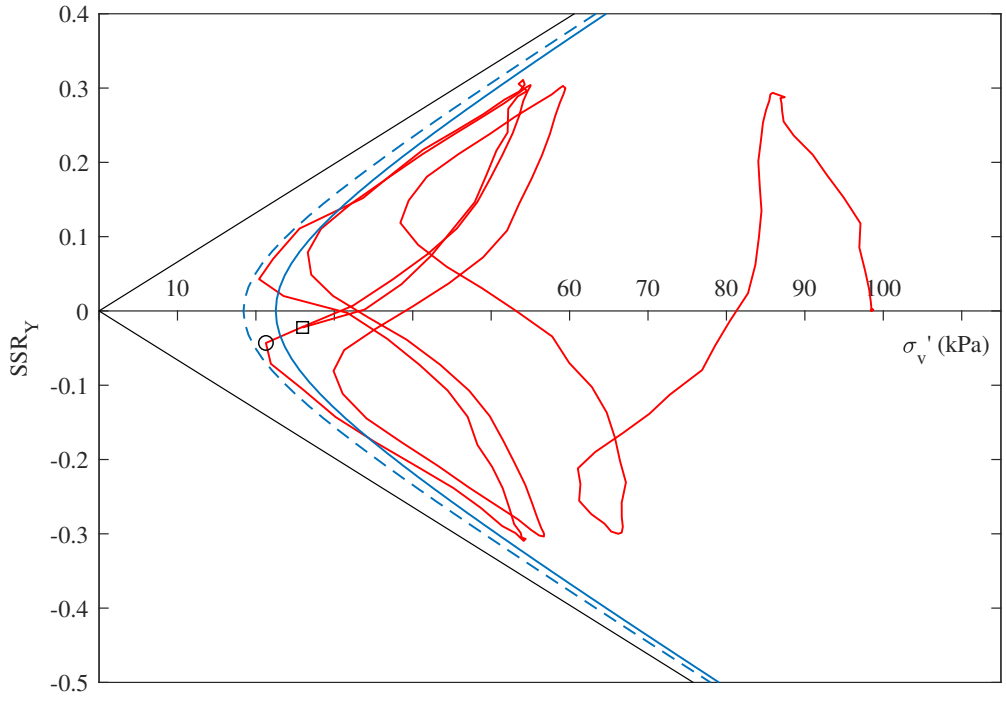

(b) Stress in strike direction (cyclic shearing)

Fig. 6.5 Stress paths of test Bilinear-8

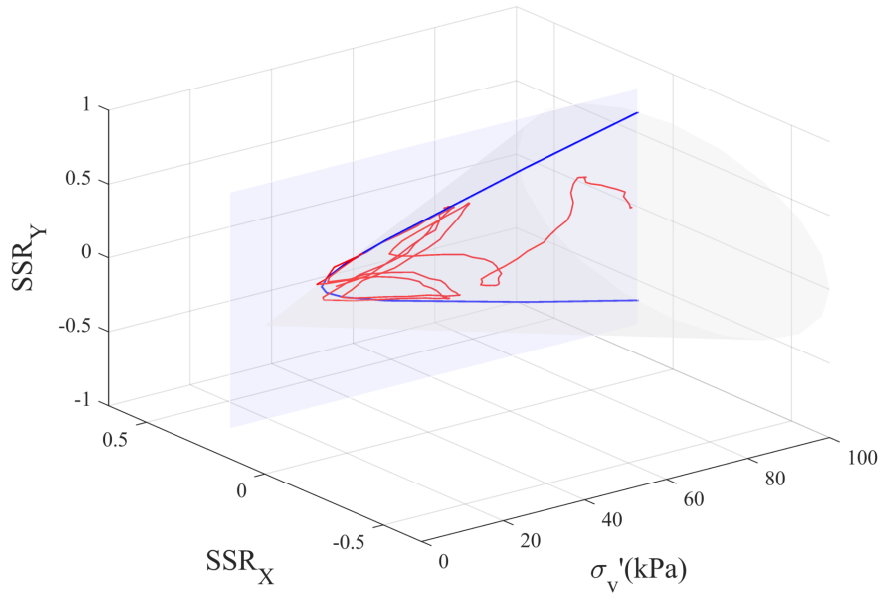

Fig. 6.6 The stress path of test Bilinear-8 and hyperbolic conic section in 3D $\tau - \sigma_v'$ space

cone. When its stress path reaches the failure cone, the circular loading has no choice but to stay on the conical surface and develops along a circular route. It is impossible to go beyond that point with such a loading condition.

Test C20-X20-1, by contrast, has static shearing towards the positive X direction. The part of the stress path that has high SSR_X values and is closer to the conical failure surface is restricted by the failure cone, while the other side of the stress path which has low SSR_X values has more freedom to develop towards the origin.

The stress paths of the oval test and the figure-8 test also support this conclusion. The co-vertices of the oval loading path and the junctions in the figure-8 test obviously have lower shear stress values. The failure states corresponding to these special points, therefore, always develop higher excess pore pressure and are closer to the origin.

Recalling the projections of stress paths onto X and Y directions as presented in Figure 5.22, 5.23, 5.26, and 5.29, it should be emphasized again that the information regarding the spatial structure of stress paths is lost in the process of projection, and the effects of the shape of loading paths cannot be interpreted comprehensively from the projections. Stress-path

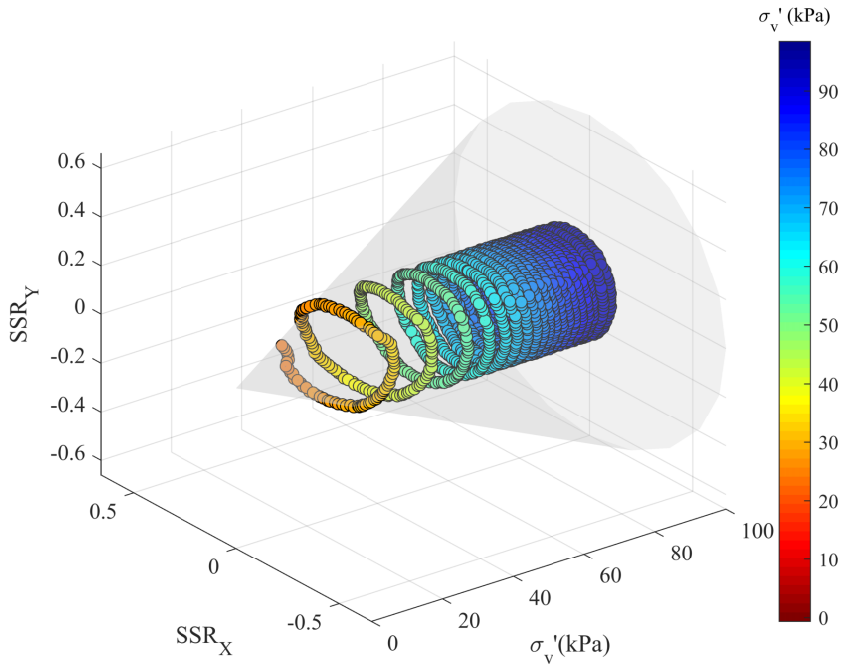

Fig. 6.7 The stress path of circular test C20-3 in 3D $\tau - \sigma_v'$ space

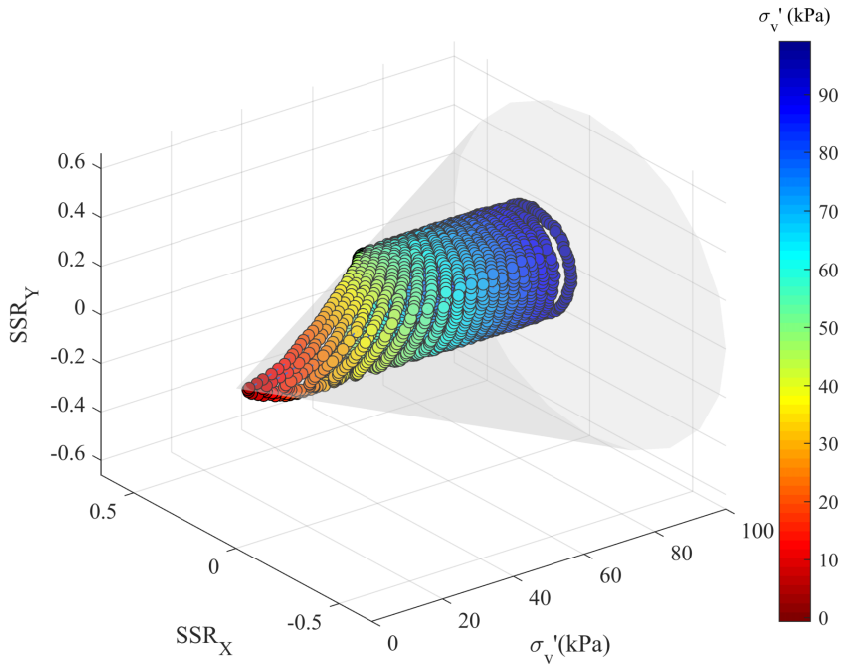

Fig. 6.8 The stress path of circular test C20-X20-1 in 3D $\tau - \sigma_v'$ space

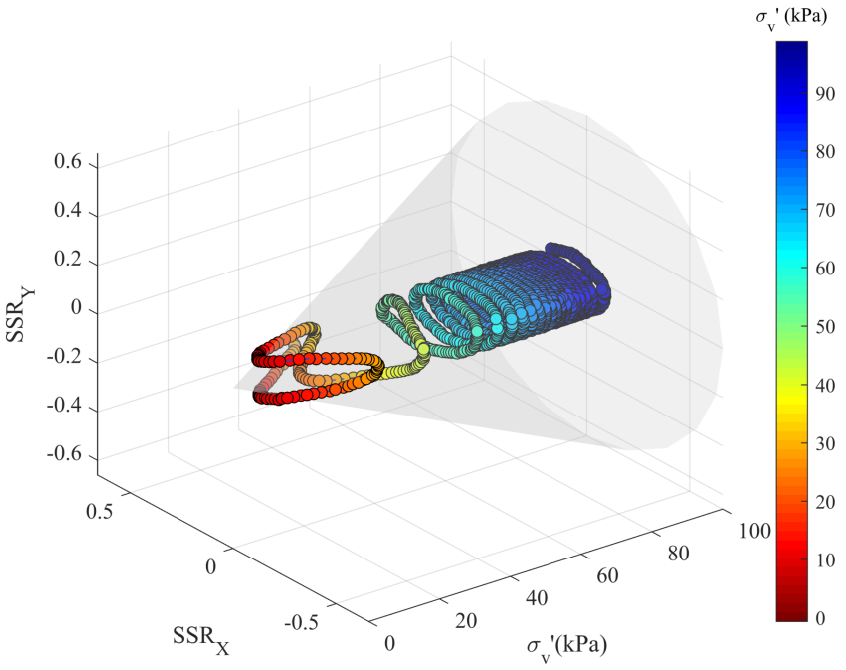

Fig. 6.9 The stress path of circular test E2010-1 in 3D $\tau - \sigma'_v$ space

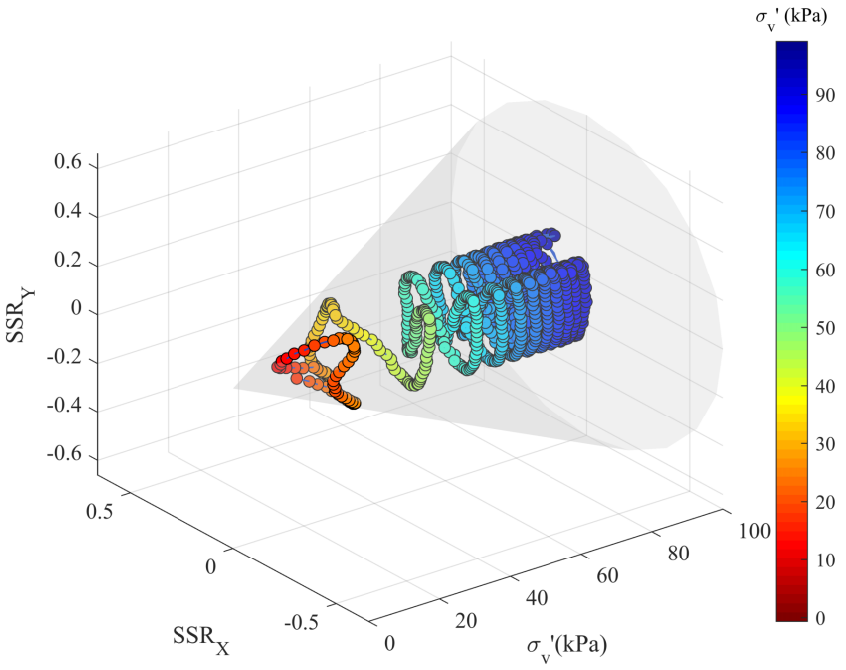

Fig. 6.10 The stress path of circular test F8-3 in 3D $\tau - \sigma'_v$ space

analysis in three-dimensional $\tau - \sigma_v'$ space should be preferred, with the projections as a supplement to enhancing the understanding of spatial stress paths.

6.1.3 Determination of failure states with failure cone

Through the analysis of the failure states of linear tests, bi-directional linear tests and multi-directional tests, a general method to determine the failure envelope can be established in $\tau - \sigma_v'$ space under the framework of the failure cone.

The failure state envelope corresponding to a specific loading path can be predicted by projecting the loading path in the $\tau_X - \tau_Y$ plane onto the conical failure surface, which can be described by:

$$\begin{cases} {\tau_X}^2 + {\tau_Y}^2 = {\sigma_v'}^2 \tan^2 \phi_{FL} \\ g(\tau_X, \tau_Y) = 0 \end{cases} \tag{6.7}$$

where X and Y represent any two orthogonal directions arbitrarily assigned, and $g(\tau_X, \tau_Y)$ gives a cylinder or a plane intersecting the envelope of a certain loading path along the axis of cone.

For uni-directional linear tests, a loading path is a line segment, from which a axial section plane can be constructed as $g(\tau_X, \tau_Y) = \sqrt{\tau_X^2 + \tau_Y^2} - \tau_{dir} = 0$ with the subscript dir indicating the direction of loading. The failure envelope reduces to the uni-directional Mohr-Coulomb failure criterion, $\tau_{dir} = \sigma_v' \tan \phi_{FL}$.

In bi-directional linear tests, loading paths are also in the shape of a line segment, but the plane constructed from it does not contain the axis of cone. To simplify the calculation, the direction of cyclic loading is assigned as direction Y, and the orthogonal direction is designated as X, so that the plane function has $g(\tau_X, \tau_Y) = \tau_X^2 - \tau_{static}^2 = 0$ and the failure envelope becomes the hyperbola expressed by equation 6.4.

For circular loading scenarios, the equation of a cylinder can be built from the loading path following $g(\tau_X, \tau_Y) = (\tau_X - \tau_{X0})^2 + (\tau_Y - \tau_{Y0})^2 - r^2 = 0$, where r represents the radius of the loading-path circles or the amplitude of applied shearing. Equation 6.7 needs to be solved

in polar coordinates for general circular loading paths as $(\tau_{X0} + r \cdot \cos t)^2 + (\tau_{Y0} + r \cdot \sin t)^2 = \sigma_v'^2 \tan^2(\phi_{FL})$.

Parametrization needs to be conducted to attain solutions of equation 6.7 for more general type of loading paths. Numerical methods are required when necessary. In general, equation 6.7 provides a fundamental method to locate the failure states of a loading path, with which a more specific failure criterion can be established for multi-directional shearing.

6.2 Phase transformation in 3D $\tau - \sigma_v'$ space

Since the 1970s when Ishihara et al. (1975) observed the existence of phase transformation in undrained tests on medium to dense sands, it has attracted intense interest among geotechnical researchers and engineers. The phenomenon of phase transformation, which is commonly described as the stress state where excess pore pressure turns from growing to declining with the increase of shearing, is observed and reported in almost every experimental work conducted on undrained sands. Recent development of discrete element modelling method has also contributed to the understanding of this phenomenon. Although the mechanisms behind it is still unclear, it is widely accepted nowadays that phase transformation states form a line in 2D $\tau - \sigma_v'$ space, whose angle is lower than that of failure line and affected by the state parameter and stress states of sands.

A natural inference arises from the similarity between phase transformation line and failure line: since the failure line can be extrapolated to a failure cone in 3D $\tau - \sigma_v'$ space, the same extrapolation should be applicable to phase transformation line as well. If such a hypothesis can be proved, a phase transformation cone should exist in 3D $\tau - \sigma_v'$ space following:

$$\tau_{total} = \sigma_v' \tan \phi_{PT} \tag{6.8}$$

where ϕ_{PT} is the angle of phase transformation line measured from uni-directional tests. Sands should exhibit contractive tendenies when shear stress paths are inside this cone and turn to show dilative tendencies after crossing outside the cone. The aim of this section is to

investigate the hypothesis of conical phase transformation surface with the testing data in this study.

6.2.1 The validity of phase transformation cone in multi-directional tests

When the data of circular, oval and figure-8 tests were analysed in Chapter 5, the concept of phase transformation cone had already been applied explicitly and tentatively without demonstration. In fact, the ability of the assumed phase transformation cone in explaining effectively the soil behaviour under these multi-directional loading scenarios is an important indicator of its validity.

In the first instance, the results of test C20-X20-1 are recalled: excess pore pressure peaks vary significantly among cycles as shown in Figures 5.16 and 5.17. This intriguing phenomenon was explained with a phase transformation line in $SSR_{total} - \sigma_v'$ plot in Figure 5.18. On the one hand, it is conspicuous that the suggested phase transformation line divides the stress space into two regions. Before the phase transformation line is reached, the increase of total shear stress decreases effective vertical stress as expected in typical contractive sand behaviour. After it is passed through, the increase of total shear stress results in the increase of effective vertical stress, which is consistent with the dilative tendency appearing due to phase transformation. It is evident that this line holds the characteristics of phase transformation. On the other hand, the total shear stress values of the assumed phase transformation line can be pinned on the polar loading path as presented in Figure 5.17(a). The corresponding angular coordinates obtained coincide perfectly with the locations of peak excess pore pressure in Figure 5.17(b). It is demonstrated that the phase transformation hypothesis is capable of providing spatial information about the peaks of excess pore pressure.

Although the existence of such a phase transformation line was in fact a hypothesis rather than a validated theory, the results of test C20-X20-1 support its role. Considering that the phase transformation line in Figure 5.18 is the graphical reflection of equation 6.8, it can be concluded that a phase transformation cone exists, at least in test C20-X20-1.

The hypothesis can be examined further in 3D $\tau_{total} - \sigma'_v$ space. Figure 6.11a presents the 3D stress path of test C20-X20-1 together with the failure cone and the phase transformation cone. The data points outside the phase transformation cone are marked with circles and coloured by the variation of effective vertical stress, with blue indicating the effective vertical stress of this point is smaller than that of the previous point and red otherwise. Loading proceeds clockwise, which can be told from the initial part of the stress path that has the highest σ'_v. When the stress path moves outside the phase transformation cone, the trend of effective vertical stress is reversed, reflected in both the swerve of the stress path and the change of data points' colour from blue to red. At the maximum SSR_X, shearing changes from loading to unloading, resulting in another abrupt change in the development of effective vertical stress.

Figure 6.11b shows the same stress path in a different way. All the data points after stress path emerges from phase transformation cone for the first time are highlighted. While the data points outside the phase transformation cone are still marked with circles, points inside the cone are marked with diamonds. The colours have new meanings. For the points inside the cone, if effective vertical stress of a point is lower than previous one, that is, excess pore pressure keeps increasing, the point is in agreement with the typical behaviour inside the phase transformation and coloured blue; otherwise, it is coloured red to indicate atypical behaviour. For the points outside the phase transformation cone, however, if the increase of total shear stress results in the increase of effective vertical stress, or the unloading of shear reduces the effective vertical stress, the points are coloured blue to suggest that the typical post-phase-transformation behaviour is occurring; the points become red if such a behaviour is not observed. In other words, blue points support the phase transformation cone hypothesis while red points do not.

Red points are dispersed in the early cycles where excess pore pressure is relatively low or moderate. This is similar to the fluctuation of excess pore pressure seen in the initial part of uni-directional simple shear tests. Since the oscillation is not steady or repeating with a clear pattern, the odds are that it is caused by the imperfect control of the testing apparatus or sensor noise instead of some law of soil mechanics. In the last few pre-liquefaction cycles,

however, red points become rare, indicating the phase transformation cone hypothesis is satisfied almost everywhere on the loading path.

The test results of oval tests and figure-8 tests also support the hypothesis of a phase transformation cone. The stress path of oval test E2010-1 is presented in Figure 6.12 in the same manner as Figure 6.11. After stress path passes through the conical phase transformation surface, the increase of shear loading bends the stress path away from origin. When checking the discrepancy between the hypothesis and measured data in Figure 6.12b, test data agrees closely with the hypothesis, demonstrating the existence of phase transformation cone in oval tests. Shown in Figure 6.13 is the results of test F8-3 which has a figure-8 shaped loading path. The visually indistinguishable division between loading and unloading periods of such loading path hinders judgement-making based on the variation of effective vertical stress in Figure 6.13a. But an inspection of Figure 6.13b reveals that the measured data from this test show great consistency with the hypothesized phase transformation cone.

In conclusion, the existence of a phase transformation cone can be proved in multi-directional shearing conditions with the testing data in this study. Inside the cone, sand exhibits contractive tendencies, and both loading and unloading in terms of total shear stress results in the increase of excess pore pressure. Outside the cone, by contrast, sand shows dilative tendencies with further loading and excess pore pressure turns to decrease with the increase of total shear stress; in unloading period, however, the dilation-like behaviour is inhibited and excess pore pressure increases again. The analysis of undrained multi-directional testing results should take both failure cone and phase transformation cone into consideration so that a more comprehensive understanding of soil behaviour can be developed.

6.2.2 The invalidity of phase transformation cone in bi-directional linear tests

Although the concept of phase transformation cone has been applied successfully in multi-directional loading scenarios including circular, oval and figure-8 shaped loading paths, it is

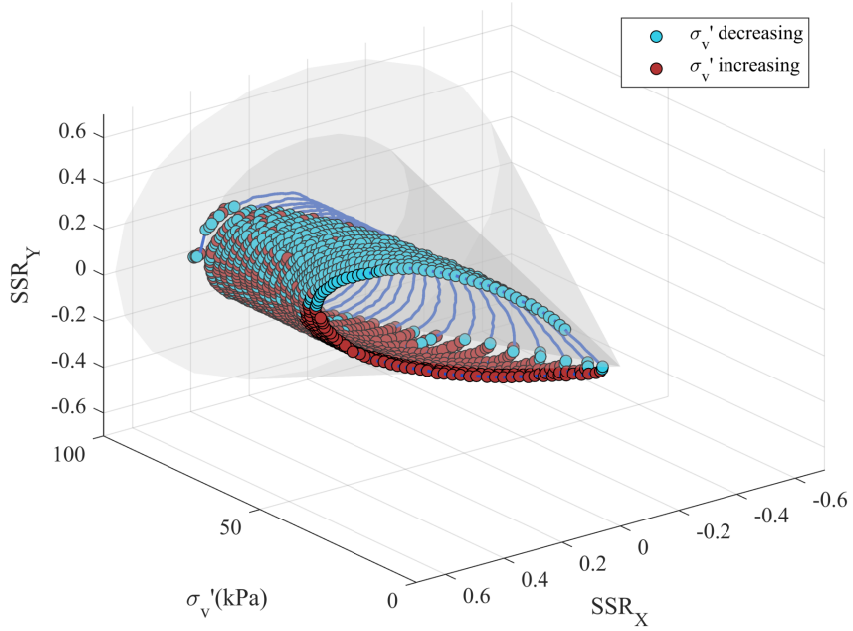

(a) The variation of effective vertical stress of the points outside the hypothesised phase-transformation cone

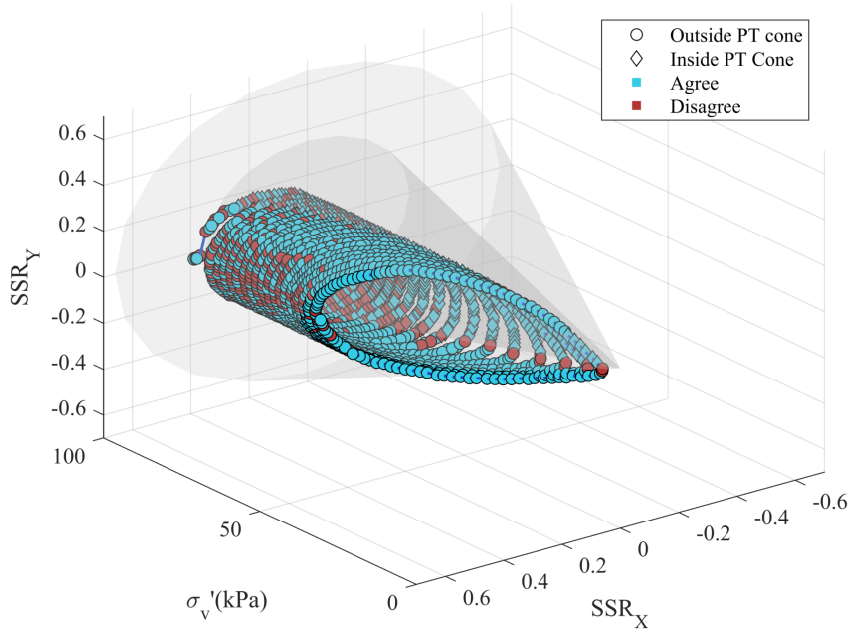

(b) The agreement between test data and the phase-transformation cone hypothesis (for points inside the hypothesised PT cone, agreement is achieved if σ_v' decreases with both loading and unloading; for points outside the PT cone, agreement is achieved if σ_v' increases during loading or decreases during unloading)

Fig. 6.11 The verification of phase-transformation cone hypothesis with 3D stress path of test C20-X20-1, with the outer cone indicating failure cone and the inner one representing the hypothesised PT cone

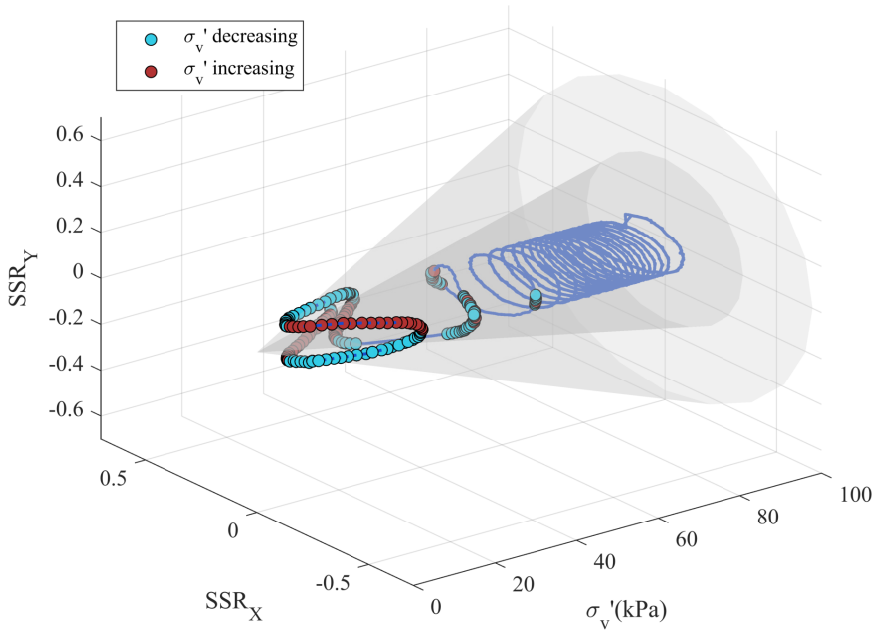

(a) The variation of effective vertical stress of the points outside the hypothesised phase-transformation cone

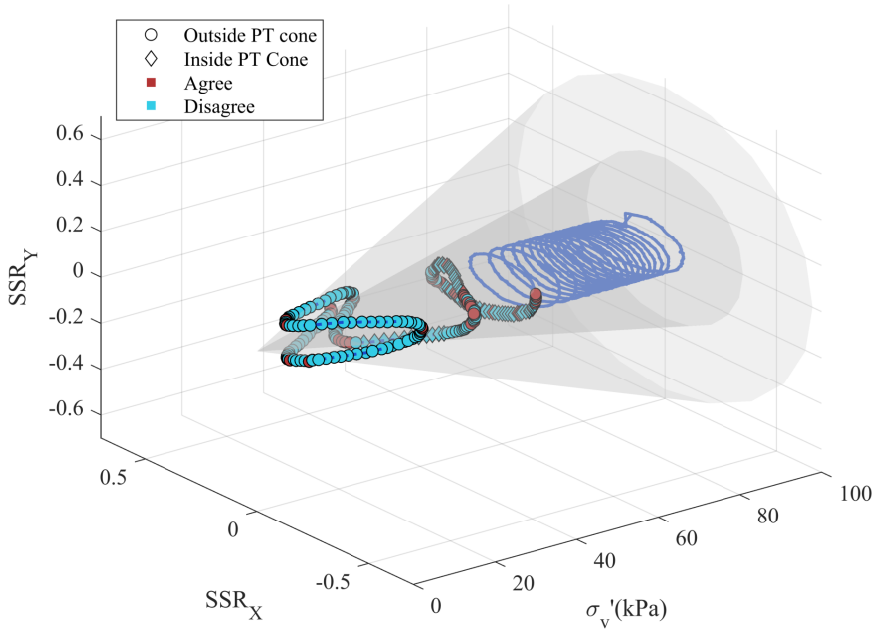

(b) The agreement between test data and the phase-transformation cone hypothesis (for points inside the hypothesised PT cone, agreement is achieved if σ_v' decreases with both loading and unloading; for points outside the PT cone, agreement is achieved if σ_v' increases during loading or decreases during unloading)

Fig. 6.12 The verification of phase-transformation cone with 3D stress path of test E2010-1, with the outer cone indicating failure cone and the inner one representing the hypothesised PT cone

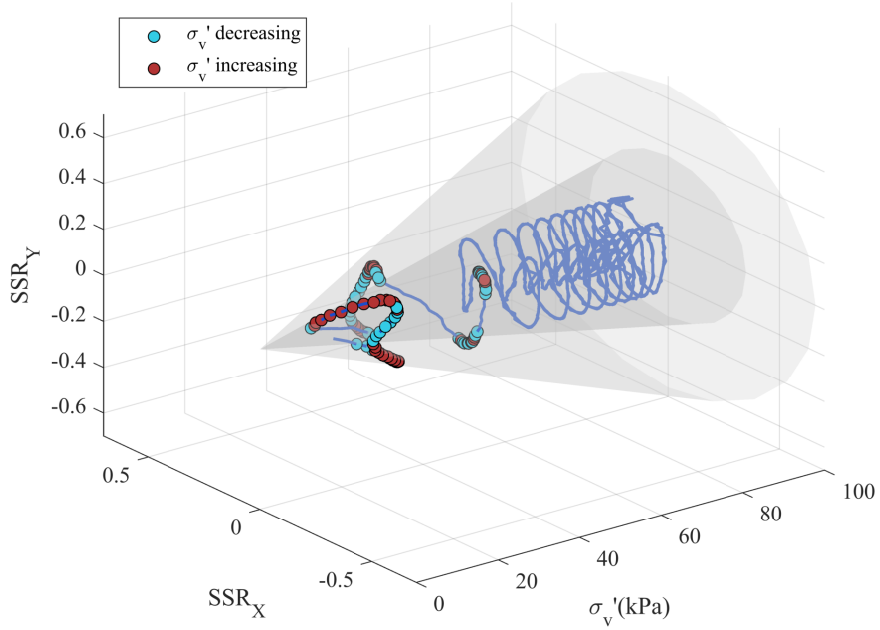

(a) The variation of effective vertical stress of the points outside the hypothesised phase-transformation cone

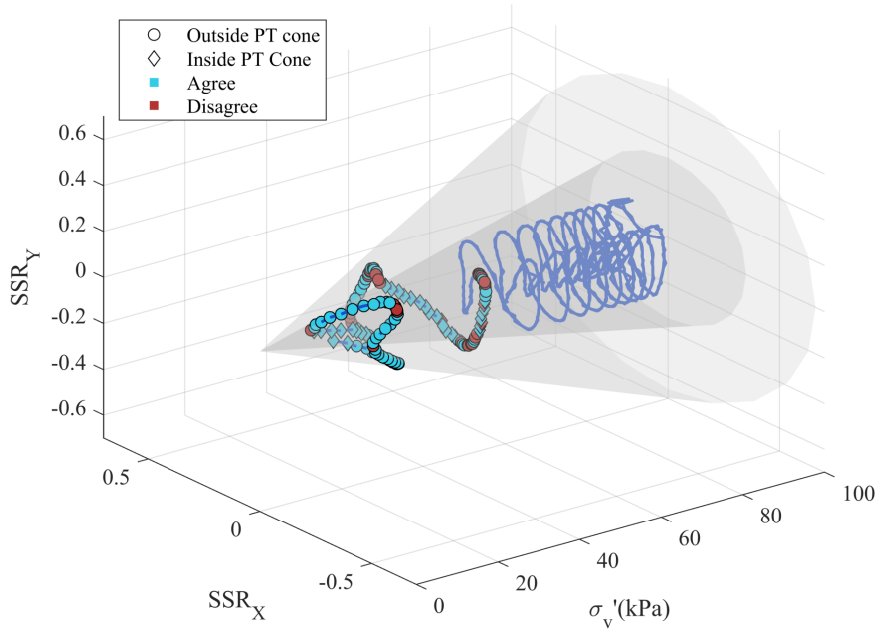

(b) The agreement between test data and the phase-transformation cone hypothesis (for points inside the hypothesised PT cone, agreement is achieved if σ_v' decreases with both loading and unloading; for points outside the PT cone, agreement is achieved if σ_v' increases during loading or decreases during unloading)

Fig. 6.13 The verification of phase-transformation cone with 3D stress path of test F8-3, with the outer cone indicating failure cone and the inner one representing the hypothesised PT cone

still imprudent to take it for granted that such a cone must exist in bi-directional linear tests. In fact, a careful examination of bi-directional linear tests brings different results.

As elucidated in the preceding section, the 3D stress path of a bi-directional linear test is contained in a plane whose distance from σ_v' axis or the axis of cone equals to static shear stress. The 3D stress paths can thus be analysed in that plane through scrutinizing strike-direction cyclic shearing. The intersection between this plane and a cone gives a hyperbolic conic section. The conic section produced by the failure cone being intersected forms the failure envelope on this plane, which can be derived from the geometry as equation 6.4. Similarly, should a phase transformation cone exist in bi-directional linear tests, a hyperbolic phase transformation envelope could be delineated by:

$$tan^2(\phi_{PT})\frac{\sigma_v'^2}{\tau_{static}^2} - \frac{\tau_{cyclic}^2}{\tau_{static}^2} = 1 \tag{6.9}$$

If a stress path escapes from this hyperbola and enters the space between it and the failure envelope, sand is expected to exhibit dilative tendencies with increase of shear stress resulting in the decrease of excess pore pressure.

The strike-direction stress paths of test Bilinear-6, Bilinear-7 and Bilinear-8, which were shown in Figure 5.5a, are replotted in Figure 6.14. The failure envelopes of the tests are calculated with measured minimum static shear stress in dip direction and are represented by solid hyperbolas, while the hypothesized phase transformation envelopes are indicated by dashed ones. Minimum static shear stress is used as the representative value in the calculation to provide the largest hyperbolic conic section and account for the influence of the fluctuations of static shearing. The hyperbolas are differentiated by grayscale. The higher the number in test name, the darker the hyperbolas.

Since the three tests have the same target value of α, their stress-path planes are roughly identical, as are their failure envelopes. The success of the failure envelopes in enclosing the stress paths validates again the existence of a failure cone.

The assumed phase transformation envelopes, however, fail to envelop the turning points on the stress paths. In test Bilinear-6 (blue curve), for instance, the loading period in negative SSR_{strike} side clearly reduces the effective vertical stress, which is the typical soil behaviour

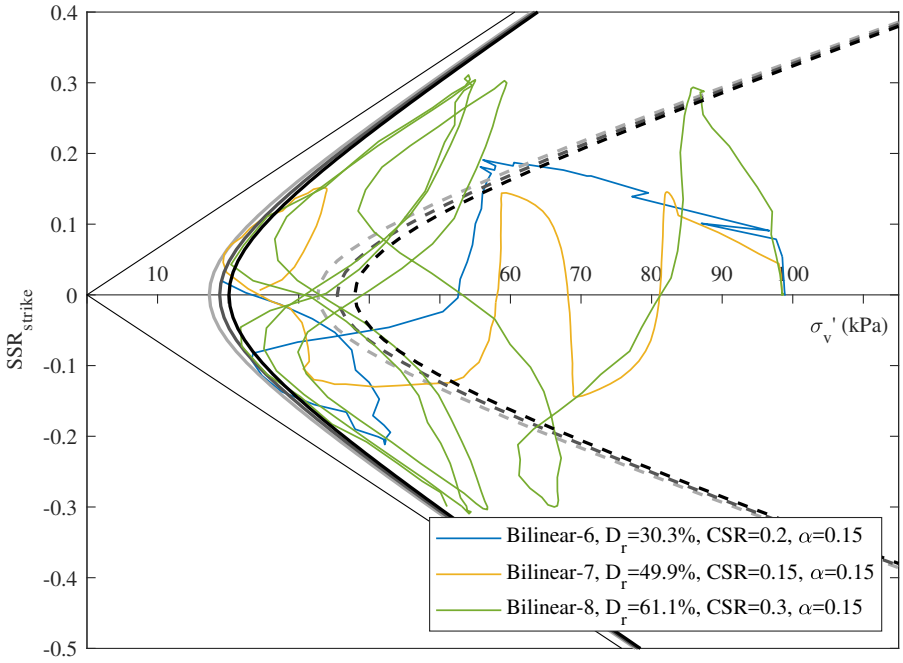

Fig. 6.14 The strike-direction stress paths of test Bilinear-6, Bilinear-7 and Bilinear-8, with hyperbolic failure envelopes and hypothesized hyperbolic phase-transformation envelopes (the hyperbolas are differentiated by grayscale: the higher the number in test name, the darker the hyperbola)

before the phase transformation is reached. Similar phenomenon is also observed in the other two tests. The significant inconsistency impairs the effectiveness of phase transformation cone, and the application of this concept in bi-directional linear tests becomes dubious.

The results of test Bilinear-4, Bilinear-5 and Bilinear-13 are presented in a similar manner in Figure 6.15. The static shear stress ratios of the three are 0.075, 0.12 and 0.3, respectively. The locations of the planes containing the stress paths of these tests are thus different, but such a variation does not alter the observation that the phase transformation cone hypothesis cannot be applied successfully in bi-directional linear tests. There is no recognised relationship between the turning points on the stress paths and the hyperbolas.

The stress path of an example bi-directional linear test (ms50cyck) from Kammerer (2002) are modified and presented in Figure 6.16. The values of $\tan\phi_{FL}$ and $\tan\phi_{PT}$ are determined

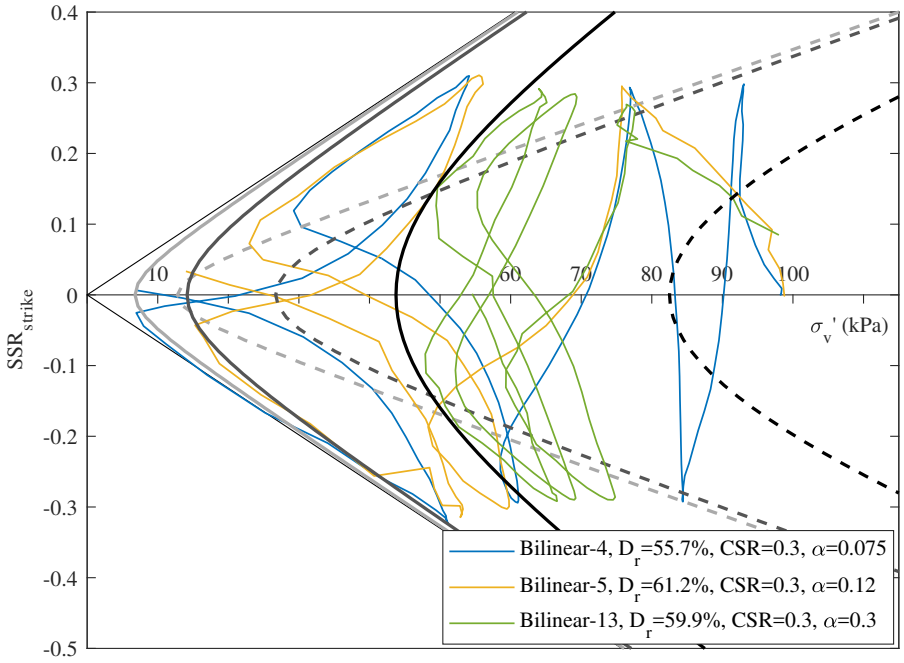

Fig. 6.15 The strike-direction stress paths of test Bilinear-4, Bilinear-5 and Bilinear-13, with hyperbolic failure envelopes and hypothesized hyperbolic phase-transformation envelopes (the hyperbolas are differentiated by grayscale: the higher the number in test name, the darker the hyperbola)

from the uni-directional tests conducted by Wu (2002), at 0.59 and 0.248, respectively. The failure envelopes of this test do not coincide perfectly with the predicted hyperbola, but this is acceptable considering Kammerer used different sample preparation techniques and data processing methods. Like test Bilinear-13 in this study, test ms50cyck of Kammerer (2002) also holds a large α that prohibits the development of high excess pore pressure. The tendency of stress path stacks eventually along a hyperbolic boundary demonstrates qualitatively that a failure cone must exist. As for phase transformation states, by contrast, it is evident that the dashed PT hyperbola cannot locate the stress-state points where phase transformation takes place.

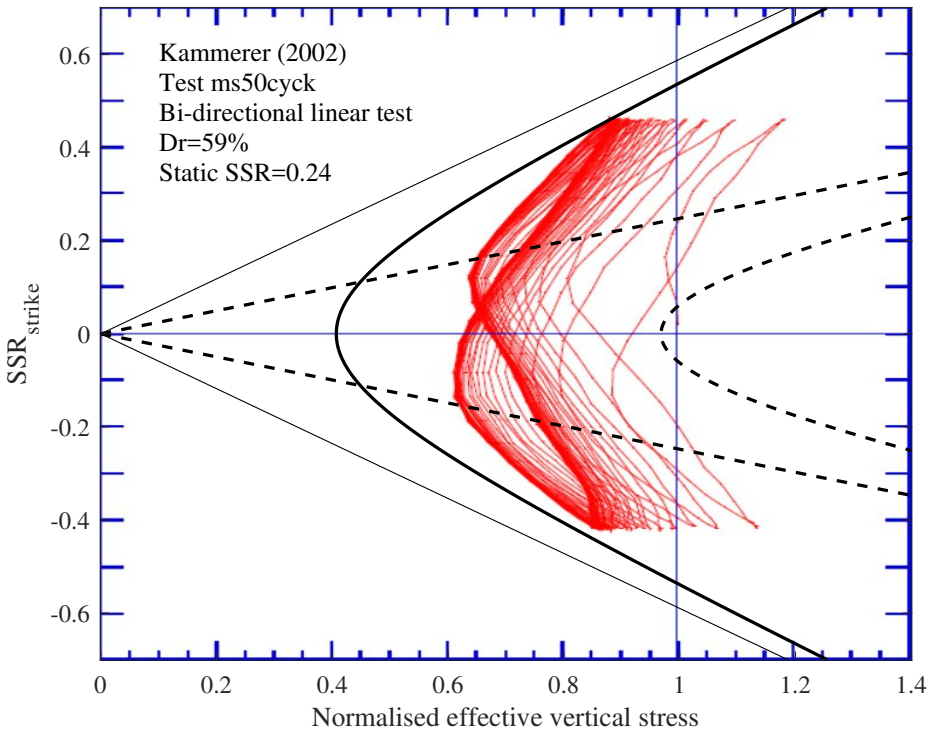

Fig. 6.16 The stress path of bi-directional linear test ms50cyck from Kammerer (2002), modified to include hyperbolic failure envelope (solid), hypothesized phase transformation hyperbola (dashed) and phase transformation lines (dashed).

In conclusion, test results suggest that the concept of phase transformation which was applied successfully in multi-directional tests becomes ineffective under bi-directional linear loading scenarios.

6.2.3 Discussions on the phase transformation in multi-directional loading conditions

The examination of the test results in this study revealed a bimodal feature of the phase transformation surfaces in 3D $\tau - \sigma_v'$. In multi-directional loading condition, phase transformation stress states form a conical surface that is analogous to the failure cone. Under uni-directional or bi-directional linear loading scenarios, however, the hypothesis of phase transformation cone is not valid.

Unfortunately, there has not been a model that can explain this phenomenon and match existing test data. But the observations in this study still has some implications worthy of discussions.

Firstly, it is confirmed that the multi-directionality of loading paths can affect the phase transformation of sands. Conventional analysis methods that ignore the geometry of the loading paths cannot provide thorough information about the response of soil under multi-directional loading conditions. The interpretation of undrained soil behaviour should be conducted with loading paths taken into consideration to avoid deceptive or misleading conclusions.

Secondly, the bimodal phenomenon of phase transformation raises more questions about the mechanisms of phase transformation. On the one hand, the existence phase transformation cone in the circular, oval and figure-8 tests suggests that phase transformation is comparable to failure in the sense that they both hold the characteristics of friction. On the other hand, differently from the failure surface that is always a cone, phase transformation surface (or surfaces) cannot be determined unless the loading path is known. Phase transformation appears to be a type of soil behaviour that is similar to friction but not identical to it.

While the mechanics of phase transformation remains unclear, a potential explanation is proposed here based on the observations from this study. Sands are a type of heterogeneous granular materials that exhibit pronounced elasto-plastic behaviours. Huge plastic deformation can happen to accommodate the stress applied to it. But frictional behaviour is not enabled unless localized deformation happens, that is, shear bands appear in the profile of soil. Failure happens when the shear bands in soil develop to the state that a soil profile is partitioned by it, with which unlimited deformation is allowed to accumulate. In drained tests, the formation of shear bands results in localized increase of volume. In undrained tests, it results in the dilative tendencies of phase-transformed soil behaviour. The formation of shear bands is not immediate, instead, it takes time. If the end of this process is failure, the start is likely to be phase transformation.

There is no intention to investigate in depth the details of shear bands or the mechanisms of phase transformation in this work. But the existence of shear bands reminds us to reassess

the situation when loading is applied in a multi-directional manner. It is likely that shear bands will not be plenary in multi-directional loading conditions, which, if verified, may throw light on the discrepancies observed in this study. Further exploration can be conducted to advance the understanding of phase transformation, especially under multi-directional loading scenarios.

Chapter 7

THE EFFECTS OF MULTI-DIRECTIONAL SHEARING ON SOIL LIQUEFACTION

Multi-directional simple shear tests differ from uni-directional tests in various aspects, among which one of the most prominent is seen in the pattern of the development of shear stress and shear strain. The multi-directionality of loading paths clearly poses challenges to the definition of shear stress and shear strain.

Shear stress and strain defined in a certain direction (denoted by subscript dir as in τ_{dir} and γ_{dir} in this study) can help in examining the soil behaviour in a certain direction or at a certain time point on a loading sequence. But the cost is that the information about other directions or time points cannot be extracted and a comprehensive perspective is lost. Although resultant shear stress and strain (represented by subscript $total$ as in τ_{total} and γ_{total}) takes directionality into account and provides a big picture of soil behaviour, it cannot give information about how shear stress and strain are distributed physically.

The issues regarding the definition of shear stress and strain impairs significantly the effectiveness of the conventional liquefaction analysis framework that has been widely accepted in liquefaction research with uni-directional simple shear tests. The liquefaction criterion based on double-amplitude shear strain needs modifications to account for the multi-directionality

of shear strain. Liquefaction resistance estimated from $N_L - CSR$ (number of cycles to liquefaction versus cyclic shear stress ratio) curves becomes problematic, since cyclic shear stress ratio cannot be defined consistently due to the existence of multi-directionality. The pronounced non-coaxiality between shear stress and shear strain makes the problem even more complex. Shear stress-strain hysteresis loops cannot be plotted conveniently because the stress-strain relationships now become four-dimensional and, correspondingly, shear modulus determined from stress-strain curves is no longer effective, which weakens the effectiveness of the the models based exlusively on shear modulus.

To the best of the author's knowledge, there have not been expedient analysis tools or stress and strain definitions that can extrapolate the uni-directional analysis framework to multi-directional scenarios in a compatible manner, partly because the data of multi-directional tests are still too scarce to develop such tools and also partly because the effects of multi-directional loading has not been extensively explored. With increasing efforts being made to investigate the effects of multi-directional loading in recent years, these problems are gradually becoming more prominent. Therefore, a discussion about these issues is covered in this chapter with the objective of summarizing the insights from this study and providing suggestions for research in the future.

7.1 Liquefaction criterion for multi-directional simple shear tests

In chapter 4 and Chapter 5 where the test results in this study were presented, the occurrence of liquefaction was defined as shear stress path in any direction reaching the failure line. With the concept of failure cone introduced later, this criterion can be rephrased such that liquefaction takes place when the conical failure surface is reached by multi-directional shear stress paths. Such a liquefaction criterion is effective in analysing the soil behaviour in stress space since it defines liquefaction directly as the failure envelope being reached. But in practice, it may be more convenient to relate the implicit failure to other measurable

parameters such as excess pore pressure and shear strain, as conducted in the two most widely accepted categories of liquefaction criterion.

The excess pore pressure ratio based liquefaction criterion defines the occurrence of liquefaction as excess pore pressure ratio reaching unity. This criterion is extensively adopted in liquefaction-related laboratory research including both element-level tests and physical modelling tests. However, the test results of this study indicate that the application of such a criterion is not as straightforward as expected. The maximum excess pore pressure is affected by the multi-directional loading conditions because the conical failure surface constrains the ultimate development of shear stress paths. An excess pore pressure ratio of unity is thus not achievable in all categories of loading paths. In fact, whether this criterion is applicable in uni-directional simple shear tests is also questionable even though it has been widely used in existing research. If a testing apparatus cannot provide perfect loading control and have shear stress in other directions, which is rather typical or just inevitable when the stiffness of a sand sample is reduced dramatically, the loading scenario becomes bi-directional or multi-directional and the maximum excess pore pressure ratio should not reach unity.

Since the maximum excess pore pressure ratio under a loading scenario can be estimated from the failure cone, a potential modification of the r_u-based liquefaction criterion is to define liquefaction as excess pore pressure ratio reaching certain theoretical values. When the maximum excess pore pressure ratio reaches the value given by equation 5.4, liquefaction can be considered as occurring. However, the existence of static shearing also influences the maximum excess pore pressure ratio generated. When static shearing is so high that stress reversal is eliminated, maximum excess pore pressure can fall below the theoretical values, with the mechanism still unclear. Therefore, the r_u-based liquefaction criterion should be addressed separately when a high level of static shearing is applied.

Alternatively, liquefaction can be correlated to a certain level of shear strain, as discussed in Chapter 3. The strain-based liquefaction criterion also needs reassessment under multi-directional loading scenarios because shear strain can be defined now in different ways. In the first instance, the development of total shear strain γ_{total} with the number of cycles is presented in a semilogarithmic manner in Figure 7.1. The γ_{total} here refers to the maximum total shear

strain in a cycle. In uni-directional tests, γ_{total} becomes equivalent to the maximum absolute amount of shear strain achieved in a cycle. The blue dashed line represents $\gamma_{total} = 3\%$, the liquefaction criterion proposed by Ishihara and Yamazaki (1980). When γ_{total} exceeds 3%, 39 of the 75 cyclic tests reach liquefaction, as seen in most of the curves turning to proceed vertically after passing through the blue dashed line. One test (F8-7) liquefies before γ_{total} grows to 3%, but it is counted in the 39 tests because it is reasonable to expect γ_{total} in this test to reach 3% with one more shearing cycle. The other 36 tests, however, cannot liquefy with $\gamma_{total} = 3\%$. The four dash-dotted tests need a large amount of shearing cycles to initiate liquefaction after total shear strain exceeds 3%. Test LS6 needs up to 45 more cycles to trigger liquefaction. It demonstrates the criterion of Ishihara and Yamazaki (1980) is not able to envelope the liquefaction failure in all the tests in this study, and remarkable discrepancy in terms of liquefaction resistance can arise from it.

An attempt to modify this criterion can be made through adjusting the total shear strain level. The red dashed line in Figure 7.1 examples a modified criterion requiring $\gamma_{total} > 6\%$. Although the increase in required strain level makes it applicable to more tests (61 out of 75), there are still 14 tests that cannot reach liquefaction under this criterion, with the largest discrepancy in terms of N_L shrinking to 3 cycles. It appears that γ_{total} based criterion is not particularly effective, if at all, in determining the occurrence of liquefaction. The tests which do not fit the criterion are mainly those involving initial static shearing. Recalling the results of test LS7, LS10 and C20-X20-1 presented in Figure 4.12, 4.16 and 5.18, considerable shear strain (far more than 3%) can accumulate towards the direction of initial static shearing without the stress path reaching the failure line. There is clearly a possibility that the contribution of static-shear induced shear strain to γ_{total} is so large that a γ_{total}-based liquefaction criterion is severely biased and misleading. Thus, liquefaction criterion is not recommended to be established on γ_{total}.

To overcome the incompatibility associated with initial static shearing, a double amplitude strain level can be used conveniently in uni-directional tests, but whether the concept of double amplitude is applicable to multi-directional tests remains unclear. Two types of double amplitude shear strain are constructed in this study and examined: $\gamma_{total,DA}$ and $\gamma_{dir,DA}$.

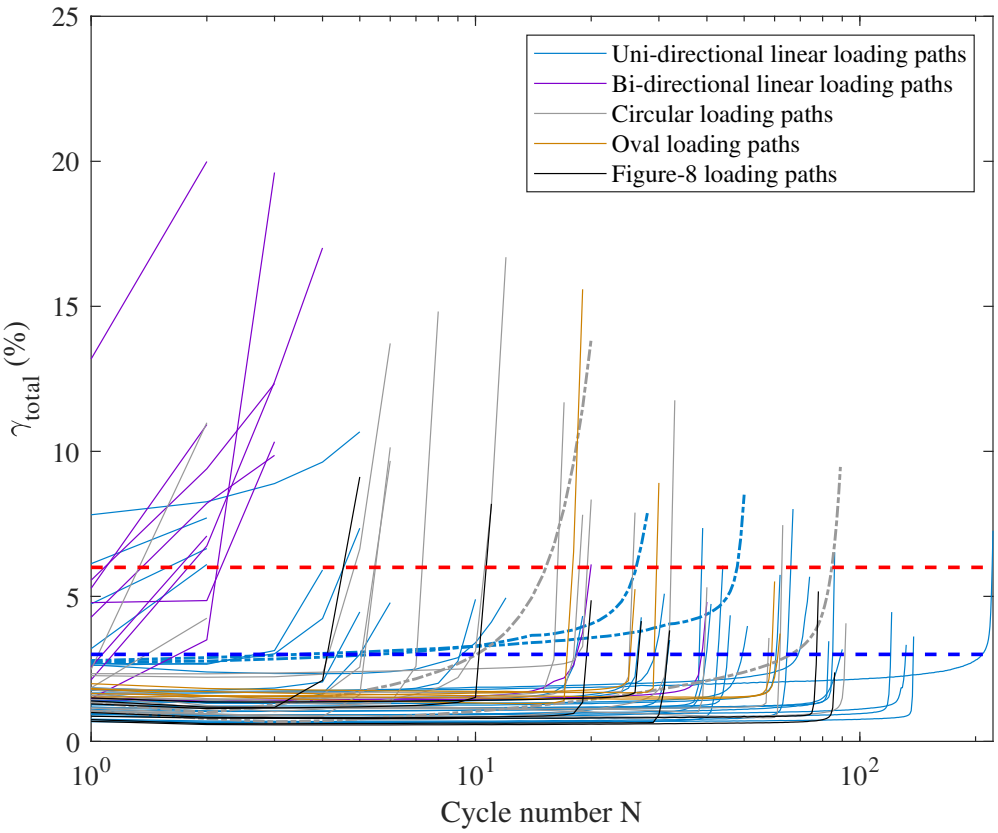

Fig. 7.1 The development of γ_{total} with cycle number in all tests in this study

$\gamma_{total,DA}$ is the difference between the maximum γ_{total} and minimum γ_{total} in a cycle. It is termed "double amplitude total shear strain" because it adopts a calculation method similar to γ_{DA} in uni-directional tests, though it does not necessarily refer to the actual "double amplitudes" of total shear strain. $\gamma_{total,DA}$ is not equal to the increase of γ_{total} between cycles, and the contribution of the strain components induced by static shearing and cyclic shearing to γ_{total} cannot be distinguished. Qualitatively, when the excess pore pressure is relatively low, both the static-shear induced strain increment and cyclic-shear induced strain increment are roughly constant in a cycle, and $\gamma_{total,DA}$ is supposed to remain small and change little. When liquefaction is approached, static-shear induced strain and the cyclic-shear induced strain will both increase rapidly, resulting in a swift growth of $\gamma_{total,DA}$. Thus, a potential liquefaction criterion can be built based on $\gamma_{total,DA}$.

Figure 7.2 presents the development of $\gamma_{total,DA}$ with cycle number for all the tests conducted in this study. A red dashed line is plotted to represent $\gamma_{total,DA} = 3\%$. The strain level of 3% is selected to make this criterion equivalent to single amplitude shear strain of 3% in uni-directional loading scenarios. 7 tests liquefy before $\gamma_{total,DA}$ reaches 3% but are expected to meet the criterion with one more shearing cycle. 19 tests cannot liquefy when $\gamma_{total,DA}$ exceeds 3%, with the largest discrepancy in N_L at 3 cycles (test LS2 and LS4). The deviation is acceptable considering the numbers of cycles to liquefaction of test LS2 and LS4 are 222 and 74. $\gamma_{total,DA}$ in 9 tests exceeds 3% from the initial loading cycle due to overlarge initial static shearing, but liquefaction occurs in a few cycles later (up to 4 more cycles in test LS10). Extra efforts are required to cope with the situation where $\gamma_{total,DA}$ reaches 3% in the initial shearing cycle.

Generally, the performance of $\gamma_{total,DA} = 3\%$ criterion in enveloping liquefaction is satisfactory, but two pronounced drawbacks still remain. Firstly, the physical and mathematical meaning of $\gamma_{total,DA}$ is not straightforward and the relationship between it and the abrupt increase of shear strain is not explicit, from which remarkable inconsistency in liquefaction resistance assessment can arise. Secondly, the calculation of total shear strain can be altered if the zero point of strain is changed. Shear strain measurements are always zeroed before cyclic loading starts in this study, but a ramp loading stage is conducted prior to cyclic loading if cyclic shear stress does not start from zero such as in circular and oval tests. If zero strain is assigned to the point before the ramp loading is applied, $\gamma_{total,DA}$-based liquefaction criterion is likely to give different results. The consistency of applying such a criterion in determining liquefaction resistance is thus not guaranteed.

A convenient method to avoid the influences of the alteration of the zero strain point is to define a strain parameter in a relative manner and $\gamma_{dir,DA}$ is thus proposed to achieve this objective. Subscript dir is used to differentiate it from $\gamma_{total,DA}$ and double amplitude uni-directional shear strain γ_{DA}. $\gamma_{dir,DA}$ amounts to the maximum relative strain between any two strain points within a cycle. Assuming two points γ^i and γ^j on a strain path in a loading

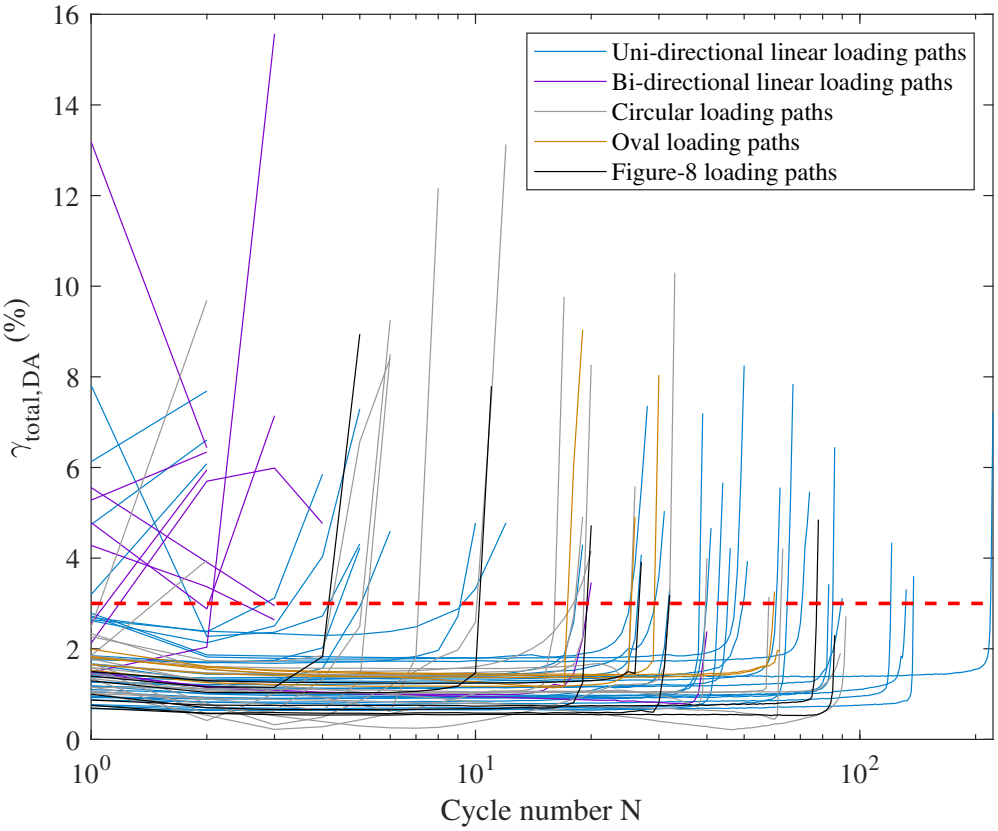

Fig. 7.2 The development of $\gamma_{total,DA}$ with cycle number in all tests in this study

cycle that contains N points, $\gamma_{dir,DA}$ can be defined as:

$$\gamma_{dir,DA} = \max_{i,j=1}^{N} \sqrt{(\gamma_X^i - \gamma_X^j)^2 + (\gamma_Y^i - \gamma_Y^j)^2} \tag{7.1}$$

where X and Y represent two arbitrarily assigned directions that have to be orthogonal, γ_X^i and γ_Y^i represent the projections of the shear strain of ith point in X and Y direction.

Figure 7.3 presents the $\gamma_{dir,DA}$ in each loading cycle in all the tests conducted in this study. The red dashed line gives $\gamma_{dir,DA} = 6\%$ which, in uni-directional tests, is equivalent to the criterion requiring $\gamma_{DA} = 6\%$. Seven out of the 75 tests reach liquefaction before the red dashed line is passed through, but $\gamma_{dir,DA}$ in these tests is expected to exceed 6% with one more cycle since their curves have become almost vertical at liquefaction, suggesting a rapid increase in shear strain after that. Ten tests cannot liquefy when $\gamma_{dir,DA} = 6\%$ is

satisfied; however, liquefaction is initiated with one or two more cycles in 9 of them. It can be concluded that $\gamma_{dir,DA} = 6\%$ is effective in enveloping liquefaction in these tests with only limited inaccuracy in terms of N_L. Compared with the preceding two criteria, the performance of this one is evidently better.

The application of such a criterion in three tests, nevertheless, is problematic. Test LS10 achieves a $\gamma_{dir,DA}$ of 7.8% in the first cycle but liquefaction happens 4 cycles later. $\gamma_{dir,DA}$ in test Bilinear-11 and Bilinear-13 cannot reach 6% and does not increase rapidly at occurrence of liquefaction as other tests. However, the three tests share the common characteristics of $\gamma_{dir,DA}$ decreasing significantly in the second loading cycle. Their first cycle witnesses the accumulation of huge amount of shear strain due to the presence of initial static shearing, but the development of shear strain in the next cycle becomes sluggish, as shown in Figure 4.16 for test LS10. Since such a pattern of shear strain accumulation threatens the use of the $\gamma_{dir,DA}$-based liquefaction criterion, it should be addressed separately if the criterion is applied. However, the effectiveness of this criterion is at least not worse than the widely-accepted uni-directional liquefaction criterion $\gamma_{DA} = 6\%$, given the fact that liquefaction in uni-directional test LS10 cannot be captured by $\gamma_{DA} = 6\%$ either.

The comparison of the three examined strain-based liquefaction criteria in this section can be summarised as follows:

(1) $\gamma_{total} = 3\%$ is the least effective liquefaction criterion. Almost half of the tests in this study do not liquefy when this criterion is satisfied. Increasing the required level of γ_{total} can improve the performance of γ_{total} based criterion, but there is no convincing evidence that a certain level can be selected consistently to make this criterion applicable to all categories of multi-directional tests. Furthermore, the alteration of zero-strain point changes the calculation of γ_{total}, which aggravates the inconsistency of this criterion.

(2) Single amplitude shear strain of 3% in uni-directional tests is extended to $\gamma_{total,DA} = 3\%$ for multi-directional tests. This criterion has a better ability in enveloping liquefaction, but the application of it is constrained critically by its lack of physical and mathematical meaning as well as the issue regarding the definition of zero-strain point for the calculation of γ_{total}.

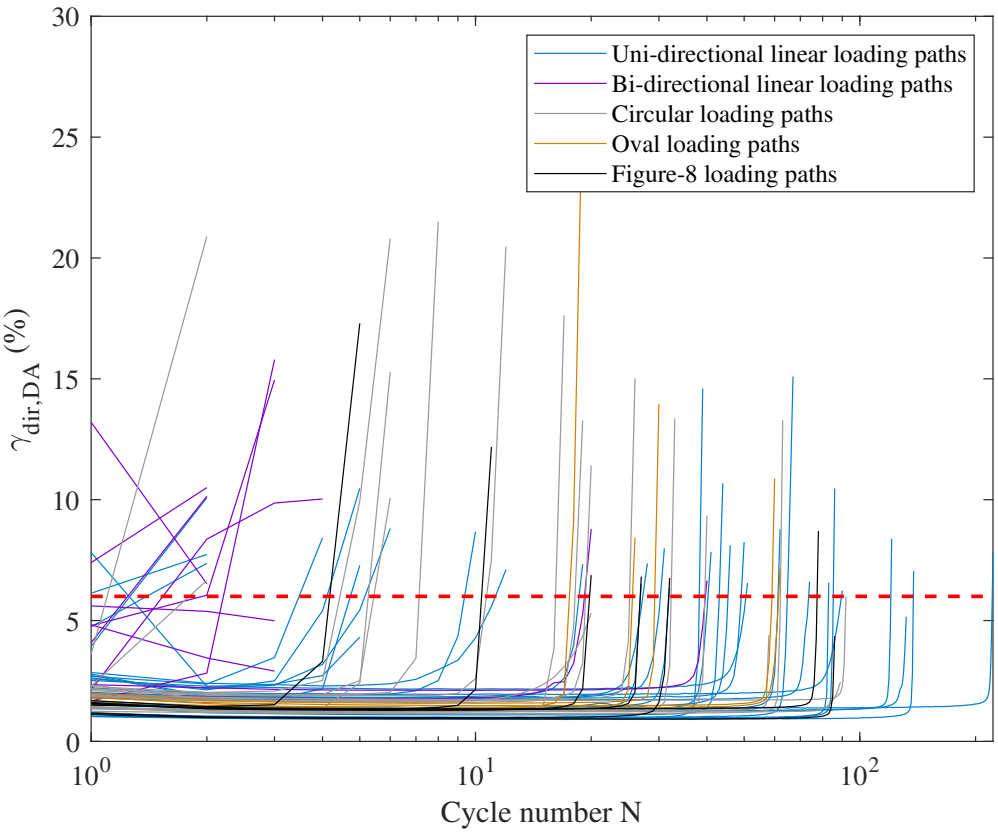

Fig. 7.3 The development of $\gamma_{dir,DA}$ with cycle number in all tests in this study

(3) Double amplitude shear strain of 6% $\gamma_{dir,DA} = 6\%$ in uni-directional tests is modified as $\gamma_{dir,DA} = 6\%$ to be applied in multi-directional loading scenarios. $\gamma_{dir,DA}$ is defined in a relative manner as the maximum distance between two points on a multi-directional strain path and is thus not altered by varying definition of zero-strain point. This criterion is the most effective one among the three criteria, but the situations where $\gamma_{dir,DA}$ decreases need to be considered separately.

In summary, liquefaction criteria hinged on either excess pore pressure ratio or shear strain need modifications before being used for multi-directional loading conditions. The maximum excess pore pressure predicted by equation 5.4 can be used as the modified r_u-based liquefaction criterion. $\gamma_{dir,DA} = 6\%$ is recommended as the strain-based criterion against which liquefaction resistance can be investigated and compared consistently. It should

be noted, however, that the essence of liquefaction rests virtually in the stress path reaching the failure envelope. Thus, failure defined from stress-state perspective should be given priority and considered as the liquefaction criterion whenever possible, before resorting to r_u-based or strain-based criteria.

7.2 The effects of multi-directional loading on liquefaction resistance

Although the research regarding soil liquefaction has now a 50-year history,a reliable and effective method to fully mitigate the effects of liquefaction on structures has not been developed. The assessment of liquefaction resistance is of vital importance in engineering practice to minimize or even eliminate the hazard of soil liquefaction.

Liquefaction assessment is typically based on case histories correlated to in situ tests. Seed and Harder (1990) correlated standardised SPT blowcount $(N)_{60}$ to the equivalent uniform uni-directional cyclic shear stress ratio CSR_{field} required to trigger liquefaction in the soils consolidated under standard vertical stress (usually 1 tsf or 100 kPa) and sheared by an earthquake with a magnitude $M = 7.5$. CSR_{field} also needs to be standardised as follows:

$$CSR_{field} = CSR \cdot C_M \cdot K_\sigma \cdot K_\alpha \tag{7.2}$$

where C_M is the coefficient to account for the magnitude of earthquakes, K_σ represents the coefficient of consolidation stress, and K_α is the coefficient of static shearing. The design codes nowadays generally adopt his recommendation with adjustments.

Research in the last a few decades demonstrated the effects of irregular loading and multi-directional loading should also be accounted for, but no consistent conclusions could be drawn regarding how to take them into consideration. The influence of irregular loading is out of the scope of this study and will not be discussed here. This section presents insights into the problem of the effects of multi-directional loading.

An unavoidable issue in evaluating the effects of multi-directional loading on liquefaction resistance is to select a parameter against which different types of loading paths can be compared or standardised. If the tests are compared, for instance, based on cyclic shear stress ratio in certain directions, the differences in terms of the stress states in 3D $\tau - \sigma'_v$ space cannot be reflected. If the tests are compared by total shear stress ratio, however, the effects of the geometric characteristics of the loading paths are not accounted for. A dilemma arises from the trade-offs among different types of parameters, and unfortunately, a perfect parameter that retains all crucial information of multi-directional loading paths has not been found.

Following the prevalent liquefaction assessment method proposed by Seed and Harder (1990), however, liquefaction resistance can be indicated by shear stress ratio versus the number of cycles to initiate liquefaction, that is, $N_L - CSR$ curves. CSR is replaced by CSR_{dir} in mutli-directional test, which refers to the maximum directional cyclic shear stress ratio throughout all directions, following:

$$\tau_{dir,DA} = \max_{i,j=1}^{N} \sqrt{(\tau_X^i - \tau_X^j)^2 + (\tau_Y^i - \tau_Y^j)^2} \tag{7.3}$$

$$CSR_{dir} = \frac{\tau_{dir,DA}}{2\sigma_{v,i}} \tag{7.4}$$

Figure 7.4 presents the liquefaction resistance of different categories of tests in the form of $N_L - CSR_{dir}$. The curves in the figure are the ones fitted for uni-directional tests without initial static shearing, which are the same as those in Figure 4.17. With the relative density and the number of cycles to liquefaction of a test, an equivalent uni-directional $CSR_{equivalent}$ can be determined on the curves fitted to uni-directional test data, and a coefficient of multi-directional loading paths, denoted by K_μ in this study, can be obtained as:

$$K_\mu = \frac{CSR}{CSR_{equivalent}} \tag{7.5}$$

Figure 7.5 plots K_μ versus CSR_{dir} for the tests having no initial static shearing in this study (derived from plot (c),(e) and (f) in Figure 7.4), together with the data presented by

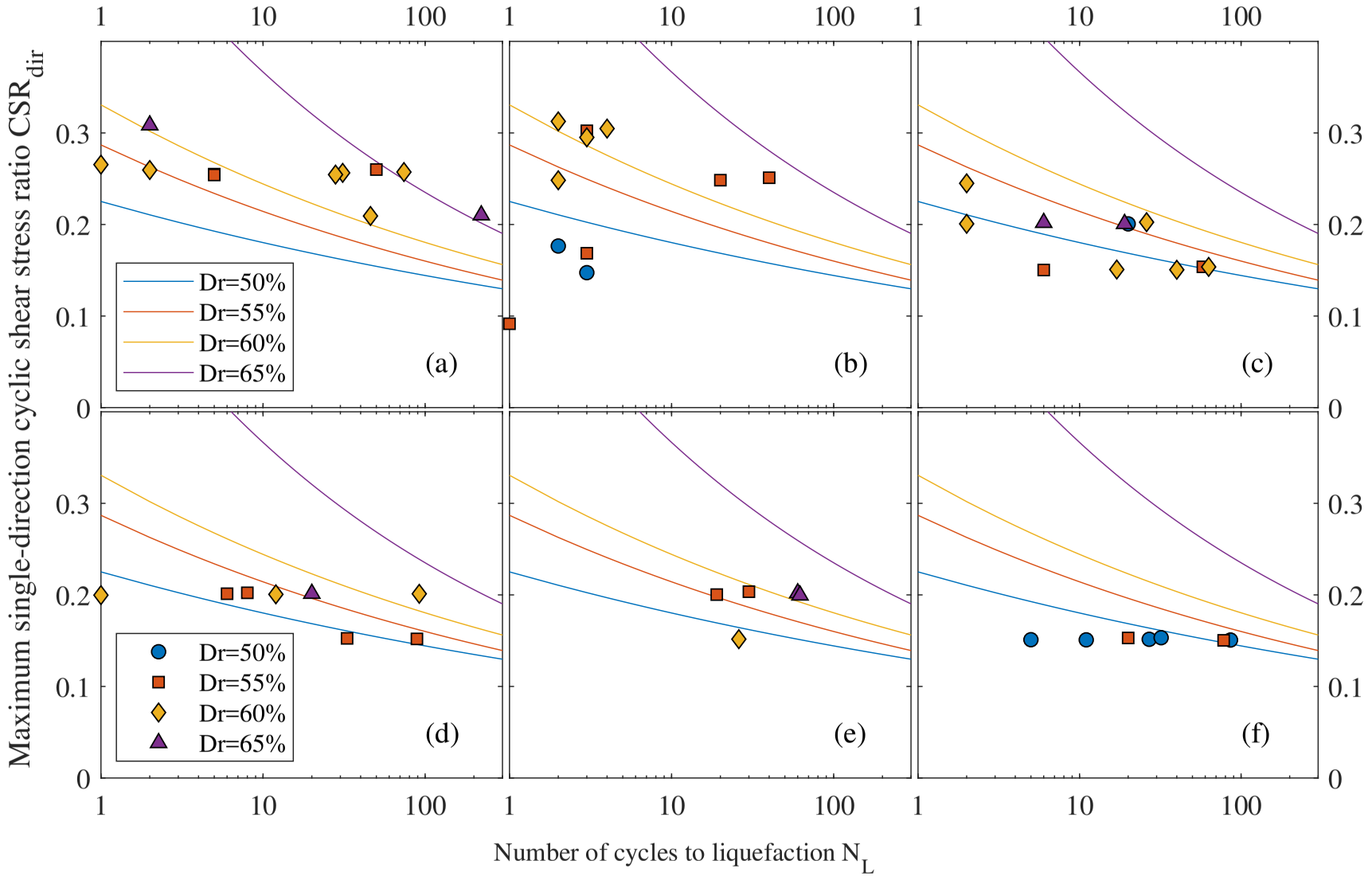

Fig. 7.4 Liquefaction resistance reflected in the form of $N_L - CSR_{dir}$: (a)Uni-directional tests with static shearing; (b)Bi-directional tests; (c)Circular tests without static shearing; (d)Circular tests with static shearing; (e)Oval tests; (f)Figure-8 tests

Kammerer (2002). Data points in this study are colour-filled, with the colours indicating relative density, while the data from Kammerer (2002) are hollow. The categories of loading paths are suggested by the marker types. Linear interpolation is conducted in-between $N_L - CSR$ curves to account for the deviation of actual relative density from the nominal densities.

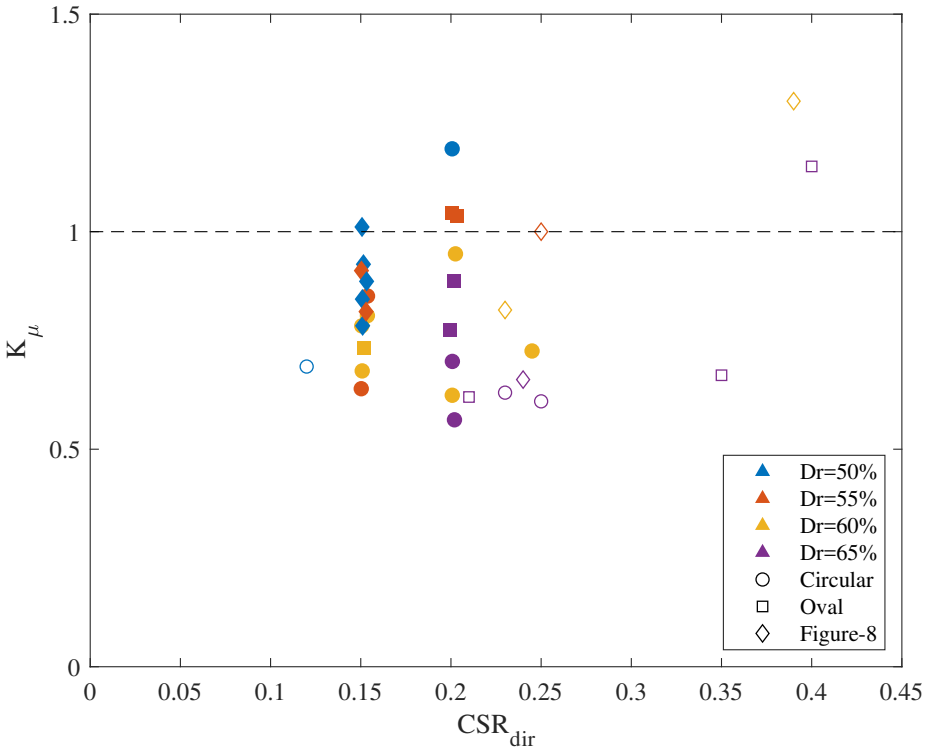

Fig. 7.5 The coefficient of multi-directional loading K_μ versus CSR_{dir}

K_μ obtained in this study ranges from 0.57 to 1.19, with the majority below 1.0. It suggests that from the point of view of required CSR_{dir} to trigger liquefaction, the effects of multi-directional loading on liquefaction resistance can be either positive or negative, but negative in most cases. In extreme situations, CSR_{dir} can be reduced by up to 43%. The largest reduction of required CSR_{dir} in multi-directional loading scenarios reported previously was 30% by Ishihara and Yamazaki (1980), 50% by Reddy and Saxena (1992), 40% by Kammerer (2002) and 33% by Mirbaha (2017). The smallest K_μ of 0.57 in this study is in agreement with their findings. The scatter in the graph are remarkable but inevitable because

both the numerator and denominator in the calculation of K_μ are affected by experimental uncertainties.

The fact that K_μ is below unity in most cases, regardless of relative density, suggests that ignoring the reduction of liquefaction resistance in multi-directional loading condition is un-conservative. Furthermore, there is a general tendency of K_μ to decrease more in the tests with higher relative density. Dense sands, which are conventionally considered resistant to liquefaction in uni-directional tests, may experience more dramatic reduction in liquefaction resistance when it comes to multi-directional loading. Caution should thus be taken in assessing the liquefaction resistance of dense sands.

Another observation from Figure 7.5 is that circular loading paths tend to result in lower K_μ if CSR_{dir} and relative density are around the same, compared with oval and figure-8 loading paths. The effects of varying categories of loading paths have been studied. Ishihara and Yamazaki (1980) reported that the most significant reduction of CSR_{dir} occurs when the amplitudes of the loading in two perpendicular directions are equal. But little advancement has been seen in terms of the parametrization of the differences among loading paths. Kammerer (2002) proposed to use aperture ratio ($AR = \frac{CSR_{perp}}{CSR_{dir}}$) and reversal parameter ($RP = \frac{CSR_\alpha - \alpha}{CSR_{dir}}$) to indicate the geometrical characteristics of a loading path (illustrated in section 3.7). The higher the aperture ratio, the lower the K_μ. Circular paths have the highest aperture ratio and thus the lowest K_μ.

Similar trends are also observed in this study, but the effects of aperture ratio on K_μ recorded in this study are not as pronounced as Kammerer suggested. Figure 7.6 presents the relationship between K_μ and aperture ratio for the tests having reversal parameters of 0 and 0.5. The five figure-8 tests (blue diamond) in Figure 7.6(a) have the same relative density, CSR_{dir} and reversal parameter, but the decrease of K_μ with increasing AR in these tests is only marginal.

The effects of reversal parameter on K_μ are also examined. Figure 7.7 shows the relationship between K_μ versus absolute reversal parameter $|RP|$ for the tests which have aperture ratios of 0 and 1. $|RP| = 0$ means static shearing is not involved, while higher values of $|RP|$ indicate generally larger static shearing. The tests shown with $AR = 0$ are

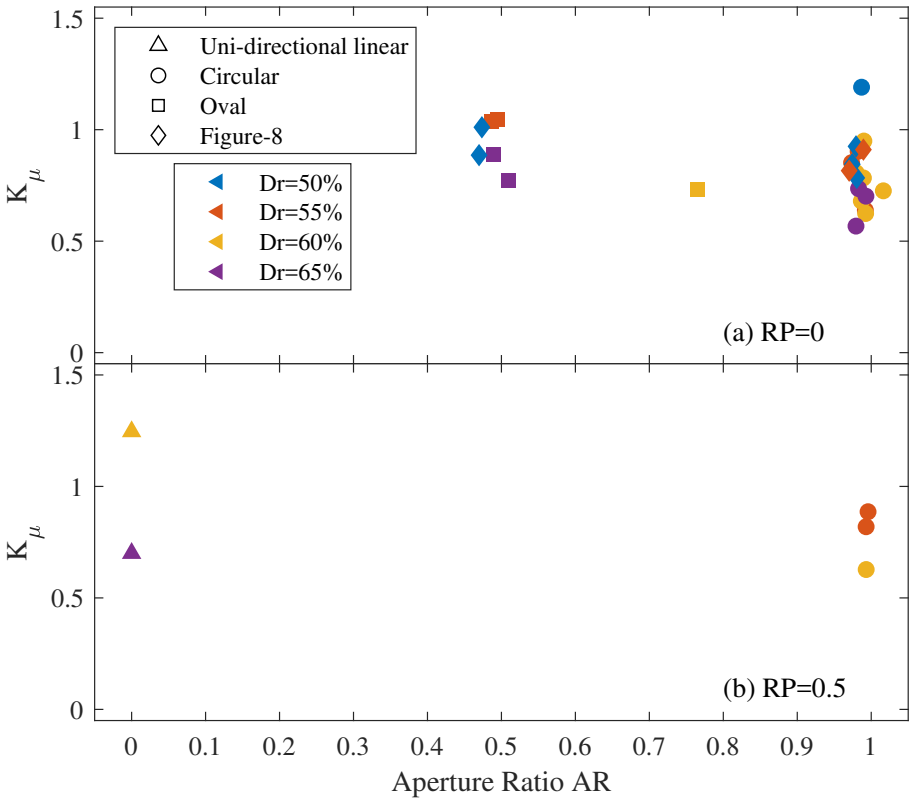

Fig. 7.6 The coefficient of multi-directional loading K_μ versus aperture ratio AR for tests with reversal parameter at 0 and 0.5

uni-directional linear tests with static shearing and bi-directional linear tests. For the former, the coefficient to account for the effects of loading paths is equivalent to the coefficient of initial static shearing K_α for uni-directional tests as presented in Figure 4.18. As discussed in section 4.2, the relationships between K_α and static shear stress ratio α are complex and controversial since factors including relative density, stress reversal, and maximum shear stress are all claimed to exert an influence. It is inferred that similar complexity should exist in multi-directional tests.

Uni-directional and bi-directional tests exhibit the tendency of K_μ to grow with increasing RP in each density group when $|RP|$ is smaller than 0.5. That is, a moderate increase of downhill static shearing may help increase liquefaction resistance. But the trend is reversed with further growth of $|RP|$. Large static shearing can result in over-large total shear stress,

in which case liquefaction can happen in the first one or two loading cycles. However, such a tendency is not seen in circular, oval and figure-8 tests. As seen in Figure 7.7(b), K_μ remains relatively constant in these test regardless of $|RP|$.

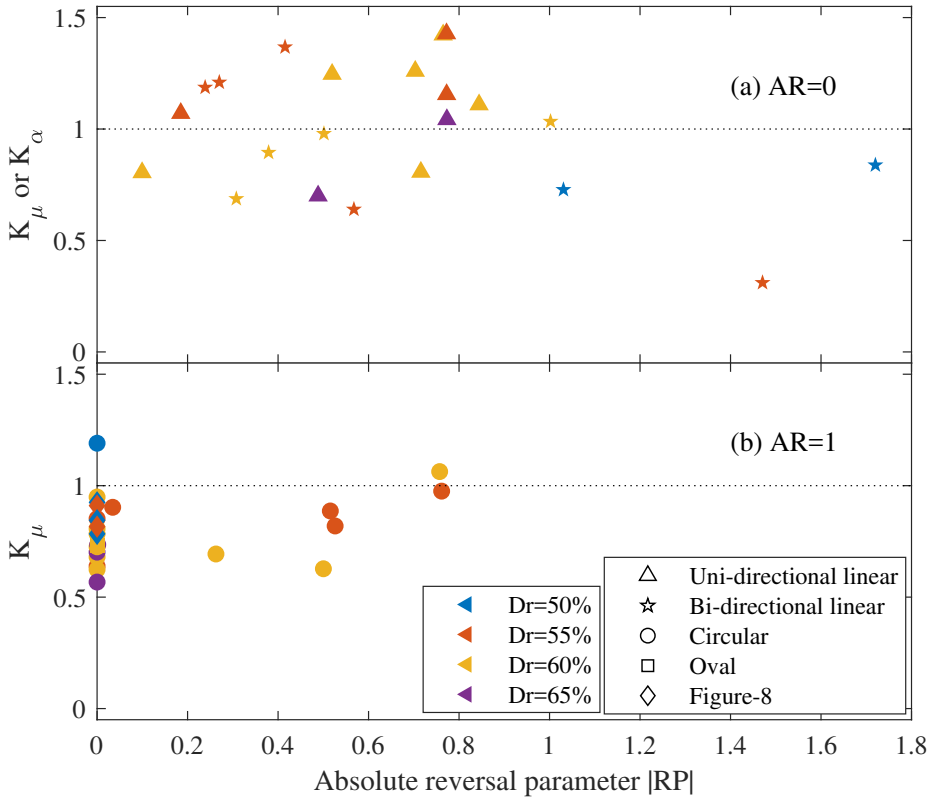

Fig. 7.7 The coefficient of multi-directional loading K_μ versus reversal parameter RP for tests with aperture ratio at 0 and 1

The inconsistency and scatter in the relationships between K_μ and $|RP|$ as well as AR suggests that reversal parameter and aperture ratio may not be able to fully capture the features of a loading path with static shearing. But the philosophy contained in this pioneering attempt to characterise loading paths raises thought-provoking questions.

Firstly, should the influence of static shearing be decoupled from that of multi-directional, or, is it possible? The conventional liquefaction assessment method following Seed and Harder (1990) uses coefficient K_α to involve the influence of static shearing on liquefaction resistance. K_α can be obtained conveniently in uni-directional tests because the reduction of

CSR is caused exclusively by static shear. In multi-directional loading conditions, the reduction of *CSR* results from the combined effect of static shearing and the multi-directionality of loading paths. If the effects of either of the two were unambiguous, they could be decoupled and described by two coefficients; however, there is no consensus yet.

Furthermore, from the perspective of total shear stress and geometry, there is a possibility that the existence of static shearing can be included in more fundamental characteristics of loading paths. It is likely that K_α is just a "particular solution" of K_μ in uni-directional loading condition, and that the controversy in terms of K_α is a consequence of the lack of understanding of multi-directional loading. The aperture ratio and reversal parameter proposed by Kammerer can be regarded as an example of the attempt towards a generalised way of characterising loading paths. More effective parameters are needed in the future to explore the essence of multi-directional loading.

Secondly, is it reasonable to correlate N to *CSR* and are there alternatives to it? The convenience of relating liquefaction resistance to cyclic shear stress ratio rests in that *CSR* indicates effectively the amplitude of shearing in uni-directional tests without static shearing. When it comes to multi-directional loading or uni-directional loading with static shear, the effectiveness of *CSR* becomes questionable. On the one hand, *CSR* cannot reflect the maximum shear stress applied if static shearing is involved. On the other hand, the definition of *CSR* in multi-directional tests requires a direction to be designated and the representative cyclic shear stress ratio CSR_{dir} is the maximum *CSR* across all directions. A natural defect of CSR_{dir} is that the information of shearing on other directions is lost, which is what the aperture ratio aims to complement. In this case, to correlate liquefaction resistance to CSR_{dir} is still reasonable, but not necessarily optimal.

In addition, cyclic shear stress ratio *CSR* is actually equivalent to maximum total shear stress ratio $SSR_{total,max}$ in uni-directional tests without static shearing, that is, $N_L - CSR$ curves and $N_L - SSR_{total,max}$ coincide under such loading condition. The coefficients including C_M and K_σ in equation 7.2 will remain the same in $SSR_{total,max}$ based liquefaction resistance. The resemblance suggests a possibility that $SSR_{total,max}$ may have been misinter-

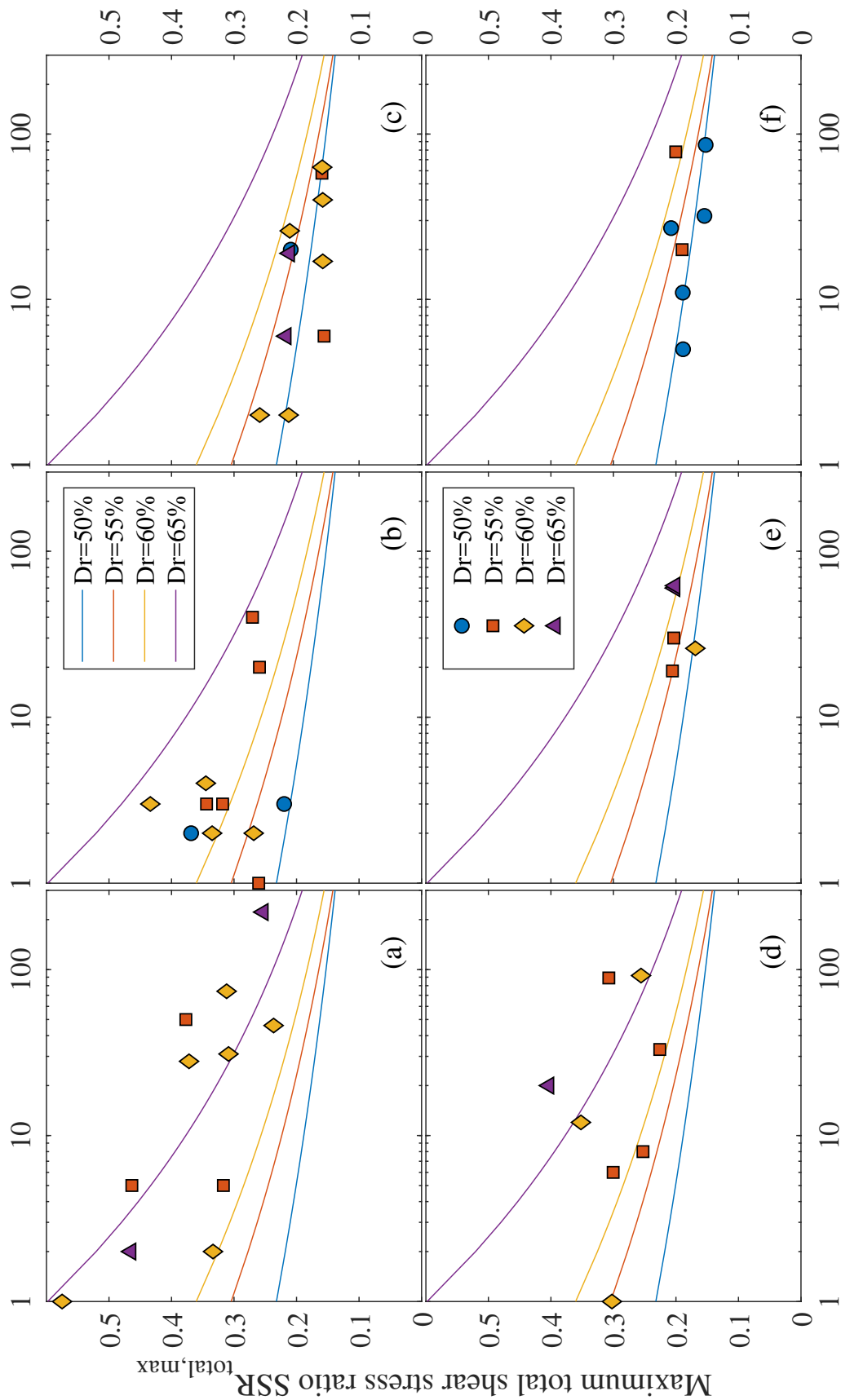

Fig. 7.8 Liquefaction resistance reflected in the form of $N_L - SSR_{total,max}$: (a)Uni-directional tests with static shearing; (b)Bi-directional tests; (c)Circular tests without static shearing; (d)Circular tests with static shearing; (e)Oval tests; (f)Figure-8 tests

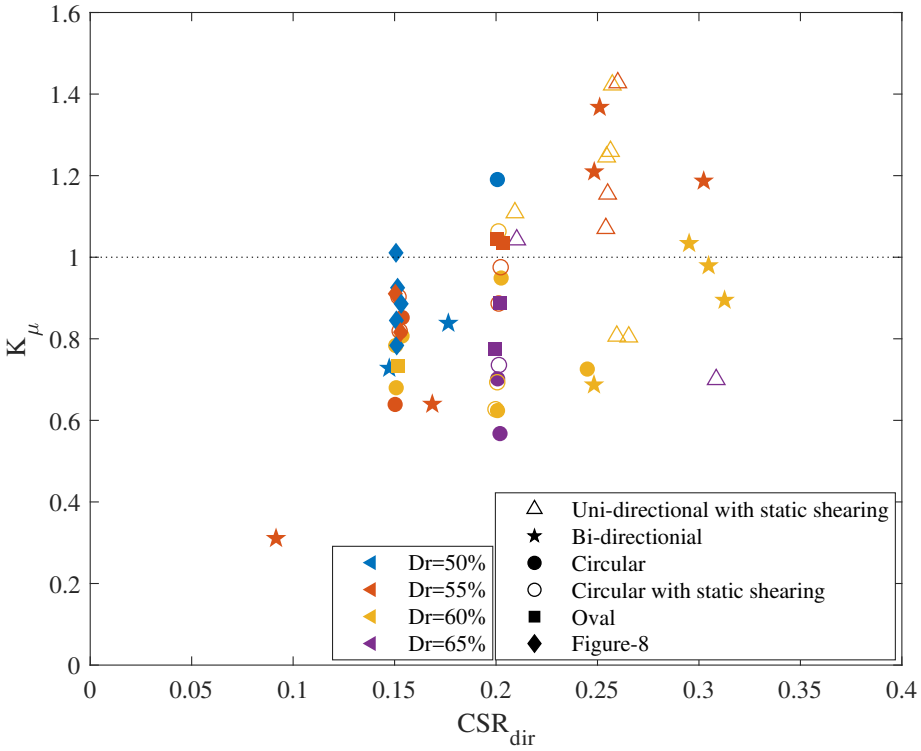

(a) $N_L - CSR$

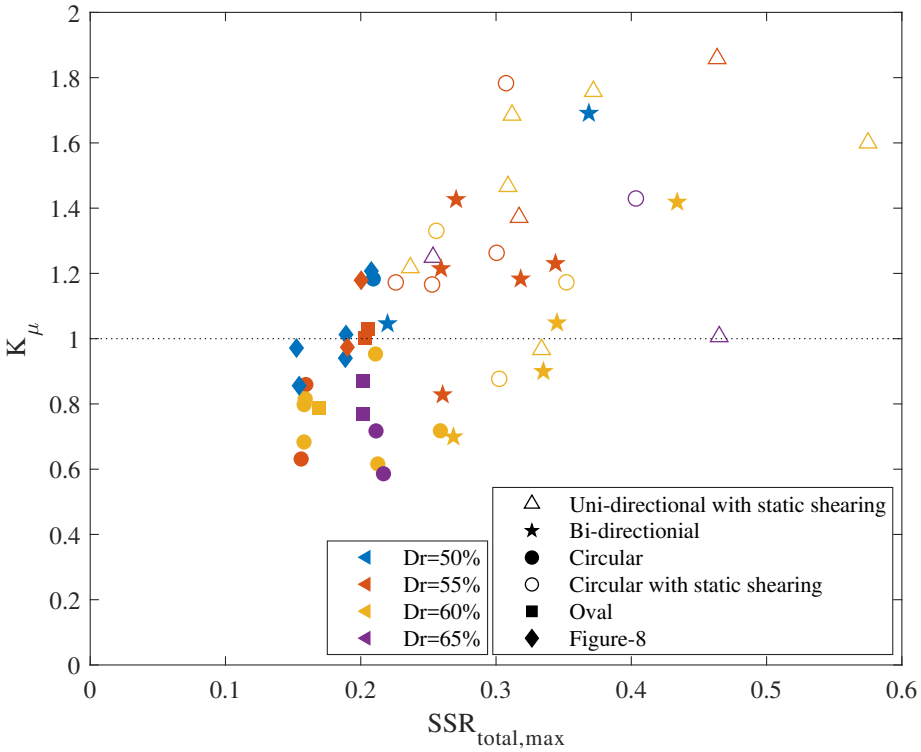

(b) $N_L - SSR_{total,max}$

Fig. 7.9 Comparison of K_μ derived from $N_L - CSR$ and $N_L - SSR_{total,max}$ relationships

preted as CSR and $N_L - SSR_{total,max}$ is a potential alternative to the $N_L - CSR$ relationship in the assessment of liquefaction resistance.

Figure 7.8 presents the $N_L - SSR_{total,max}$ relationship for the tests in this study. The curves are the ones fitted to uni-directional level-ground tests. They are slightly different from the $N_L - CSR$ curves in Figure 7.4 because a small amount of shear stress exists perpendicular to cyclic shearing, resulting in a slight difference between CSR and $SSR_{total,max}$. Remarkable differences can be found in uni-directional tests with static shearing, bi-directional tests, circular tests with static shearing and figure-8 tests (comparing plot (a),(b),(d) and (f) in Figures 7.4 and 7.8) because the maximum total shear stress in these tests differ from CSR_{dir} due to static shear or the special geometry of loading paths (such as non-standard figure-8 paths).

Based on $N_L - SSR_{total,max}$ curves, a set of coefficients of multi-directional loading can be derived. Figure 7.9 compares the K_μ derived from $N_L - CSR$ and $N_L - SSR_{total,max}$ relationships. Tests with static shear are also presented and K_α is not decoupled from K_μ. Different from CSR-based K_μ which is below unity in most situations, half of the tests have $SSR_{total,max}$-based K_μ larger than unity. This is particularly true for tests with static shearing (points marked by hollow triangle, hollow circle and solid pentagon), which suggests that the effects of static shearing are positive in these cases from the perspective of $SSR_{total,max}$-based liquefaction resistance. The circular and oval tests without static shearing, by contrast, have generally unchanged K_μ, which in most situations is below unity. Furthermore, the $SSR_{total,max}$-based K_μ exhibits a stronger tendency to increase with $SSR_{total,max}$ in each category of tests of similar density. This indicates the increase of $SSR_{total,max}$ due to variation of loading paths can be beneficial in a counter-intuitive manner.

There is no intention in this study to demonstrate $N_L - SSR_{total,max}$ is a more effective method to assess liquefaction resistance. Multi-directional shearing has only been investigated experimentally in element-level tests and test data are far from sufficient to determine if a new liquefaction assessment method is compatible with the field. $SSR_{total,max}$ also has drawbacks, such as the lack of information about directionality of loading. A series of parameters analogous to aperture ratio and reversal parameter need to be proposed and work

in a consistent manner with $N_L - SSR_{total,max}$ if such a method is to be validated. However, the thoughts about $N_L - SSR_{total,max}$ suggest that there are potential alternatives to $N_L - CSR$ for the assessment of liquefaction, especially in multi-directional loading scenarios. The coefficient of static shearing K_α and multi-directional loading K_μ and even the potential coefficient of loading irregularity is not reliable without more comprehensive demonstration. The effect of multi-directional loading on liquefaction resistance is an area worthy of more examination in the future so that more effective and accurate methods can be developed for liquefaction assessment in engineering practice.

7.3 The development of excess pore pressure in multi-directional simple shear tests

The development of excess pore pressure has attracted extensive attention in the field of liquefaction research because the occurrence of liquefaction is caused by the generation of positive excess pore pressure. Great efforts have been made towards correlating excess pore pressure to liquefaction resistance, shear modulus and deformation based on experimental and numerical studies. However, the understanding of how excess pore pressure develops in multi-directional loading scenarios is far from extensive. Boulanger (1990) and Kammerer (2002) observed an inverse relationship between limited excess pore pressure ratio and shear stress ratio, but the mechanisms were not investigated in depth. Little discussions have taken place on whether the conclusions regarding the development of excess pore pressure in uni-directional tests are also applicable to multi-directional conditions. This section will summarize the test results of this study and examine the influence of multi-directional loading on excess pore pressure generation with the newly-developed test database and the newly-established concept of failure cone. The findings from this study can provide a foundation for modelling work in the future.

7.3.1 Maximum excess pore pressure ratios in multi-directional simple shear tests

The concept of failure cone has been introduced in Chapter 6 and will be considered as the actual failure envelope for multi-directional simple shear tests. Important inferences can be drawn from the theory of the failure cone regarding the limits of excess pore pressure ratios.

When liquefaction is initiated, the shear stress path should reach and develop along the failure line in $\tau_{total} - \sigma'_v$ space during loading. The point on the failure line, which has minimum total shear stress ratio, also has the minimum effective vertical stress, or the maximum excess pore pressure ratio. In contrast, the point that holds the maximum total shear stress ratio sets the limit for the maximum effective vertical stress in a loading cycle. Figure 7.10 shows the relationships between limiting excess pore pressure ratios and total shear stress ratios of all the tests in this study. The solid lines represent the correlation following equation 6.5.

As shown in Figure 7.10a, the measured maximum excess pore pressure ratios are scattered around equation 6.5. The maximum pore pressure ratios in 16 of the tests are higher than the predicted values mainly because the loading system cannot sustain constant vertical stress after the stiffness of soil sample becomes extremely low and thus causes unanticipated increase of excess pore pressure. The other tests, however, all have $r_{u,max}$ lower than the predicted values, which is attributed to two primary reasons. Firstly, the effects of relative density on the angle of the failure line are not taken into consideration here. The actual value of ϕ_{FL} is likely to be lower than 33.4° so that $r_{u,max}$ reduces correspondingly. Secondly, extremely low effective vertical stress is difficult to achieve in simple shear tests because the large deformation of the soil sample increases the discrepancies between realistic boundary conditions and the ideal ones. The phenomenon that effective vertical stress cannot approach zero can be observed in Figures 4.10, 4.15, 5.18, and 5.31. One point (test LS11) deviates remarkably from the prediction line because the lack of stress reversal results in a different pattern of stress development in this test, as reported in Chapter 4 and presented in Figure 4.13. With the scatter clarified, a strong inverse linear correlation can be identified between

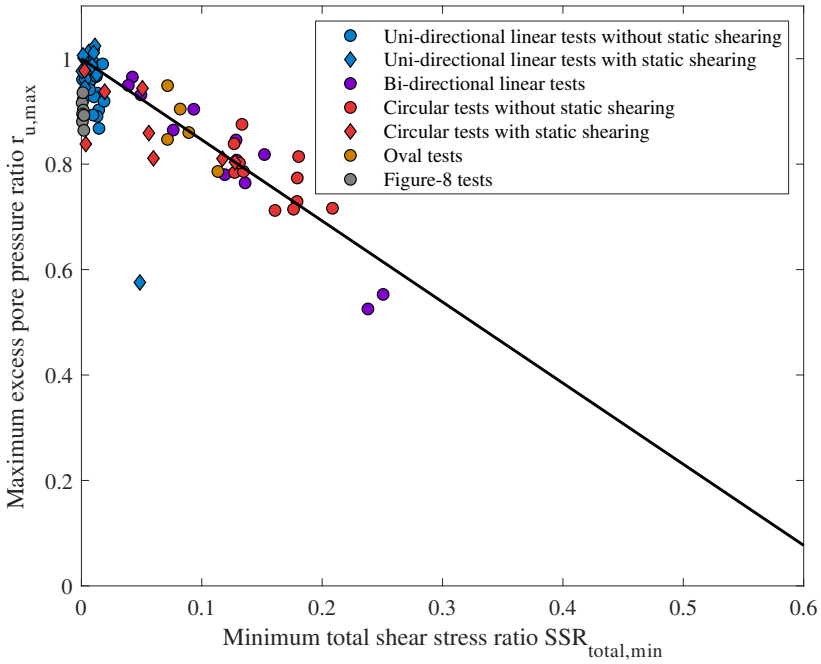

(a) Inverse correlation between maximum excess pore pressure ratio and minimum total shear stress ratio

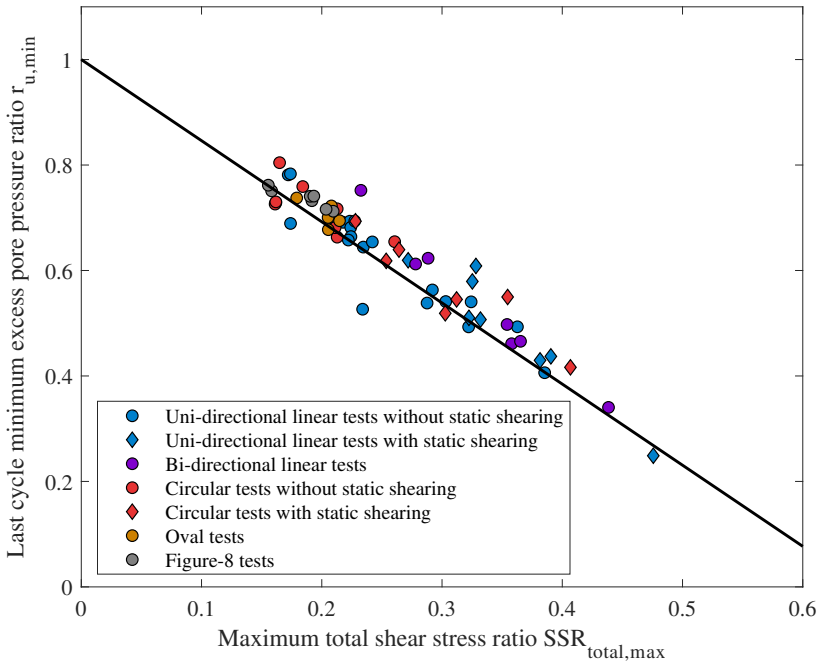

(b) Inverse correlation between the largest minimum excess pore pressure ratio and maximum total shear stress ratio

Fig. 7.10 Relationships between limiting excess pore pressure ratios and total shear stress ratios

$r_{u,max}$ and minimum total shear stress, validating the theory of failure cone in enveloping stress states under multi-directional loading conditions.

Figure 7.10b presents maximum total shear stress ratio versus the largest single-cycle minimum excess pore pressure ratio.The largest single-cycle minimum excess pore pressure ratio is denoted as $r_{r,min}$ and is determined as the minimum excess pore pressure ratio in the loading phase of the loading cycle where liquefaction is triggered. If the failure cone exists and the shear stress paths stay on the conical failure surface after reaching it during loading, the stress point with the largest SSR_{total} should give $r_{r,min}$ in this cycle. Clearly, the data points in Figure 7.10b show a strong inverse correlation. The reason why most of the points are located above the prediction line is total shear stress paths tend to deviate slightly backward from the failure line at the end of the loading phase, as seen in Figures 5.18 and 5.31. In general, the strong correlation between $r_{u,min}$ and $SSR_{total,max}$ demonstrates the failure cone is effective in predicting the critical values of excess pore pressure ratios.

The test results of Kammerer (2002) and the correlations proposed by Boulanger (1990), as well as the prediction line from this study are presented in Figure 7.11, which is modified from figure 5.60 of Kammerer (2002). The red dashed line is calculated following equation 6.5 with $\phi_{FL} = 30.5^\circ$ (after the data of Wu (2002)). The relationship proposed in this study is capable of correlating Kammerer's data with limited scatter. In fact, the degree of scatter is acceptable given that different methods were adopted in processing test data and the effects of sample density on ϕ_{FL} were not taken into consideration. The linear-regression correlations proposed by Kammerer (2002) were actually statistical approximation of equation 6.5.

Evidently, the existence of an inverse relationship between limited excess pore pressure ratios and critical total shear stress ratios has significance in soil mechanics. Such a relationship is not a statistical coincidence, instead, it is predicted by the failure cone that constrains the stress states at failure in multi-directional simple shear tests. This correlation is an important feature of multi-directional simple shear tests and an essential theoretical basis for interpreting simple shear test data. The generation of excess pore pressure in multi-directional loading scenarios should be understood in 3D $\tau - \sigma'_v$ space, whenever possible, to avoid misleading results.

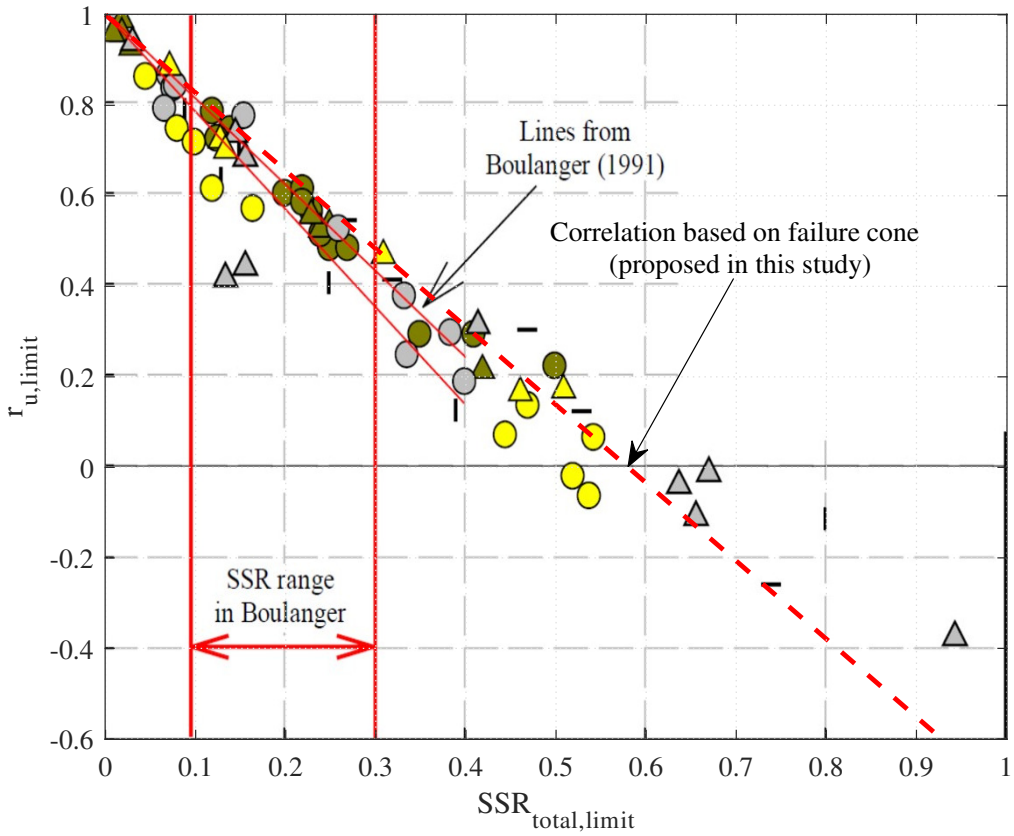

Fig. 7.11 Correlation between limiting excess pore pressure ratios and total shear stress ratios (modified from Kammerer (2002))

7.3.2 Development of excess pore pressure in multi-directional simple shear tests

While the existence of a failure cone constrains the largest single-cycle maximum and minimum excess pore pressures that can be generated in multi-directional simple shear tests, the pattern of excess pore pressure development within a single loading cycle, on the other hand, is affected by phase transformation states. With τ_{total} increasing in the loading phase of a cycle, excess pore pressure increases first, but the tendency is reversed after phase transformation states are reached. When the increase of τ_{total} reverses and the unloading phase begins, excess pore pressure turns to grow again until another loading period starts. The variation of excess pore pressure within an individual cycle should not be examined in an

isolated manner because the lack of information of the phase transformation states prevents accurate interpretation. Instead, it must be understood with real-time stress states. Readers are referred to Chapter 6 where the effects of the phase transformation states on the change of excess pore pressure within a single shearing cycle were discussed.

The development of excess pore pressure between loading cycles, however, needs to be addressed because it provides valuable insights for constitutive modelling. As reported in Chapter 4 in Figures 4.19 and 4.19, the development of excess pore pressure shows a three-stage pattern that is not altered by initial static shearing in uni-directional tests. It is worth exploring if such a pattern holds true in multi-directional loading scenarios as well.

Figure 7.12 presents the development of normalised excess pore pressure ratio with normalised cycle number for all the tests in this study. The format in Figure 4.19 that plots the absolute values of excess pore pressure ratio is not used because maximum excess pore pressure ratios vary from a test to another due to the influence of the failure cone, resulting in the end points of curves being widely scattered, from which undesirable confusion arises. Instead, a normalisation of excess pore pressure ratios by their maxima is applied to make the curves reach the same final point. There is no clear influence of multi-directional loading paths on the development of excess pore pressure, indicating that the pattern of excess pore pressure generation is one of the characteristics of Hostun sands that is not altered by the multi-directionality of loading paths, at least for the tested range of relative densities and vertical consolidation stresses in this study.

The patterns of excess pore pressure development can be categorised into three groups, as shown in Figure 7.13. Group I is composed of the tests with $N_L > 5$. All the curves of these tests fall into a band. The same pattern of excess pore pressure generation is shared among these tests, which feature three stages: excess pore pressure ratio jumps in the initial phase and enters subsequently a stable period where excess pore pressure accumulates gradually, followed by a period of excess pore pressure ratio increasing rapidly to its maximum amount. This is congruous with the typical strain-softening type of behaviour of sands observed in uni-directional tests.

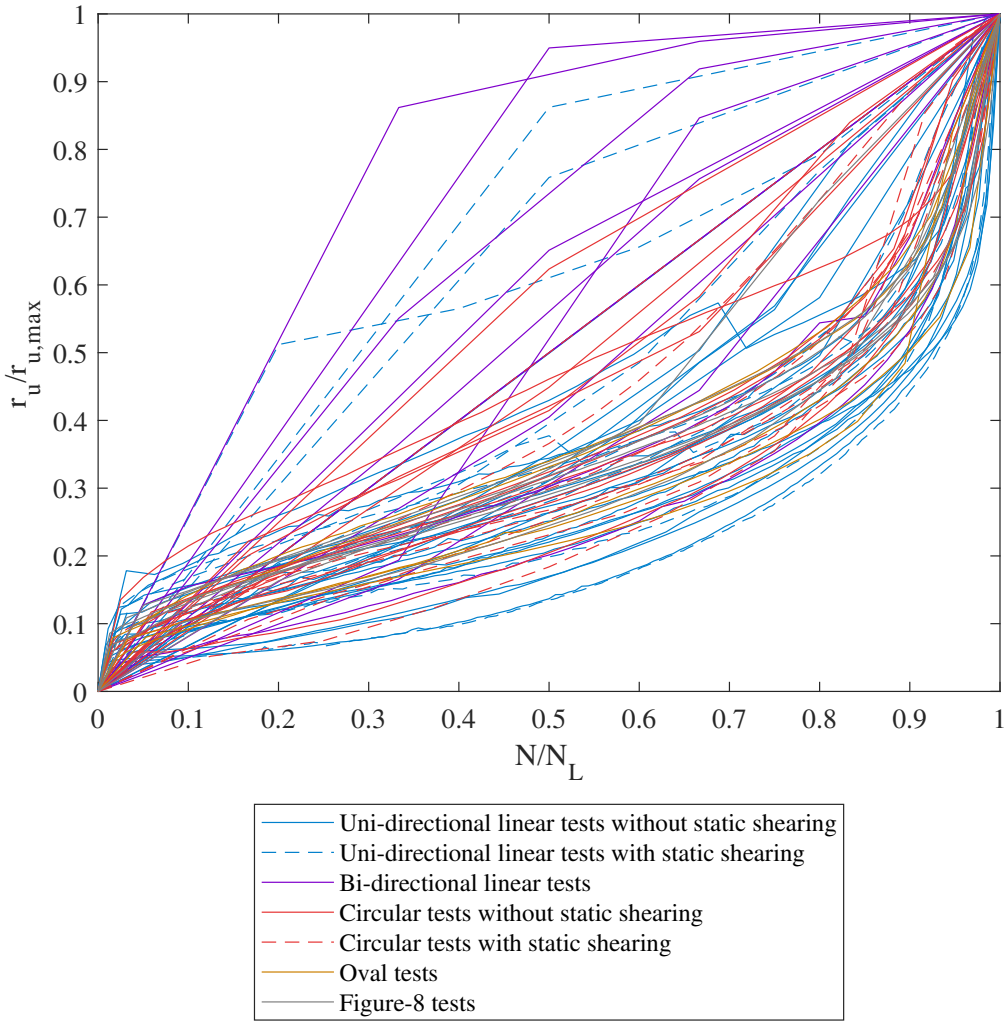

Fig. 7.12 The development of normalised excess pore pressure ratio with normalised cycle number

Group II represents the tests that have $N_L \leqslant 5$ and normalised excess pore pressure ratio lower than 0.5 in the first cycle. Excess pore pressure in these tests keeps rising until the maximum values are achieved, without distinguishable stages or distinct variations in the increment rate of excess pore pressure ratio.

Group III, by contrast, contains the tests where normalised excess pore pressure ratio jumps to over 0.5 in the first cycle, including the tests that liquefy with only one loading

cycle. The tests in group III manifest a two-stage increase of excess pore pressure, with a considerable increase of excess pore pressure (more than half of $r_{u,max}$) taking place in the first cycle, followed by moderate increase in the subsequent cycles. The scatter of group III results is much more significant than for the other two groups, suggesting that there may not be a consistent way to describe the pattern in this group.

The examination of patterns of excess pore pressure development in the tests with low liquefaction resistance reveals that the three-stage pattern of excess pore pressure increase is applicable only in tests that have moderate to high liquefaction resistance. For the tests that are prone to liquefaction, however, the development of excess pore pressure needs to be considered individually, especially when the increase of pore pressure in the first loading cycle is extraordinarily high. Although $N_L = 5$ appears to work satisfactorily in dividing the tests into a group which is prone to liquefaction and a group which is not, whether this threshold is applicable to other types of sands or tests with different testing conditions remains unconfirmed. Only the qualitative conclusions should be transferable.

Another relationship worthy of inspection is that between liquefaction resistance and the excess pore pressure ratio developed in the first loading cycle of a test. Such a correlation was proposed for uni-directional tests by Oda et al. (2001) and supported by Wu (2002) as shown in Figure 4.21, but whether it is applicable to multi-directional loading scenarios needs to be examined. Figure 7.14a plots the first-cycle excess pore pressure ratio $r_{u,1}$ versus the number of cycles to liquefaction N_L for the tests in this study. The solid curve is the same one as in Figure 4.21 following equation 4.4. It appears that the same correlation is applicable to multi-directional loading scenarios in general. The number of cycles to liquefaction reduces rapidly with increasing first-cycle excess pore pressure ratio. The role of $r_{u,1}$ seems to be equivalent to either a descriptor of the stiffness of sands of a certain density under a certain consolidation pressure or an indicator of the detriments that sands have experienced during the first loading cycle, but in either way it indicates the ability of sands to withstand shearing and resist liquefaction.

But considering the influence of multi-directional loading on achievable maximum excess pore pressure ratio, it is reasonable to consider excess pore pressure in a normalised manner.

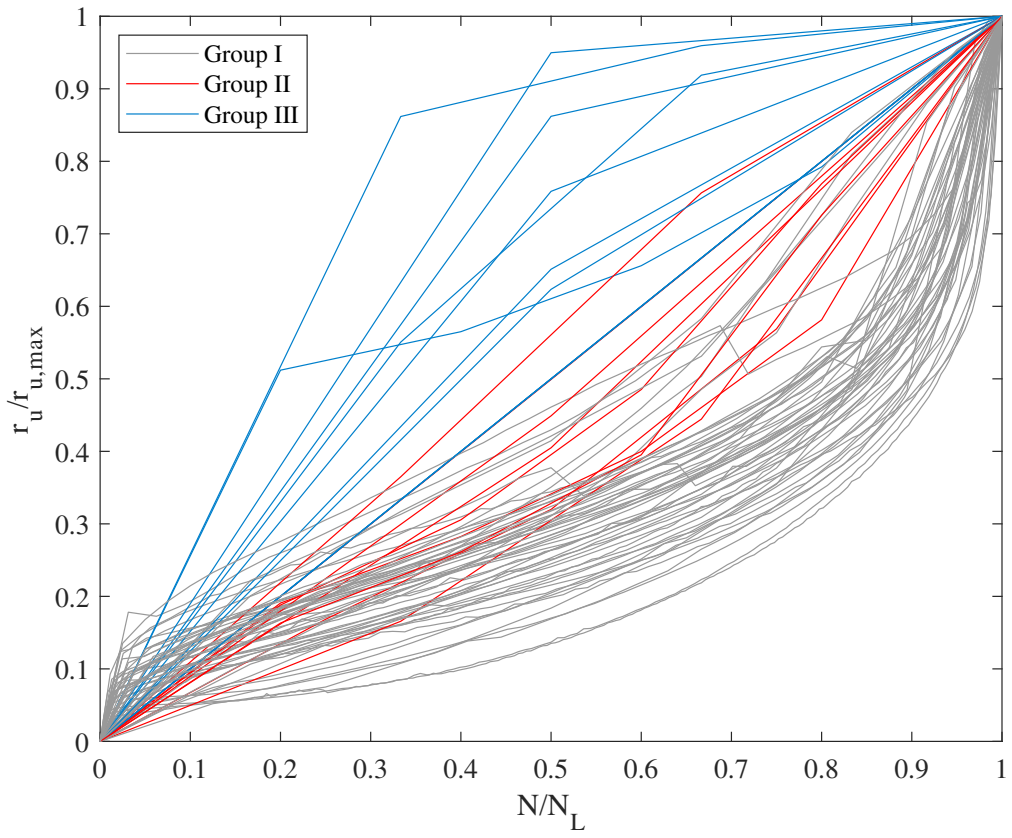

Fig. 7.13 The development of normalised excess pore pressure ratio with normalised cycle number categorised into three groups

Figure 7.14b presents the normalised first-cycle excess pore ratio versus liquefaction resistance. The same solid curve is seen to work adequately, though the degree of scatter becomes dramatic for the tests with rather low liquefaction resistance. Inevitable inaccuracies exist in the determination of liquefaction resistance because factors such as unconsidered change of ϕ_{FL} with relative density, overshooting issues of the loading system, imperfections in samples and inhomogeneity induced by realistic simple shear testing setup can all contribute to the uncertainties in determining liquefaction resistance. The inaccuracies are exaggerated when the number of cycles to liquefaction is small, resulting in the seemingly large scatter. Considering this, the solid curve is deemed as capable of describing the relationship between liquefaction resistance and normalised first-cycle excess pore pressure ratio. Equation 4.4 can be hence modified as follows:

$$\frac{r_{u,1}}{r_{u,max}} = N_L^{-(0.67+\frac{1.53}{N_L})} \tag{7.6}$$

It should be noted that 0.67 and 1.53 are the coefficients fitted from unnormalised excess pore pressure ratios in uni-directional tests. They are not modified partly because they still work satisfactorily from the statistical point of view and partly because their use can highlight the similarities between equations 4.4 and 7.6. It is recommended to replace equation 4.4 with 7.6 so that the effects of varying maximum excess pore pressure ratios under multi-directional loading conditions can be accounted for.

In summary, while the multi-directionality of loading paths can influence the upper limits of excess pore pressure and the variation of pore pressure within a single loading cycle, it does not influence the development of normalised excess pore pressure ratios as well as the relationship between liquefaction resistance and normalised first-cycle excess pore pressure ratio. The latter can be regarded as an intrinsic characteristic of sands that is independent of loading paths.

7.4 The development of shear strain in multi-directional simple shear tests

Although shear strain and deformation is one of the most intriguing topics in geotechnical research because of its value in practical engineering design, the understanding of shear strain development in multi-directional loading remains insufficient. As discussed in Chapter 5, the development of shear strain induced by multi-directional shearing also occurs in a multi-directional manner. It can not only pose a challenge to current models for geotechnical deformation prediction, but also bring about problems for the seismic design of structures. It is very likely that multi-directional motion of soil, depending on the specific path, can result in detrimental torque in construction and aggravate the whiplash effects on high-rise buildings. The accumulation of shear strain under multi-directional shearing is worthy of more investigation.

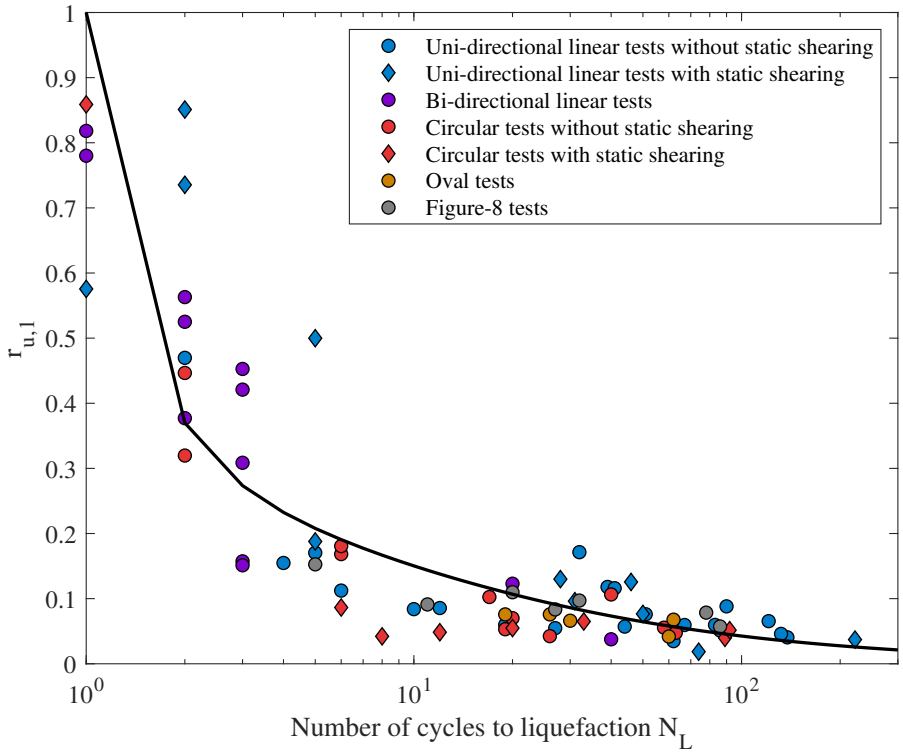

(a) The relationship between the excess pore pressure ratio in the first cycle and the number of cycles to liquefaction (the solid curve gives equation 4.4)

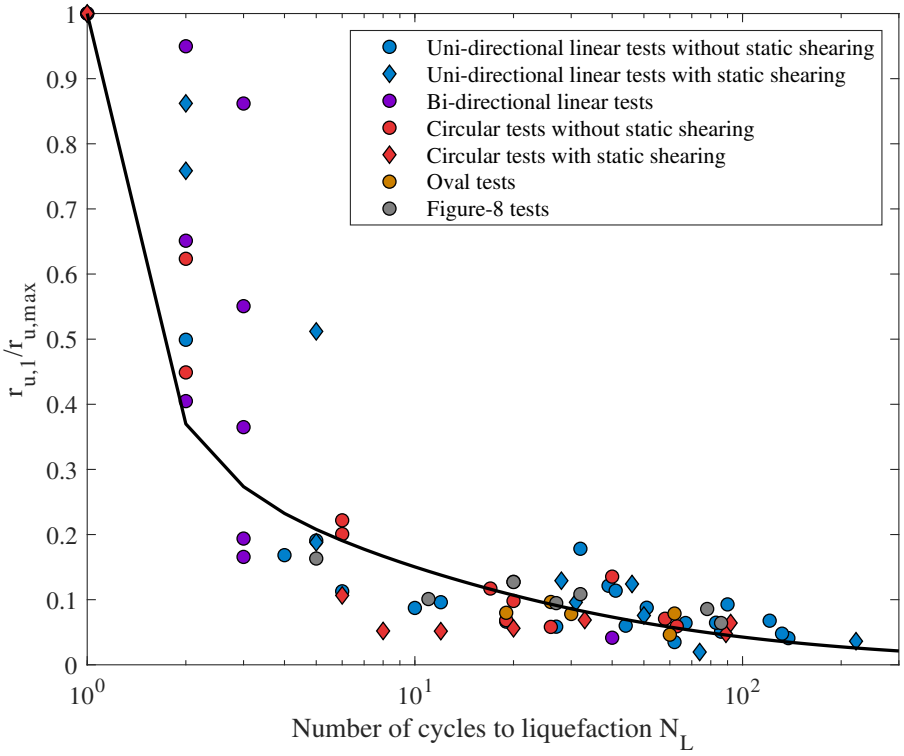

(b) The relationship between the normalised excess pore pressure ratio in the first cycle and the number of cycles to liquefaction (the solid curve gives equation 7.6)

Fig. 7.14 The relationship between the excess pore pressure ratios in the first cycle and the number of cycles to liquefaction in all tests in this study

This section summarizes the characteristics of multi-directional shear strain development that are observed in the tests in this study. It needs to be emphasized again that the sudden change of stress from zero to a point on the loading path was avoided in the tests. For loading paths such as circular and oval ones, a ramp loading was conducted first in drained conditions to drive the shear stress to a point on the loading paths before cyclic shearing is applied in undrained condition. The "zero" strain point is defined as the point before cyclic loading starts rather than the point prior to ramp loading. Different values of total shear strain were obtained if zero-strain point is assigned differently.

First and foremost, the geometry of strain paths is analogous to that of stress paths. Figure 7.15 compares the plan-view shear stress and strain of uni-directional linear test LC-7, oval test E2010-3 and circular test C20-3 (loading proceeded in the anticlockwise direction). The three tests have the same CSR_{dir} at 0.2 with the primary shear directions assigned to the X axis, as shown in Figure 7.15a. Clearly, the strain paths of the these tests reflect the geometrical features of their stress paths. The shear strain accumulates in a circular way in the circular test. By contrast, the uni-directional test has minimal shear stress on the direction perpendicular to cyclic shearing and thus has only marginal shear strain in that direction. The major direction of the shear strain development in the oval test is generally in accordance with the orientation of the major axis of its elliptical stress paths. Similar trends can also be seen in other categories of loading paths. For instance, three figure-8 tests which have similar relative density and the same major-direction shear stress ratio of 0.15 are compared in Figure 7.16. The plan-view shear strain of the three tests all show the butterfly-like geometry. As test F8-6 has smaller shearing in the perpendicular direction ($SSR_{Y,max}$ is 0.075 in test F8-6 and 0.15 in F8-2 and F8-5), the strain accumulated in Y direction in test F8-6 is limited compared with the other two tests.

However, it is found that the strain paths of oval tests and figure-8 tests exhibit special characteristics that are not seen explicitly in uni-directional and circular tests. The strain paths in oval tests tend to rotate when the amplitude of shear strain increases dramatically and liquefaction is approached. The explanation is related the variation of excess pore pressure within a loading cycle.

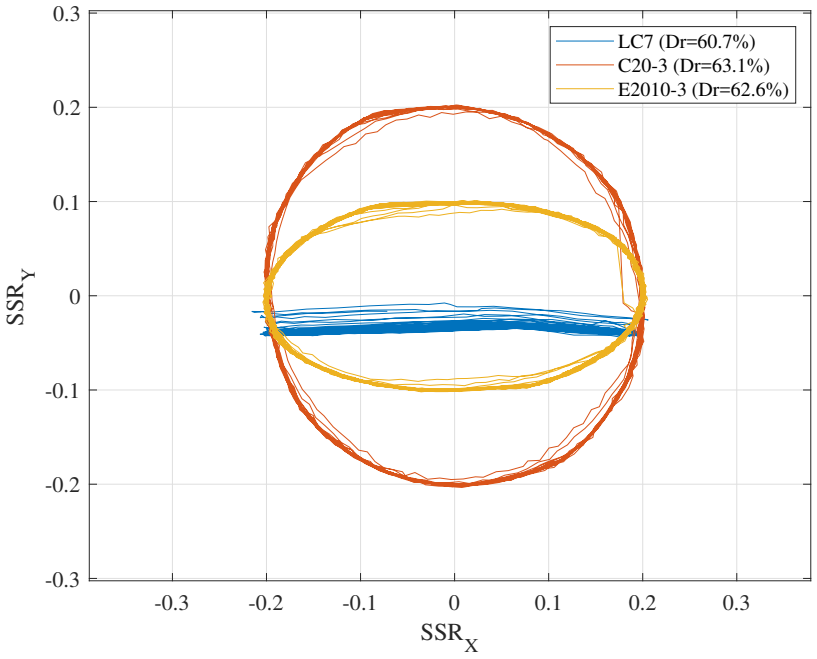

(a) Plan view of shear stress ratio

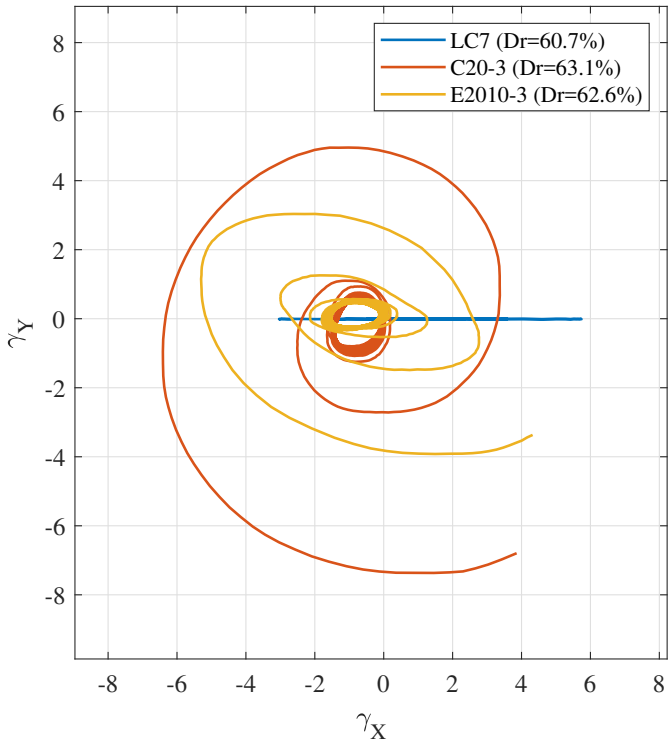

(b) Plan view of shear strain

Fig. 7.15 Comparison of uni-directional linear, oval and circular tests with the same CSR_{dir} at 0.2

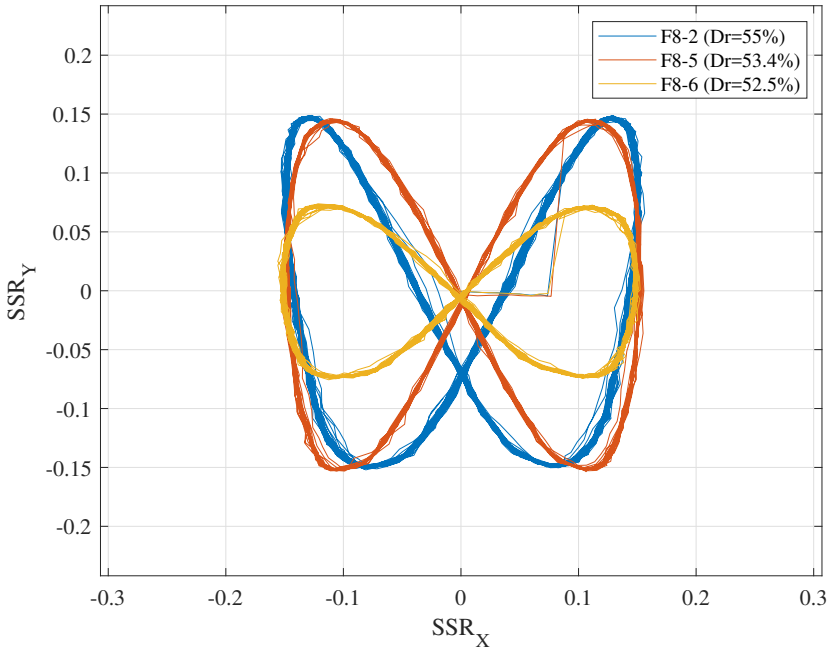

(a) Plan view of shear stress ratio

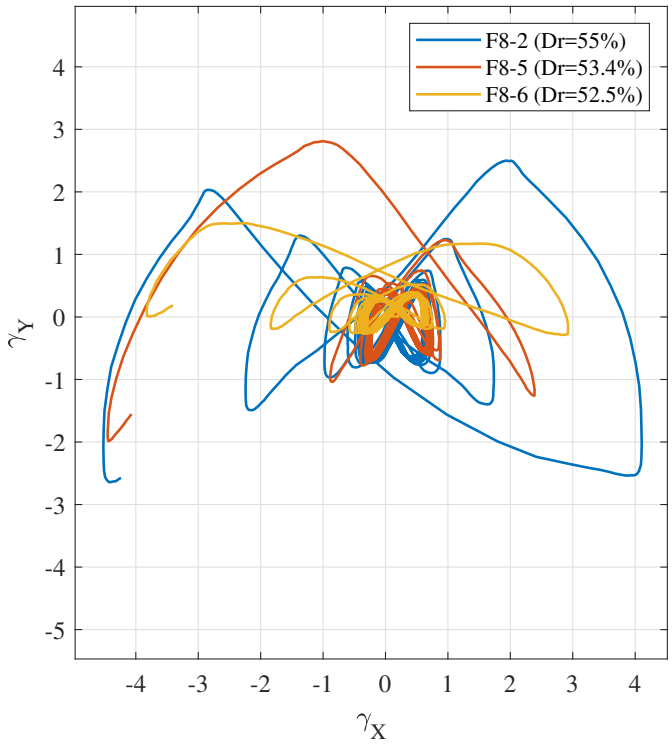

(b) Plan view of shear strain

Fig. 7.16 Comparison of three figure-8 tests with the same CSR_{dir} at 0.15

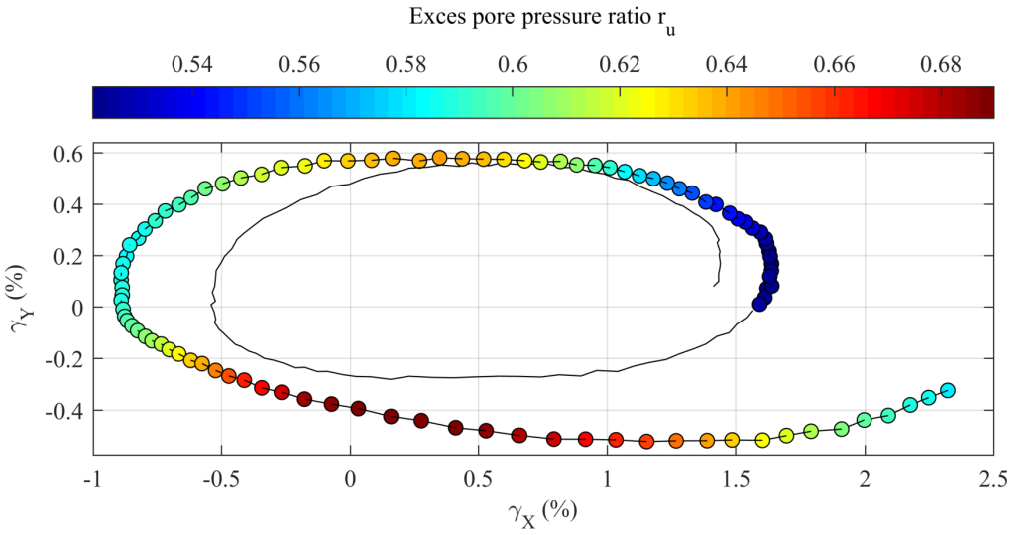

(a) Plan view of shear strain with excess pore pressure ratio

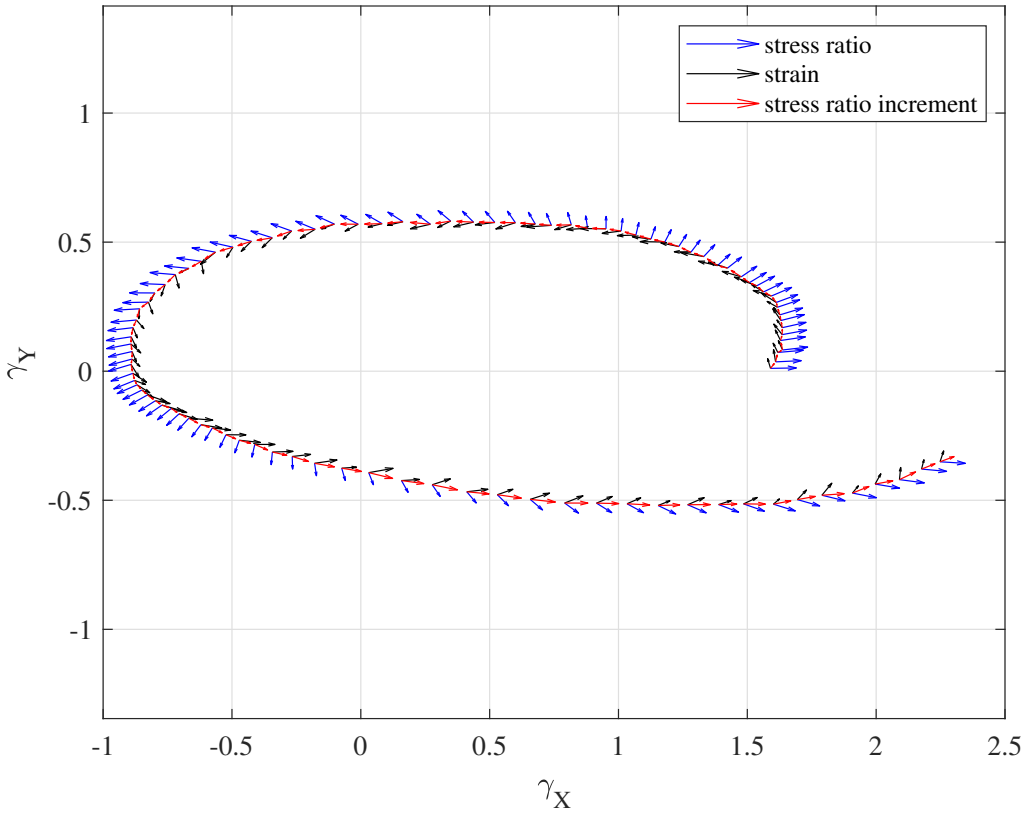

(b) Plan view of stress ratio vector, stress ratio increment vector and strain increment vector

Fig. 7.17 Plan-view shear strain analysis of the 58th cycle in test E2010-3

Figure 7.17a presents the plan view of shear strain of the 58th cycle of oval test E2010-3. Excess pore pressure ratio is indicated by the colour of the data points. The strain of the 57th cycle is also shown as a reference, without excess pore pressure ratio. This cycle is the one where the strain path of the test starts to rotate considerably as shown in Figure 7.15. The shear strain accumulates along an oval route in a similar alignment to the elliptical stress path in the first half of the cycle, but dramatic deviation takes place subsequently. The most distinct development of shear strain occurs when excess pore pressure ratio exceeds 0.65, which is reflected in the increasing distance between neighbouring data points.

Figure 7.17b plots the same strain path with stress ratio vectors and stress ratio increment vectors calculated from the plan view of the shear stress but plotted onto the strain path. The length of the stress ratio vectors is equivalent to SSR_{total}. Strain vector is not shown to prevent the "zero" strain issue from misleading the interpretation of test results. Comparing Figure 7.17b with 7.17a, there is a close connection between the length of strain increment vectors and excess pore pressure ratio. The shortest strain increment vectors are seen in the section where excess pore pressure is also the lowest, while the longest strain increment vectors appear where excess pore pressure is the highest (the dark red part in Figure 7.17a). Before excess pore pressure reaches 0.65, the variation of strain increment vectors follows a roughly symmetrical pattern, maintaining a stable geometry of the strain path. When excess pore pressure ratio exceeds 0.65, the difference between the smallest and largest strain increment increases. Huge strain accumulates towards the direction of those long strain increment vectors, while less strain develops in the direction of short ones. As a consequence, the development of the strain path is diverted, appearing like a rotation.

Furthermore, there is a seemingly inverse relationship between the length of strain increment vectors and stress ratio vectors. Where strain increment vectors are long, stress ratio vectors are always shorter. However, such a relationship is in fact a biased perception of that between excess pore pressure and strain increment. The reason why such a relationship seems to exist is that the length of stress ratio vectors can reflect the general results of loading and unloading, while the latter, as discussed in Chapter 6, affects the variation of excess pore pressure within a shearing cycle. This can be demonstrated by the fact that the points of

equal SSR_{total} do not necessarily have the same excess pore pressure ratio. In Figure 7.17b, for instance, the initial point and the end point on the path have almost the same rightward stress ratio vector with SSR_{total} at 0.2, but the strain increment vector of the end point is much longer than the initial one because the excess pore pressure ratio at the end of this cycle is larger than that at the beginning.

The relationship between the increment of total shear strain versus excess pore pressure is presented in Figure 7.18 for all tests, with the data of test E2010-3 coloured red. Despite considerable scatter, it appears that an excess pore pressure threshold exists in all tests, before which the strain increment is low and stable but after which strain increment starts to rise. For test E2010-3, this threshold is around 0.65, consistent with the preceding observations. The examination of all the tests indicates that the threshold ranges from 0.55 to 0.7 across different tests. This finding suggests that the softening of undrained sands reaches a significant degree when excess pore pressure exceeds a certain threshold. Measures should be taken in geotechnical engineering practice to prevent this threshold from being reached to avoid detrimental deformation.

Close inspection of Figure 7.17b unveils more implications. The relationship between strain increment vectors and stress ratio increment vectors is not clear. The insignificant variation of the length of stress ratio increment vectors suggests that the amplitude of stress ratio increment does not affect directly that of the strain increment. Discernible non-coaxiality also exists between stress increment and strain increment, with strain increment vectors rotating gradually towards the direction of shear stress ratio increment counterparts. Clearly, the interaction between shear strain and stress involves not only amplitude but also orientation in multi-direction loading conditions. The effects of directionality should be taken into consideration if the objective of predicting multi-directional soil deformation is to be achieved.

The pattern of shear strain development is further complicated if static shearing is introduced. Figure 7.19 compares three circular tests with different static shearing. The shear strain of post-liquefaction cycles is also included in Figure 7.19b in dotted form. Test C15-2 has no static shearing and thus has a spiral strain path. Test C15-X15-1, on the contrary, has

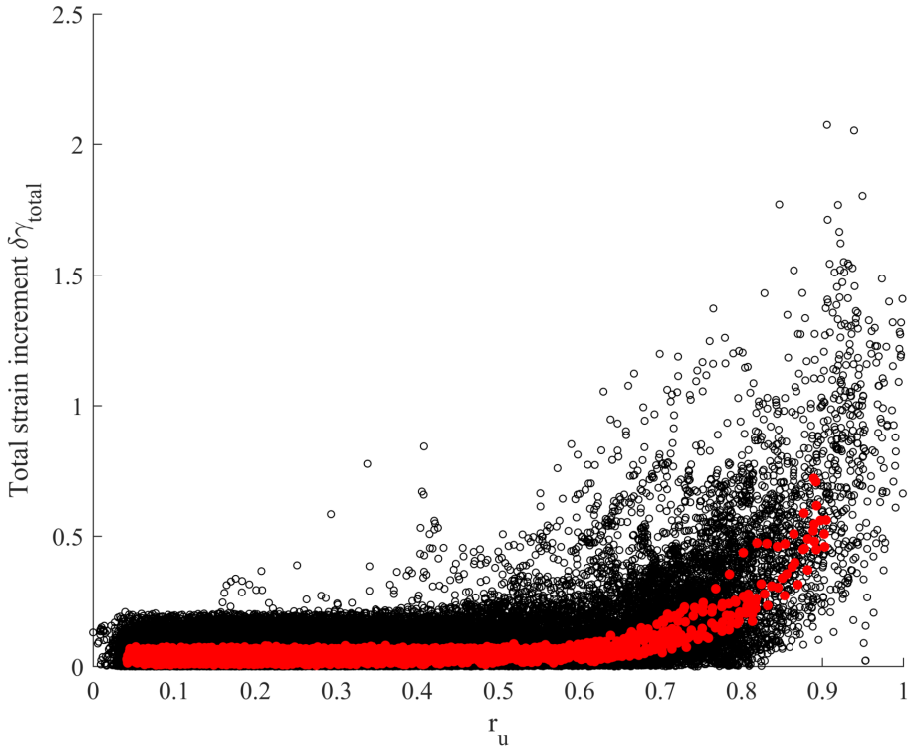

Fig. 7.18 The increment of total shear strain versus excess pore pressure ratio in all tests (test E2010-3 is coloured red)

the largest static shearing that eliminates stress reversal in the X direction. Shear strain in this test accumulates primarily along the X direction with only marginal strain developing in the Y direction. By contrast, test C15-X7.5-1 has moderate static shearing, whose strain path has off-centred spiral geometry that combines the features of the other two tests.

There is a clear tendency of shear strain to accumulate towards the direction of static shearing. A similar observation has been reported for both sands and clay (Biscontin et al., 2004; Kammerer, 2002; Rutherford, 2012). This implies that downhill deformation (landslide) can take place in sloping ground no matter what direction the cyclic shearing is in. The seismic safety of the structures and infrastructures constructed on sloping ground cannot be taken for granted even if the inclination is small, especially when serviceability is crucial.

Another observation is related to the case with static shearing larger than the amplitude of cyclic shearing resulting in no stress reversal in the downhill direction, such as test C15-X15-1. The deformation potential in the strike direction is limited under such circumstance. After

liquefaction happens, shear strain increases rapidly in both dip (X) and strike (Y) direction in test C15-2 and C15-X7.5-1. In test C15-X15-1, by contrast, shear strain rises only in the dip direction, while in the strike direction is restrained though stress reversal occurs. Kammerer (2002) suggested that this phenomenon is a result of limited stress rotation. The orientations of stress vectors range roughly from -90° to 90° relative to positive X axis in test C15-X15-1, while ranging from -180° to 180° in the other two tests. Full rotation of stress vector does not occur when stress reversal is inhibited in a direction, resulting in limited development of strain in test C15-X15-1. Evidently, the specific geometry of a loading path exerts influence over the deformation of soil, which should not be overlooked by academic and practical seismic research.

The findings regarding the development of shear strain in multi-directional loading scenarios are summarised:

(1) Shear strain in multi-directional loading conditions develops in an analogous manner to shear stress. The general geometry of the strain path reflects the features of the stress path. Strain paths are diverted, depending on the specific loading path, when excess pore pressure exceeds a certain threshold.

(2) A threshold in terms of excess pore pressure ratio is found to separate the period of limited strain accumulation from the period of flow-type strain development. The excess pore pressure ratio threshold ranges from 0.55 to 0.7 for the tests in this study. Within a loading cycle, the parts with excess pore pressure higher than this threshold witness more pronounced shear strain increments, while the other parts have less significant strain increments. The variation of excess pore pressure within a shearing cycle can result in the deviation of a strain path from the expected course.

(3) There is no clear correlation between the amplitude of strain increment and that of stress increment. The direction of the stress increment vector is related to the stress increment vector. The complex non-coaxiality between stress increment and strain increment needs to be taken into consideration in predicting the development of shear strain in multi-directional loading conditions.

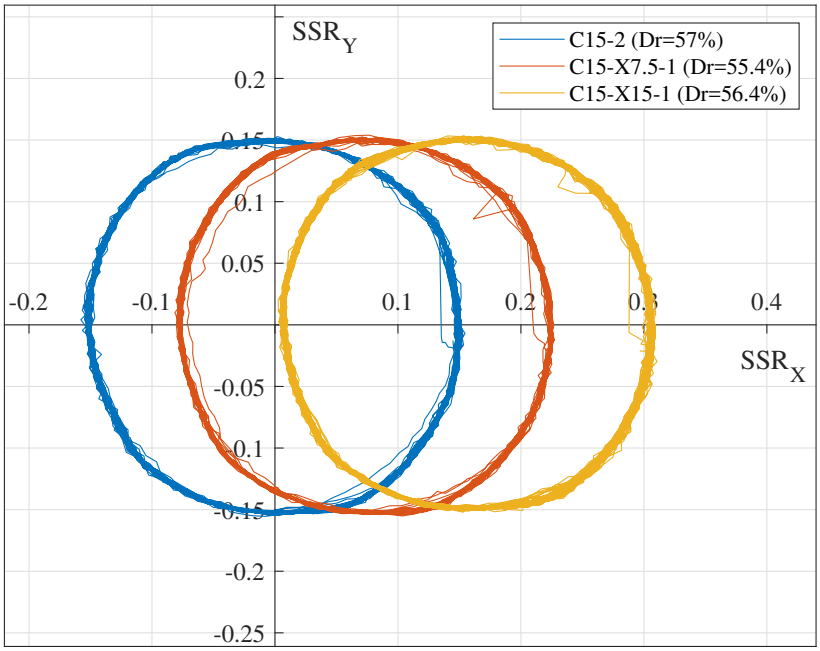

(a) Plan view of shear stress ratio

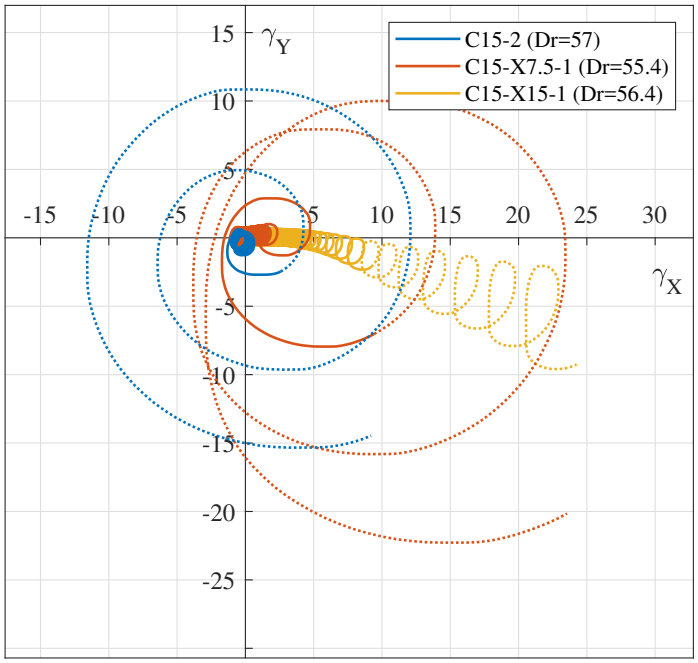

(b) Plan view of shear strain (post-liquefaction cycles are included)

Fig. 7.19 Comparison of three circular tests with different initial static shearing

(4) The existence of static shearing can further complicate the development of shear strain. Downhill accumulation of shear strain happens no matter what direction cyclic shearing is applied in, which can put the seismic safety and the serviceability of the structures on sloping ground in peril. Over-large static shearing can also eliminate stress reversal and constrain the rotation of shear stress and thus restrain the development of shear strain in strike direction.

7.5 The degradation of Shear modulus in multi-directional simple shear tests

Shear modulus degradation is one of most important characteristics of soil under shearing. In uni-directional simple shear tests, secant shear modulus is commonly selected to produce shear modulus degradation curves, which is defined conveniently through stress-strain hysteresis loops as the ratio of double-amplitude cyclic shear stress over double-amplitude shear strain. In multi-directional shearing condition, this definition of shear modulus becomes inadequate.

A unique stress-strain hysteresis loop cannot be obtained. If the direction of shear stress and strain is taken into account, the relationship between stress and strain becomes a four-dimension problem, and there is yet an effective method to derive such a relationship. If the directionality is by-passed through the use of parameters such as total shear stress and total shear strain, the meaning of stress-strain curves becomes doubtful. For instance, the total shear stress-strain curve of circular test C20-3 as presented in Figure 5.11 is actually a straight line. Should a secant total shear modulus be determined from it, the modulus will always be zero, which does not give much information about the actual relationship between shear stress and strain, if any.

Although a shear modulus can still be defined by the real-time shear stress and shear strain, the significance of this modulus is ambiguous because of the non-coaxiality between shear stress and shear strain, as well as between stress increment and strain increment, not to mention the mathematical difficulty in coping with zero strain.

Furthermore, the definition of zero strain is another issue that can cause misleading estimates of shear modulus. In the tests in this study, cyclic loading always starts from a point on the loading paths rather than zero-shear state to avoid an abrupt increase in shearing, and zero-strain is assigned correspondingly at the point where cyclic loading starts. If the condition of zero-shear is selected as the point to begin the measurement of shear strain, all the calculation related total shear strain changes, including total-strain-based shear modulus.

Under this circumstance, a multi-directional secant shear modulus G is proposed here for multi-directional shearing condition as follows:

$$G = \frac{\tau_{dir,DA}}{\gamma_{dir,DA}} \tag{7.7}$$

where $\tau_{dir,DA}$ is the maximum distance between any two points on the plan view of shear stress path of a loading cycle, as defined by equation 7.3, while $\gamma_{dir,DA}$ represents the maximum distance on strain path, following equation 7.1. It should be noted that $\tau_{dir,DA}$ and $\gamma_{dir,DA}$ does not necessarily occur simultaneously like τ_{DA} and γ_{DA} does in uni-directional tests, because of the non-coaxiality.

Figure 7.20 presents the degradation of multi-directional secant shear modulus G with multi-directional double-amplitude shear strain $\gamma_{dir,DA}$ in all the tests in this study. A similar plot for uni-directional tests was shown in Figure 4.22. G_{max} is the small-strain shear modulus proposed by Hardin and Drnevich (1972) based on uni-directional tests, and the cyan dotted curves are their prediction curves (equation 4.6). What is impressive is that $G/G_{max} - \gamma_{dir,DA}$ of multi-directional tests fits satisfactorily with the prediction of Hardin and Drnevich, even though the latter was derived from hyperbolic stress-strain curve assumption which is tenable only in uni-directional loading condition. Whether this finding holds true for small strain cannot be examined with the tests in this study, but for the shear strain range over 1%, the degradation of multi-directional secant shear modulus can be predicted adequately by Hardin and Drnevich's method.

In addition to shear strain, the degradation of shear modulus with excess pore pressure is also worthy of examination because they are both related to soil softening. Figure 7.21

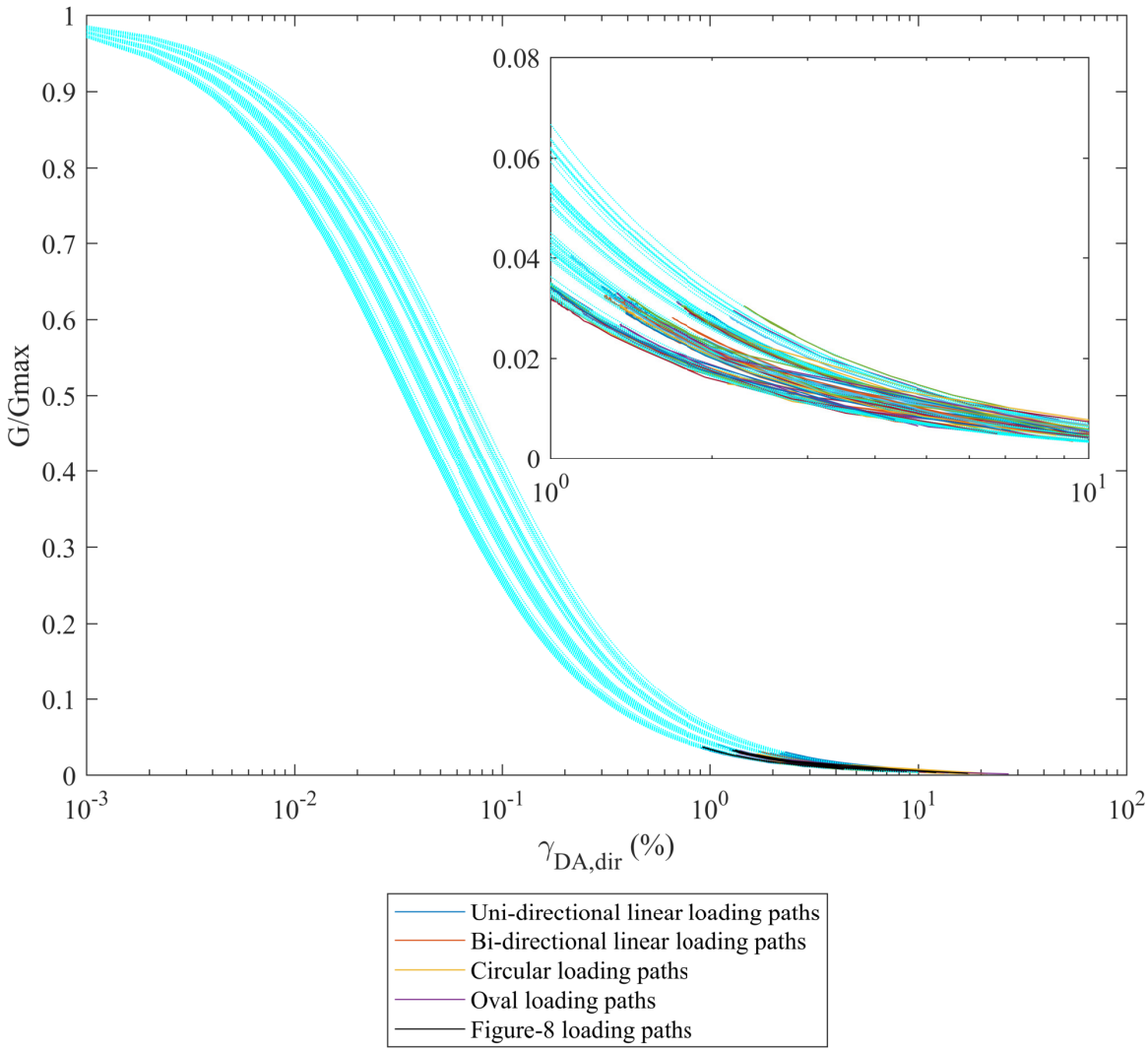

Fig. 7.20 The degradation of multi-directional secant shear modulus with multi-directional double-amplitude shear strain

presents the degradation of multi-directional secant shear modulus with excess pore pressure ratio. The shear modulus is normalised by the 2nd-cycle shear modulus with the same reason as discussed in section 4.4. The bold black curve represents equation 4.7, which was fitted from uni-directional test results in Figure 4.23.

Compared with Figure 4.23, the degradation curves of multi-directional tests are more scattered at large excess pore pressures, especially in the cases where the maximum excess

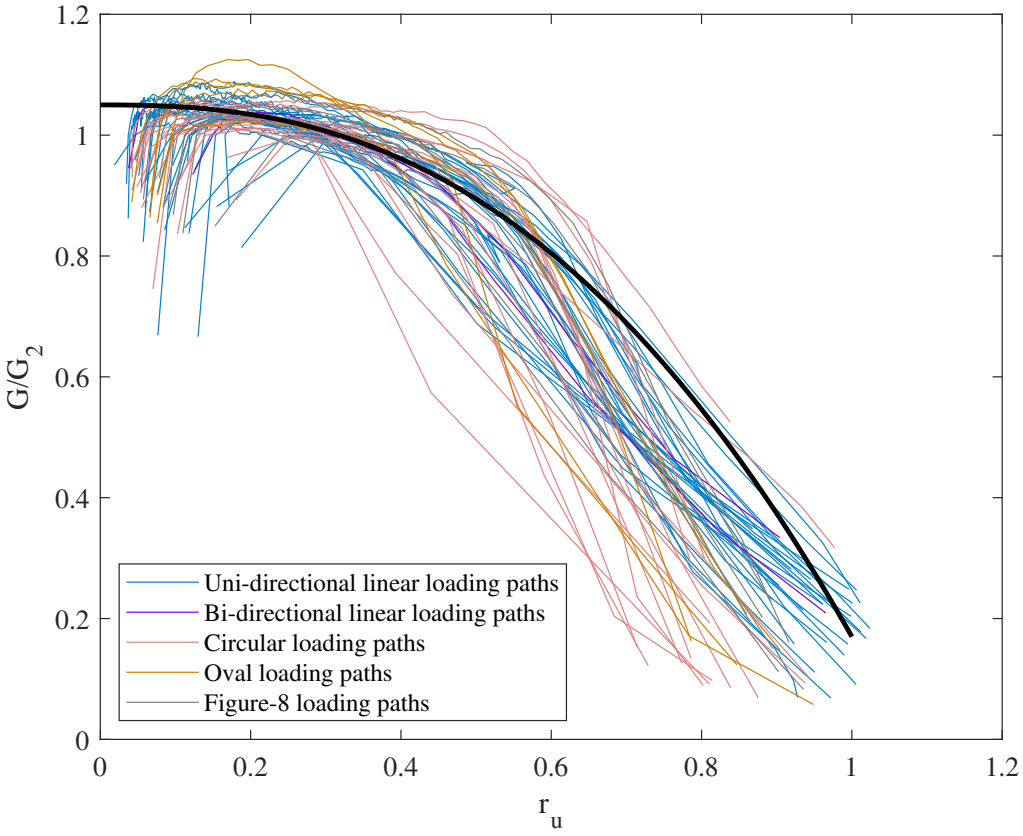

Fig. 7.21 The degradation of shear modulus with excess pore pressure ratio

pore pressure ratio is far less than unity. However, the two-stage overall degradation tendency is unchanged. When excess pore pressure ratio is lower than 0.3-0.4, the softening of sands is not significant and shear modulus degrades with a slow but almost constant rate. After excess pore pressure exceeds the threshold, the decline of shear modulus accelerates. Shear modulus decreases generally to less than 40% of G_2 when liquefaction takes place. Furthermore, the degradation of normalised shear modulus with excess pore pressure is not affected significantly by the category of loading paths. This suggests that such a degradation is a type of potential characteristic of saturated sands in undrained simple shear tests, regardless of loading paths.

In conclusion, multi-directional secant shear modulus following equation 7.7 is recommended as an alternative to the uni-directional counterpart. The relationship between G/G_{max} and $\gamma_{dir,DA}$ in multi-directional tests is in accordance with the prediction proposed by Hardin

and Drnevich (1972) for uni-directional tests. The degradation of multi-directional secant shear modulus with either double-amplitude shear strain or excess pore pressure ratio can be regarded as a characteristic of saturated sands which is not altered by loading paths.

Chapter 8

CONCLUSIONS AND FUTURE WORK

8.1 Conclusions

Four decades after it was investigated experimentally for the first time, the influence of multi-directional shearing on soil behaviour, especially the undrained behaviour of saturated sands, remains one of the least understood areas in geotechnics. This study presents a new test database of Hostun sand using the modified multi-directional simple shear testing apparatus and testing techniques. Remarkable differences between undrained soil behaviour under uni-directional and multi-directional shearing were observed. The effectiveness, as well as the necessity, of interpreting the stress paths of soil in a three-dimensional $\tau - \sigma'_v$ space were illustrated. A conical failure surface is found to be the best description of the failure envelope. Phase transformation was shown to exhibit bimodal features, with a conical phase transformation surface observed in the tests with circular, oval and figure-8 loading paths but not in bi-directional linear tests. Liquefaction criteria, liquefaction resistance assessment, development of excess pore pressure and shear strain, as well as the degradation of shear modulus, were investigated in multi-directional shearing conditions, with a discussion of the definitions of shear stress, shear strain and shear modulus in multi-directional loading scenarios.

The findings of this study are summarised as follows:

(1) The membrane problem in undrained simple shear tests can be solved by applying physical constraints to the full height of sample assembly. The modified multi-directional simple shear testing apparatus and testing techniques produce reasonable test data.

(2) Interpretation of multi-directional tests exclusively in 2D $\tau - \sigma_v'$ plane is not adequate because the spatial features of the stress path and excess pore pressure development are not fully captured. Multi-directional shearing should be analysed in a 3D $\tau - \sigma_v'$ space where the soil response can be fully examined.

(3) A conical failure surface is derived from the 2D failure lines. The failure cone is a more useful concept to describe the failure envelope of sand. Failure lines in 2D $\tau - \sigma_v'$ plane are the cross section of the failure cone on a plane through its axis.

(4) The phenomenon that the stress paths in bi-directional linear tests cannot reach failure lines in the 2D $\tau - \sigma_v'$ plane can be explained by the failure cone. The stress paths of bi-directional linear tests are located on a plane that is parallel to the failure cone axis. The conic section between the plane and the cone is a hyperbola. The stress paths of bi-directional linear tests viewed in 2D $\tau - \sigma_v'$ plane cannot exceed the hyperbolic failure envelope.

(5) The widely-observed inverse correlation between the limiting excess pore pressure ratio and shear stress amplitude is also a result of the failure cone. The smaller the minimum total shear stress ratio, the closer a stress path can approach the vertex of failure cone, thus the higher the maximum excess pore pressure ratio. By contrast, the higher the maximum total shear stress ratio, the farther away from the cone vertex a stress path can reach after failure, hence the lower the minimum excess pore pressure ratio in post-liquefaction cycles.

(6) Phase transformation in multi-directional shearing conditions exhibits a bimodal feature. A conical phase transformation surface is found in the tests with circular, oval and figure-8 loading paths, as evidenced by the changing location of phase transformation

state points, whereas in bi-directional linear tests, the phase transformation states on the plane containing stress paths do not fall on a hyperbola.

(7) Liquefaction criteria based on either excess pore pressure ratio or shear strain need to be modified for multi-directional tests. It was found in this study that $r_{u,max} = 1 - \frac{SSR_{total,min}}{tan\phi_{FL}}$ and $\gamma_{dir,DA} = 6\%$ can be used as an effective liquefaction criterion in multi-directional shearing conditions.

(8) Based on the liquefaction resistance assessment method proposed by Seed and Harder (1990), a coefficient of multi-directional loading defined by K_μ was used in this study for the convenience of analysis. The lowest K_μ obtained was 0.57, corresponding to a reduction of 43% of the required cyclic shear stress ratio to trigger liquefaction. K_μ is smaller than unity in most cases, indicating that multi-directional shearing tends to reduce the liquefaction resistance of the medium to dense sand tested in this study.

(9) It is recognised that the cyclic shear stress ratio CSR equals the maximum total shear stress ratio SSR_{total} in the uni-directional tests on which Seed's liquefaction assessment method was based. There is a possibility that $N - SSR_{total}$ curves can be used as the alternative to the $N - CSR$ curves. The assessment of liquefaction resistance with $N - SSR_{total}$ relationships indicated that contradictory conclusions may be obtained regarding the effects of initial static shearing.

(10) The relationship between the excess pore pressure and normalised cycle number is not altered significantly by the type of loading path, as is the relationship between the number of cycles to trigger liquefaction and the excess pore pressure ratio generated in the first loading cycle.

(11) The development of shear strain within a loading cycle is highly associated with the variation of the excess pore pressure ratio in the same cycle. An excess pore pressure ratio threshold was found at approximately 0.55-0.7, beyond which the strain increment increases dramatically.

(12) When initial static shearing is applied, shear strain accumulates towards the direction of static shearing regardless of the direction of the cyclic shearing. If the initial static shear is large enough to eliminate stress reversal in the downhill direction, the shear strain in the strike direction will be restrained, which can be attributed to the reduced stress rotation reported by Kammerer (2002).

8.2 Future work

The insights gained in this study provide novel perspectives to understand undrained soil behaviour under multi-directional loading and can be used to modify existing models to better predict the response of sands of interest. Nonetheless, further research regarding multi-directional shearing should be conducted to develop a more advanced understanding of this topic. The recommendations for future work are summarised as follows:

(1) More in-depth investigation on the formation of shear band under multi-directional loading is needed to develop insights into the mechanisms of phase transformation.

(2) Simple shear testing techniques could be further improved for more accurate measurements of the critical state void ratio, thereby integrating the critical state theory to consistently investigate the effects of the state parameter.

(3) The liquefaction assessment method based on $N - CSR$ relationships should be re-evaluated systematically to provide better safety guidelines for engineering design.

(4) Methods to characterise loading paths need to be developed so that the effects of an arbitrary loading path can be identified.

(5) Tests with irregular multi-directional loading paths could be conducted to provide a more consistent determination of the effects of realistic loading paths.

(6) The effects of the degree of saturation on multi-directional soil behaviour should be examined to provide a more comprehensive understanding of unsaturated soil.

(7) The effects of the fines content should be explored in multi-directional loading scenarios. The multi-directional deformation of soil matrix may have interactions with different soil structure caused by the existence of the fines content.

(8) The anisotropy of soil in terms of stiffness and fabrics may affect the soil behaviour under multi-directional loading and is worthy of investigation.

(9) Deformation-related models, especially those based on the degradation of shear modulus, should be re-examined to account for the directionality of shear stress and strain.

(10) Multi-directional discrete element modelling could be developed to investigate the effects of multi-directional shearing from a micro mechanical perspective.

(11) Dynamic soil-structure and soil-foundation-structure models need to be modified to take the effects of multi-directional stress and strain into consideration. Multi-directional dynamic deformation of soils, foundation and structures may result in unexpected torque in high-rise structures with peculiar layout and facets, thus resulting in more severe damage.

(12) Multi-directional physical modelling tests, particularly centrifuge tests, should be conducted to explore the influence of loading paths from a more practical point of view.

References

Amini, F. and Qi, G. (2000). Liquefaction testing of stratified silty sands. *Journal of Geotechnical and Geoenvironmental Engineering*, 126(3):208–217.

Ampadu, S. K. and Tatsuoka, F. (1993). A hollow cylinder torsional simple shear apparatus capable of a wide range of shear strain measurement. *Geotechnical Testing Journal*, 16(1):3–17.

ASTM D6467-13 (2013). Standard test method for torsional ring shear test to determine drained residual shear strength of cohesive soils. Standard, ASTM.

Been, K., Jefferies, M., and Hachey, J. (1991). Critical state of sands. *Geotechnique*, 41(3):365–381.

Been, K. and Jefferies, M. G. (1985). A state parameter for sands. *Géotechnique*, 35(2):99–112.

Bernhardt, M. L. (2013). *Examination of granular material behavior in a laminar-type direct simple shear device using laboratory validated discrete element method simulations*. PhD thesis, Texas A&M University.

Biscontin, G., Pestana, J., and Nadim, F. (2004). Seismic triggering of submarine slides in soft cohesive soil deposits. *Marine Geology*, 203(3-4):341–354.

Bjerrum, L. and Landva, A. (1966). Direct simple-shear tests on a norwegian quick clay. *Geotechnique*, 16(1):1–20.

Black, D. K. and Lee, K. L. (1973). Saturating laboratory samples by back pressure. *Journal of the soil mechanics and foundations division*, 99(1):75–93.

Boulanger, R. W. (1990). *Liquefaction behavior of saturated cohesionless soils subjected to uni-directional and bi-directional static and cyclic simple shear stresses*, volume 2. University of California, Berkeley.

Boulanger, R. W., Chan, C. K., Seed, H. B., Seed, R. B., and Sousa, J. B. (1993). A low-compliance bi-directional cyclic simple shear apparatus. *Geotechnical Testing Journal*, 16(1):36–45.

Boulanger, R. W. and Seed, R. B. (1995). Liquefaction of sand under bidirectional monotonic and cyclic loading. *Journal of Geotechnical Engineering*, 121(12):870–878.

Broms, B. and Casbarian, A. (1965). Effects of rotation of the principal stress axes and of the intermediate principal stress on the shear strength. In *Proceedings of the 6th ICSMFE*, volume 1, pages 179–183.

Carraro, J. A. H. (2004). *Mechanical behavior of silty and clayey sands*. PhD thesis, Purdue University.

Casagrande, A. (1936). Characteristics of cohesionless soils affecting the stability of slopes and earth fills. *Journal of Boston Society of Civil Engineers*, 23(1):13–32.

Casagrande, A. (1976). *Liquefaction and cyclic deformation of sands-a critical review*. Harvard Soil Mechanics Series No. 88, Cambridge: Harvard University.

Casagrande, A. and Rendon, F. (1978). Gyratory shear apparatus; design, testing procedures, and test results on undrained sand. Technical report, Harvard University Soil Mechanics Lab, Cambridge.

Castro, G. (1969). *Liquefaction of sands*. PhD thesis, Harvard University.

Castro, G. (1975). Liquefaction and cyclic mobility of saturated sands. *Journal of the Geotechnical Engineering Division*, 101(6):551–569.

Chang, C. S. and Whitman, R. V. (1988). Drained permanent deformation of sand due to cyclic loading. *Journal of geotechnical engineering*, 114(10):1164–1180.

Clough, G. W., Iwabuchi, J., Rad, N. S., and Kuppusamy, T. (1989). Influence of cementation on liquefaction of sands. *Journal of Geotechnical Engineering*, 115(8):1102–1117.

Coelho, P. (2007). *In situ densification as a liquefaction resistance measure for bridge foundations*. PhD thesis, University of Cambridge.

DeGroot, D. J. (1992). *The multidirectional direct simple shear apparatus with application to design of offshore arctic structures*. PhD thesis, Massachusetts Institute of Technology.

DeGroot, D. J., Germaine, J. T., and Ladd, C. C. (1993). The multidirectional direct simple shear apparatus. *Geotechnical Testing Journal*, 16(3):283–295.

DeGroot, D. J., Germaine, J. T., and Ladd, C. C. (1994). Effect of nonuniform stresses on measured dss stress-strain behavior. *Journal of geotechnical engineering*, 120(5):892–912.

Degroot, D. J., Ladd, C. C., and Germaine, J. T. (1996). Undrained multidirectional direct simple shear behavior of cohesive soil. *Journal of geotechnical engineering*, 122(2):91–98.

Doanh, T., Ibraim, E., and Matiotti, R. (1997). Undrained instability of very loose hostun sand in triaxial compression and extension. part 1: experimental observations. *Mechanics of Cohesive-frictional Materials*, 2(1):47–70.

Duku, P. M., Stewart, J. P., Whang, D. H., and Venugopal, R. (2007). Digitally controlled simple shear apparatus for dynamic soil testing. *Geotechnical Testing Journal*, 30(5):368–377.

Duku, P. M., Stewart, J. P., Whang, D. H., and Yee, E. (2008). Volumetric strains of clean sands subject to cyclic loads. *Journal of geotechnical and geoenvironmental engineering*, 134(8):1073–1085.

Escribano, D. E., Nash, D. F. T., and Diambra, A. (2018). Local and global volumetric strain comparison in sand specimens subjected to drained cyclic and monotonic triaxial compression loading. *Geotechnical Testing Journal*. https://doi.org/10.1520/GTJ20170054.

Ezaoui, A. and Benedetto, H. D. (2009). Experimental measurements of the global anisotropic elastic behaviour of dry hostun sand during triaxial tests, and effect of sample preparation. *Géotechnique*, 59(7):621–635.

Franke, E., Kiekbusch, M., and Schuppener, B. (1979). A new direct simple shear device. *Geotechnical Testing Journal*, 2(4):190–199.

Fukutake, K. and Matsuoka, H. (1989). A unified law for dilatancy under multi-directional simple shearing. *Doboku Gakkai Ronbunshu*, 1989(412):143–151.

Georgiannou, V. and Konstadinou, M. (2014). Effects of density on cyclic behaviour of anisotropically consolidated ottawa sand under undrained torsional loading. *Géotechnique*, 64(4):287.

Goodman, R. E. (1989). *Introduction to rock mechanics*. New York: Wiley.

Harder, J., Leslie, F., and Boulanger, R. (1997). Application of K_σ and K_α correction factors. In *Technical Report NCEER*, volume 97, pages 167–179. US National Center for Earthquake Engineering Research (NCEER).

Hardin, B. O. and Drnevich, V. P. (1972). Shear modulus and damping in soils: design equations and curves. *Journal of Soil Mechanics & Foundations Div*, 98(sm7).

Høeg, K., Dyvik, R., and Sandbækken, G. (2000). Strength of undisturbed versus reconstituted silt and silty sand specimens. *Journal of geotechnical and geoenvironmental engineering*, 126(7):606–617.

Iai, S., Matsunaga, Y., and Kameoka, T. (1992). Analysis of undrained cyclic behavior of sand under anisotropic consolidation. *Soils and Foundations*, 32(2):16–20.

Ishihara, K. (1985). Stability of natural deposits during earthquakes. In *Proceedings of 11th ICSMFE*, volume 1, pages 321–376.

Ishihara, K. (1993). Liquefaction and flow failure during earthquakes. *Geotechnique*, 43(3):351–451.

Ishihara, K. and Li, S.-I. (1972). Liquefaction of saturated sand in triaxial torsion shear test. *Soils and Foundations*, 12(2):19–39.

Ishihara, K. and Nagase, H. (1988). Multi-directional irregular loading tests on sand. *Soil Dynamics and Earthquake Engineering*, 7(4):201–212.

Ishihara, K., Tatsuoka, F., and Yasuda, S. (1975). Undrained deformation and liquefaction of sand under cyclic stresses. *Soils and foundations*, 15(1):29–44.

Ishihara, K. and Yamazaki, F. (1980). Cyclic simple shear tests on saturated sand in multi-directional loading. *Soils and Foundations*, 20(1):45–59.

Ishihara, K. and Yasuda, S. (1975). Sand liquefaction in hollow cylinder torsion under irregular excitation. *Soils and Foundations*, 15(1):45–59.

Jefferies, M. (1993). Nor-sand: a simle critical state model for sand. *Géotechnique*, 43(1):91–103.

Jefferies, M. and Been, K. (2015). *Soil liquefaction: a critical state approach*. London: CRC press.

Jin, D., Luan, M.-t., and Yang, Q. (2008). Liquefaction and cyclic failure of sand under bidirectional cyclic loading. *Electronic Journal of Geotechnical Engineering*, 13.

John, K. W. (1968). Graphical stability analysis of slopes in jointed rock. *Journal of Soil Mechanics & Foundations Div*, 94(2):497–526.

Kammerer, A., Wu, J., Riemer, M., Pestana, J., and Seed, R. (2004a). A new multi-directional direct simple shear testing database. In *Proceedings of 13th World Conference on Earthquake Engineering*, number 2083.

Kammerer, A., Wu, J., Riemer, M., Pestana, J., and Seed, R. (2004b). Shear strain development in liquefiable soil under bi-directional loading conditions. In *Proceedings of 13th World Conference on Earthquake Engineering*, number 2081.

Kammerer, A. M. (2002). *Undrained response of Monterey 0/30 sand under multidirectional cyclic simple shear loading conditions*. PhD thesis, University of California, Berkeley.

Kuerbis, R. and Vaid, Y. (1988). Sand sample preparation-the slurry deposition method. *Soils and Foundations*, 28(4):107–118.

Ladd, R. (1978). Preparing test specimens using undercompaction. *Geotechnical Testing Journal*, 1(1):16–23.

Lade, P. (1973). Cubical triaxial tests on cohesionless soils. *Journal of the Soil Mechanics and Foundation Division*, 99(10):793–812.

Lashkari, A., Karimi, A., Fakharian, K., and Kaviani-Hamedani, F. (2017). Prediction of undrained behavior of isotropically and anisotropically consolidated firoozkuh sand: instability and flow liquefaction. *International Journal of Geomechanics*, 17(10):04017083.

Lee, K. L. and Fitton, J. (1968). Factors affecting the cyclic loading strength of soil. *Vibration Effects of Earthquakes on Soils and Foundations*, 450:71–95.

Li, X. S. and Dafalias, Y. F. (2011). Anisotropic critical state theory: role of fabric. *Journal of Engineering Mechanics*, 138(3):263–275.

Li, Y., Yang, Y., Yu, H.-S., and Roberts, G. (2016). Monotonic direct simple shear tests on sand under multidirectional loading. *International Journal of Geomechanics*, 17(1):04016038.

Matsuda, H., Hendrawan, A. P., Ishikura, R., and Kawahara, S. (2011). Effective stress change and post-earthquake settlement properties of granular materials subjected to multi-directional cyclic simple shear. *Soils and foundations*, 51(5):873–884.

Matsuda, H., Shinozaki, H., Okada, N., Takamiya, K., and Shinyama, K. (2004). Effects of multi-directional cyclic shear on the post-earthquake settlement of ground. In *Proceedings of 13th World Conference on Earthquake Engineering*, number 2890.

Matsuoka, H. and Nakai, T. (1974). Stress-deformation and strength characteristics of soil under three different principal stresses. In *Proceedings of the Japan Society of Civil Engineers*, volume 232, pages 59–70. Japan Society of Civil Engineers.

Meneses, J., Ishihara, K., and Towhata, I. (1998). Effects of superimposing cyclic shear stress on the undrained behavior of saturated sand under monotonic loading. *Soils and Foundations*, 38(4):115–127.

Mirbaha, K. (2017). Bi-directional cyclic behaviour and liquefaction analysis of a silica-carbonate sand. Master's thesis, The University of Western Ontario.

Mitrani, H. (2006). *Liquefaction remediation techniques for existing buildings*. PhD thesis, University of Cambridge.

Miura, S. and Toki, S. (1982). A sample preparation method and its effect on static and cyclic deformation-strength properties of sand. *Soils and foundations*, 22(1):61–77.

Mulilis, J., Townsend, F., and Horz, R. (1978). Triaxial testing techniques and sand liquefaction. In *Dynamic geotechnical testing*. ASTM International.

Murthy, T., Loukidis, D., Carraro, J., Prezzi, M., and Salgado, R. (2007). Undrained monotonic response of clean and silty sands. *Géotechnique*, 57(3):273–288.

Nagase, H. and Ishihara, K. (1987). Effects of load irregularity on the cyclic behaviour of sand. *Soil Dynamics and Earthquake Engineering*, 6(4):239–249.

Oda, M. (1972). The mechanism of fabric changes during compressional deformation of sand. *Soils and foundations*, 12(2):1–18.

Oda, M., Kawamoto, K., Suzuki, K., Fujimori, H., and Sato, M. (2001). Microstructural interpretation on reliquefaction of saturated granular soils under cyclic loading. *Journal of Geotechnical and Geoenvironmental Engineering*, 127(5):416–423.

Oda, M., Koishikawa, I., and Higuchi, T. (1978). Experimental study of anisotropic shear strength of sand by plane strain test. *Soils and foundations*, 18(1):25–38.

Peacock, W. H. (1968). Sand liquefaction under cyclic loading simple shear conditions. *Journal of Soil Mechanics & Foundations Div*, 94(3):689–708.

Priest, S. D. (1985). *Hemispherical projection methods in rock mechanics*. Allen & Unwin.

Pyke, R., Seed, H., and Chan, C. (1975). Settlement of sands under multidirectional shaking. *Journal of Geotechnical and Geoenvironmental Engineering*, 101(ASCE# 11251 Proceeding).

Reddy, K. R. and Saxena, S. K. (1992). Liquefaction resistance of cemented sands under multidirectional cyclic loading. *Canadian Geotechnical Journal*, 29(6):989–993.

Renouf, M., Acary, V., and Dumont, G. (2005). 3D frictional contact and impact multibody dynamics. A comparison of algorithms suitable for real-time applications. In *Mutlibody Dynamics 2005, ECCOMAS Thematic Conference*.

Roscoe, K. (1953). An apparatus for the application of simple shear to soil samples. In *Proceedings of 3rd ICSMFE*, volume 1, pages 186–191.

Roscoe, K. H., Schofield, A., and Wroth, C. (1958). On the yielding of soils. *Geotechnique*, 8(1):22–53.

Rothenburg, L. and Bathurst, R. (1989). Analytical study of induced anisotropy in idealized granular materials. *Geotechnique*, 39(4):601–614.

Rudolph, C., Grabe, J., and Albrecht, I. (2014). Simple shear tests with a varying shearing direction during cyclic shearing. *Géotechnique Letters*, 4(2):102–107.

Rutherford, C. and Biscontin, G. (2013). Development of a multidirectional simple shear testing device. *Geotechnical Testing Journal*, 36(6):858–866.

Rutherford, C. J. (2012). *Development of a multi-directional direct simple shear testing device for characterization of the cyclic shear response of marine clays*. PhD thesis, Texas A&M University.

Sako, N. and Adachi, T. (2004). Effect of two-directional input motion on charateristics of sands liquefaction based on pseudo-dynamic tests. In *Proceedings of 13th World Conference on Earthquake Engineering*, number 10.

Salgado, R., Bandini, P., and Karim, A. (2000). Shear strength and stiffness of silty sand. *Journal of Geotechnical and Geoenvironmental Engineering*, 126(5):451–462.

Sauer, J. and Schömer, E. (1998). A constraint-based approach to rigid body dynamics for virtual reality applications. In *Proceedings of the ACM symposium on Virtual reality software and technology*, pages 153–162. ACM.

Schofield, A. N. (2005). *Disturbed soil properties and geotechnical design*. London: Thomas Telford.

Schofield, A. N. and Wroth, P. (1968). *Critical state soil mechanics*. London: McGraw-Hill.

Seed, H., Arango, I., and Chan, C. (1975). Evaluation of soil liquefaction potential for level ground during earthquakes. a summary report. Technical report, Shannon and Wilson.

Seed, H. B. (1979). Soil liquefaction and cyclic mobility evalution for level ground during earthquakes. *Journal of Geotechnical and Geoenvironmental Engineering*, 105(2):201–255.

Seed, H. B., Idriss, I., and Arango, I. (1983). Evaluation of liquefaction potential using field performance data. *Journal of Geotechnical Engineering*, 109(3):458–482.

Seed, H. B. and Lee, K. L. (1966). Liquefaction of saturated sands during cyclic loading. *Journal of Soil Mechanics & Foundations Div*, 92(6):105–134.

Seed, H. B., Martin, G. R., and Pyke, R. M. (1978). Effect of multidirectional shaking on pore pressure development in sands. *Journal of the Geotechnical Engineering Division*, 104(1):27–44.

Seed, R. B. and Harder, L. (1990). SPT-based analysis of cyclic pore pressure and undrained residual soil strength. In *Proc., H. Boldon Seed Memorial Symp.*, volume 2, pages 351–376.

Sivathayalan, S. and Ha, D. (2011). Effect of static shear stress on the cyclic resistance of sands in simple shear loading. *Canadian Geotechnical Journal*, 48(10):1471–1484.

Sladen, J., D'hollander, R., and Krahn, J. (1985). The liquefaction of sands, a collapse surface approach. *Canadian Geotechnical Journal*, 22(4):564–578.

Stringer, M. and Madabhushi, S. (2009). Novel computer-controlled saturation of dynamic centrifuge models using high viscosity fluids. *Geotechnical Testing Journal*, 32(6):559–564.

Takahashi, H., Kitazume, M., Ishibashi, S., and Yamawaki, S. (2006). Evaluating the saturation of model ground by p-wave velocity and modelling of models for a liquefaction study. *International Journal of Physical Modelling in Geotechnics*, 6(1):13–25.

Talobre, J. (1957). *La Mccanique ties Roches*. Paris: Dunod.

Tatsuoka, F., Muramatsu, M., and Sasaki, T. (1982). Cyclic undrained stress-strain behavior of dense sands by torsional simple shear test. *Soils and Foundations*, 22(2):55–70.

Tokimatsu, K. and Yoshimi, Y. (1982). Liquefaction of sand due to multidirectional cyclic shear. *Soils and Foundations*, 22(3):126–130.

Ueng, T.-S., Wang, M.-H., Chen, M.-H., Chen, C.-H., and Peng, L.-H. (2005). A large biaxial shear box for shaking table test on saturated sand. *Geotechnical Testing Journal*, 29(1):1–8.

Vaid, Y. and Chern, J. (1985). Cyclic and monotonic undrained response of saturated sands. In *Advances in the art of testing soils under cyclic conditions*, pages 120–147. ASCE.

Vaid, Y. and Negussey, D. (1988). Preparation of reconstituted sand specimens. *Advanced Triaxial Testing of Soil and Rock*, pages 405–417.

Vaid, Y. and Sivathayalan, S. (2000). Fundamental factors affecting liquefaction susceptibility of sands. *Canadian Geotechnical Journal*, 37(3):592–606.

Vaid, Y., Stedman, J., and Sivathayalan, S. (2001). Confining stress and static shear effects in cyclic liquefaction. *Canadian Geotechnical Journal*, 38(3):580–591.

Vaid, Y. and Thomas, J. (1995). Liquefaction and postliquefaction behavior of sand. *Journal of Geotechnical Engineering*, 121(2):163–173.

Verdugo, R. and Ishihara, K. (1996). The steady state of sandy soils. *Soils and foundations*, 36(2):81–91.

Vucetic, M. and Lacasse, S. (1982). Specimen size effect in simple shear test. *Journal of the Geotechnical Engineering Division*, 108(12):1567–1585.

Wriggers, P. and Krstulović-Opara, L. (2004). The moving friction cone approach for three-dimensional contact simulations. *International Journal of Computational Methods*, 1(01):105–119.

Wu, J. (2002). *Liquefaction triggering and post-liquefaction deformation of Monterey 0/30 sand under uni-directional cyclic simple shear loading*. PhD thesis, University of California, Berkeley.

Yamamuro, J. A. and Covert, K. M. (2001). Monotonic and cyclic liquefaction of very loose sands with high silt content. *Journal of geotechnical and geoenvironmental engineering*, 127(4):314–324.

Yamamuro, J. A. and Lade, P. V. (1998). Steady-state concepts and static liquefaction of silty sands. *Journal of geotechnical and geoenvironmental engineering*, 124(9):868–877.

Yamazaki, F., Towhata, I., and Ishihara, K. (1985). Numerical model for liquefaction problem under multi-directional shearing on horizontal plane. In *Proceedings of 5th International Conference on Numerical Methods in Geomechanics*, pages 1–5.

Yee, E., Duku, P. M., and Stewart, J. P. (2013). Cyclic volumetric strain behavior of sands with fines of low plasticity. *Journal of Geotechnical and Geoenvironmental Engineering*, 140(4):04013042.